Alma Mater Studiorum – Università di Bologna

DOTTORATO DI RICERCA IN
INGEGNERIA BIOMEDICA, ELETTRICA E DEI SISTEMI

Ciclo 33

Settore Concorsuale: 09/E1 - ELETTROTECNICA

Settore Scientifico Disciplinare: ING-IND/31- ELETTROTECNICA

ANALYSIS OF ELECTRODYNAMIC TRANSIENTS IN HIGH TEMPERATURE
SUPERCONDUCTING TAPES AND COILS

Presentata da: Musso Andrea

Coordinatore Dottorato

Prof. Michele Monaci

Supervisore

Marco Breschi

Co-supervisore

Pier Luigi Ribani

Esame finale anno 2021

Abstract

As the technical interest in AC applications of devices realized with second generation High Temperature Superconductors (HTS) arises, the need of reliable numerical tools and experimental techniques to predict and measure the losses generated during electrodynamic transients increases. Besides, the performances of certain superconducting devices can be affected by time-varying regimes and must be carefully evaluated. In particular, this work focuses on superconducting coils for magnetic applications, wound in different configurations. Following a bottom-up methodology, the various aspects are first investigated at the conductor level and then extended to coils wound with such tapes.

In the first part of the work, two numerical models are presented to investigate losses in coated conductors due to a combination of an AC transport current and an AC magnetic field, by applying 2-D approximations. The first model implements a FEM analysis based on the *H*-formulation, and allows to investigate tapes including ferromagnetic layers. The second model implements an integral analysis based on the *A-V* formulation and is faster compared to the FEM model. Both methods can compute the operating conditions for which the contribution of the non-superconducting layers to the power dissipation of the whole tape are not negligible, an assumption often made in the literature. Furthermore, a methodology is presented to determine the influence of the configuration of the voltage measurement circuit on the AC losses measured in tapes, calculating a corrective factor to be applied to the experimental results. The measurement configuration most adopted in literature is compared with an alternative geometry. Conclusions are drawn regarding the correct arrangement of the signal acquisition system to reduce this undesired contribution without creating an excessive area for the linking of the fluxes in the voltage circuit.

Then, an electromagnetic methodology and a post-processing technique for the acquired signals are developed to measure the AC losses in different tapes. The method does not involve the use of lock-in amplifiers and has some advantages over traditional techniques. The experimental results are compared with those obtained by other laboratories worldwide with the same tapes, as well as with the numerical results with the developed methods.

Whereupon, the analysis is extended to the operation of HTS coils with or without electrical insulation between turns. The *defect-irrelevant* behaviour of a no-insulation (NI) coil in a pancake-wound configuration, in which some defects are intentionally inserted at desired locations, is verified. The results of the experiments carried out at different temperatures, from 4.7 K to 80 K, are treated to determine the parameters of a simple equivalent circuit in order to estimate the amount of current flowing radially in the winding in the proximity of the defects, due to the absence of insulation.

Secondly, the electrical characteristics of two HTS coils in a layer-wound configuration, with and without insulation, are compared. The coils have almost identical geometric parameters, but the electric field profiles acquired at the ends of each layer during the supply current ramp are distinct. These discrepancies are explained by the use of an equivalent lumped parameter

circuit, which allows to derive the current distribution between the turns during the tests as well as to identify the most stressed locations in terms of Joule dissipation.

Finally, the same layer-wound coils are supplied with an AC current and their power dissipation is measured experimentally, modifying properly the experimental set-up developed for HTS tapes. The measurements are discussed and correlated with the results obtained through two models which can describe the different power dissipation mechanisms involved. An equivalent circuit with lumped parameters is adopted to compute the losses due to the transverse currents, while a model obtained by extending the *H*-formulation method for the geometry of a coil is used to calculate the distribution of currents and losses inside the conductor.

Contents

Fundamentals of superconductivity

This chapter aims to give the reader an overview about superconductivity, allowing a better framing of this work with respect to the state of the art, as well as introduce some fundamental concepts necessary to understand the following chapters.

1.1.   The discovery of superconductivity

The discovery of superconductivity is attributed to the physicist Heike Kamerlingh Onnes (Nobel Prize in 1913), in 1911. At Leiden University laboratories (Netherlands), Onnes was conducting experiments about the electrical properties of various materials at low temperatures. In 1908, he was the first to liquefy helium, the last of the inert gas to be condensed, reaching the temperature of 4.2 K. This milestone opened to a new field of experiments at temperatures previously unattainable. Then, three years later he noted how the electrical resistivity of mercury abruptly drops to negligible values (*"…it disappeared",* as the physicist reported [1]) when the material was immersed in liquid helium. Fig. 1.1.1 shows some measurements about the dependence of the electrical resistivity of mercury on the temperature, as reported by Onnes [2]. It was already noted that decreasing the temperature of any material, a lowered electrical resistance would have been achieved, but such a sudden fall was not predicted by the theories of the time. Onnes declared that the mercury had entered a new state, calling it the superconductivity state. This phenomenon did not occur for all materials, thus outlining a new class of materials, called superconductors.
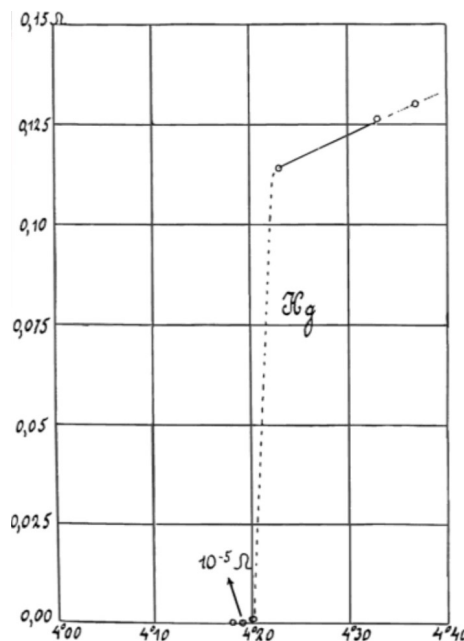
Figure 1.1.1. *Electrical resistance of mercury as a function of the temperature, as directly reported by H. K. Onnes in 1911 [2].*

1.2.   Superconductors properties

Compared to other materials, superconductors present two distinguishable properties [3]: the superconducting transition of the electrical resistivity and the *Meissner-Ochsenfeld effect*.

1.2.1.   Superconducting transition of the electrical resistivity

In classical electromagnetism, when the temperature of a material reduces, its electrical resistance lowers due to the decrease of the vibration amplitude of the crystal lattice ions. For ordinary metallic conductors, the resistance does not nullify completely in correspondence of the absolute zero (besides, a temperature never achieved in practice), but it tends to a residual value, caused by the presence of defects in the crystal lattice. The *Matthiessen's rule* is used for an empirical evaluation of this phenomenon [4]:

$$\rho = \rho_t + \rho_0 \qquad (1.2.1.1)$$

Where ρ is the material resistivity, ρ_t is thermal resistivity, which tends to nullify tending to absolute zero, while the resistivity ρ_0 depends on the degree of purity of the crystal lattice. This last parameter can persist regardless of the temperature.

Fig. 1.2.1.1 compares the trend of the electrical resistance with temperature for an ordinary metal, for an ideally pure metal ($\rho_0 = 0$) and for a superconductor. When the superconducting material is cooled down below a specific temperature T_c, called critical temperature, its resistance drops sharply to almost unmeasurable values ($\rho < 10^{-25}$ Ωm [5]).
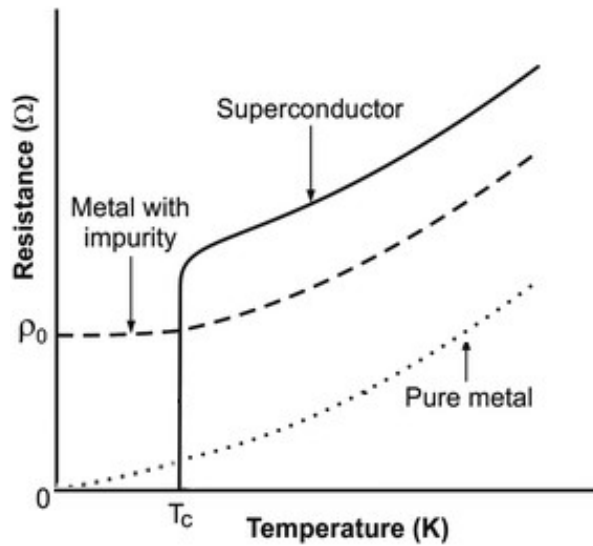
Figure 1.2.1.1. Temperature dependence of the electrical resistance of a superconductor, of a metal with impurity and of an ideally pure metal. The curves are not in scale.

1.2.2. Meissner-Ochsenfeld effect

The perfect diamagnetism is the (ideal) phenomenon exhibited by perfect conductors, capable to perfectly oppose to an applied magnetic field acting at their interior. This property stands only if the conductor is cooled down below T_c (≈ 0 K for normal materials) before the application of the external magnetic field. If the cooling occurs after the application of the magnetic field, the field cannot be excluded from the interior of the material. Contrariwise, a superconducting material can expel the external field at its interior, regardless of the moment at which the field is applied: before or after it is cooled down below T_c (which can be considerably higher compared to absolute zero). This phenomenon is called the *Meissner-Ochsenfeld effect*. Fig. 1.2.2.1 compares the behaviour of a perfect conductor (a) and a superconductor (b). The upper figures refers to the case in which the conductor is cooled down below T_c before the application of the external field, while the lower figures refers to the case in which the cooling happens after the application of the field. Anyhow, this phenomenon subsists if the external field does not pass a critical value, B_c, whose amplitude depends on the material itself.
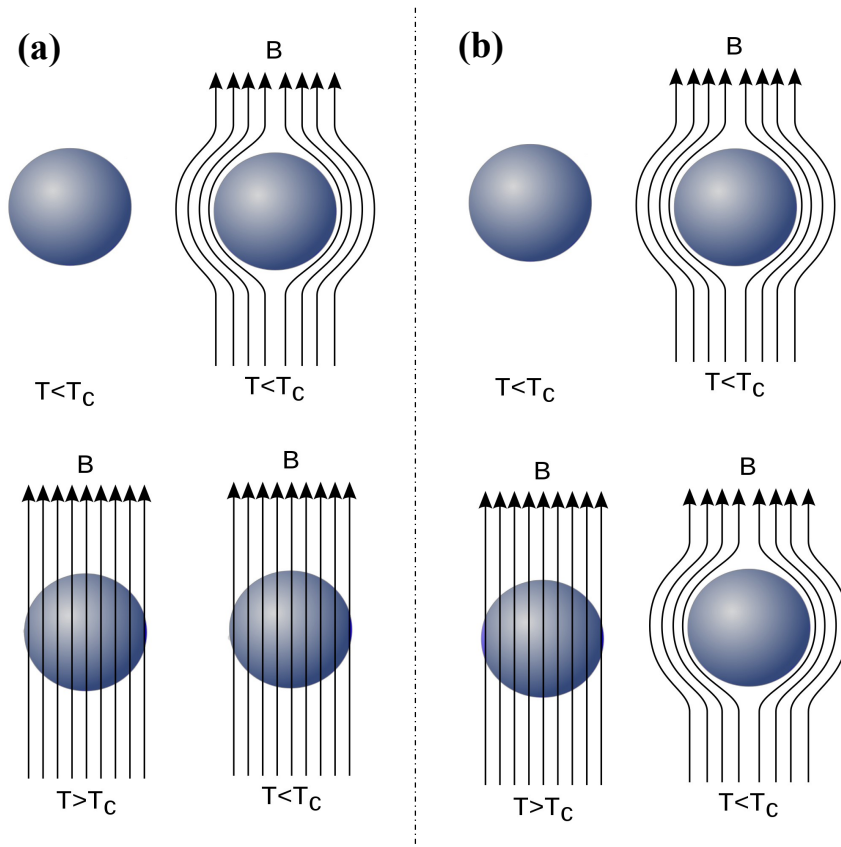
Figure 1.2.2.1. *Magnetic behaviour of a perfect conductor (a) and of a superconductor (b), when subjected to an external magnetic field, depending on the temperature.*

The *Meissner-Ochsenfeld effect* happens in a superconductor by the induction of persistent screening currents near the surface, which generate a self-field equal and opposite to the external one. In real terms, the external field persists within the material for a small space from

its surface, called depth of penetration λ. Within this distance, the field attenuates exponentially from its external amplitude to a null value, as shown in Fig. 1.2.2.2.
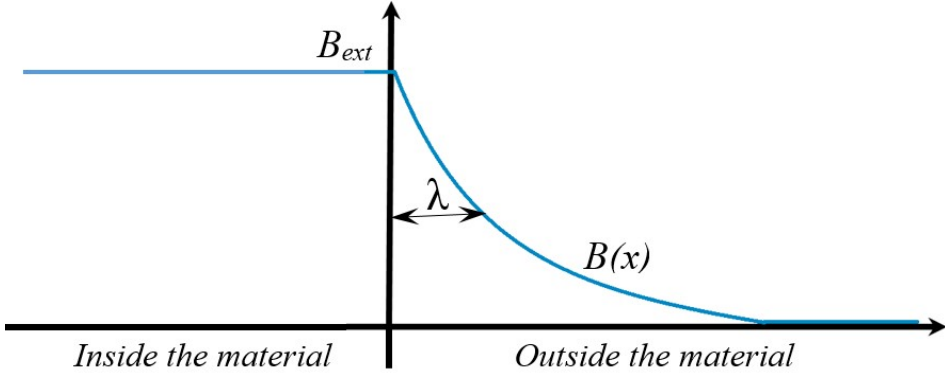
Figure 1.2.2.2. *Penetration depth an external magnetic field within a superconductor.*

1.3.   The critical surface

As already mentioned, a superconducting material exhibits its distinctive properties only if kept within specific operating conditions, described by a suitable set of state variables, that do not depend on time history. In particular, the temperature, the magnetic field and the current density must not exceed their critical values, respectively T_c, B_c and J_c. If even one of these limits is exceeded, the material loses its properties and enters in a dissipative state. These three parameters are strictly related to each other (*e.g.* by increasing the operating temperature, the critical current density of the superconductor is reduced) and they define the so-called critical surface of the superconductor (see Fig. 1.3.1). The shape of the critical surface depends on the type of superconductor, the quality of the production process, the quantity of impurities and the possible damages that occur during operations.

It is worth noting that the parameters defining the critical surface of a superconductor are usually measured as average values within the entire material, and often within a complex superconducting device. In reality, due to possible anisotropies or to the inhomogeneity of the production processes, these parameters vary locally in the material.

For completeness, a fourth critical parameter is generally adopted to define the conditions for which the superconducting state of a material persists. This parameter is the strain ε, which is the mechanical elongation per unit length of the material along a given direction, due to stresses. This parameter particularly affects the critical current density of a superconductor [6, 7]. However, its calculation is not trivial and this dependence is neglected for this work.
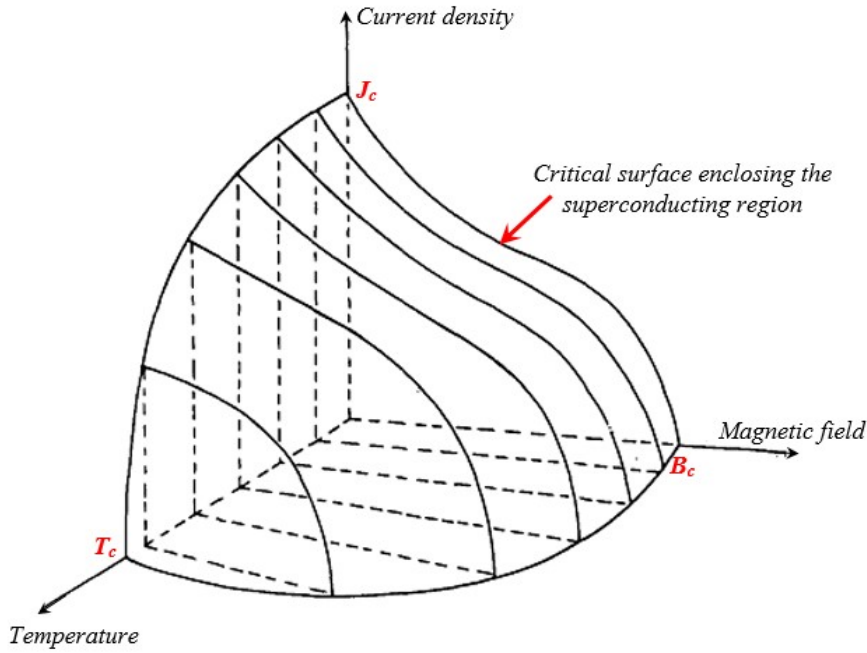
Figure 1.3.1. *Critical surface of a generic superconductor.*

1.4.   Superconductor materials

Since 1911, superconductivity generated an enormous interest in the scientific community, which over the years, has worked hard in the search for superconductors with better and better performances. An enhancement in the test conditions achievable (*e.g.* temperature or magnetic fields) or the detection of superconducting properties in a novel alloy, quickly directed the efforts of many laboratories towards the discovery of new superconducting materials belonging to the same families.

Based on their magnetic properties, superconducting materials can be distinguished between *type I* or *type II* superconductors.

1.4.1.   Type I and Type II superconductors

The magnetic behaviour of *Type I* superconductors corresponds to the one described in *Section 1.2.2*. In particular, when the B_c field is exceed, the material is no longer in its superconducting phase and it loses its properties. Since B_c usually corresponds to few dozens of mT, this make their use unpractical for the majority of the applications, especially for electromagnets. This was the first type of superconductors discovered; many elements (see Fig. 1.4.1.1) and some metal alloys belong to this group.

Then in 1935, L. Shubnikov and J. N. Rjabinin experimentally demonstrated the existence of a new type of superconductors whose magnetic properties differed from classical superconductors [9]. A first accepted theoretical explanation of these results was published several years later, from the theories of V. L.Ginzburg and L.D. Landau [10], and then

improved by A. A. Abrikosov [11]. These materials, called *Type II* superconductors, exhibit a "*double transition*" and have two different magnetic field thresholds. Below a lower critical magnetic field B_{c1}, they are in the same operating conditions as *Type I* superconductors. Once this (indeed very low) first limit is exceeded, *Type II* superconductors do not immediately enter in their normal state, but they exhibit a mixed state where the superconducting state and normal state coexist. In this case, the material as a whole is no longer perfectly diamagnetic and magnetic field vortices (the so-called *fluxons*) start to penetrate into the material in closed regions that enter the normal state while the surrounding areas remain in the superconductive phase. Macroscopically, the material behaves like a superconductor since the size of the fluxons is very limited. Their density increases as the field amplitude rises. This mixed state persists up to an upper critical magnetic field B_{c2}; when even this threshold is passed, the material is fully penetrated by the fluxons and the superconductor turns completely in the resistive state. Thus, the operating conditions in which *Type II* superconductors can operate are greatly enhanced compared to *Type I* materials, since the B_{c2} limit is considerably higher than the field limit of *Type I* superconductors. In some alloys, the upper critical field can exceed amplitudes of several Tesla (depending on the temperature), making them suitable for magnetic applications. For this reason, almost all of the superconducting materials adopted nowadays belongs to *Type II*. For a better understanding, Fig. 1.4.1.2 compares the magnetic behaviour of *Type I* and *Type II* superconductors.
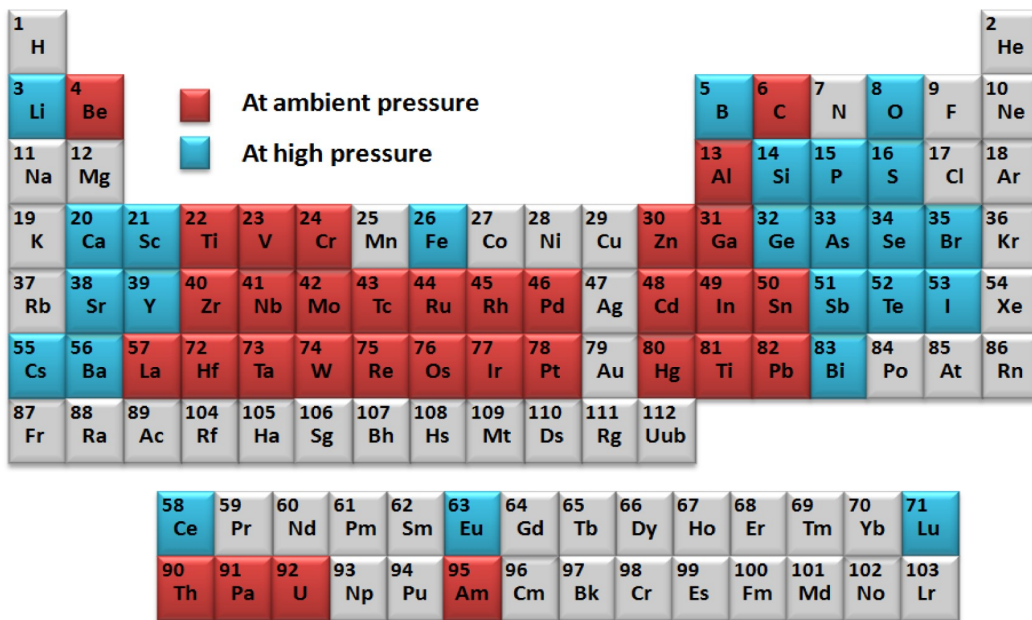
Figure 1.4.1.1. *Periodic table of the elements, highlighting the superconducting elements [8].*
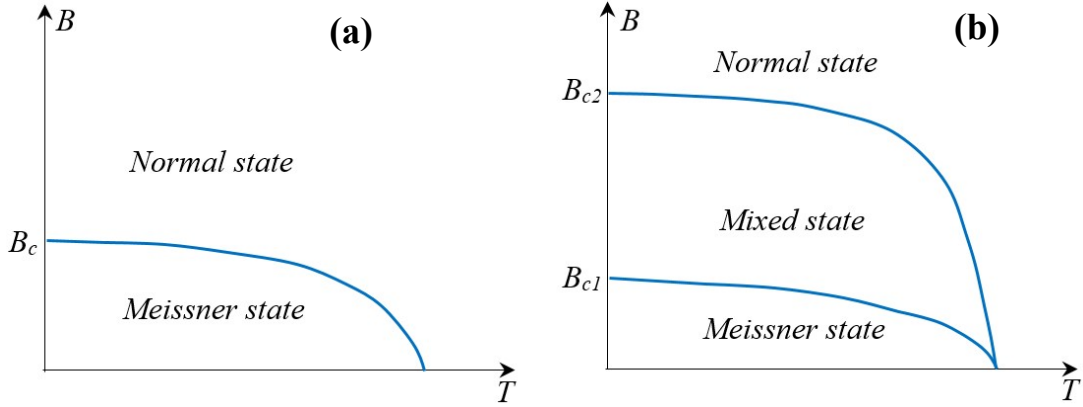
Figure 1.4.1.2. *Magnetic behaviour of Type I (a) and Type II (b) superconductors. The magnetic fields limits B_c, B_{c1} and B_{c2} are not in scale.*

1.4.2. Low Temperature and High Temperature Superconductors

It is clear to the reader that one limitation to the wide use of (actually) known superconductors lies in the maintenance of the operating conditions within the critical surface of the material. In particular, keeping the required cryogenic temperatures is a particularly complex and expensive task, making superconducting devices less competitive on the market. An increase in the T_c allows to relax the temperature safety margins and permits a greater choice between the cryogenic coolants exploitable. Fig. 1.4.2.1 presents the evolution of superconductive materials through the years, depending on their critical temperature [12]. Conventionally, superconductors can be distinguished between Low and High Temperature Superconductors (LTS and HTS).
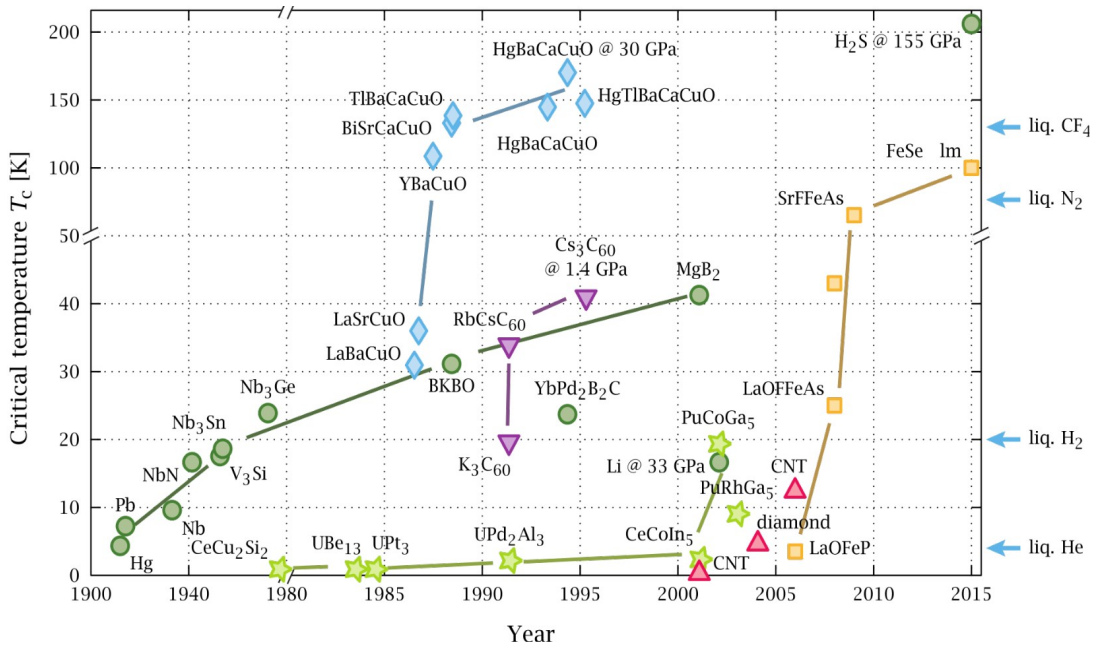
Figure 1.4.2.1. *Evolution of superconductive materials through the years, depending on their T_c [12].*

LTS have a T_c of few degrees above absolute zero. They have to be cooled down using liquid helium (mostly) or hydrogen, which are expensive and complex to handle. However, these conductors were the first to be discovered and manufactured; nowadays, their unitary cost is comparable with traditional conductors, such as copper [13]. Their electromagnetic properties have also been considerably improved over the years, and to date they are the only superconductors widely used in biomedical applications and for large-scale particle physics devices. Most of LTS are Niobium alloys, essentially NbTi and Nb_3Sn. Both of these alloys are manufactured as flexible multifilament cables (*e.g. Rutherford cables* and *Cable-in-Conduit* conductors) capable of carrying enormous currents. NbTi is primarily adopted for its ductility, which makes its fabrication relatively easy and cheap; the technique is called *powder in tube*. Nb_3Sn have superior performances (B_{c2} greater than 20 T at 4.2 K, while $B_{c2} \approx 12$ for NbTi, at the same temperature), but its manufacturing cost is higher since it is more brittle and it requires to be thermally threated before or after being wound in its final configuration (the so-called *react-and-wind* and *wind and react* alternative techniques, respectively).

A new milestone in the superconductivity field was achieved in 1986, when G. Bednorz and A. Müller obtained the transition of a new class of ceramic materials (called *cuprates*) to the superconducting state at a temperature above 30 K, which was consistently higher compared to LTS critical temperatures and not predicted by the theories of the time [14]. Conventionally, this T_c is the threshold distinguishing HTS from LTS. In the following years, researches about many materials enable to develop HTSs with critical temperatures above 77 K; this limit is much more significant because it allows the use of liquid nitrogen as a coolant, a cryogenic fluid less expensive and easier to retrieve and handle compared to liquid helium. To date, the most studied and industrially produced HTS materials belongs to two classes: Bismuth-Strontium-Calcium-Copper-Oxides (contracted as BSCCO, known as 1st generation HTS) and Rare Earth-Barium-Copper-Oxides (contracted as (RE)BCO, known as 2nd generation HTS).

Current carrying BSCCO cables are produced in the form of tapes or round wires, with a technique similar to the *powder in tube*, in which the filaments of superconducting material are dispersed in a metallic matrix (usually silver). However, BSCCO tapes are expensive compared to LTS cables. However, they have a great J_c and the possibility to work above 90 K. Lastly, their current carrying capacity is particularly affected by the orientation of the magnetic field to which they can be subjected: if the field is parallel to the main face of the tape, their critical surface reduces greatly compared to the case in which the same field acts perpendicularly to their main face [15].

(RE)BCO is a family of ceramic compounds, in which the Rare Earths can be Yttrium, Samarium, Neodymium or Gadolinium. (RE)BCOs are the only superconductors that can operate in a medium/high magnetic field ($7 \div 10$ T) at temperatures above 77 K. Moreover, they have less anisotropy with respect to the magnetic field compared to the BSCCO compounds. Therefore, they are considered good candidates for the realization of future high-field magnets on large scale. 2nd generation HTS are produced in the form of tapes containing different materials, in which the superconductive compound constitutes a minimal part of the conductor. The different materials are arranged as stacked layers and for this reason they are often referred as *coated conductors*. The (RE)BCO layer has to be biaxially textured during

the manufacturing processes, in order to obtain an optimal arrangement of its grains and guarantee an optimal performance. Obtaining sufficiently long tapes (several hundred meters) with homogeneous properties along their length, requires slow and expensive processes which are currently a bottleneck for this technology. This is generally necessary to avoid having weak points in a superconductor device, which can affect the overall performances, as in the case of a coil. In *Chapter 4*, a technique to utilize short portions of the same tape to realize a coil without affecting its performances considerably is analysed; it allows to reduce the costs compared to the use of a single tape of considerable length. Fig. 1.4.2.2 gives an example of the structure of a 2nd generation HTS tape: the metallic substrate guarantees flexibility to the conductor, the thin layers below the superconductor are called *buffer layers* and they ensure the proper "growth" of the superconducting layer, while the metallic layers are introduced as electrical and thermal stabilizers. The cross-section of the HTS tapes has a peculiar aspect ratio: it is few tens of microns thick and few centimetres wide.
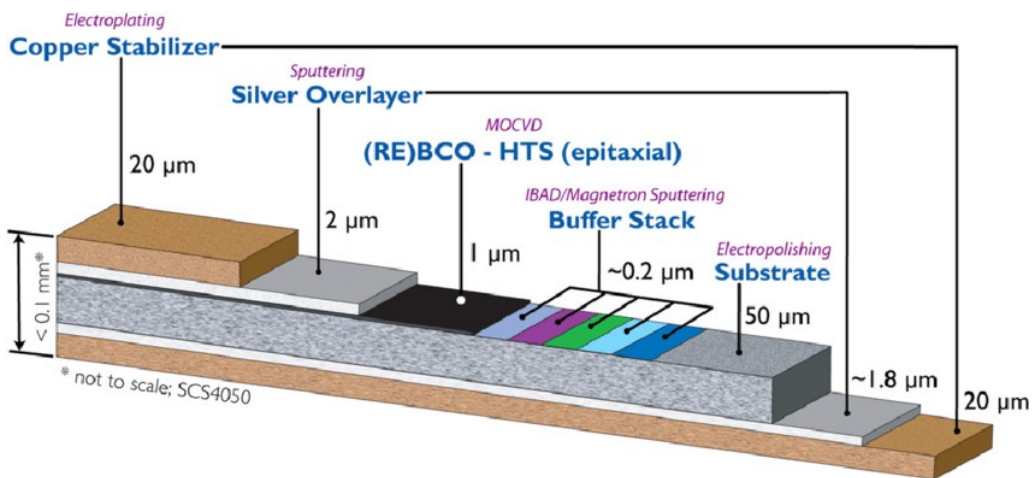
Figure 1.4.2.2. *Structure of a 2nd generation HTS tape (SuperPower SCS4050), not in scale. The names of the techniques adopted to produce the different layers are shown in purple. [16].*

1.5.   *Superconductors stability*

Any superconducting device or even single tapes can be subjected to different heat sources during their operations. They can be external sources dependent on the type of application (*e.g.* particle showers in accelerator magnets or cracks/leakages in the cryogenic vessels) or internal sources. Internal sources can be due to flux creep and flux flow mechanisms [17], ohmic losses and coupling losses, as well as the so-called AC losses. The latter in particular, are described in detail in this work.

Once a superconductor is cooled down and connected to a power supply, the cryogenic system should be able to remove all the heat introduced in the system, maintaining the operating temperature at its project value. This requires the careful design of the refrigerating system and an accurate estimation of the energy introduced from each possible source. If it does not happen or if an unexpected disturbance of sufficient duration and intensity occurs, a temperature rise

can develop even in limited regions of the superconducting material. This determines a local reduction of the critical current of the tape, which can cause a transition to the resistive state introducing an additional power dissipation due to Joule effect. Again, if the refrigeration system is unable to remove the supplementary heat, heat production can extend to the neighbouring regions and turn the whole material resistive. This irreversible transition is called *quench*, which for most applications is a highly undesired event. Contrariwise, if the balance between the heat deposited and the heat removed through the different cooling mechanisms is preserved, the resistive region is reduced; this alternative phenomenon is called *recovery*. A quench forces the immediate shutdown of the power supply and the rapid discharge of the circulating current to avoid irreversibly damaging the material; quench protection systems are present in almost all devices and can be active (using mechanical or superconductor switches) or passive (embedded in the device design, they cannot be turned on or off). In order to trigger an active quench protection system, the quench must first be detected. The quench detection is more complex in HTS than in LTS, since in the former the *Normal Zone Propagation Velocity* (NZPV, the speed at which the superconductor transition spreads) is lower: between 2 to 10 cm/s for HTS [18] and up to 7.5 km/s for LTS [19]. Low speed favours the formations of hot spots and require a finer control over the device. An example of a passive protection system consists in coupling superconducting materials to traditional conductors when realizing a tape. It is worth explaining this mechanism in more detail.

1.5.1. *The current-sharing phenomenon*

As stated in *Section 1.4.2*, superconductor tapes and cables are manufactured as composite materials, including one or more metals characterized by a lower resistivity than that of the superconductor in its normal state. This can improve the thermo-electrical stability of the tape or cable, favouring the current-sharing phenomenon. Fig. 15.1.1 show an equivalent electric circuit of the tape, with the steps occurring when the superconductor temperature rises due to internal or external heat sources that are not compensated fast enough by the cryogenic system.

As long as the temperature does not exceed a limit value T_{cs}, the resistance of the superconductor remains low and the whole operating current flows in the superconducting layer of the tape (Fig. 1.5.1.1(a)). The current-sharing temperature T_{cs} is a function of the conductor configuration: a combination of the properties of the superconductor and the metallic layers. When this limit is exceeded, but the temperature has not yet exceeded the critical value T_c (Fig. 1.5.1.1(b)), the superconductor resistance starts to be comparable with that of the metal in parallel. Therefore, the metal carries a portion of the operating current, preventing the heat generated in the superconductor due to the Joule effect from being excessive. Finally, if the temperature exceeds T_c (Fig. 1.5.1.1(c)), the superconductor turns completely to the resistive state and its resistance exceeds that of the metallic parallel. If the current is not interrupted, it produces a large amount of heat in the superconducting layer which risks a permanent damage. In this case, the operating current flows completely in the metal layers avoiding compromising the superconductor. This situation can last for a few instants of time, since the cross-section of the metal layers is too tiny to withstand the operating current. If the current is not interrupted

quickly, these layers also heat up and risk melting. Moreover, due to their high thermal conductivity, the metals in parallel helps the temperature redistribution along the conductor, reducing the possibility to form hot-spots and improving the quench detection.

$$T < T_{cs} \qquad T_{cs} < T < T_c \qquad T > T_c$$

(a) $I_{sc} = I_{op}$ ... I_{Cu} **(b)** I_{sc} ... I_{Cu} **(c)** $I_{sc} = 0$ ... I_{Cu}

$$I_{sc} = I_c(T) \qquad I_{sc} = 0$$
$$I_{Cu} = I_{op} - I_c(T) \qquad I_{Cu} = I_{op}$$
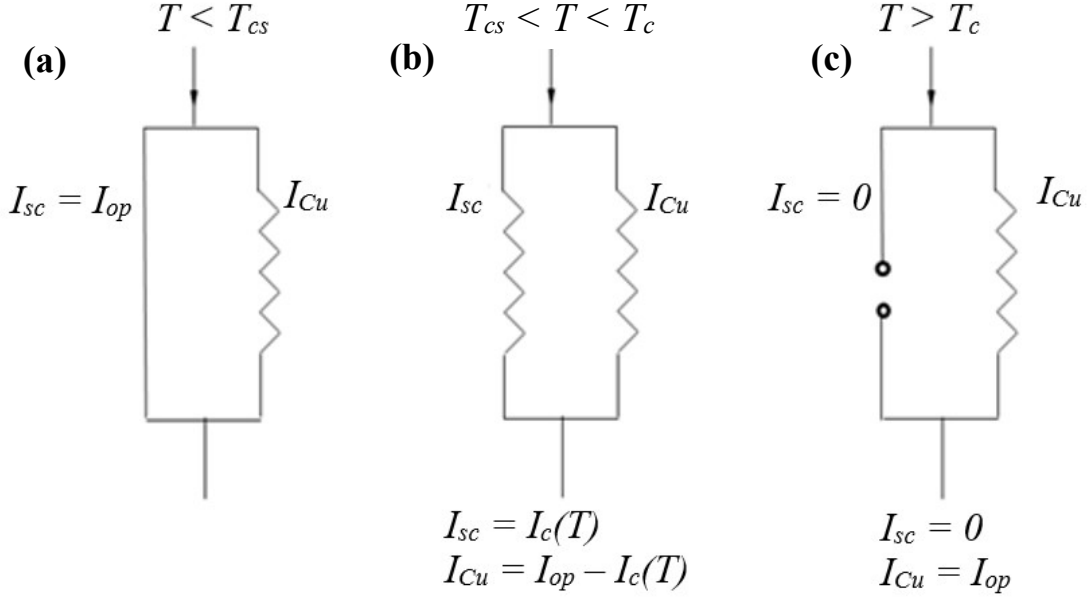
Figure 1.5.1.1. Schematic representation of the current-sharing phenomenon when the superconductor temperature is: below T_{cs} (a), included between T_{cs} and T_c (b) and above T_c (c).

1.6. HTS applications

This thesis deals with 2nd generation HTS. These superconductors are relatively new and are not widely used yet. However, many studies show their great potential for use in magnet [20 – 22] and power applications [23 – 25]. Prototypes and full-scale devices have been developed for high field magnets [26], NMR spectrometers [27] and MRI magnets [28], as well as power cables [29], wind generators [30], SFCL [31] and SMES [32] systems.

Part of this work deals with solenoidal coils wound with HTS tapes. Usually, these windings can be realized with two different winding techniques, which is worth describing in the next section.

1.6.1. Coil winding techniques

HTS coils can be realized using the layer or the pancake techniques [33 – 35]. In both cases, the tape geometry and its flexibility, makes them suitable to be wound around cylindrical mandrels.

In the layer technique, the tape is wound helically on the mandrel, until the set number of turns is reached. A certain pitch can be maintained between the turns. Once the first layer is concluded, the second layer is wound over the first one inverting the winding direction (while

maintaining the same tilt angle); the procedure is repeated until the set number of layers is reached. In this way, the consecutive layers are in series, allowing ideally to avoid having jointed sections inside the winding. The tape ends to be connected to the power supply are located in the innermost and the outermost layers of the coil. This technique is relatively simple to implement for coils of limited size, however it has some disadvantages when the number of layers and turns is considerable. Making a homogeneous coil is complex and often involves the use of spacers to maintain the pitch during the winding phase. Furthermore, any damage that occurs in any internal layer requires to unwind the coil to insert a joint or to completely rebuild the winding. Fig. 1.6.1.1(a) shows a coil wound with this technique, taken from [36].
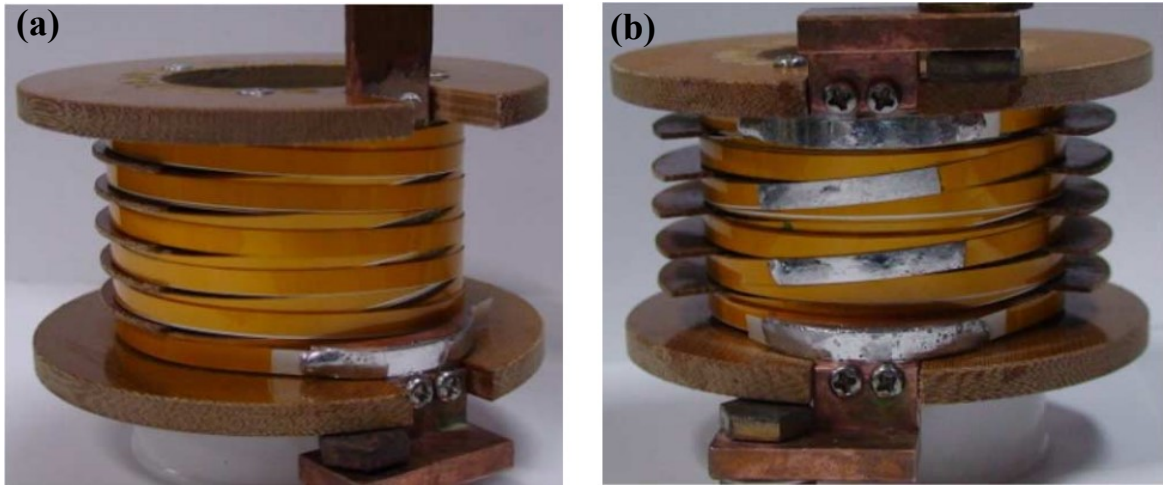
Figure 1.6.1.1. *(a) Layer-wound and (b) double-pancake-wound coils [36]. In the double-pancake coil, the silver areas visible in the oblique segments represents the connections between the stacked pairs of pancakes.*

In the pancake technique, the tape is radially wound on the mandrel, until the set number of turns is reached. In the single pancake configuration, the tape end located on the inner side cannot be connected directly to the power supply as it is obstructed by the upper layers. This end is generally soldered to the mandrel, made of conductive material, which is in turn connected to a current lead. Thus, the winding has a height equal to that of the single tape, and the magnetic field generated in the bore is limited in magnitude and not very homogeneous. This technique is suitable for small laboratory coils only. To solve this problem, the double-pancake technique is used. In this alternate configuration, two pancakes are wound at the same time around the mandrel using a single tape. The pancakes can then be separated by a small spacer. At the end of the winding phase, both tape ends are located on the outer diameter of the two pancakes and can be easily connected to the power supply. Alternatively, when the coil needs to have a certain height, multiple double-pancakes are stacked coaxially one above the other and connected in series with joints. This configuration is very easily scalable, but requires the insertion of at least one joint for each pair of double-pancakes. Furthermore, if one coil portion is damaged, it is possible to extract and replace the single damaged double-pancake, avoiding to unwind the whole coil. Finally, unlike the layer-wound technique, the double-pancake technique allows to realize multi-width configuration coils [37], since pancakes with

a different numbers of layers can be stacked in the coil axial direction. Fig. 1.6.1.1(b) shows a coil wound with this technique, taken from [36].

1.6.2. No-insulation coils

As described in *Section 1.5*, the occurrence of a quench is problematic for the operation of a superconducting device, especially in the case of HTS coils. To mitigate the problem, the protection and refrigeration systems implemented are often overestimated and the current flowing in the windings is limited to amplitude that are consistently lower than the critical current. However, in a traditional coil where the turns are electrically insulated from each other, the risk of the formation of a local hot spot persists as the only alternative path for the current are the metal layers of the tape, which can sustain just limited amounts of current (the current-sharing phenomenon presented in *Section 1.5.1*). Thus, a local quench must be quickly detected and the energy stored in the coil be dissipated by providing active and/or passive protection systems.

A possible solution to the quench protection issues is offered by the use of no-insulation (NI) coils, wound without electrical insulation between turns [38]. In these windings, the current can flow also in the radial direction and avoid the damaged/quenched areas, thus improving the overall thermal stability [39 – 42]. Fig. 1.6.2.1 presents a conceptual drawing of this so called *defect-irrelevant* behaviour [40]. These coils are often referred as *self-protecting*, meaning that they can fully recover after a quench without any external protection mechanism to dissipate the stored energy [43]. In fact, the current redistribution determines a heat diffusion over larger areas (easier to detect), which can involve the whole coil, that finally transits gradually and globally; the current supply can therefore be interrupted and resumed more easily. Consequently, an NI coil can be wound with a tape having a minimal amount of stabilizer layers, thus increasing the winding compactness and significantly reducing the amount of tape required compared to the insulated version [44].
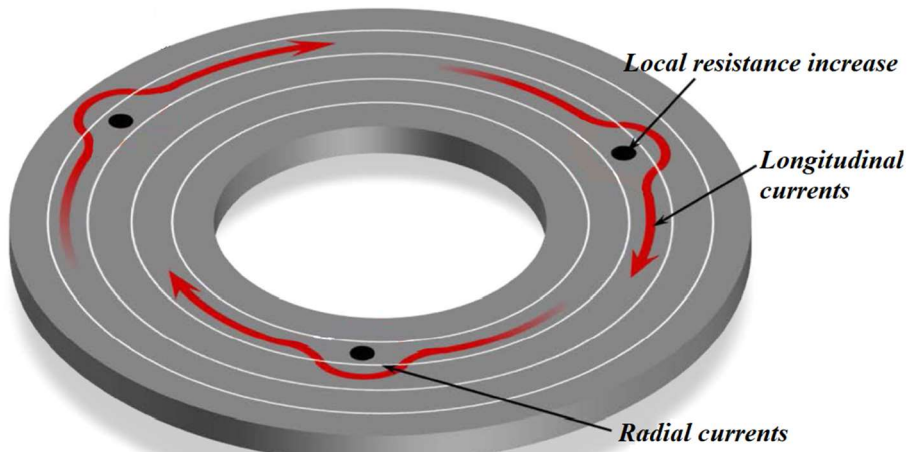
Figure 1.6.2.1. *Conceptual drawing of the current flowing radially in a NI coil with local high-resistive sections [40].*

NI coils can usually be realized with either the pancake-wound technique [34, 45 – 48] or the layer-wound technique [49 – 56], which can result in different current distributions (other winding techniques are not taken into account in this work). In NI pancake coils, the turns are in radial contact with adjacent layers that are relatively close along the tape length. In NI layer-wound coils instead, a turn can be in contact with adjacent turns that are considerably distant along the tape length, depending on their location inside the layers. Therefore, the two configurations should be analyzed separately. In *Chapter 4*, the behaviour of a pancake-wound NI coil is investigated, while in *Chapter 5* some layer-wound coils are analyzed.

Numerical analysis of AC losses in HTS coated conductors

In electromagnets, current ramps and variable magnetic fields are involved, while most power applications operate with AC currents. When a coated conductor is subjected to these electrodynamic transients, time-varying magnetic fields are generated inside the material, thus giving rise to the AC losses. The heat produced by these losses has to be removed by the cooling system in order to safely operate the superconducting device, as described in *Section 1.5*. An increasing amount of heat enhances the cooling costs thus reducing the overall system efficiency. The correct computation of losses is therefore of great importance for the design of the cryogenic system and to avoid the insurgence of unexpected transitions from the superconductive to the resistive state.

This chapter deals with the numerical calculation of AC losses in 2nd generation HTS tapes, describing and comparing different formulations implemented in various solvers. This analysis is complementary to the study described in *Chapter 3* regarding the experimental measurement of AC losses.

2.1.   General conditions for the calculation of AC losses in HTS coated conductors with an electromagnetic method

As a general approach, consider an HTS tape of rectangular cross-section (a coated conductor, for example) of finite length (L) connected to a power supply imposing a current along the tape equal to $I_{Tot}(t)$, which is a sinusoidal function in time of frequency f. It is supposed that after a certain period of time the system has reached the regime conditions, where all its parameters are a periodical function of time, with period T.

$$I_{Tot}(t) = I_{Amp} \sin(\omega t)$$
$$\omega = 2\pi f$$
$$T = \frac{1}{f}$$

(2.1.1)

where I_{Amp} is the amplitude of the sinusoidal current imposed by the current generator.

The tape is placed over a horizontal straight support and connected to the current leads at its extremities. The length of the central portion of tape, not covered by the connections with the current leads is equal to L. The tape, with width w, thickness δ and length L, has a rectilinear axis directed along the z-axis of a Cartesian reference system. The origin of the reference system is placed halfway along the tape length, as shown in Fig. 2.1.1.
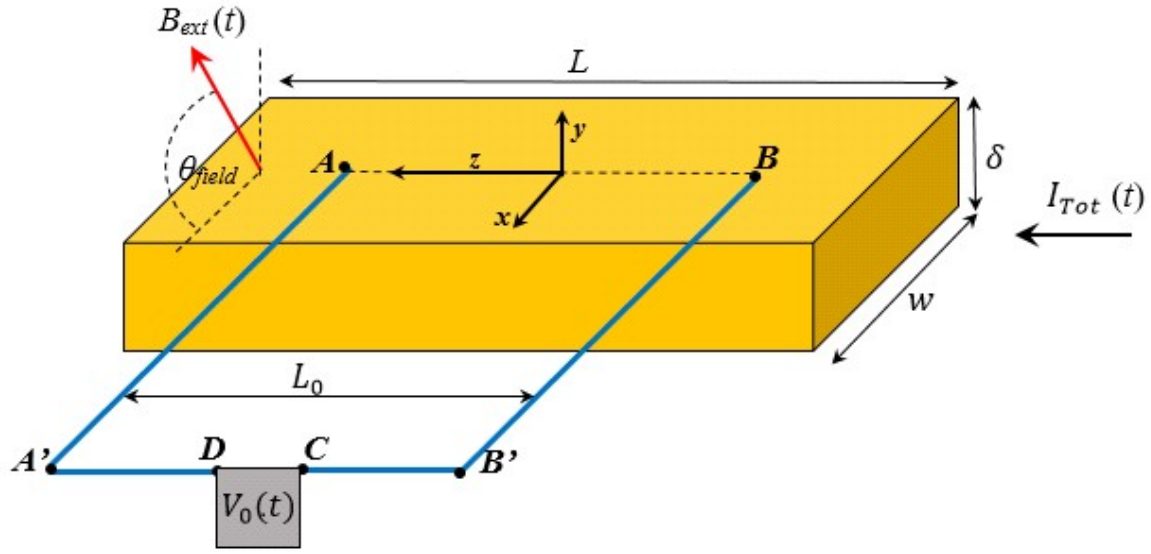
Figure 2.1.1. *Reference system and geometrical parameters for an HTS tape subjected to AC conditions.*
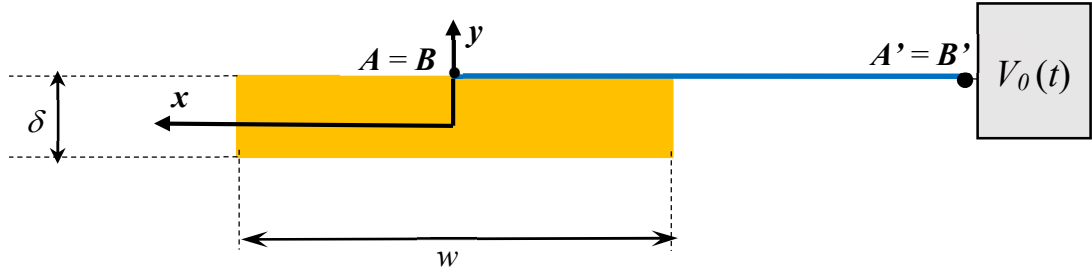
Figure 2.1.2. *Cross-section of the tape on the x-y plane, not in scale.*

A time-dependent external magnetic field, $\boldsymbol{B_{ext}}(t) = \boldsymbol{B_m} \sin(\omega t)$, can also be applied to the tape with a generic orientation.

An electromagnetic method can be used to measure the AC losses. This approach requires the simultaneous acquisition of the current and voltage signals from the tape. The current signal is acquired using a shunt resistor placed in series with the tape supply circuit. For the voltage measurements, two voltage taps are soldered to the upper surface of the tape, in its central region. The two voltage taps are soldered at a distance equal to L_0, represented in Fig. 2.1.1 by the points A and B; each voltage tap is at a distance $\frac{L_0}{2}$ from the center. From these points, small section copper wires are connected to the terminal of a voltmeter/acquisition card (only the voltmeter term is used in the following). Before reaching the instrumentation, the two wires are twisted together to reduce the area where external flux can link and generate undesired electromagnetic noise in the acquired signal. The points where the wires are deviated from their paths to be twisted together are indicated as A' and B' in Fig. 2.1.1. Fig. 2.1.2 reports the tape cross-section, not in scale. It is assumed that these points are at the same y and z-coordinates with respect to points A and B. $V_0(t)$ is the value measured by the voltmeter and used for the calculation of AC losses.

For simplicity, the contacts *A* and *B* are reported in Fig. 2.1.2 at the same location along the *x*-axis, but in general, their *x*-coordinate can be different. Also the wires connecting the voltage taps to the voltmeter terminals are displayed as straight lines but they could have any path. In the following sections, the geometry of the voltage measurement circuit for two different configurations is described in detail.

Even if the amplitude of the AC transport current is well below the tape critical current, it can generate non-negligible power dissipation inside the tape due to the hysteretic behaviour of the superconductor and to the presence of the other materials of the tape (different layers in a coated conductor). Note that the term hysteresis can be ambiguous for superconducting devices, as reported in [57], since this behaviour does not appear explicitly into the superconductor's constitutive laws. Analytically, they do not differ from the classic *Joule* losses. With reference to the tape portion included between the two voltage taps ($z \in \left[-\frac{L_0}{2}, \frac{L_0}{2}\right]$), the power $p(t)$, dissipated at the time instant *t*, has the following expression:

$$p(t) = \int_{-\frac{L_0}{2}}^{\frac{L_0}{2}} \int_{-\frac{\delta}{2}}^{\frac{\delta}{2}} \int_{-\frac{w}{2}}^{\frac{w}{2}} \boldsymbol{E}(x,y,z,t) \cdot \boldsymbol{J}(x,y,z,t) dx dy dz \tag{2.1.2}$$

where $\boldsymbol{E}$ is the electric field vector and $\boldsymbol{J}$ is the transport current density vector. The mean value in a period of the dissipated power *p(t)*, is equal to:

$$\langle p(t) \rangle = \frac{1}{T} \int_0^T p(t) \, dt \qquad [W] \tag{2.1.3}$$

Since generally the power dissipation is reported per unit of length, Eq. (2.1.3) should be divided by L_0:

$$\langle p(t) \rangle_{per\ unit} = \frac{1}{L_0\ T} \int_0^T p(t) \, dt \qquad \left[\frac{W}{m}\right] \tag{2.1.4}$$

The AC losses per cycle (in J/m) can easily be computed by dividing Eq. (2.1.4) by the frequency.

The purpose of this study is the numerical calculation of $\langle p(t) \rangle_{per\ unit}$. In the following, when the loss dependency on the amplitude of the transport current or the magnetic field is analysed, the average power dissipation is presented, in terms of W/m. When the loss dependency on the frequency is considered the AC losses are presented, in terms of J/m.

Moreover, in this analysis the current amplitude is henceforth referred to as the ratio between the I_{Amp} value and the tape critical current I_c:

$$I_m = \frac{I_{Amp}}{I_c} \tag{2.1.5}$$

2.2. *Numerical calculation of AC losses in HTS coated conductors*

Since it is impractical to carry out measurements in all possible operating conditions, the use of some predictive tools for the AC losses computation is very useful in many situations. While analytical formulae are fast and easy to implement [58, 59] they can generally be adopted in simplified cases, which limits their applicability [60]. On the other hand, numerical models can describe more complex systems in spite of longer calculation times [61, 62].

Over the years, various finite element methods (FEM) models have been developed for the analysis of the electromagnetic behaviour of HTS tapes, based on the resolution of the time dependent Maxwell's equations to compute the time evolution of the electric field and current density distributions in coated conductors. The evaluation of these quantities starts from the differential form of Maxwell's equations:

$$\begin{cases} \nabla \cdot \boldsymbol{E} = \dfrac{\rho_c}{\varepsilon} \\ \nabla \cdot \boldsymbol{B} = 0 \\ \nabla \times \boldsymbol{E} = -\dfrac{\partial \boldsymbol{B}}{\partial t} \\ \nabla \times \boldsymbol{B} = \mu \left(\boldsymbol{J} + \dfrac{\partial \boldsymbol{D}}{\partial t} \right) \end{cases} \qquad (2.2.1)$$

where μ, ρ_c and ε are the magnetic permeability, the charge density and the permittivity of the material.

Depending on the equations adopted, different methods are distinguished (summarized in Table 2.2.1 [61]): $\boldsymbol{H}$-formulation [63 – 69], $\boldsymbol{T}-\boldsymbol{\Phi}$ formulation [70 – 74], $\boldsymbol{A}-V$ formulation [75 – 80] and $\boldsymbol{E}$-formulation [81 – 84]. These formulations are used to solve the time dependent Maxwell's equations with a non-linear resistivity to describe the superconductor's electrical behaviour [62]. The non-linear resistivity of a superconductor (ρ_{SC}) is usually expressed in the form of a power law:

$$\rho_{SC} = \frac{E_C}{J_C} \left(\frac{|J|}{J_C} \right)^{n-1} \qquad (2.2.2)$$

where J is the current density, J_C is the critical current density of the tape, n is the *n-value* and E_C is the critical electric field. Conventionally, E_C is set equal to one of the following values: 10 µV/m (lower critical field) or 100 µV/m (upper critical field). For this work, the upper critical electric field is selected.

Various geometric approximations, 1-D [80, 85], and 2-D [64, 71, 81, 86] have been proposed in the literature to reduce the computational burden of the simulation of 3-D geometries of real devices. Multidimensional approaches allow computing the losses generated in the non-superconducting layers of a tape. Those layers are often neglected from the calculation in order to reduce the number of system unknowns; however, this choice should be carefully evaluated since their contribution can be relevant in various operating conditions of technical interest. These considerations have been proposed for both Bi-2223 tapes [87 – 89] and (RE)BCO

coated conductors [90 – 96], even if for the latter the interest is mainly focused on the influence of the ferromagnetic substrate.

Two numerical models implemented for the calculation of AC losses in coated conductors are described in this work. The models are based on different formulations and are implemented in different solvers. The first numerical model analysed in this work, described in *Section 2.3*, is a finite element method (FEM) model based on the *H*-formulation and it is implemented in *COMSOL Multiphysics* environment [97]. The second model, described in *Section 2.4*, is an innovative integral model based on the *A-V* formulation and is implemented in MATLAB environment [98]. Both models apply simplifying hypothesis in order to approximate the 3-D geometry of the coated conductor and to reduce the computational burden for the solver.

Table 2.2.1. *Common formulations to numerically solve Maxwell's equations.*

Formulation	Equations	Definitions
Vector and scalar potential $A-V$	$\nabla^2 A = \mu\,\sigma\left(\frac{\partial A}{\partial t} + \nabla V\right)$ $\nabla \cdot \sigma\left(\frac{\partial A}{\partial t} + \nabla V\right) = 0$	$B = \nabla \times A$ $E = -\dfrac{\partial A}{\partial t} - \nabla V$ $\sigma = \sigma(E)$
Current potential $T-\Phi$	$\nabla \times \rho\,\nabla \times T = -\mu\,\sigma\,\dfrac{\partial(T - \nabla\Phi)}{\partial t}$ $\nabla \cdot \mu(T - \nabla\Phi) = 0$	$J = \nabla \times T$ $H = T - \nabla\Phi$ $\rho = \rho(J)$
E - formulation	$\nabla \times \nabla \times E = -\mu\,\dfrac{\partial(\sigma E)}{\partial t}$	$\dfrac{\partial B}{\partial t} = -\nabla \times E$ $\sigma = \sigma(E)$
H - formulation	$\nabla \times \rho\,\nabla \times H = -\mu\,\dfrac{\partial H}{\partial t}$	$J = \nabla \times H$

In order to identify the contribution of the different layers of a coated conductor, two different types of analyses are performed with both numerical models. In the first case, referred as "*Whole_Tape*", all layers of the tape cross-section are included in the model. In the second case instead, named "*SC_only*", only the superconducting layer is implemented in the model, thus neglecting all the other layers of the tape

Developing two different models allows comparing their results to investigate for flaws in the respective calculation methods. Furthermore, individual models may be more effective in simulating certain operating conditions or some specific tape electrical/geometrical properties rather than others. Even the solver chosen to implement the equations is a relevant parameter. It affects the calculation times and one solver could be more suitable to be used for a specific formulation rather than others.

Once the models are described, their results are compared in *Section 2.5* and some conclusions are drawn regarding their pros and cons.

2.3. *FEM model based on the H-formulation*

This section describes the numerical calculation of AC losses in HTS coated conductors using the *H*-formulation.

2.3.1 *Simplifying hypothesis for the numerical model based on the H-formulation*

The tape is considered to be sufficiently long so that the current distribution is equal to the one flowing in an infinitely long tape. Thus, the 3-D geometry is simplified by means of a 2-D approximation, where the two dimensions represent the tape cross-section (*x-y* plane in Fig. 2.1.2). It follows that all the system parameters can be considered to be independent of the *z*-coordinate. The electric field and the current density have their *z*-component only, while the magnetic field *H* has its *x* and *y* components only (H_x and H_y):

$$\boldsymbol{E}(x,y,z,t) = E(x,y,t)\,\boldsymbol{k}$$
$$\boldsymbol{J}(x,y,z,t) = J(x,y,t)\,\boldsymbol{k} \tag{2.3.1.1}$$
$$\boldsymbol{H}(x,y,z,t) = H_x(x,y,t)\,\boldsymbol{i} + H_y(x,y,t)\,\boldsymbol{j}$$

where $\boldsymbol{i}$, $\boldsymbol{j}$ and $\boldsymbol{k}$ are the unit vectors directed along the *x, y* and *z* axes.

Consequently, Eq. (2.1.2) can be simplified as:

$$p(t) = L_0 \int_{-\frac{\delta}{2}}^{\frac{\delta}{2}} \int_{-\frac{w}{2}}^{\frac{w}{2}} \boldsymbol{E}(x,y,t) \cdot \boldsymbol{J}(x,y,t)\, dx\, dy \qquad [W] \qquad (2.3.1.2)$$

Note that the power dissipated can be expressed in terms of W/m by dividing Eq. (2.3.1.2) by L_0. In this way, the calculation becomes independent of this distance.

$$p(t)_{per\ unit} = \int_{-\frac{\delta}{2}}^{\frac{\delta}{2}} \int_{-\frac{w}{2}}^{\frac{w}{2}} \boldsymbol{E}(x,y,t) \cdot \boldsymbol{J}(x,y,t)\, dx\, dy \qquad \left[\frac{W}{m}\right] \qquad (2.3.1.3)$$

Finally, the instantaneous values of the power dissipated can be integrated over a period, leading to the formulation of the AC losses.

$$\langle p(t) \rangle_{per\ unit} = \frac{1}{T} \int_0^T \int_{-\frac{\delta}{2}}^{\frac{\delta}{2}} \int_{-\frac{w}{2}}^{\frac{w}{2}} \boldsymbol{E}(x,y,t) \cdot \boldsymbol{J}(x,y,t)\, dx\, dy\, dt \qquad \left[\frac{W}{m}\right] \qquad (2.3.1.4)$$

2.3.2. *H-formulation in 2-D*

The *H*-formulation formulation can be easily implemented in commercial FEM solvers, such as COMSOL *Multyphysics*, and it allows setting intuitively the state variables of the problem [66]. As explained in *Section 2.3.1*, a 2-D approximation of the *H*-formulation is implemented, excluding the tape length from the equations. This offers a considerable

reduction in terms of computational burden for the calculator, while on the other hand it can obviously introduce a certain level of inaccuracy in the results.

Faraday's equation is initially considered:

$$\nabla \times \boldsymbol{E} = -\frac{\partial \boldsymbol{B}}{\partial t} \tag{2.3.2.1}$$

With the 2-D hypothesis of Eq. (2.3.1.1) and separating the vector components, Eq. (2.3.2.1) can be written as:

$$\begin{cases} \dfrac{\partial B_x(x,y,t)}{\partial t} + \dfrac{\partial E(x,y,t)}{\partial y} = 0 \\[3mm] \dfrac{\partial B_y(x,y,t)}{\partial t} - \dfrac{\partial E(x,y,t)}{\partial x} = 0 \end{cases} \tag{2.3.2.2}$$

Then, assuming $\boldsymbol{B} = \mu\,\boldsymbol{H}$, and considering μ as a constant (see further details in *Section 2.4*) yields:

$$\begin{cases} \mu\dfrac{\partial H_x(x,y,t)}{\partial t} + \dfrac{\partial E(x,y,t)}{\partial y} = 0 \\[3mm] \mu\dfrac{\partial H_y(x,y,t)}{\partial t} - \dfrac{\partial E(x,y,t)}{\partial x} = 0 \end{cases} \tag{2.3.2.3}$$

Eq. (2.3.2.3) is the standard expression of the problem with the *H*-formulation. In the FEM model, it is coupled with Ohm's law:

$$\boldsymbol{E} = \rho\,\boldsymbol{J} \tag{2.3.2.4}$$

It is worth noting that the expression of the *H*-formulation here reported might lead to conditioning problems when numerically solved in FEM models for non-conductive regions having extremely high ρ values. However, since this work focuses on the analysis of composite conductors not containing insulation materials, this problem is neglected.

Then, Ampere's law is used to express the current density as a function of the magnetic field, neglecting the displacement field due to the quasi-static approximation:

$$\nabla \times \boldsymbol{H} = \boldsymbol{J} \tag{2.3.2.5}$$

which, in 2-D, can be written as:

$$J_z\,(x,y,t) = \frac{\partial H_y(x,y,t)}{\partial x} - \frac{\partial H_x(x,y,t)}{\partial y} \tag{2.3.2.6}$$

where J_z is the *z*-component of the current density vector. The other Cartesian components of the current density vector are null, since in the 2-D approximation it is considered that the current flows only parallel to the main direction of the tape.

It is worth noting that J cannot be introduced directly in the model or used in boundary conditions, since it is not a state variable [99]. The solution to this problem is explained in *Section 2.3.4.*

2.3.3. H-formulation for coated conductors including a ferromagnetic substrate

The magnetic permeability of a material can be expressed as:

$$\mu = \mu_0 \, \mu_r \tag{2.3.3.1}$$

where μ_0 is the permeability of vacuum ($4\pi \cdot 10^{-7}$ H/m) and μ_r is the relative permeability of the material considered. Since most of the materials constituting the layers of a (RE)BCO coated conductor are often non-ferromagnetic materials, their μ_r value can be reasonably approximate to 1. Thus, it can be neglected when solving Eq. (2.3.2.3).

However, some manufacturers produce tapes including a substrate layer composed of ferromagnetic materials. When trying to solve the problem for the points belonging to the ferromagnetic layer of the tape, Eq. (2.3.2.3) cannot longer be considered valid. Therefore, the equation must be rewritten inserting the term $\mu_0 \, \mu_r$ inside the derivative term. In fact, if μ_r is no longer constant but it is a function of the magnetic field module H, its value changes in time. Thus, Eq. (2.3.3.2) should be used:

$$\begin{cases} \dfrac{\partial \mu_0 \, \mu_r(H) \, H_x(x,y,t)}{\partial t} + \dfrac{\partial E(x,y,t)}{\partial y} = 0 \\[4mm] \dfrac{\partial \mu_0 \, \mu_r(H) \, H_y(x,y,t)}{\partial t} - \dfrac{\partial E(x,y,t)}{\partial x} = 0 \end{cases} \tag{2.3.3.2}$$

Then, using the derivative properties, the derivative term of Eq. (2.3.3.2) can be written as:

$$\begin{cases} \mu_0 \left[\dfrac{\partial \mu_r(H)}{\partial t} H_x(x,y,t) + \dfrac{\partial H_x(x,y,t)}{\partial t} \mu_r(H) \right] + \dfrac{\partial E(x,y,t)}{\partial y} = 0 \\[4mm] \mu_0 \left[\dfrac{\partial \mu_r(H)}{\partial t} H_y(x,y,t) + \dfrac{\partial H_y(x,y,t)}{\partial t} \mu_r(H) \right] - \dfrac{\partial E(x,y,t)}{\partial x} = 0 \end{cases} \tag{2.3.3.3}$$

where μ_0 is taken out of the derivate since constant. The magnetic permeability is a function of the magnetic field module which in turn is a function of time. It is useful to separate these functions in the first derivative term of Eq. (2.3.3.3), resulting in:

$$\begin{cases} \mu_0 \left[\dfrac{\partial \mu_r(H)}{\partial H} \dfrac{\partial H}{\partial t} H_x(x,y,t) + \dfrac{\partial H_x(x,y,t)}{\partial t} \mu_r(H) \right] + \dfrac{\partial E(x,y,t)}{\partial y} = 0 \\[4mm] \mu_0 \left[\dfrac{\partial \mu_r(H)}{\partial H} \dfrac{\partial H}{\partial t} H_y(x,y,t) + \dfrac{\partial H_y(x,y,t)}{\partial t} \mu_r(H) \right] - \dfrac{\partial E(x,y,t)}{\partial x} = 0 \end{cases} \tag{2.3.3.4}$$

Taking into account that the module of the magnetic field corresponds to:

$$H = \sqrt{H_x{}^2 + H_y{}^2} \qquad (2.3.3.5)$$

It follows that the term $\dfrac{\partial H}{\partial t}$ of Eq. (2.3.3.4) can be rewritten as:

$$\frac{\partial H}{\partial t} = \frac{\partial \sqrt{H_x{}^2 + H_y{}^2}}{\partial t} =$$

$$= \frac{1}{2}\left(\frac{1}{\sqrt{H_x{}^2 + H_y{}^2}} \right)\left(2H_x \frac{\partial H_x}{\partial t} + 2H_y \frac{\partial H_y}{\partial t} \right) = \frac{1}{H}\left(H_x \frac{\partial H_x}{\partial t} + H_y \frac{\partial H_y}{\partial t} \right) \qquad (2.3.3.6)$$

Then, Eq. (2.3.3.6) can be inserted into Eq. (2.3.3.4). For ease of reading, the dependence of the variables on the respective quantities is omitted in the following expressions.

$$\begin{cases} \mu_0 \left[\dfrac{1}{H}\dfrac{\partial \mu_r}{\partial H}\left(H_x \dfrac{\partial H_x}{\partial t} + H_y \dfrac{\partial H_y}{\partial t} \right)H_x + \dfrac{\partial H_x}{\partial t}\mu_r \right] + \dfrac{\partial E}{\partial y} = 0 \\[4mm] \mu_0 \left[\dfrac{1}{H}\dfrac{\partial \mu_r}{\partial H}\left(H_x \dfrac{\partial H_x}{\partial t} + H_y \dfrac{\partial H_y}{\partial t} \right)H_y + \dfrac{\partial H_y}{\partial t}\mu_r \right] - \dfrac{\partial E}{\partial x} = 0 \end{cases} \qquad (2.3.3.7)$$

It is useful to rename the term $\dfrac{1}{H}\dfrac{\partial \mu_r}{\partial H}$ as *f(H)*, since it does only depend on the magnetic field module. Performing this substitution and gathering some variables yields:

$$\begin{cases} \mu_0 \left[f(H)\left(H_x{}^2 \dfrac{\partial H_x}{\partial t} + H_x H_y \dfrac{\partial H_y}{\partial t} \right) + \dfrac{\partial H_x}{\partial t}\mu_r \right] + \dfrac{\partial E}{\partial y} = 0 \\[4mm] \mu_0 \left[f(H)\left(H_y{}^2 \dfrac{\partial H_y}{\partial t} + H_x H_y \dfrac{\partial H_x}{\partial t} \right) + \dfrac{\partial H_y}{\partial t}\mu_r \right] - \dfrac{\partial E}{\partial x} = 0 \end{cases} \qquad (2.3.3.8)$$

Eq. (2.3.3.8) corresponds to Eq. (2.3.2.3) for the points of the tape belonging to the ferromagnetic layers [100 – 102].

2.3.4. *Implementation of the H-formulation in COMSOL Multiphysics to compute the AC losses in HTS coated conductors*

In COMSOL *Multiphysics* environment, the general form to represent a system of partial differential equations has the following expression:

$$e_a \frac{\partial^2 u}{\partial t^2} + d_a \frac{\partial u}{\partial t} + \nabla \cdot \Gamma = f_s \qquad (2.3.4.1)$$

where u is the state variable of the system, e_a and d_a are the mass and dump coefficients, Γ is the conservative flux vector and f_s is the source term. For the 2-D case of the *H*-formulation,

in the non-ferromagnetic materials, u is equal to $\begin{bmatrix} H_x \\ H_y \end{bmatrix}$, e_a is zero since it is a first order differential equation, d_a is equal to μ, Γ depends only on the electric field (specifically on its z-component, using the simplifying hypothesis of Eq. (2.3.1.1)) and the source term is null [102].

Thus, in the absence of ferromagnetic materials, the H-formulation expressed by Eq. (2.3.2.3) can be implemented in the solver in matrix form, as follows:

$$\begin{bmatrix} \mu_0\,\mu_r & 0 \\ 0 & \mu_0\,\mu_r \end{bmatrix} \begin{bmatrix} \dfrac{\partial H_x}{\partial t} \\ \dfrac{\partial H_y}{\partial t} \end{bmatrix} + \begin{bmatrix} \dfrac{\partial}{\partial x} & \dfrac{\partial}{\partial y} \end{bmatrix} \begin{bmatrix} 0 & E \\ -E & 0 \end{bmatrix} = 0 \qquad (2.4.4.2)$$

If the tape analysed contains a ferromagnetic substrate, Eq. (2.3.2.3) should be applied in some points of the tape cross-section while Eq. (2.3.3.8) should be applied elsewhere. This would complicate the resolution of an FEM model. Therefore, for these specific cases it is preferable to use Eq. (2.3.3.8) for each point of the tape, which is more generic, by entering the appropriate μ_r values. It is useful to rearrange Eq. (2.3.3.8) as:

$$\begin{cases} \mu_0 \left(f(H)H_x{}^2 + \mu_r \right) \dfrac{\partial H_x}{\partial t} + \mu_0\, f(H)\, H_x H_y \dfrac{\partial H_y}{\partial t} + \dfrac{\partial E}{\partial y} = 0 \\[3mm] \mu_0 \left(f(H)H_y{}^2 + \mu_r \right) \dfrac{\partial H_y}{\partial t} + \mu_0\, f(H)\, H_x H_y \dfrac{\partial H_x}{\partial t} - \dfrac{\partial E}{\partial x} = 0 \end{cases} \qquad (2.3.4.3)$$

Then, Eq. (2.2.4.3) can be reported in matrix form as follows:

$$\begin{bmatrix} \mu_0 \left(f(H)H_x{}^2 + \mu_r \right) & \mu_0\, f(H)\, H_x H_y \\ \mu_0\, f(H)\, H_x H_y & \mu_0 \left(f(H)H_y{}^2 + \mu_r \right) \end{bmatrix} \begin{bmatrix} \dfrac{\partial H_x}{\partial t} \\ \dfrac{\partial H_y}{\partial t} \end{bmatrix} + \begin{bmatrix} \dfrac{\partial}{\partial x} & \dfrac{\partial}{\partial y} \end{bmatrix} \begin{bmatrix} 0 & E \\ -E & 0 \end{bmatrix} = 0 \quad (2.3.4.4)$$

It is worth noting how, for both Eq. (2.3.4.2) and Eq. (2.3.4.4), the damping coefficients matrix that multiplies the derivative vector is symmetrical. In the case of non-ferromagnetic materials, $f(H)$ is equal to zero and thus Eq. (2.3.4.4) returns equal to Eq. (2.3.4.2).

In some cases, the solution of a COMSOL simulation tends to diverge when applying Eq. (2.3.4.4) [102]. The computational burden of the simulation is often so great that the simulation fails or runs indefinitely without reporting specific errors, producing misleading results. Therefore, Eq. (2.3.4.3) has to be modified accounting the ferromagnetic influence on losses not in the damping coefficient matrix but rather in the source term. Restarting from Eq. (2.3.4.4), Eq. (2.3.4.4) can be rewritten in a new formulation, more favourable for the solver, as follows:

$$\begin{bmatrix} \mu_0\,\mu_r & 0 \\ 0 & \mu_0\,\mu_r \end{bmatrix} \begin{bmatrix} \dfrac{\partial H_x}{\partial t} \\ \dfrac{\partial H_y}{\partial t} \end{bmatrix} + \begin{bmatrix} \dfrac{\partial}{\partial x} & \dfrac{\partial}{\partial y} \end{bmatrix} \begin{bmatrix} 0 & E \\ -E & 0 \end{bmatrix} = \begin{bmatrix} -\mu_0 \dfrac{\partial \mu_r}{\partial t} H_x \\ -\mu_0 \dfrac{\partial \mu_r}{\partial t} H_y \end{bmatrix} \qquad (2.3.4.5)$$

Since the state variables of the *H*-formulation in 2-D are the *x* and *y* components of the magnetic field and not the tape current, it is not possible to impose directly a condition in COMSOL regarding the transport current flowing into the tape cross-section. This problem is solved imposing a *Dirichelet boundary condition* for the state variables on the domain of the system. The boundary of the domain is represented by a circumference with radius *R* around the center of the tape, as in Fig. 2.3.4.1. Air is considered into the 2-D space between this contour and the conductor surface.

The magnetic field at the domain boundary is set equal to the one produced by the current filament laying along the conductor longitudinal axis. In fact, if the boundary radial distance *R* is much greater compared to the dimensions of the tape cross-section (its width, in particular) the real geometry of the tape can be neglected and the magnetic field is calculated as the one produced by a straight conductor of infinite length. That allows to simplify the expression of the magnetic field.

Then, the expression for the boundary condition is found starting from the circulation of the magnetic field along the circular boundary of the domain:

$$\oint \boldsymbol{H} \, \boldsymbol{dl} = I_{Amp} \, sin(\omega t) \tag{2.3.4.6}$$

Solving the integral of Eq. (2.3.4.6), the expression for the magnetic field module at the boundary (see Fig. 2.3.4.1) results as follows:

$$H(t) = \frac{I_{Amp} \, sin(\omega t)}{2 \, \pi \, R} \tag{2.3.4.7}$$

Fig. 2.3.4.1 displays the parameters involved in the calculation of the magnetic field components. It shows the superconductor cross-section 'seen' from the boundary of the domain (the tape cross-section is simplified by using a circular cross-section, since the radial distance *R* from the tape center is great compared to the tape width and thickness). The transport current is considered outgoing and therefore the magnetic field vector has the direction shown in Fig. 2.3.4.1, following the right-hand rule. θ is the angle, variable with to the coordinates of the point of the boundary (*x, y*), formed between the middle *x-axis* of the system and the segment joining the center of the system with each edge point of the domain, having length *R*. χ is the complement to θ with respect to $\frac{\pi}{2}$.

Thus, the *x* and *y* components of the magnetic field are written as follows:

$$\begin{cases} H_x(t) = -H(t) \cos \chi = -H(t) \cos\left(\frac{\pi}{2} - \theta\right) = -H(t) \sin \theta \\ H_y(t) = H(t) \sin \chi = H(t) \sin\left(\frac{\pi}{2} - \theta\right) = H(t) \cos \theta \end{cases} \tag{2.3.4.8}$$

The sine and cosine of the θ angle can be written with respect to the radius *R* and the coordinates of the edge point:

$$\begin{cases} \sin\theta = \dfrac{y}{\sqrt{x^2+y^2}} = \dfrac{y}{R} \\[3mm] \cos\theta = \dfrac{x}{\sqrt{x^2+y^2}} = \dfrac{x}{R} \end{cases} \qquad (2.3.4.9)$$

Then, inserting Eq. (2.3.4.9) and Eq. (2.3.4.7) into Eq. (2.3.4.8), the following expression for the *Dirichelet boundary conditions* can be expressed, referred to as the *state variables* of the *H*-formulation, accounting for the AC transport current flowing into the tape.

$$\begin{cases} H_x(t) = -H(t)\cos\chi = -H(t)\sin\theta = -\dfrac{I_{Amp}\sin(\omega t)}{2\pi R}\left(\dfrac{y}{R}\right) \\[3mm] H_y(t) = H(t)\sin\chi = H(t)\cos\theta = \dfrac{I_{Amp}\sin(\omega t)}{2\pi R}\left(\dfrac{x}{R}\right) \end{cases} \qquad (2.3.4.10)$$

Note that Eq. (2.3.4.10) is equivalent to imposing a condition of null magnetic field at an infinite distance from the tape, since when R tends to infinite, both magnetic field components tend to zero.
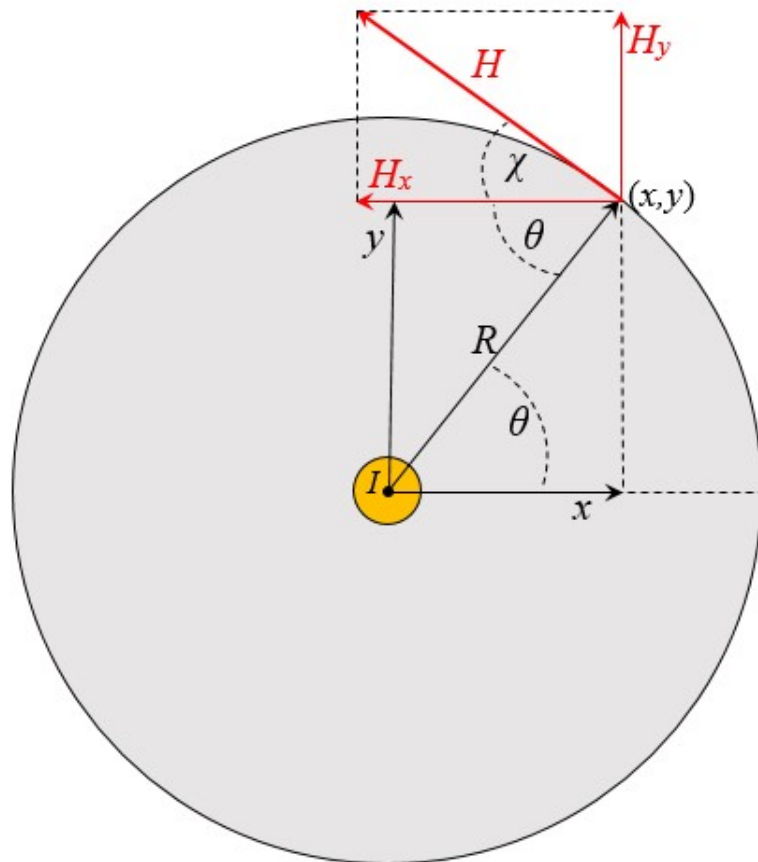
***Figure 2.3.4.1**. Cross-section the system domain (in grey) and the superconductor (in yellow), and the parameters of the magnetic field generated at the system boundary.*

Eq. (2.3.4.10) can be further modified to account for the presence of a time-varying external magnetic field. For simplicity, let us assume that an external sinusoidal magnetic field is applied perpendicular to the tape main surface (which is the worst case for an HTS tape in terms of critical current reduction [103 – 106]):

$$H_y(t) = H_{Amp} \sin(\omega_B \, t) \quad , \quad H_x(t) = 0$$
$$\omega_B = 2\pi f_B$$

(2.3.4.11)

where f_B and ω_B can be different from the terms f and ω reported in Eq. (2.1.1) since the transport current and the external magnetic field can have different frequencies. Thus, a more general expression for the *Dirichelet boundary conditions*, to account for both an AC transport current and an AC external magnetic field corresponds to:

$$\begin{cases} H_x(t) = -\dfrac{I_{Amp} \sin(\omega t)}{2 \, \pi \, R} \left(\dfrac{y}{R}\right) \\ H_y(t) = \dfrac{I_{Amp} \sin(\omega t)}{2 \, \pi \, R} \left(\dfrac{x}{R}\right) + H_{Amp} \sin(\omega_B \, t) \end{cases}$$

(2.3.4.12)

Note that the boundary condition for the H_x component is not affected by the external magnetic field considered in this case, since H_{ext_x} is considered to be null.

To solve the system, an initial condition must be set. Physically, the problem would require an initial condition regarding the current (*i.e.* null current equal at each point of the domain), however, as seen for the boundary conditions, the current is not a state variable of the problem. Therefore, the initial condition is imposed on the magnetic field. In fact, if the current is null at the initial instant, the tape self-field in every point of the domain is accordingly null. The same condition is also set on the derivatives of the magnetic field:

$$\begin{cases} H_x(0) = 0 \\ H_y(0) = 0 \end{cases} \quad , \quad \begin{cases} \dfrac{dH_x}{dt}(0) = 0 \\ \dfrac{dH_y}{dt}(0) = 0 \end{cases}$$

(2.3.4.13)

Furthermore, it is necessary to add an equation that takes into account that the surface integral of the current density on the tape cross-section must be equal to the transport current at all instants (current conservation equation). Into a FEM model, this is equal to state that the sum of the products between the areas and the current densities flowing in each discretization element of the tape cross-section must be equal to the transport current flowing in the tape. In order to include an additional equation to the system of Eq. (2.3.2.3) (or Eq. (2.3.3.8) for ferromagnetic materials) in COMSOL environment a *Pointwise Constraint* is used, even if it has not exactly the same purpose for which *Pointwise Constraint* are designed in the solver:

$$I_{Tot}(t) = \sum_{j=1}^{N} Area_i \, J_i(t)$$

(2.3.4.14)

where N is the number of elements discretizing the tape cross-section and $Area_i$ and $J_i(t)$ are the area and current density of each element. By imposing this condition on a single point of the domain, the desired current continuity condition is applied during the numerical solution and therefore the physics of the problem is respected. COMSOL allows to set a *Pointwise Constraint* on the junction points between the different layers of the tape, but selecting one point rather than another does not change the results.

Furthermore, some considerations are discussed regarding the meshing technique implemented in the FEM model. Selecting the proper spatial discretization is not trivial: due to the high aspect ratio of a coated conductor, typically between 10^3 and 10^4, the choice of a uniform discretization can lead to a rapid increase of the computational burden and the calculation times due to the large number of elements even in 2-D models [107, 108]. Conventional meshing techniques adopted in FEM models (not only to simulate superconductors) work with elements with aspect ratio close to unity (squares) [109]. This solution is impractical for most superconducting tapes. As described in [110], it is preferable to adopt a mapped mesh, with elongated quadrangular elements. These rectangular elements have a longer side along the tape width and a smaller side across its thickness. Maintaining a certain aspect ratio in the meshing elements allows varying the number of discretization points of the domain with respect to the tape width and thickness. A convergence analysis makes it possible to identify the minimum number of points that allows obtaining an acceptable result (within the convergence criteria) by reducing the computational burden.

It should be noted that each layer of an HTS coated conductor has its individual aspect ratio. Moreover, when the amplitude of the AC transport current is below the critical current of the tape (as is the case of this study), most of the current flows within the superconducting layer, and as a consequence most of the AC losses are generated in this layer. Therefore, it is undoubtedly convenient to differentiate the refinement of the discretization points and therefore the dimensions of the mesh elements from one layer to another. However, when implementing an inhomogeneous mesh in COMSOL, some problems can arise in correspondence of the separation surfaces between layers (or rather lines, in 2-D) inside the tape. In fact, the solver generates the mesh starting from the discretization points. Consider the example of two adjacent layers having the same width and different thickness, placed one above the other. The solver fails to build the quadrangular elements in the border between the two layers because the same *y*-coordinate (across the tape thickness) corresponds to an undefined number of *x*-coordinates (across the tape width). This generates an error message, not allowing running the simulation. Therefore, while it is still possible to set independently the number of mesh points across the thickness of each layer, it is preferable to set the same number of mesh points across their width. The same reasoning is applied for adjacent layers whose common surface is across their thickness; it is the case, for example, of a soldering alloy or a surrounding copper positioned at the tape sides. In this case, the adjacent layers must have the same number of discretizing points across their thickness, but the number of mesh points may vary across their width.

Fig. 2.3.4.2 shows a portion of the superconductor cross-section, as implemented in COMSOL. The vertical and horizontal lines represent the rectangular mesh elements used; the black dots represent the edge element delimiting a layer from the upper/lower one. The discretization

across the tape width is constant since the edge elements of every contact line dividing two layers belong to both layers, while the discretization across the tape thickness is set for each layer.
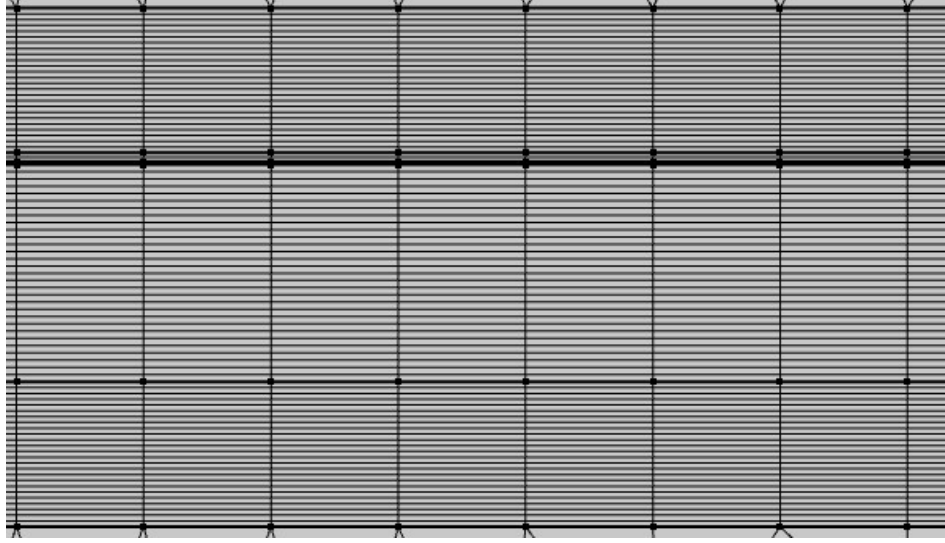
Figure 2.3.4.2. Portion of the tape cross-section with the rectangular mesh elements used in COMSOL.

As for the air part of the domain included between the tape contour and the external circumference at a distance R, a triangular mesh is adopted, since it allows to spatially vary the dimensions of the elements. The mesh discretization should be finer near the tape and can be coarser at increasing distance. This is easily set in COMSOL using the *"free triangular"* mesh technique. Fig. 2.3.4.3, shows the discretization of this section of the domain, as realized in COMSOL.

Subsequently, the geometry of the tape is implemented in the solver and each layer is correlated with its material properties, in terms of μ_r and ρ, remembering that for the superconducting tape Eq. (2.2.2) must be used. For the surrounding air μ_r is taken equal to 1. Moreover, since no current is supposed to flow in the surrounding air, as it represents a dielectric region, its resistivity is set equal to 1 Ωm, according to [94].
Then, the simulation can run and the results produced. When the magnetic field components are computed, the local critical current density can be determined from Eq. (2.3.2.6). Then, Eq. (2.3.2.4) is used to calculate the electric field, remembering that if the element belongs to the superconducting layer, the power law expressed in Eq. (2.2.2) should be used.

Finally, the AC losses generated in each layer can be calculated. Different formulations exist to compute the AC losses produced in ferromagnetic layer, which are more precise compared to Eq. (2.3.1.4). In fact, several works show that the magnetic properties of these layers can strongly affect the overall AC losses in HTS tapes [91, 93, 111 – 113]. The hysteresis losses in a ferromagnetic material are equal to the area of the hysteresis *B–H* loop, and the formulation usually depends on the maximum value assumed by the magnetic field in this layer during a hysteresis period. The formulation generally does not have a unique expression but it is written

from the fitting of the experimental data available in the literature for the type of substrate analysed [91, 100]. Summarizing:

$$
\begin{cases}
\langle p(t) \rangle_{per\ unit} = \dfrac{1}{T} \int_0^T \int_{-\frac{\delta}{2}}^{\frac{\delta}{2}} \int_{-\frac{w}{2}}^{\frac{w}{2}} Q_{fe}(x,y,t) dx\ dy\ dt \\[4pt]
\qquad\qquad if\ the\ element\ \in to\ a\ ferromagnetic\ layer \\[8pt]
\langle p(t) \rangle_{per\ unit} = \dfrac{1}{T} \int_0^T \int_{-\frac{\delta}{2}}^{\frac{\delta}{2}} \int_{-\frac{w}{2}}^{\frac{w}{2}} \mathbf{E}(x,y,t) \cdot \mathbf{J}(x,y,t) dx\ dy\ dt \\[4pt]
\qquad\qquad if\ the\ element\ \in to\ a\ non-ferromagnetic\ layer
\end{cases}
\tag{2.3.4.16}
$$

where Q_{fe} is the fitting function used to calculate AC losses in a specific ferromagnetic layer. As an example, in *Section 2.3.5* the fitting function for the substrate layer of the *American Superconductor* (*AMSC*) *8501* tape is presented.
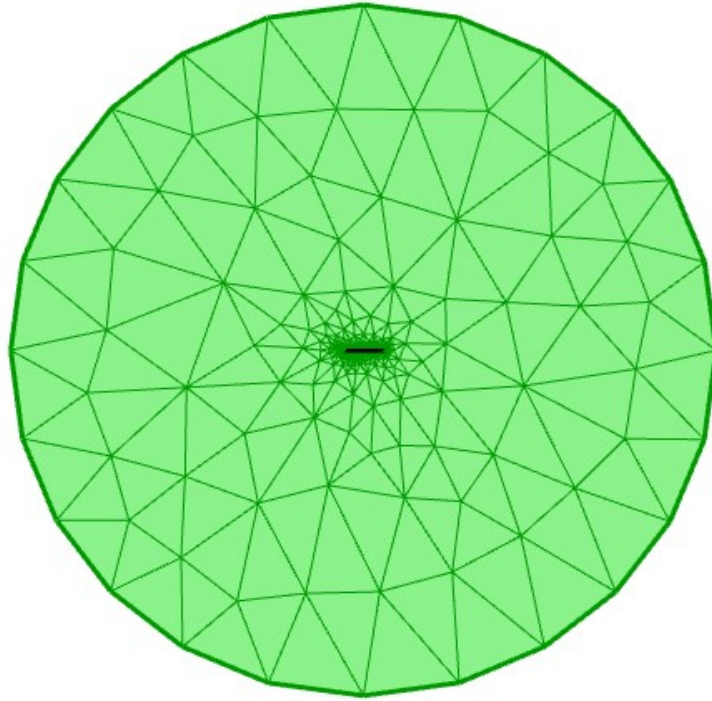
Figure 2.3.4.3. *System domain and discretizing mesh implemented in COMSOL Multiphysics. The portion highlighted in green represents the triangular mesh used to discretize the region of air between the tape and the boundary of the domain.*

2.3.5. Results of the numerical model based on the H-formulation

The geometry and the electrical properties of the *AMSC 8501* tape is implemented in COMSOL *Multiphysics*, as a test case. The tape geometrical parameters are shown in Fig. 2.3.5.1, while its electrical characteristics are reported in Table 2.3.5.1, according to [95]. Note

that the buffer layer is not considered, since its influence on the AC losses is assumed to be negligible compared to the other layers given its particularly small thickness (≈ 0.3 μm).
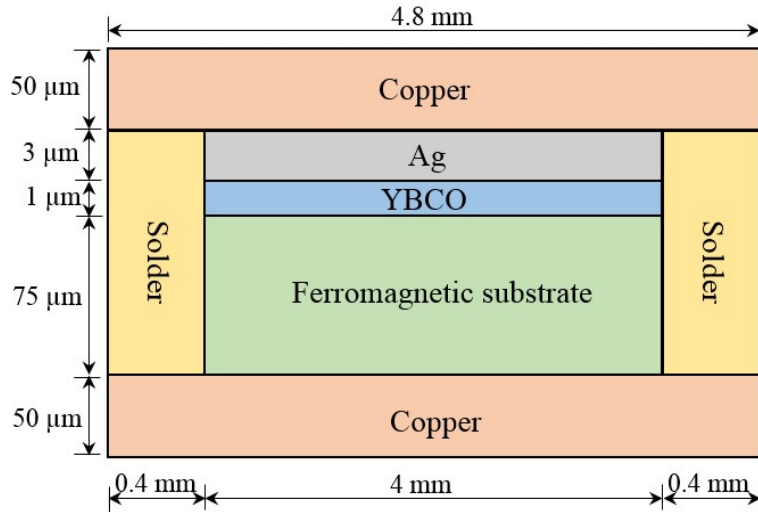
Figure 2.3.5.1. *Sketch of the cross-section of the AMSC 8501 tape. The figure in not in scale.*

Table 2.3.5.1. *Electrical parameters of the AMSC 8501 tape.*

Parameter	Unit	Value
I_c (77 K , $E_c = 1$ μV/cm)	[A]	104.3
n- value (77 K , $E_c = 1$ μV/cm)		35
ρ_{Cu}	[nΩ m]	1.97
ρ_{Ag}	[nΩ m]	2.70
ρ_{Sub}	[nΩ m]	63.0
ρ_{Solder}	[nΩ m]	31.0
ρ_{Air}	[Ω m]	1
μ_{Cu}	[H/m]	1
μ_{Ag}	[H/m]	1
μ_{Sub}	[H/m]	See Eq. (2.3.5.1)
μ_{Solder}	[H/m]	1
μ_{Air}	[H/m]	1

The *AMSC 8501* tape has a ferromagnetic substrate (*Ni-5at.%W*), thus all the considerations made in *Section 2.2.4* must be implemented to account for this layer. In particular, the relative magnetic permeability of the substrate is expressed in Eq. (2.3.5.1), as a function of the magnetic field modulus *H* [91, 94, 100].

$$\mu_{Sub}(H) = 1 + 30600\left(1 - \exp\left(-\left(\frac{H}{295}\right)^{2.5}\right)\right)H^{-0.81} + 45\exp\left(-\left(\frac{H}{120}\right)^{2.5}\right) \quad (2.3.5.1)$$

Fig. 2.3.5.2 shows the μ_{Sub} function for a limited interval of H values.
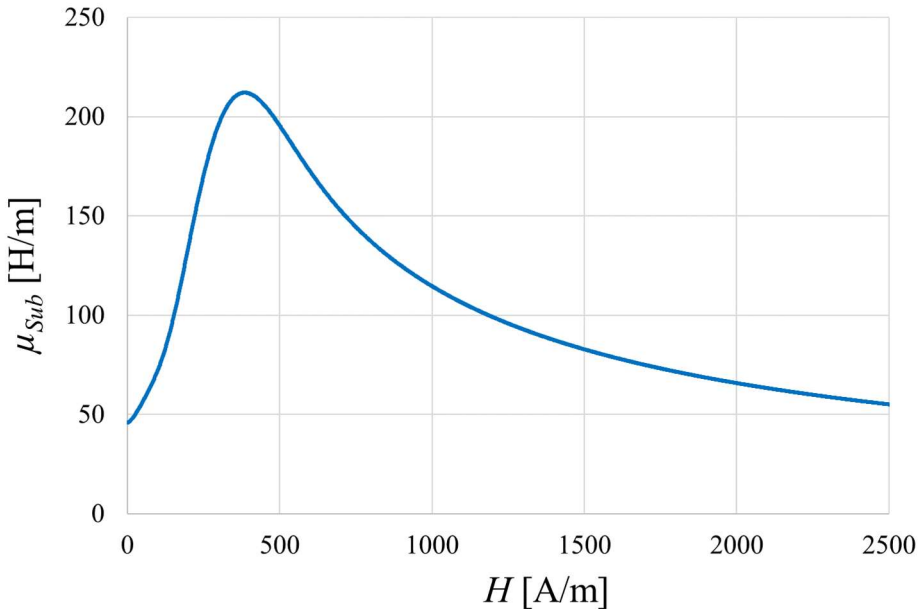
Figure 2.3.5.2. *$\mu_{Sub}(H)$ function for the substrate layer of the AMSC 8501 tape.*

Eq. (2.3.4.16) is adopted to calculate the AC losses in the tape, using the following Q_{fe} fitting function for the ferromagnetic layer:

$$\begin{cases} Q_{fe}(B_{max}) = 4611.4\,(B_{max})^{1.884} & if\ B_{max} \leq 0.164\ T \\ Q_{fe}(B_{max}) = 210(1 - exp(-(6.5\,B_{max})^4)) & if\ B_{max} > 0.164\ T \end{cases} \quad (2.3.5.2)$$

where B_{max} is the maximum value assumed by the magnetic field in the substrate layer during the simulated time [94].

As regards the meshing technique adopted to discretize the *AMSC 8501* tape, an aspect can be underlined. The tape is not composed by perfectly stacked layers only, but there are also regions of solder on both sides of the tape with a different aspect ratio compared to the other layers (they are narrower and thicker). The discretization of the solder regions across their width is constrained by the discretization of the upper and lower layers, which in this case are two identical copper layers. The discretization of the solder regions across their thickness is more complex, since they are in contact with 3 different layers having their own thicknesses: the silver, the superconducting and the substrate layers. In order to follow the mesh conditions reported in *Section 2.2.4*, the easiest solution would be to impose a discretization across the thickness of the solder regions equal to the finer one used in the 3 central layers. This would be problematic for a couple of reasons. Firstly, the same discretization applied across the

thickness of the superconducting layer (extremely fine due to its small thickness) would be applied for the thicker solder regions. Secondly, even the discretization across the thickness of the silver and substrate layers would be affected: once the discretization along the solder regions is imposed, it must be applied to all these central layers. The result would be a very fine discretization in several layers, most likely not necessary to reach convergence criteria and which would cause an increase in calculation times. Fig. 2.3.5.3 shows a portion of the cross-section of the tape with the mesh described in this paragraph. The figure is not in scale and the discretization is coarser with respect to that really required, so that overall the picture appears clearer to the reader.

Alternatively, in this thesis it is proposed to divide the lateral solder regions into different layers, having the same electrical properties. It is an artifice allowing to respect the physics of the system while reducing the computational burden. It is convenient to divide each solder region into a number of elements equal to the number of central layers (3, in the case of the *AMSC 8501* tape). The thickness of each of these sub-layers is equal to the one of its adjacent central layer, and thus, it can be discretised with the same number of elements set for its corresponding central layer. Fig. 2.3.5.4 shows an example of the application of the discretization technique described in this paragraph. Comparing it with Fig. 2.3.5.3, a reduction in the number of mesh elements is notable, which in turns can lower the computational times for the FEM model.

Table 2.3.5.2 reports the geometrical parameters used to generate the mesh in COMSOL. The number of elements discretizing each layer (or sub-layer) of the tape are presented, as well as the width and thickness (Δx and Δy) of each resulting discretizing element.
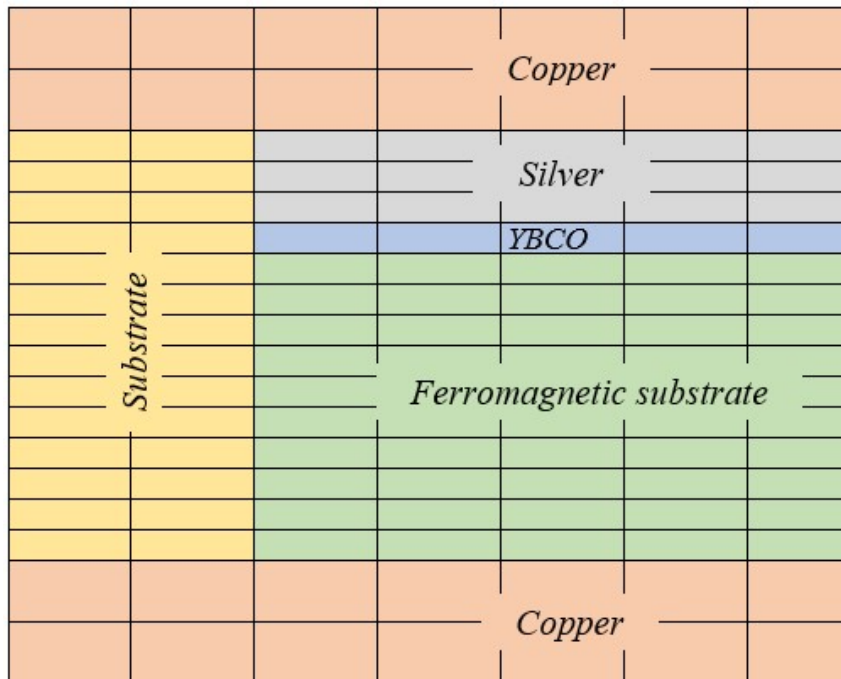
Figure 2.3.5.3. *Mesh technique adopted in a portion of the AMSC 8501 tape when the lateral solder regions are considered as single geometric elements. The figure is not in scale.*
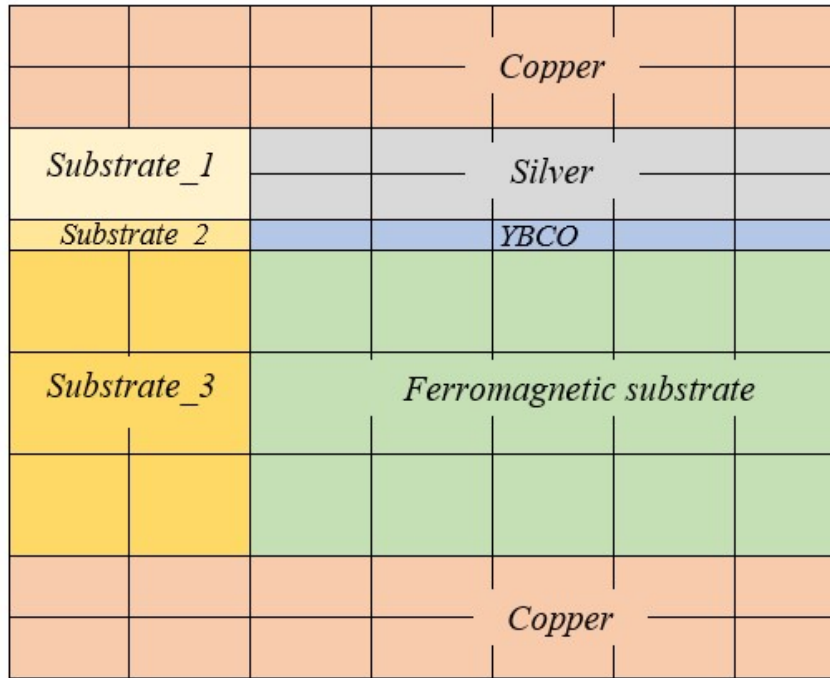
Figure 2.3.5.4. *Mesh technique adopted in a portion of the AMSC 8501 tape when each of the lateral solder regions are considered as three different elements with the same electrical properties but different geometrical characteristics. The figure is not in scale.*

Table 2.3.5.2. *Mesh parameters implemented in COMSOL Multiphysics for the 2-D FEM model based on the H-formulation.*

	Discretization across the tape thickness		Discretization across the tape width	
	# elements	Δy [μm]	*# elements*	Δx [μm]
Upper Cu layer	20	2.5	110	43.5
Ag layer	2	1.5	92	43.5
SC layer	2	0.5	92	43.5
Substrate layer	25	3	92	43.5
Lower Cu layer	20	2.5	110	43.5
Left / right solder layers adjacent to the Ag layer	2	1.5	9	43.5
Left / right solder layers adjacent to the SC layer	2	0.5	9	43.5
Left / right solder layers adjacent to the substrate	25	3	9	43.5

Table 2.3.5.3 reports the main simulation parameters set in the solver. The number of periods is set as the minimum number that allows the system to reach regime conditions; in fact, reducing the number of the simulated periods corresponds to shorter calculation times. Fig. 2.3.5.5 shows the trend of the power dissipation during the first 4 periods, at $I_m = 1.1$ (see Eq. (2.1.5)) The frequency is set to 55 Hz, thus a period corresponds to 18.18 ms. From this preliminary test, it is evident how, starting from the second period, the loss profile does not change. Thus, only 2 periods are simulated and the results are obtained by integrating the losses profile in the second period.

Table 2.3.5.3. *Simulation parameters implemented in COMSOL Multiphysics for the 2-D FEM model based on the H-formulation.*

Parameter	Value
Number of periods simulated	2
Intervals per period simulated	100
Absolute tolerance	10^{-3}
Relative tolerance	10^{-4}
Time stepping method	Backward differentiation formula
Domain boundary radius (R)	$10 \cdot (tape\ width) = 4$ cm
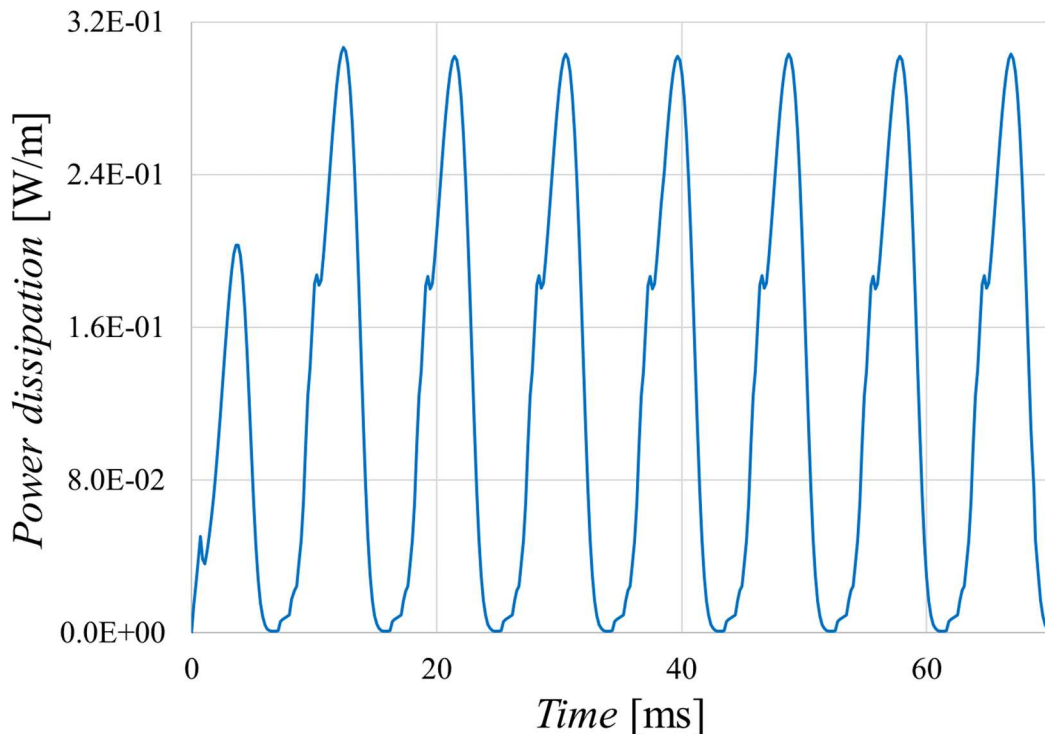
Figure 2.3.5.5. *Power dissipation during time (4 periods simulated) in the AMSC 8501. The frequency is set to 55 Hz and $I_m = 0.9$.*

The radius R of the domain boundary is set equal to 10 times the tape width. It is considered that at this distance the tape cross-section can be simplified as that of an infinite straight cylindrical conductor.

For the study carried out in this section, the presence of an external magnetic field is neglected.

The reader might be wondering whether the continuity condition of the tangent component of the magnetic field (H_x) in correspondence of the contact surfaces of the various layers is satisfied. This condition is not imposed in the equations, and it is useful to check its validity. In fact, while the continuity of the normal component (H_y) can be assumed to be achieved a priori, this is not obvious for the horizontal component. In the *AMSC 8501* tape, for example, some layers with different relative magnetic permeability are in contact to each other, and this could be problematic for the solver. Therefore, a test is performed in this regard, once the simulation is completed. However, performing this analysis exactly at the y-coordinate corresponding to the boundary surface (a line in 2-D) is not practical, but the continuity can be reasonably verified by comparing the H_x values inside each layer at a y-coordinate very close to the boundary line. Calling $y_{boundary}$ the y-coordinate of the boundary line, the H_x values are compared at coordinates equal to $y_{boundary}+\Delta y$ (inside the upper layer) and $y_{boundary}-\Delta y$ (inside the lower layer), where Δy is kept very small. Fig. 2.3.5.6, Fig. 2.3.5.7 and Fig. 2.3.5.8 show the tangent component of the magnetic field for three different couples of layers. Within each couple of layers selected there is a boundary line at a specific $y_{boundary}$ coordinate. In the upper part of Fig. 2.3.5.6, Fig. 2.3.5.7 and Fig. 2.3.5.8 the tape cross-section is presented highlighting the approximate locations at which the comparison is performed. Fig. 2.3.5.6 shows the comparison between the silver and superconducting layers, Fig. 2.3.5.7 between the superconducting layer and the substrate and Fig. 2.3.5.8 between the substrate and the lower copper layers. It is worth noting that in the first case, μ_r is equal for both layers ($\mu_r = 1$), while in the second and third cases, μ_r varies between the layers. As it can be seen from the figures, the continuity of the tangent component of the magnetic field is verified in all cases.

It is worth noting how the value of the magnetic field changes approaching the sides of the layers. This might be due to the fact that, at these coordinates, the solder region is nearer and this could modify the local value of the magnetic field. However, checking the validity of this assumption goes beyond the scope of this work
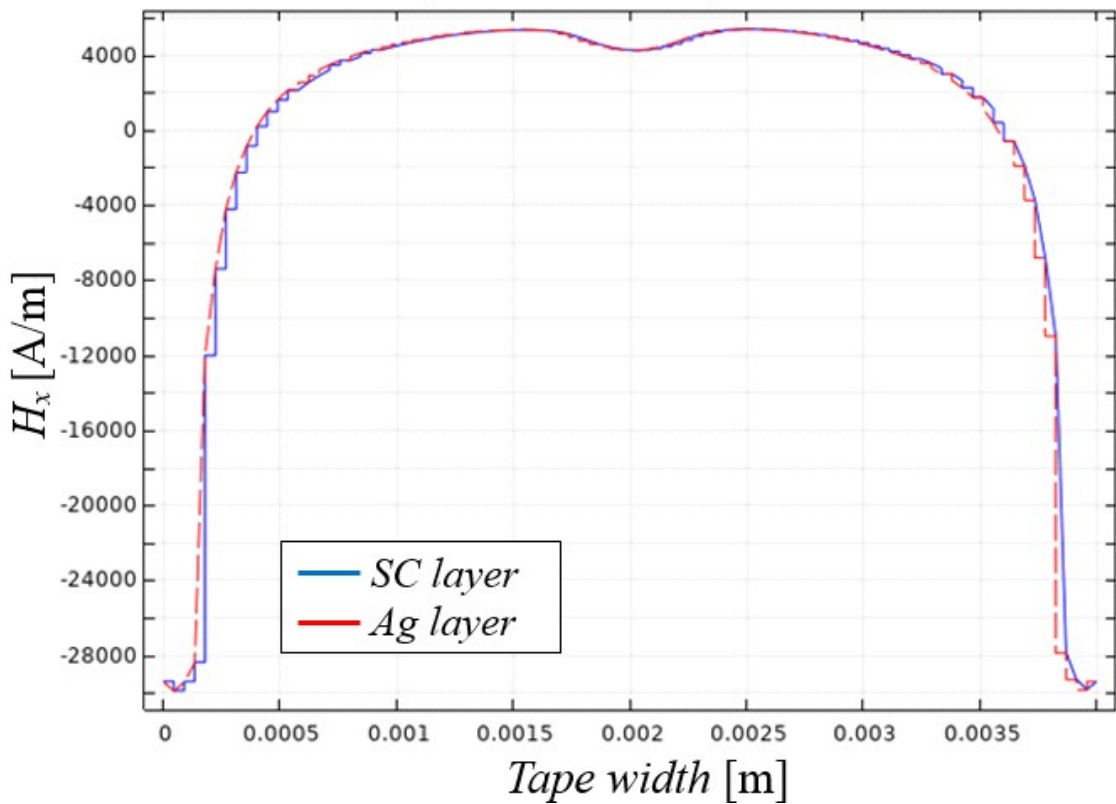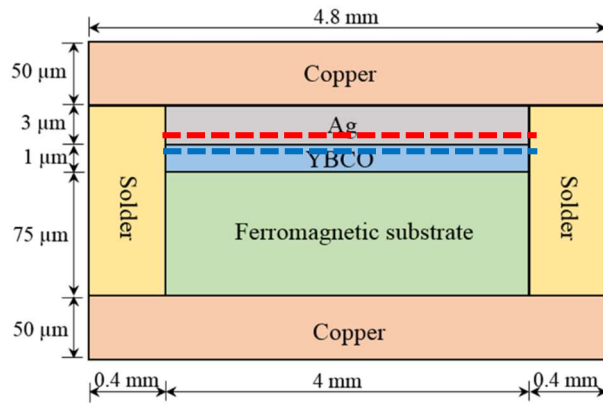
Figure 2.3.5.6. *Comparison of the tangent component of the magnetic field (H_x) inside the silver and the superconducting layers of the AMSC 8501 tape, at a y-coordinate very close to their boundary surface. The frequency is set to 55 Hz and $I_m = 0.9$. The instant selected corresponds to the end of the second period.*
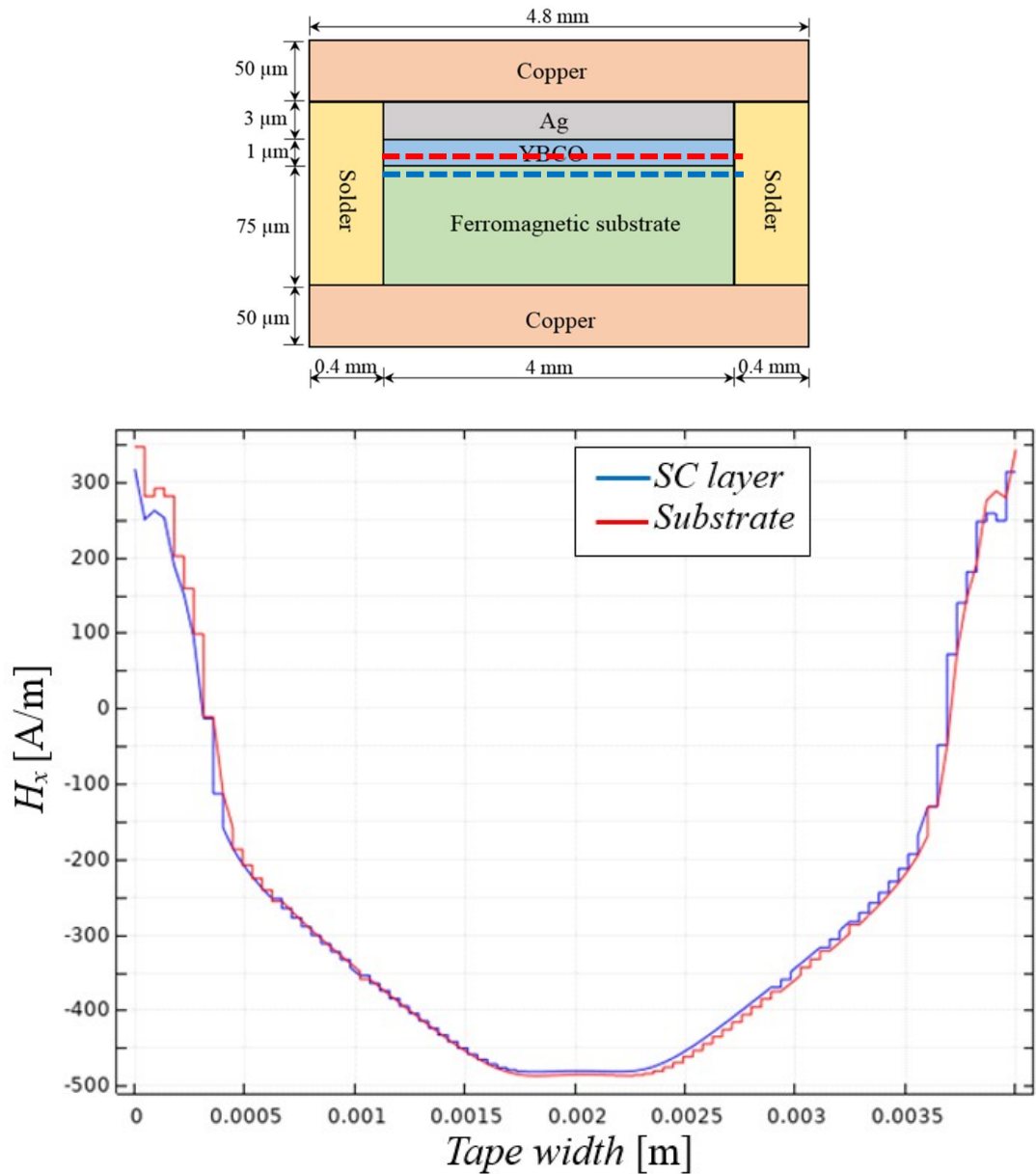
Figure 2.3.5.7. *Comparison of the tangent component of the magnetic field (H_x) inside the superconducting layer and the substrate of the AMSC 8501 tape, at a y-coordinate very close to their boundary surface. The frequency is set to 55 Hz and $I_m = 0.9$. The instant selected corresponds to the end of the second period.*
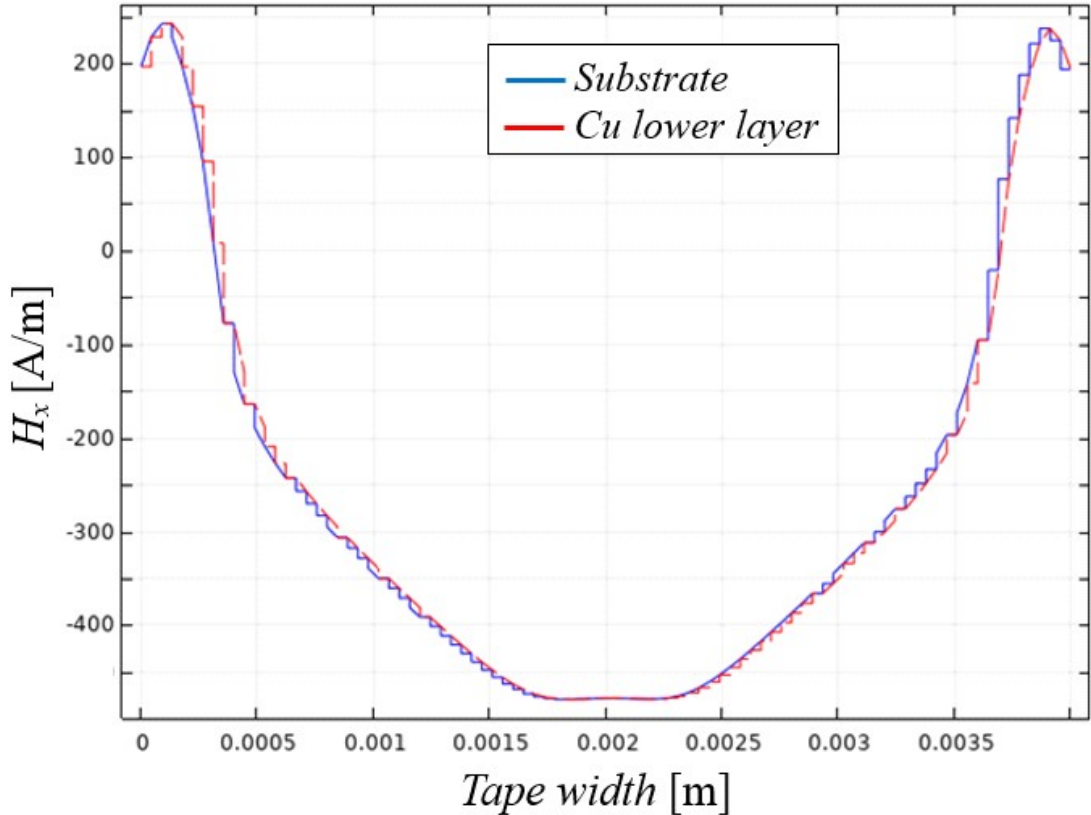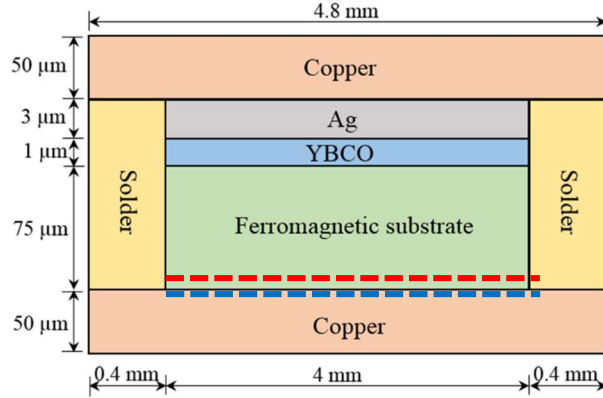
Figure 2.3.5.8. Comparison of the tangent component of the magnetic field (H_x) inside the substrate and the lower copper layer of the AMSC 8501 tape, at a y-coordinate very close to their boundary surface. The frequency is set to 55 Hz and I_m = 0.9. The instant selected corresponds to the end of the second period.

The numerical results are compared with those obtained through the well-known analytical formula developed for a thin rectangular tape of finite length, the so-called *Norris' formulation for a thin strip* [58]:

$$\langle p(t) \rangle_{Analytic} = f \frac{I_c \mu_0}{\pi} \left[(1 - I_m) \ln(1 - I_m) + (1 + I_m) \ln(1 + I_m) - I_m^2 \right] \left[\frac{W}{m} \right] \quad (2.3.5.3)$$

Eq. (2.3.5.3) considers a 1-D approximation of the system, neglecting the tape thickness and length. The tape is supposed to be composed by its superconducting layer only. Therefore,

great attention must be paid when testing the convergence of a 2-D numerical model (implementing all the different layers of a coated conductor) using this approximated formulation.

Fig. 2.3.5.9 shows the average power dissipation for the *AMSC 8501* tape calculated at different I_m values and for a frequency set to 55 Hz. The power dissipation increases in as the current amplitude rises. The "*SC_only*" and the analytical values converge at low currents, although the two curves show some discrepancies when the current approaches I_c. The "*Whole_tape*" curve is considerably higher at low amplitudes (more than 6 time higher for $I_m = 0.4$) and start converging to the other curves when the current approaches the tape critical current (but the discrepancy between the two curves does not fall below 20%).
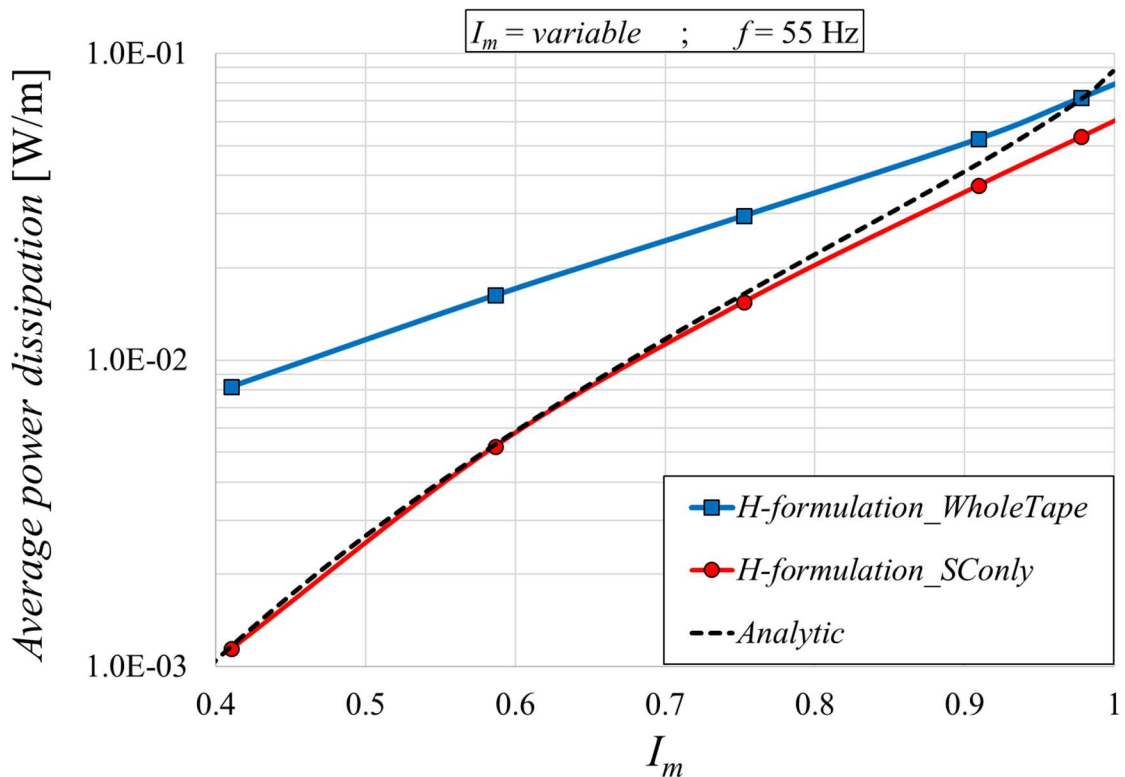
Figure 2.3.5.9. *Average power dissipation for different I_m values and for a frequency set to 55 Hz. The figure is in semi-logarithmic scale.*

Then, thanks to the versatility of the model, it is possible to calculate the losses generated in each layer of the tape by adjusting the integration parameters of Eq. (2.1.2). Fig. 2.3.5.10 presents the power dissipation produced at the layer level, for the same operating conditions of Fig. 2.3.5.9. The results for the two copper layers and those of the silver layer are summed and presented each as a single curve. The power dissipation rises with the increase of the current amplitude for all layers. The increase is almost linear for the copper and solder layers, while it is slightly exponential for the silver layers (despite the value remains very low) as well as for the superconducting layer due to its non-linear resistivity. Moreover, the power generated into the ferromagnetic substrate gradually approaches a stabilized value when the current amplitude reaches I_c, meaning that this material has reached the magnetic saturation [94].
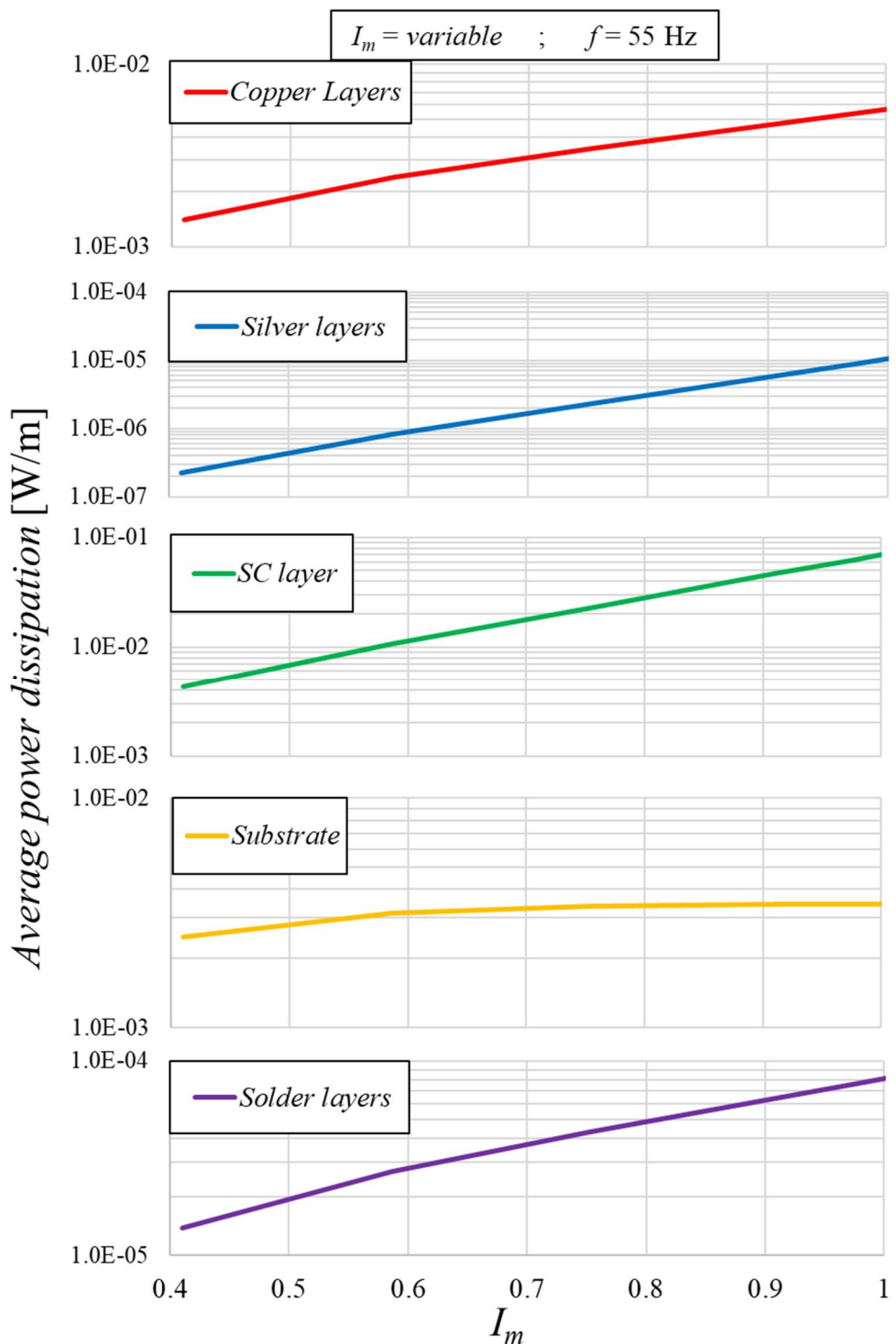
Figure 2.3.5.10. *Average power dissipation generated in each layer of the tape for different I_m values and for a frequency set to 55 Hz. The figure is in semi-logarithmic scale.*
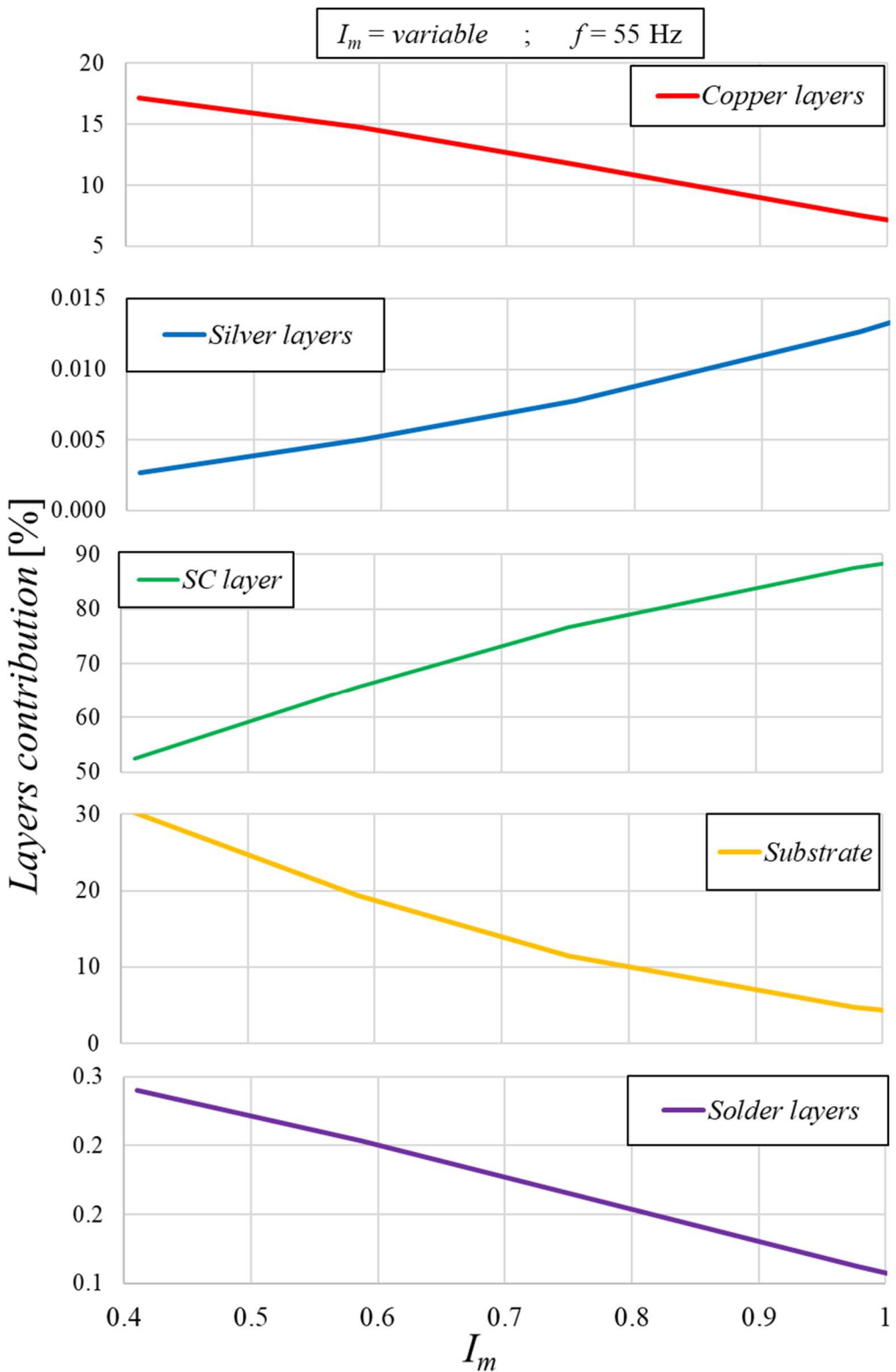
Figure 2.3.5.11. *Contribution of the layers to the average power of the whole tape, for different I_m values and for a frequency set to 55 Hz.*

The same results are displayed in Fig. 2.3.5.11, in terms of contribution of each layer to the average power dissipation of the whole tape (as a percentage). As it can be seen, the contribution to total losses of the superconducting layer increases linearly with the amplitude of the transport current, approaching 100% (meaning that the losses are generated by far in this

layer) when $I_{Amp} \approx I_c$. Conversely, the trend in the other layers decreases when I_m increases, except in the case of the silver layer (despite its contribution is marginal). It is worth noting that at low amplitudes the contributions of the ferromagnetic substrate and of the copper layers is relevant. When $I_m = 0.4$ for example, the contribution of these layers together is around 50% of the power dissipation of the whole tape. It can be concluded that the contribution of the ferromagnetic substrate (which is not included into the analytical formula or in the "*SC_only*" numerical case) dominates for low I_m values, reaching a stabilized value at higher amplitudes. Conversely, since the losses in the superconducting layer keep increasing with the amplitude, its contribution dominates for high I_m values and therefore the losses approach the analytic curve.

Then, the dependence of the AC losses on the frequency is investigated. Fig. 2.3.5.12 shows the numerical results for $I_m = 0.75$ and varying the frequency. While the analytic losses per cycle are frequency independent (the frequency does not compare into Eq. (2.3.5.3) once divided by f), the numerical results depend on the frequency. The "*Whole_tape*" curve rises when the frequency increases, thus diverging significantly from the analytic curve at high frequencies (more than 4 times higher). As expected, the "*SC_only*" curve is closer to the analytical results (maximum discrepancy equal to 30%). However, the "*SC_only*" curve decreases with frequency, conversely to the "*Whole_tape*" case.
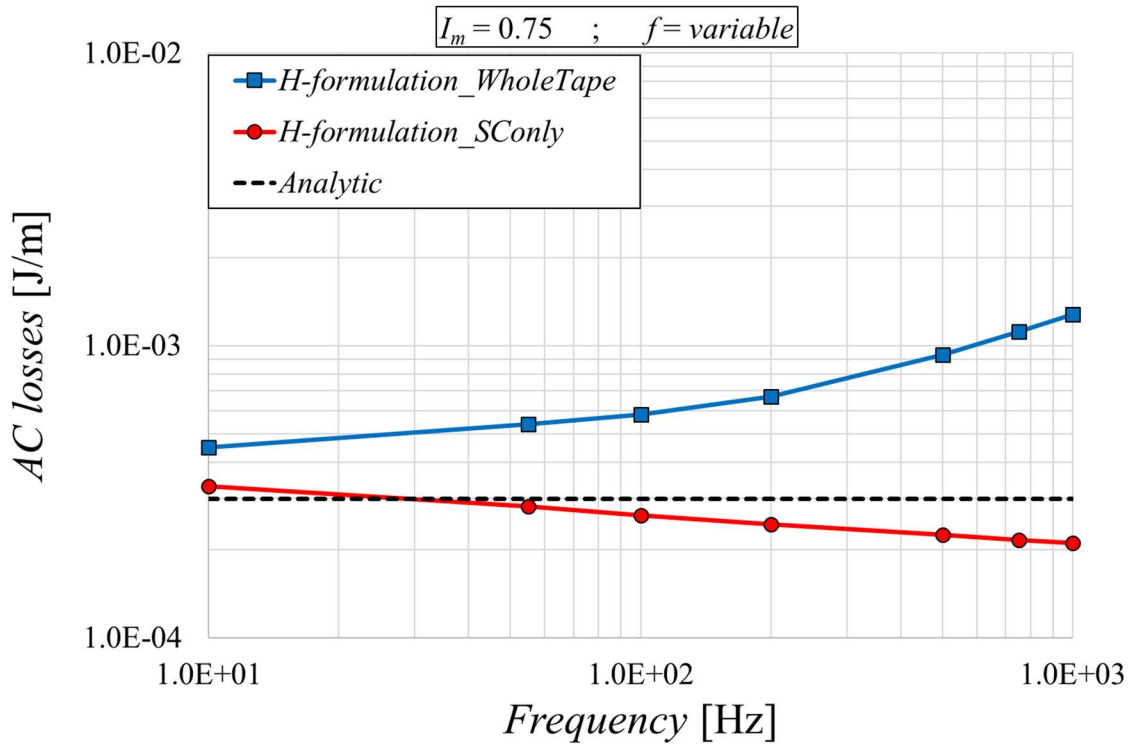
Figure 2.3.5.12. *AC losses for different frequencies and for I_m set to 0.4. The figure is in logarithmic scale.*

Fig. 2.3.5.13 presents the AC losses generated in the different layers of the tape for the same operating conditions of Fig. 2.3.5.12. The losses in the substrate are frequency independent. The losses in the superconductor are linear up to 100 Hz, and then they decrease by about 20%. As expected, the AC losses in the metallic layers increase almost linearly with the

frequency [95, 96, 114]. In particular, the losses in the copper layers exceeds the losses in the superconducting layer when the frequency is above 300 Hz.
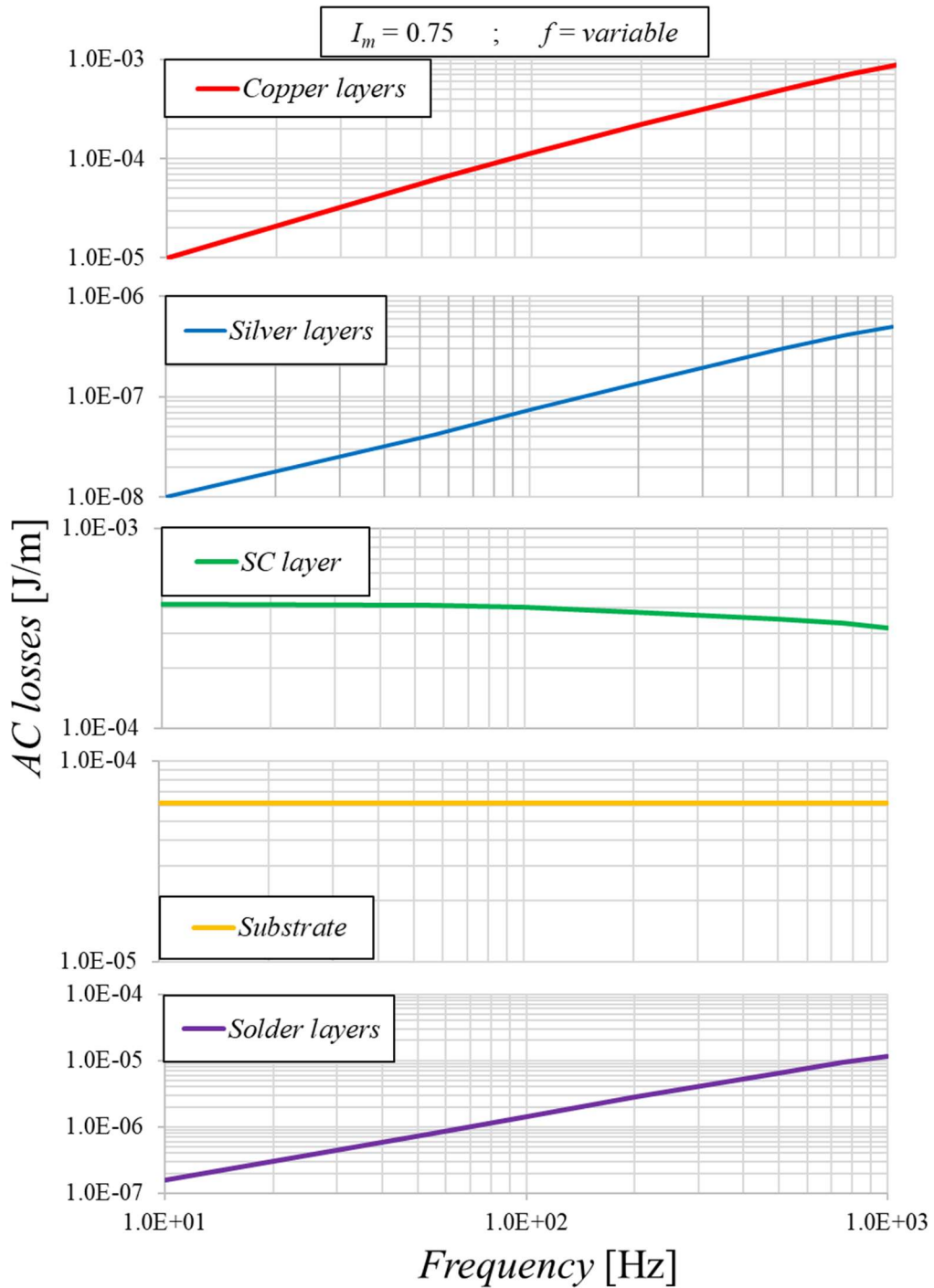
Figure 2.3.5.13. *AC losses generated in each layer of the tape for different frequencies and for I_m set to 0.4. The figure is in logarithmic scale.*
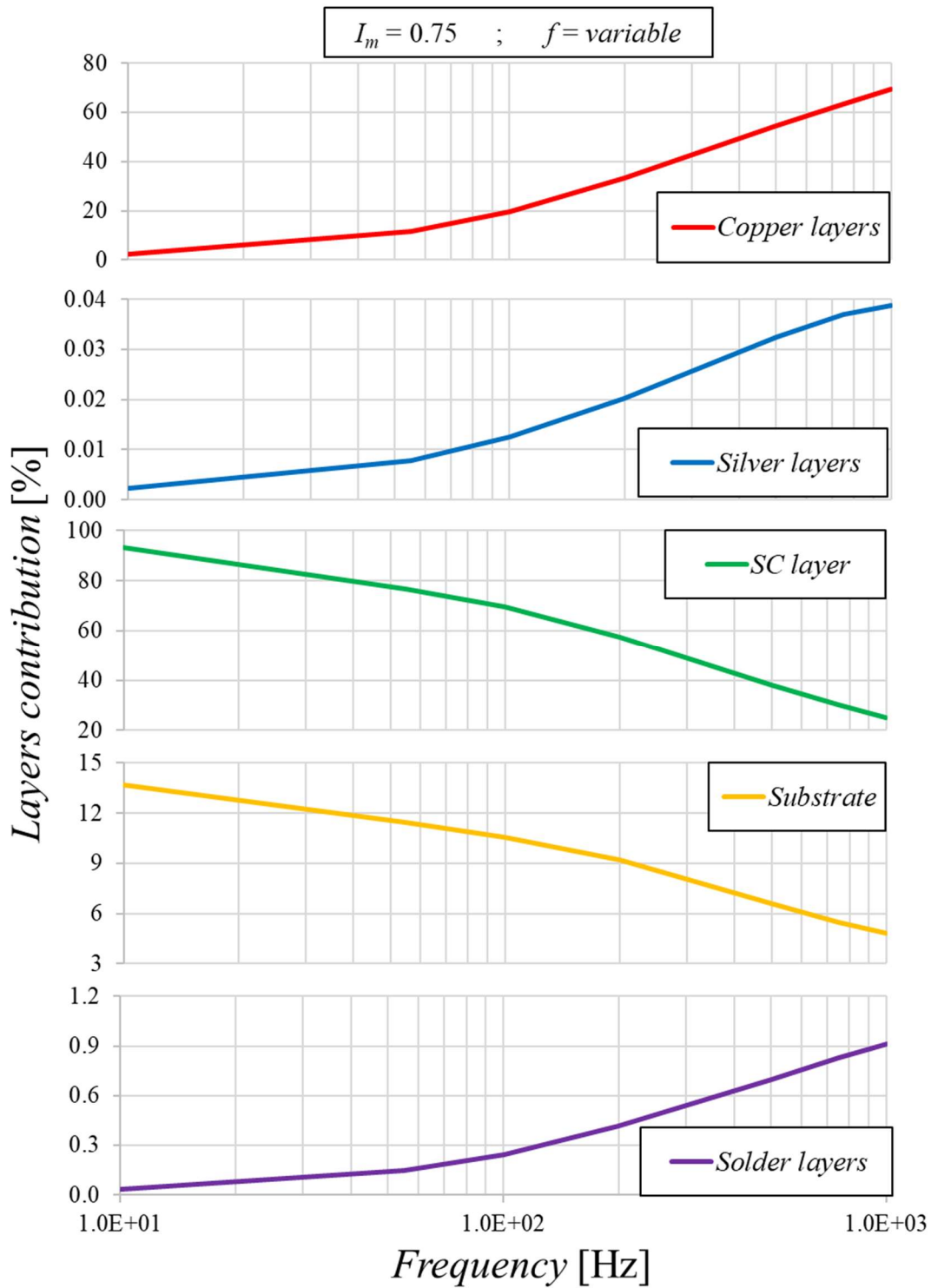
Figure 2.3.5.14. *Contribution of the layers to the AC losses of the whole tape for different frequencies and for I_m set to 0.4. The figure is in semi-logarithmic scale.*

The same results are displayed in terms of single layer contribution to the total AC losses (as a percentage) in Fig. 2.3.5.14. The contributions of the substrate and of the superconducting layers become less and less important with frequency, despite their losses are almost frequency independent. That is due to the loss increase in the other layers. In particular, the losses in the copper layers have the highest enhancement, contributing to around the 70% of the total losses

when the frequency is equal to 1 kHz. The significant contribution given by the copper layers in the tape can also be due to their thickness, which is relevant compared to the thicknesses of the copper stabilizers used in other HTS tapes [115]. Moreover, it is demonstrated that when the frequency increases, even the current distribution in the tape cross-section modifies, and the current starts migrating into the metallic paths [96]. It is concluded that the substrate and the superconducting layers dominate at low frequency, while at high frequency the current starts migrating toward the metallic layers which increase their contributions to the total losses.
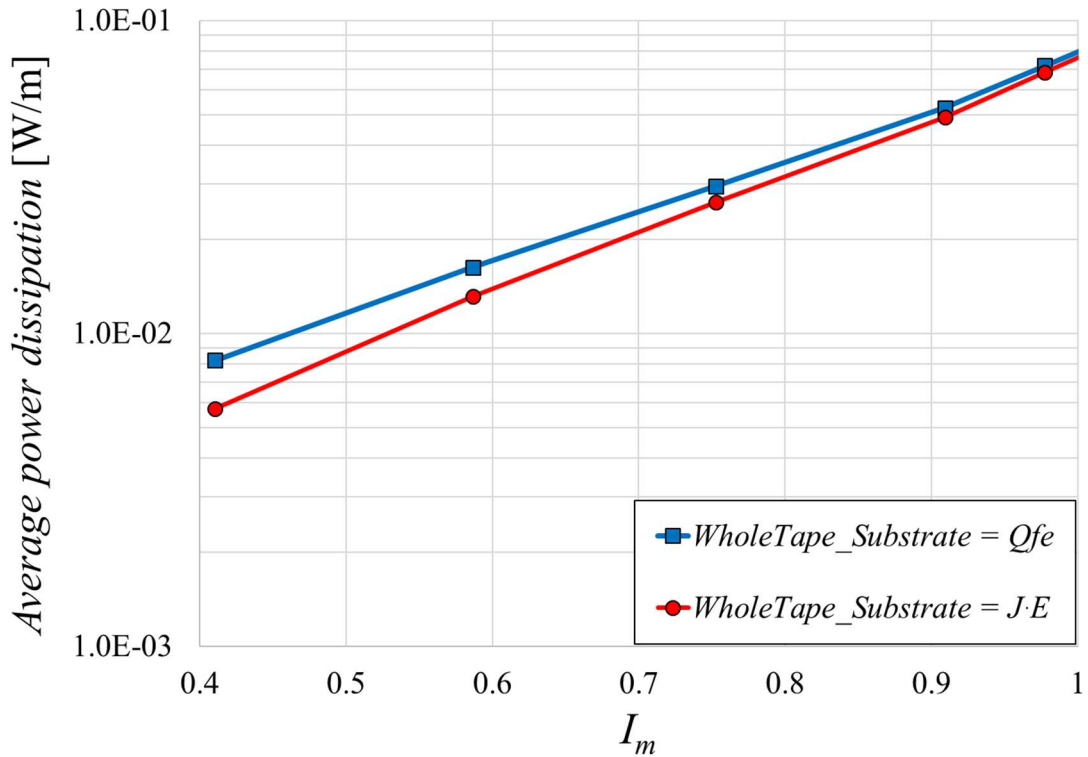
Figure 2.3.5.15. *Comparison between the average power dissipation generated in the whole tape computed with Eq. (1.6) (red) or with Eq. (4.16) (blue). The figure is in semi-logarithmic scale.*

Finally, it is interesting to analyse the impact of the equations adopted to calculate the losses in the ferromagnetic substrate of the tape, *i.e.* selecting for this layer, one of the two formulations reported in Eq. (2.3.4.16). Fig. 2.3.5.16 shows the average power dissipation for the whole tape, adopting for all layers, including the ferromagnetic layer, Eq. (2.3.4.16b) (the second one in the system); this case is referred in the figure as *WholeTape_Substrate = J·E*. Moreover, the same figure presents the dissipation computed selecting Eq. (2.3.4.16a) (the first one in the system) for the ferromagnetic substrate only, referred as *WholeTape_Substrate = Q_{fe}*. The losses computed considering a different formula for the ferromagnetic material (Q_{fe}) are slightly higher compared to the other case: for low current amplitudes the discrepancy is relevant (≈ 30% when $I_m = 0.4$), while they converge for high currents.

For a better understanding, Fig. 2.3.5.17 presents the average power dissipation generated in the substrate layer only with both methods. The two trends are very different. When the Q_{fe} function is used (left axis), the power dissipation has a logarithmic increase with the current.

When the formulation involving the product between J and E is used (right axis), the losses rises with an exponential trend. Moreover, the losses computed in the substrate results significantly different in the two cases, with at least one order of magnitude of discrepancy. It is concluded that the choice of one formulation compared to the other should be carefully evaluated because it leads to different results.
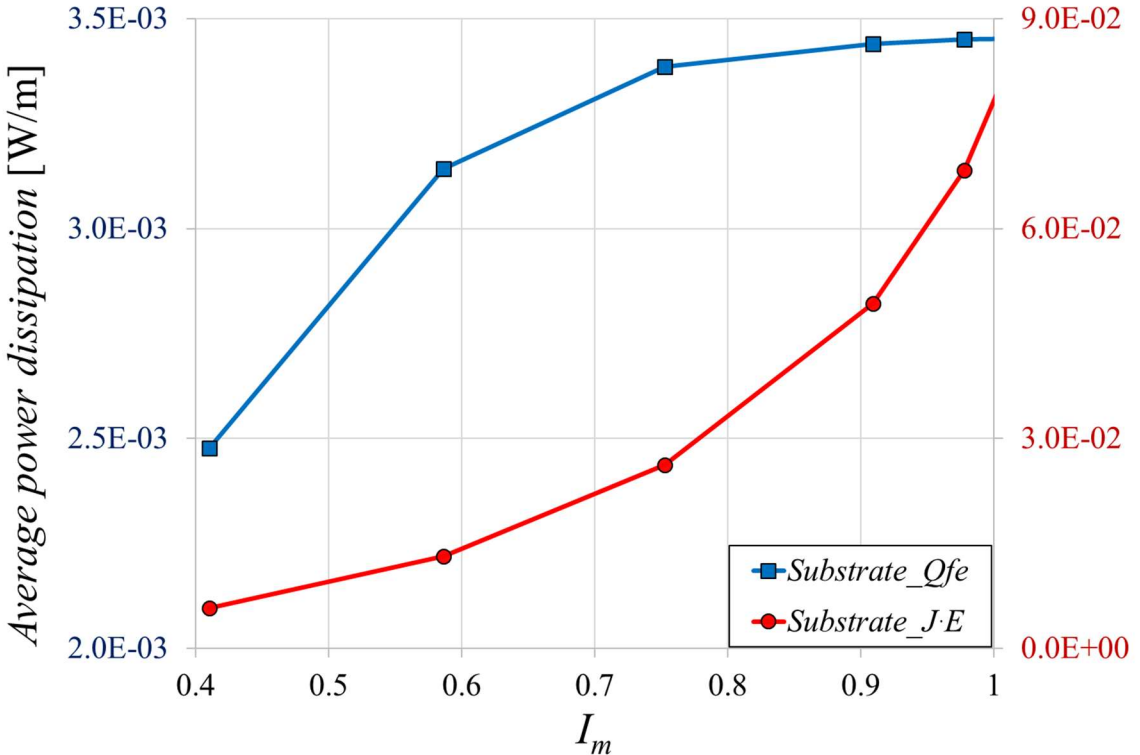
Figure 2.3.5.17. *Comparison between the average power dissipation generated in the ferromagnetic substrate, computed with Eq. (2.3.4.16) (in blue in the main axis) and with Eq. (2.3.4.14) (in red and in the secondary axis), for f = 55 Hz and varying I_m.*

2.4. *Integral model based on the A-V formulation*

This section describes an integral model based on the *A-V* formulation to calculate the AC losses in HTS tapes. The model is based on the definition of the vector potential *A* as a function of the current density. In integral models, after a spatial and time discretization of the tape, a system of ordinary differential equations is obtained, which can be solved through a solver in matrix form. Unlike FEM models, the equations are written in integral form and they are solved in the conductor volume only, avoiding the air discretization [80]. Therefore, the number of system unknowns is reduced and the computation time is lower (if the computation domain is not too large).

The method was firstly proposed in [116] and then applied later to different geometries as Bi--223 tapes [75, 77, 117], slabs [118] or cylindrical geometries [119, 120]. This approach has not yet been applied to study coated conductors in 2-D and in presence of non-superconducting layers.

2.4.1. Simplifying hypothesis for the numerical model based on A-V formulation

As performed for the model based on *H*-formulation, simplifying hypotheses are applied to the 3-D geometry of the coated conductor. It should be pointed out that in this case, the tape is not considered to be infinitely long, but the conductor has a finite length *L*. However, the following assumptions are adopted:

➢ the central portion of the tape (at least the one included between the voltage taps: $z \in \left[-\frac{L_0}{2}, \frac{L_0}{2}\right]$) is considered to be at a sufficient distance from the tape ends so that the system variables in this region are independent of the *z*-coordinate. Therefore, the same conditions expressed in Eq. (2.3.1.1) are used:

$$E(x, y, z, t) = E(x, y, t)\, \mathbf{k}$$
$$\mathbf{J}(x, y, z, t) = J(x, y, t)\, \mathbf{k} \qquad\qquad (2.4.1.1)$$
$$\mathbf{A}(x, y, z, t) = A(x, y, t)\, \mathbf{k}$$

➢ the contribution to the self-field of the electric circuit but the tape (the current leads and the power supply connections) is neglected.

These hypotheses can be applied to the equations without neglecting the tape length. This differs from the approach used in 2-D models for rectangular bars, which consider the conductor as infinitely long [61].

Following the steps used in *A-V* formulations, the electric field can be expressed as a function of the scalar and vector potentials. The relation can be deduced starting from Faraday's law, expressed in Eq. (2.3.2.1). Then, the magnetic induction field can be express as the curl of the vector potential using Gauss' law ($\mathbf{\nabla} \cdot \mathbf{B} = 0$):

$$\mathbf{B} = \mathbf{\nabla} \times \mathbf{A} \qquad\qquad (2.4.1.2)$$

Combining Eq. (2.4.1.2) into Eq. (2.3.2.1) it results:

$$\mathbf{\nabla} \times \mathbf{E} = -\frac{\partial (\mathbf{\nabla} \times \mathbf{A})}{\partial t}$$
$$\mathbf{\nabla} \times \mathbf{E} = -\mathbf{\nabla} \times \frac{\partial \mathbf{A}}{\partial t} \qquad\qquad (2.4.1.3)$$
$$\mathbf{\nabla} \times \left(\mathbf{E} + \frac{\partial \mathbf{A}}{\partial t}\right) = 0$$

Stating that the curl of a vector is equal to zero, is equivalent to assert that the vector is equal to the gradient of a scalar. In electromagnetism, the scalar corresponds to the scalar potential *V*. It results:

$$\mathbf{E} + \frac{\partial \mathbf{A}}{\partial t} = -\mathbf{\nabla} V \qquad\qquad (2.4.1.4)$$

$$E = -\nabla V - \frac{\partial \boldsymbol{A}}{\partial t}$$

From the hypothesis of Eq. (2.4.1.1), the scalar potential is independent of the x and y coordinates, since it is assumed that at every location the tape cross-sections (*x-y planes*) are equipotential sections:

$$V(x, y, z, t) = V(z, t)\, \boldsymbol{k} \qquad (2.4.1.5)$$

The same assumption is applied to the gradient term ∇V. It follows:

$$E(x, y, t) = -\frac{dV}{dz}(t) - \frac{\partial A}{\partial t}(x, y, t) \qquad (2.4.1.6)$$

2.4.2. *Equations in the case without compensation and with voltage taps twisted at a certain distance from the tape middle axis*

The configuration of the voltage measurement circuit analysed in this section is the mostly used and well described in the literature [121 – 126]. A scheme of this experimental configuration is presented in Fig. 2.4.2.1. A couple of voltage taps are soldered on the upper surface of the tape (*A* and *B* points), they are then brought perpendicularly at a certain distance in the x direction from the tape middle axis (*A'* and *B'* points) before they are twisted together (*D* and *C* points) and connected to the voltmeter terminals.

Fig. 2.4.2.2 shows a photo of the voltage measurement circuit applied to an HTS tape placed over a G-10 support and connected to a power supply using copper bars.
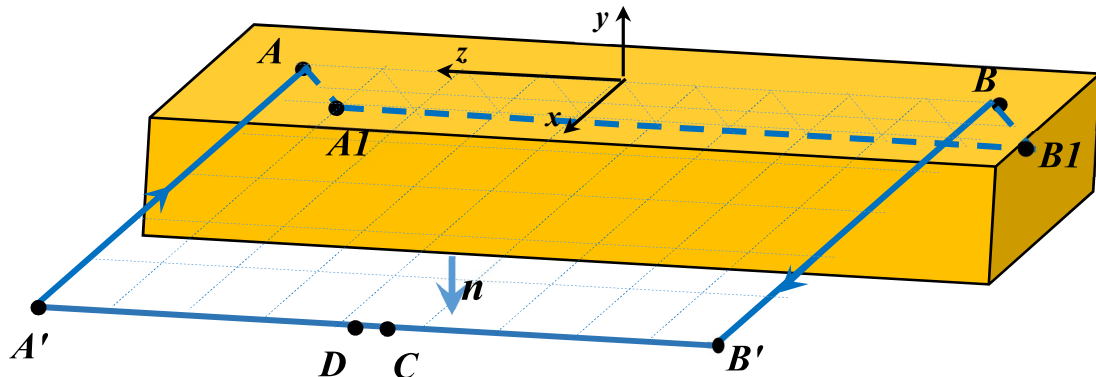
Figure 2.4.2.1. *Scheme of the voltage measurement circuit without compensation and with voltage taps twisted at a certain distance from the tape middle axis. The dashed bold path extends inside the tape surface.*
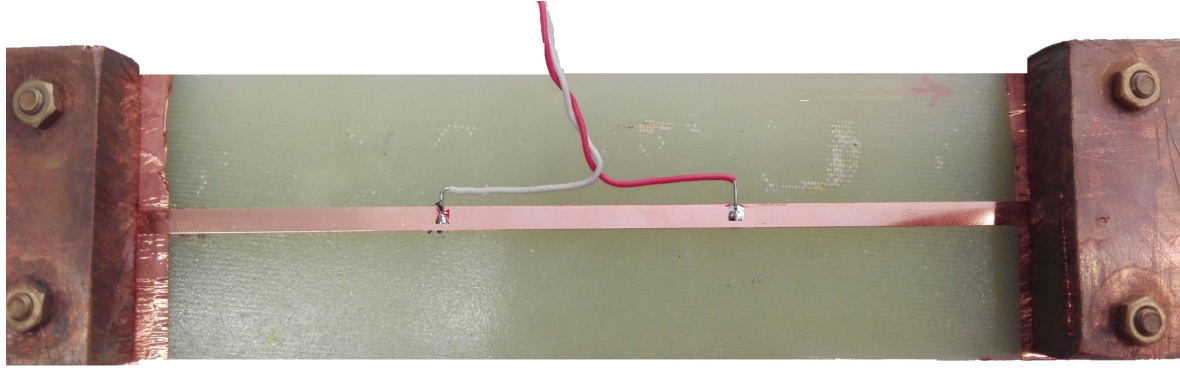
Figure 2.4.2.2. Photo of the voltage measurement circuit without compensation and with voltage taps twisted at a certain distance from the tape middle axis, applied to an HTS tape.

For the simplifying hypothesis of Eq. (2.4.1.1), the integrand of Eq. (2.1.2) can be taken out of the integral along the z-coordinate.

$$p(t) = L_0 \int_{-\frac{\delta}{2}}^{\frac{\delta}{2}} \int_{-\frac{w}{2}}^{\frac{w}{2}} E(x, y, t) J(x, y, t) dx dy \qquad (2.4.2.1)$$

Then, inserting Eq. (2.4.1.6) into Eq. (2.4.2.1), it results:

$$p(t) = L_0 \int_{-\frac{\delta}{2}}^{\frac{\delta}{2}} \int_{-\frac{w}{2}}^{\frac{w}{2}} \left(\left(-\frac{dV}{dz}(t) - \frac{\partial A}{\partial t}(x, y, t) \right) J(x, y, t) \right) dx dy =$$

$$= -L_0 \int_{-\frac{\delta}{2}}^{\frac{\delta}{2}} \int_{-\frac{w}{2}}^{\frac{w}{2}} \left(\frac{dV}{dz}(t) J(x, y, t) \right) dx dy - L_0 \int_{-\frac{\delta}{2}}^{\frac{\delta}{2}} \int_{-\frac{w}{2}}^{\frac{w}{2}} \left(\frac{\partial A}{\partial t}(x, y, t) J(x, y, t) \right) dx dy = \qquad (2.4.2.2)$$

$$= -L_0 \frac{dV}{dz}(t) I_{Tot}(t) - L_0 \int_{-\frac{\delta}{2}}^{\frac{\delta}{2}} \int_{-\frac{w}{2}}^{\frac{w}{2}} \frac{\partial A}{\partial t}(x, y, t) J(x, y, t) dx dy = V_{AB}(t) I_{Tot}(t) + p_A(t)$$

where $V_{AB}(t)$ is the voltage difference between the two points on the tape surface corresponding to the voltage taps soldering, and $p_A(t)$ is the contribution due to the part of the non-conservative electric field, given by:

$$p_A(t) = -L_0 \int_{-\frac{\delta}{2}}^{\frac{\delta}{2}} \int_{-\frac{w}{2}}^{\frac{w}{2}} \frac{\partial A}{\partial t}(x, y, t) J(x, y, t) dx dy \qquad (2.4.2.3)$$

Therefore, the average value in a period of the dissipated power has the following expression:

$$\langle p(t) \rangle = \langle V_{AB}(t) I_{Tot}(t) + p_A(t) \rangle \qquad [W] \qquad (2.4.2.4)$$

In the *Appendix* it is demonstrated that, being the regime periodic:

$$\langle p_A(t) \rangle = 0 \qquad (2.4.2.5)$$

Combining Eq. (2.4.2.4) and Eq. (2.4.2.5), it follows:

$$\langle p(t) \rangle = \langle V_{AB}(t) I_{Tot}(t) \rangle \qquad [W] \qquad (2.4.2.6)$$

The relation between what the user can obtain, the reading of the voltmeter $V_0(t)$, and what the user needs to calculate losses using Eq. (2.4.2.6), the voltage difference $V_{AB}(t)$, is derived applying the law of electromagnetic induction in integral form for the closed curve shown in Fig. 2.4.2.1 (called *Circuit1*) and consisting of:

➤ A portion of the curve, C_{AB}, that connects the points *A* and *B*, remaining inside the superconducting tape. This curve is composed of a segment C_{A-A1} that lies in the plane at z coordinate equal to $-\frac{L}{2}$ and joins point *A* with the generic point *A1* of coordinates $A1 = \left(x, y, -\frac{L}{2}\right)$, a segment C_{A-B1} connecting points *A1* and *B1* of coordinates $\left(x, y, \frac{L}{2}\right)$, and a segment C_{B-B1} that joins points *B1* and *B* lying in the plane at z-coordinate equal to $\frac{L}{2}$;

➤ The C_{B-C} curve consisting of the wire connecting the point *B* with the terminal *B*;

➤ A segment C_{C-D} connecting terminals *C* and *B*;

➤ The curve C_{D-A} consisting of the wire that connects the terminal *D* with the contact *A*.

From Faradays's law, indicating with $\emptyset_{C1}$ the flux of the magnetic induction field through the surface bounded by the closed curve *Circuit1* and having its normal unit vector parallel to the direction of travel of the curve by the right-handed screw rule, it results:

$$\oint_{Circuit1} \boldsymbol{E} \cdot \boldsymbol{dl} = -\frac{d\emptyset_{C1}}{dt}(x, y, t) \qquad (2.4.2.7)$$

Since the closed curve *Circuit1* can be divided in the segments described above, Eq. (2.4.2.7) can be written as:

$$\int_A^{A1} \boldsymbol{E} \cdot \boldsymbol{dl} + \int_{A1}^{B1} \boldsymbol{E} \cdot \boldsymbol{dl} + \int_{B1}^{B} \boldsymbol{E} \cdot \boldsymbol{dl} + \int_B^C \boldsymbol{E} \cdot \boldsymbol{dl} + \int_C^D \boldsymbol{E} \cdot \boldsymbol{dl} + \int_D^A \boldsymbol{E} \cdot \boldsymbol{dl} =$$
$$= -\frac{d\emptyset_{C1}}{dt}(x, y, t) \qquad (2.4.2.8)$$

Then, Eq. (2.4.2.8) can be simplified as follows.

The contribution of the segments C_{B-C} e C_{D-A} can be neglected, since the current that circulates in these portion of copper wires is negligible, due to the large internal impedance of the voltmeter:

$$\int_B^C \boldsymbol{E} \cdot \boldsymbol{dl} = 0; \int_D^A \boldsymbol{E} \cdot \boldsymbol{dl} = 0 \qquad (2.4.2.9)$$

The contribution of the segment C_{CD} is related to the voltmeter reading:

$$\int_C^D \boldsymbol{E} \cdot \boldsymbol{dl} = -V_0(t) \qquad (2.4.2.10)$$

The contribution of the segments C_{A-A1} e C_{B-B1} is negligible since for them the vector $\boldsymbol{dl}$ (directed along the x-coordinate) is perpendicular to the electric field (directed along the *z*-coordinate). Thus, their scalar products are null:

$$\int_A^{A1} \boldsymbol{E} \cdot \boldsymbol{dl} = 0; \quad \int_{B1}^{B} \boldsymbol{E} \cdot \boldsymbol{dl} = 0 \tag{2.4.2.11}$$

The contribution of the segment $C_{A1\text{-}B1}$ can be expressed using Eq. (2.4.1.6):

$$\int_{A1}^{B1} \boldsymbol{E} \cdot \boldsymbol{dl} =$$

$$= \int_{A1}^{B1} \left(-\frac{dV}{dz}(t) - \frac{\partial A}{\partial t}(x,y,t) \right) dz = \int_{A1}^{B1} \left(-\frac{dV}{dz}(t) \right) dz + \int_{A1}^{B1} \left(-\frac{\partial A}{\partial t}(x,y,t) \right) dz \tag{2.4.2.12}$$

where the integrand term $\frac{dV}{dz}(t)$ between the points $A1$ and $B1$ (note the position of the integration extremes) is equal to $\frac{V_{BA}}{L_0}(t) = -\frac{V_{AB}}{L_0}(t)$, corresponding to the voltage difference between points A and B, spaced by the length L_0. Since both integrand terms $-\left(-\frac{V_{AB}}{L_0}(t) \right)$ and $-\frac{\partial A}{\partial t}(x,y,t)$ of Eq. (2.4.2.12) are independent of the z-coordinate, they can be taken out the integral:

$$\int_{A1}^{B1} \boldsymbol{E} \cdot \boldsymbol{dl} = V_{AB}(t) - L_0 \frac{\partial A}{\partial t}(x,y,t) \tag{2.4.2.13}$$

Substituting the contribution of each segment of Eq. (2.4.2.8) with the results of the passages from Eq. (2.4.2.9) to Eq. (2.4.2.13), it follows:

$$0 + V_{AB}(t) - L_0 \frac{\partial A}{\partial t}(x,y,t) + 0 + 0 - V_0(t) + 0 = -\frac{d\emptyset_{C1}}{dt}(x,y,t)$$

$$V_{AB}(t) - L_0 \frac{\partial A}{\partial t}(x,y,t) - V_0(t) = -\frac{d\emptyset_{C1}}{dt}(x,y,t) \tag{2.4.2.14}$$

Isolating the term $V_0(t)$ from Eq. (2.4.2.14), it results:

$$V_{AB}(t) = V_0(t) - \varepsilon(t)$$

$$\varepsilon(t) = -L_0 \frac{\partial A}{\partial t}(x,y,t) + \frac{d\emptyset_{C1}}{dt}(x,y,t) \tag{2.4.2.15}$$

Eq. (2.4.2.15) shows the relation between the reading of the voltmeter $V_0(t)$ and the voltage difference $V_{AB}(t)$. The two quantities differ for an error term $\varepsilon(t)$. Eq. (2.4.2.14) is equivalent to state that $V_{AB}(t) = V_0(t) - \varepsilon(t)$. The error $\varepsilon(t)$ between the desired value $V_{AB}(t)$ and the measured value $V_0(t)$ produces an error η in the loss measurement. Then, the expression for $V_{AB}(t)$ can be inserted into Eq. (2.4.2.6):

$$\langle p(t) \rangle = \langle V_{AB}(t) I_{Tot}(t) \rangle = \langle V_0(t) I_{Tot}(t) - \varepsilon(t) I_{Tot}(t) \rangle = (\langle V_0(t) I_{Tot}(t) \rangle + \eta)$$

$$\eta = -\langle \varepsilon(t) I_{Tot}(t) \rangle \tag{2.4.2.16}$$

The error on the voltage measurement $\varepsilon(t)$ can be reformulated by rewriting the term due to the magnetic flux of Eq. (2.4.2.15). The flux of magnetic induction through the surface bounded

by the curve *Circuit1* can be expressed by means of the Stokes' theorem as the circulation of the vector potential along that same curve:

$$\phi_{C1}(t) = \oint_{Circuit1} \boldsymbol{A} \cdot \boldsymbol{dl} \tag{2.4.2.17}$$

Whereupon, it is convenient to split the curve *Circuit1* into two sections, the first piece corresponding to the segment *A1-B1* and the second piece corresponding to the rest of the curve, the line *B1-B-B'-C-D-A'-A-A1* of Fig. 2.4.2.1 (naming this new curve as *Circuit1bis*). It results:

$$\phi_{C1}(t) = \int_{A1}^{B1} \boldsymbol{A} \cdot \boldsymbol{dl} + \int_{Circuit1bis} \boldsymbol{A} \cdot \boldsymbol{dl} = L_0 A(x,y,t) + \int_{Circuit1bis} \boldsymbol{A} \cdot \boldsymbol{dl} \tag{2.4.2.18}$$

Inserting Eq. (2.4.2.18) into Eq. (2.4.2.15) it yields:

$$V_0(t) = V_{AB}(t) - L_0 \frac{\partial A}{\partial t}(x,y,t) + \frac{d\phi_{C1}}{dt}(t) =$$

$$= V_{AB}(t) - L_0 \frac{\partial A}{\partial t}(x,y,t) + L_0 \frac{\partial A}{\partial t}(x,y,t) + \int_{Circuit1bis} \frac{\partial A}{\partial t} \, \boldsymbol{dl} = \tag{2.4.2.19}$$

$$= V_{AB}(t) + \int_{Circuit1bis} \frac{\partial A}{\partial t} \cdot \boldsymbol{dl}$$

It follows that:

$$\varepsilon(t) = \int_{Circuit1bis} \frac{\partial \boldsymbol{A}}{\partial t} \, \boldsymbol{dl} \tag{2.4.2.20}$$

If the hypotheses of Eq. (2.4.1.1) are considered valid in the whole measurement circuit (not only in the superconducting tape), in all the points of the curve *Circuit1bis* the vector potential has its z component only. Then, with reference to the geometry of the measurement circuit of Fig. 2.4.2.1, the only portion of the curve *Circuit1bis* that contributes to the error $\varepsilon(t)$ is the line where the terminals of the voltmeter are located (line *B'-A'*), since along all the other segments the vectors $\boldsymbol{A}$ and $\boldsymbol{dl}$ are perpendicular. Moreover, since the line *B'-A'* is parallel to the *z-axis*, the integral in $\boldsymbol{dl}$ is equivalent to an integral in dz. Thus, the error term $\varepsilon(t)$ of Eq. (2.4.2.20) can be rewritten as:

$$\varepsilon(t) = \int_{B'}^{A'} \frac{\partial \boldsymbol{A}}{\partial t} \cdot \boldsymbol{dl} = \int_{B'}^{A'} \frac{\partial A}{\partial t} \, dz \tag{2.4.2.21}$$

This expression for $\varepsilon(t)$ is written for a generic case in which the vector potential may be dependent on the *z*-coordinate. This is the case occurring when the points *A'* and *B'* are not placed at a sufficient distance from the tape ends.

Then, to calculate the average power dissipation, the mean value in a period between $V_0(t)$ of Eq. (2.4.2.21) and $I_{Tot}(t)$ can be computed:

$$\langle p(t) \rangle = \langle V_{AB}(t) I_{Tot}(t) \rangle = \langle V_0(t) I_{Tot}(t) - \varepsilon(t) I_{Tot}(t) \rangle =$$
$$= \langle V_0(t) I_{Tot}(t) \rangle + \eta$$

$$\eta = -\langle \varepsilon(t) I_{Tot}(t) \rangle = -\left\langle \left(\int_{B'}^{A'} \frac{\partial A}{\partial t} \, dz \right) I_{Tot}(t) \right\rangle$$

$[W]$ (2.4.2.22)

Diving by L_0 , the power dissipation per unit length is obtained:

$$\langle p(t) \rangle_{per\,unit} = \frac{1}{L_0} \langle V_{AB}(t) I_{Tot}(t) \rangle = \frac{1}{L_0} \langle V_0(t) I_{Tot}(t) - \varepsilon(t) I_{Tot}(t) \rangle$$

$$= \frac{1}{L_0} \langle V_0(t) I_{Tot}(t) \rangle + \eta_{per\,unit}$$

$$\eta_{per\,unit} = -\frac{1}{L_0} \langle \varepsilon(t) I_{Tot}(t) \rangle = -\frac{1}{L_0} \left\langle \left(\int_{B'}^{A'} \frac{\partial \boldsymbol{A}}{\partial t} \, dz \right) I_{Tot}(t) \right\rangle$$

$\left[\dfrac{W}{m}\right]$ (2.4.2.23)

When the *z*-coordinates of points *A'* and *B'* are equal to $-\frac{L_0}{2}$ and $\frac{L_0}{2}$, as it would be for practical cases, the corrective factor $\eta_{per\,unit}$ is equal to:

$$\eta_{per\,unit} = -\frac{1}{L_0} \left\langle \left(\int_{-\frac{L_0}{2}}^{\frac{L_0}{2}} \frac{\partial \boldsymbol{A}}{\partial t} \, dz \right) I_{Tot}(t) \right\rangle$$

$\left[\dfrac{W}{m}\right]$ (2.4.2.24)

If the hypothesis of Eq. (2.4.1.1) are considered valid between the points *A'* and *B'*, or rather than the vector potential is still independent of the *z*-coordinate even at a certain distance from the tape middle axis, the integrand $\frac{\partial A}{\partial t}$ of Eq. (2.4.2.21) can be taken out of the integral and the equation can be easily solved.

It follows that for sufficiently large values of *R*, corresponding to the distance of the line *B'-A'* from the tape middle axis, the vector potential on the line *B'-A'* can be assumed to be dependent on the total current only and not on the current distribution inside the tape. This is equivalent to state that there is a constant *C*, dependent only on the position of the line *B'-A'*, satisfying the following equation:

$$A\left(R, \frac{\delta}{2}, t\right) = C\left(R, \frac{\delta}{2}\right) I_{Tot}(t)$$

(2.4.2.25)

If this hypothesis is verified, it follows that the corrective factor η of Eq. (2.4.2.24) is null, since both terms $\frac{dI_{Tot}(t)}{dt}$ and $I_{Tot}(t)$ are periodic and their mean over a period is null, while *C* is a constant. It means that the numerical AC losses should corresponds to the measured ones. Therefore:

$$\eta = -\langle \varepsilon(t) I_{Tot}(t) \rangle = -\left\langle L_0 \frac{\partial A}{\partial t}\left(R, \frac{\delta}{2}, t\right) I_{Tot}(t) \right\rangle =$$
$$= -\left\langle L_0 \, C\left(R, \frac{\delta}{2}\right) \frac{dI_{Tot}(t)}{dt} I_{Tot}(t) \right\rangle = 0$$

$[W]$ (2.4.2.26)

Diving by L_0, the power dissipation per unit length is obtained:

$$\eta_{per\ unit} = -\frac{1}{L_0}\langle\varepsilon(t)I_{Tot}(t)\rangle = -\left\langle\frac{\partial A}{\partial t}\left(R,\frac{\delta}{2},t\right)I_{Tot}(t)\right\rangle =$$

$$= -\left\langle C\left(R,\frac{\delta}{2}\right)\frac{dI_{Tot}(t)}{dt}I_{Tot}(t)\right\rangle = 0 \qquad \left[\frac{W}{m}\right] \qquad (2.4.2.27)$$

This reasoning is correct only if it is possible to find a value of R large enough so that Eq. (2.4.2.27) is applicable, while maintaining valid the hypotheses of Eq. (2.4.1.1). In fact, these two hypotheses are in contradiction with each other: if the distance $R \to \infty$, the assumption for which in the tape region the system variables are still independent of the z-coordinate becomes problematic since it implies that the tape is still sufficiently long compared to the rest of the measurement circuit. In *Section 2.4.9*, a specific study is carried out to analyse whether this assumption is verified or not for practical geometries.

2.4.3. Equations in the case with compensation and the minimization of the area of the voltage measurement circuit

A second configuration of the voltage measurement circuit is here proposed, and its scheme is shown in Fig. 2.4.3.1. Compared to the configuration described in *Section 2.4.2*, this configuration includes a second voltage measurement circuit, in red in Fig. 2.4.3.1, called *Circuit2*. The terminals of *Circuit2* are not soldered onto the tape but they are short-circuited together. These new wires are connected to the terminals *D1* and *C1* of the second channel of the voltmeter and acquired simultaneously with the first measurement. The first measurement circuit, represented in blue in Fig. 2.4.3.1, is identical to the one described in *Section 2.4.2*, named *Circuit1*. The shape of the measurement circuit for compensation must follow as much as possible the shape of the measurement circuit soldered onto the tape. The purpose of this compensation circuit is to eliminate from the measurements the undesired signal due to the linked fluxes. This concept is cleared in the following paragraphs.
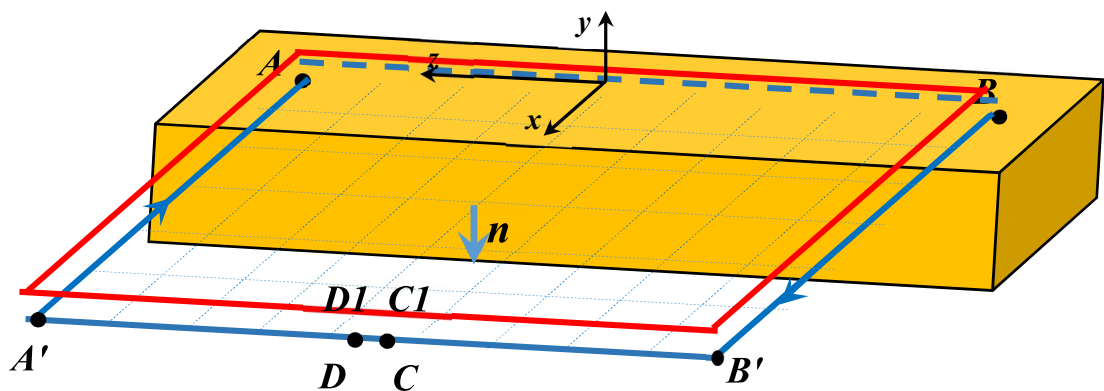
Figure 2.4.3.1. *Scheme of the voltage measurement circuit with compensation. In blue, the circuit with voltage taps soldered to the tape (called Circuit1) and in red the compensation circuit (called Circuit2).*

Fig. 2.4.3.2 shows a photo of the voltage measurement circuit applied to an HTS tape placed over a G-10 support and connected to a power supply with copper bars.
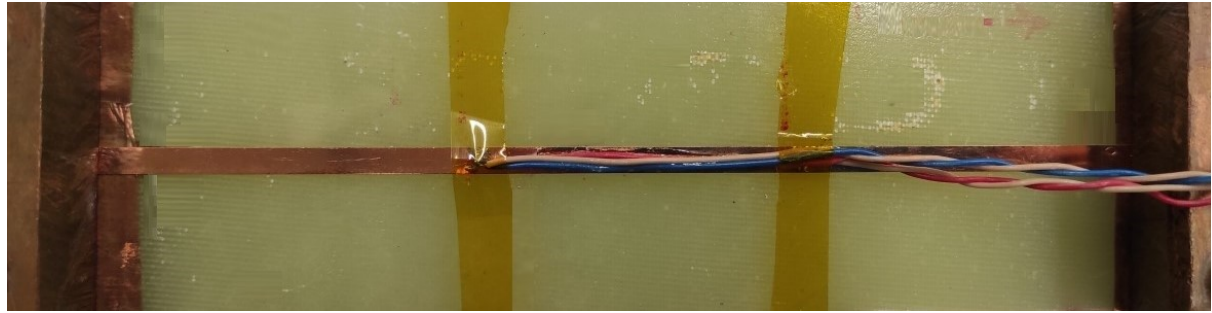
Figure 2.4.3.2. Photo of the voltage measurement circuit with compensation and the minimization of the area, applied to an HTS tape. Since Circuit2 is placed over Circuit1, in order to replicate its shape as much as possible, they may not easily distinguishable.

The derivation of the signal measured by the circuit in blue of Fig. 2.4.3.1 is identical to that performed for *Circuit1* in *Section 2.4.2*. Assuming that the contacts A and B are soldered on the upper surface of the tape ($y = \frac{\delta}{2}$) at the same coordinate x_0, and indicating with $\emptyset_{C1}$ the flux linked to the line A-B-B'-C-D-A'-A shown in Fig.2.4.3.1, from Eq. (2.4.2.14) it results:

$$V_0(t) = V_{AB}(t) + \varepsilon(t)$$

$$\varepsilon(t) = -L_0 \frac{\partial A}{\partial t}\left(x_0, \frac{\delta}{2}, t\right) + \frac{d\emptyset_{C1}}{dt}(t) \tag{2.4.3.1}$$

Following the same passages that from Eq. (2.4.2.7) led to Eq. (2.4.2.13), it is possible to write the following equation for the closed line *Circuit2*:

$$\oint_{Circuit2} \boldsymbol{E} \cdot \boldsymbol{dl} = -\frac{d\emptyset_{C2}}{dt} \tag{2.4.3.2}$$

Then, Eq. (2.4.3.2) can be rewritten as:

$$\oint_{Circuit2} \boldsymbol{E} \cdot \boldsymbol{dl} = \oint_A^B \boldsymbol{E} \cdot \boldsymbol{dl} + \oint_B^{B'} \boldsymbol{E} \cdot \boldsymbol{dl} + \oint_{B'}^{C1} \boldsymbol{E} \cdot \boldsymbol{dl} + \oint_{C1}^{D1} \boldsymbol{E} \cdot \boldsymbol{dl} + \oint_{D1}^{A'} \boldsymbol{E} \cdot \boldsymbol{dl} + \oint_{A'}^A \boldsymbol{E} \cdot \boldsymbol{dl} \tag{2.4.3.3}$$

In which the only term that it is not null is the term referred to the segment *C1-D1*:

$$\int_{C1}^{D1} \boldsymbol{E} \cdot \boldsymbol{dl} = -V_1(t) = -\frac{d\emptyset_{C2}}{dt}(t)$$

$$V_1(t) = \frac{d\emptyset_{C2}}{dt}(t) \tag{2.4.3.4}$$

where $V_1(t)$ is defined as the signal measured by the second channel of the voltmeter. In this discussion, the flux $\emptyset_{C2}$ is supposed to be equal to $\emptyset_{C1}$, as the two circuits have the same geometry.

Then, the measurement acquired with *Circuit2* is subtracted from the value measured with the *Circuit1*. This is equivalent to subtract Eq. (2.4.3.4) to Eq. (2.4.3.1):

$$V_{01}(t) = V_0(t) - V_1(t) = V_{AB}(t) - L_0 \frac{\partial A \left(x_0, \frac{\delta}{2}, t\right)}{\partial t} + \frac{d\emptyset_{C1}}{dt}(t) - \frac{d\emptyset_{C1}}{dt}(t)$$

$$V_{01}(t) = V_{AB}(t) + \xi(t) \qquad (2.4.3.5)$$

$$\xi(t) = -L_0 \frac{\partial A}{\partial t}\left(x_0, \frac{\delta}{2}, t\right)$$

where $V_{01}(t)$ is the difference between the measurement of the two channel of the voltmeter and $y = \frac{\delta}{2}$ and $x = x_0$ are the same coordinates reported in Eq. (2.4.3.1) since the compensation circuit should have the same geometrical parameters. Performing the mean value in a period of the product $V_{01}(t)I_{Tot}(t)$, allows one to compute the dissipated power unless a factor γ that depends only on the time derivative of the vector potential at the contact points:

$$\langle p(t) \rangle = \langle V_{AB}(t)I_{Tot}(t) \rangle =$$

$$= \langle V_{01}(t)I_{Tot}(t) - \xi(t)I_{Tot}(t) \rangle = \langle V_{01}(t)I_{Tot}(t) \rangle + \gamma$$

$$\gamma = -\langle \xi(t)I_{Tot}(t) \rangle = \left\langle L_0 \frac{\partial A}{\partial t}\left(x_0, \frac{\delta}{2}, t\right)I_{Tot}(t) \right\rangle \qquad [W] \qquad (2.4.3.6)$$

Diving by L_0, the power dissipation per unit length is obtained:

$$\langle p(t) \rangle_{per\ unit} = \frac{1}{L_0}\langle V_{AB}(t)I_{Tot}(t) \rangle = \frac{1}{L_0}\langle V_{01}(t)I_{Tot}(t) - \xi(t)I_{Tot}(t) \rangle =$$

$$= \frac{1}{L_0}\langle V_{01}(t)I_{Tot}(t) \rangle + \gamma_{per\ unit} \qquad \left[\frac{W}{m}\right] \qquad (2.4.3.7)$$

$$\gamma_{per\ unit} = \left\langle \frac{\partial A}{\partial t}\left(x_0, \frac{\delta}{2}, t\right)I_{Tot}(t) \right\rangle$$

With a reasoning similar to the one conducted for Eq. (2.4.2.21), it is possible to search if there is a value of x_0, which is the x-coordinate at which both voltage taps are soldered onto the tape surface, that allows expressing the vector potential as a linear function, invariant in time, of the current in the tape. In correspondence of that value, the corrective factor γ of Eq. (2.4.3.6) would ne null. In terms of equations, it is equivalent to:

$$A\left(x_0, \frac{\delta}{2}, t\right) = K\left(x_0, \frac{\delta}{2}\right)I_{Tot}(t) \qquad (2.4.3.8)$$

Which leads to:

$$\gamma = \left\langle L_0 K\left(x_0, \frac{\delta}{2}\right)\frac{dI_{Tot}(t)}{dt}I_{Tot}(t) \right\rangle = L_0 K\left(x_0, \frac{\delta}{2}\right)\left\langle \frac{d}{dt}\left(\frac{1}{2}I_{Tot}(t)^2\right) \right\rangle = 0 \qquad (2.4.3.9)$$

It is worth noting that the measurement circuits shown in Fig. 2.4.3.1 seem to form a considerable area with the tape itself. In this area, the external fluxes can link and overlap with the signal to be measured; they are sources of electromagnetic noise, making the measurement more problematic. Contrarily to the method described in *Section 2.4.2*, this configuration does

not require to find experimentally a sufficiently high value of the distance R. Instead, the method described in this section requires the minimization of this distance with the only purpose to reduce the linked fluxes. The smaller is the area of the measurement circuit, ideally null, the lower is the compensation of the linked fluxes performed with *Circuit2*. Fig. 2.4.3.2 may give a better idea of how the area minimization is practically realized.

2.4.4. Implementation of the numerical model based on the A-V formulation in MATLAB to compute the AC losses in HTS coated conductors

The integral model computes both the AC losses and the corrective terms introduced by the two measurement configurations proposed in *Section 2.4.2* and *Section 2.4.3*, respectively the term $\eta_{per\ unit}$ of Eq. (2.4.2.23) and the term $\gamma_{per\ unit}$ of Eq. (2.4.3.7). The hypothesis of Eq. (2.4.1.1) are assumed to be valid; a proper convergence analysis regarding the minimum tape length required for this assumption is performed in *Section 2.4.9*.

To compute Eq. (2.1.4), the current density $J(x, y, t)$, and the electric field $E(x, y, t)$, should be known in every point of the tape cross-section and at every instant of time. The integral (2.1.4) is numerically computed by dividing the tape cross-section into a finite number (N) of rectangular-shaped elements. Each layer of the tape is discretized with a number of elements independent of that of the neighbouring layers. Assuming that for amplitudes lower or nearer to the tape critical current, the current flows mainly in the superconducting layer of the tape, it is preferable to use a finer discretization for this layer rather than the others.

To facilitate reading, the current density values and the electric field values are expressed as $J_i(t)$ and $E_i(t)$, meaning that they depends on the coordinates (x_i, y_i, z_i) of the ith element. As it will be explained in the following paragraphs, the term z_i is constant, and thus the expressions for $J_i(t)$ and $E_i(t)$, can be simply referred to the cross-sectional coordinates (x_i, y_i).

The time period is also discretized with a finite number of intervals. Therefore, Eq. (2.1.2) and Eq. (2.1.4) can be rewritten following the abovementioned discretization as:

$$\langle p(t)\rangle_{per\ unit} = \frac{1}{L_0\ T}\int_0^T \left(\sum_{i=1}^N \left(E_i(t)\cdot J_i(t)\right)\Delta x_i\ \Delta y_i\ L_0\right)dt =$$

$$= \frac{1}{T}\int_0^T \left(\sum_{i=1}^N \left(E_i(t)\cdot J_i(t)\right)Area_i\right)dt \qquad\qquad \left[\frac{W}{m}\right]\qquad (2.4.4.1)$$

where the volume integral of Eq. (2.1.2) is replaced by the terms L_0 (length of the ith element), Δx_i (width of the ith element) and Δy_i (thickness of the ith element). Then, the term L_0 is simplified with the term $\frac{1}{L_0}$ present in Eq. (1.4). Lastly, the product $\Delta x_i\ \Delta y_i$ is substituted with the term $Area_i$, equal to the area of the cross-section of each element.

Eq. (2.4.1.6), reported here as Eq. (2.4.4.2), is applied to each element of the cross-section. As made for the current densities and the electric fields, the vector potential is also expressed as

$A_i(t)$, meaning it as a function $A_i(x_i, y_i, t)$ depending on the position of the ith element. It results:

$$E_i(t) = -\frac{dV}{dz}(t) - \frac{dA_i}{dt}(t) \qquad \text{for } i = 1{:}N \qquad (2.4.4.2)$$

The term $\frac{dV}{dz}$ is the forcing term that makes the current flow into the tape. The scalar potential V is considered independent of the x and y-coordinates (thus the points on the same cross-section are considered equipotential) and varies along the z-coordinate only.

The vector potential A_i of Eq. (2.4.4.2) can be distinguished in two different terms: $\sum_j A_{i,j}$, which takes into account the tape self-field, *i.e.* the magnetic field acting on the ith field element of the tape cross-section due to the current flowing in each jth source elements, and A_{ext_i} which takes into account the external field acting on each element of the tape.

$$E_i(t) = -\frac{dV}{dz}(t) - \sum_{j=1}^{N}\frac{dA_{i,j}}{dt}(t) - \frac{dA_{ext_i}}{dt}(t) \qquad \text{for } i = 1{:}N \qquad (2.4.4.3)$$

For simplicity, the external magnetic field is considered uniform on every point of the tape.

The electric field depends on the current density, which varies accordingly to the layer of the tape in which the ith element is located. If the element belongs to the superconducting layer, the power law is adopted to calculate the electric field, while if the element belongs to another layer the Ohm's law is used:

$$E_i(t) = E_c \left(\frac{J_i(t)}{J_c}\right)^n \quad \text{if the } i^{th} \text{ element} \in \text{to the SC layer}$$
$$E_i(t) = \rho_i J_i(t) \qquad \text{if the } i^{th} \text{ element} \notin \text{to the SC layer}$$
$$(2.4.4.4)$$

where ρ_i is the electrical resistivity of each non-superconducting layer of the coated conductor. Since $E_i(t)$ is a function of $J_i(t)$, it can be expressed as $E_i\left(J_i(t)\right)$.

The term $\sum_j \frac{dA_{i,j}}{dt}(t)$ of Eq. (2.4.4.3) can be expressed starting from the relation between the magnetic vector potential and current density. While in [80] this relation is found for an infinitely long tape using a logarithmic kernel, in this work the Biot-Savart law is considered by modelling the jth element as a longitudinal filament carrying the concentrate current J_j:

$$\sum_{j=1}^{N} A_{i,j}(t) = \frac{\mu_0}{4\pi}\int_{-\frac{L}{2}}^{\frac{L}{2}}\int_{-\frac{\delta}{2}}^{\frac{\delta}{2}}\int_{-\frac{w}{2}}^{\frac{w}{2}}\frac{J(x',y',t)}{\sqrt{(x_i-x')^2+(y_i-y')^2+(z_i-z')^2}}dx'dy'dz' =$$

$$= \frac{\mu_0}{4\pi}\int_{-\frac{L}{2}}^{\frac{L}{2}}\left(\sum_{j=1}^{N} Area_j \frac{J_j(t)}{\sqrt{(x_i-x_j)^2+(y_i-y_j)^2+(z_i-z')^2}}\right)dz'$$

$$(2.4.4.5)$$

where the term $\sqrt{\left(x_i - x_j\right)^2 + \left(y_i - y_j\right)^2 + (z_i - z')^2}$ is the distance between the center of the ith *field element* (x_i, y_i, z_i) and the jth *source element* (x_j, y_j, z_j). It is worth noting that, due to the simplified hypotheses imposed, the computation can be performed selecting a single cross-section of the tape, or rather a single coordinate z_i. For simplicity, the coordinate $z_i = 0$ is selected for the *field points*, at the tape center and at equal distance from both voltage taps. However, to make the equation more general, the term z_i is not removed from the equations.

Since the term $J_j(t)$ does not depend on the z-coordinate (the z' variable of the integral), it can be taken out of the integral, as well as the summation and the terms $Area_j$. It results:

$$\sum_{j=1}^{N} A_{i,j}(t) = \frac{\mu_0}{4\pi} \sum_{j=1}^{N} \left(Area_j\, J_j(t) \int_{-\frac{L}{2}}^{\frac{L}{2}} \frac{1}{\sqrt{\left(x_i - x_j\right)^2 + \left(y_i - y_j\right)^2 + (z_i - z')^2}}\, dz' \right) \qquad (2.4.4.6)$$

To solve the integral, it is convenient to perform the following change of variables:

$$\eta_i = z_i - z' \qquad (2.4.4.7)$$

Operating this change into Eq. (2.4.4.6), it can be rewritten as:

$$\sum_{j=1}^{N} A_{i,j}(t) = \frac{\mu_0}{4\pi} \sum_{j=1}^{N} \left(Area_j\, J_j(t) \int_{z_i+\frac{L}{2}}^{z_i-\frac{L}{2}} \frac{-d\eta}{\sqrt{\left(x_i - x_j\right)^2 + \left(y_i - y_j\right)^2 + \left(\eta_i\right)^2}} \right) \qquad (2.4.4.8)$$

The minus sign inside the integrand of Eq. (2.4.4.8) can be eliminated by inverting the integration extremes.

$$\sum_{j=1}^{N} A_{i,j}(t) = \frac{\mu_0}{4\pi} \sum_{j=1}^{N} \left(Area_j\, J_j(t) \int_{z_i-\frac{L}{2}}^{z_i+\frac{L}{2}} \frac{d\eta}{\sqrt{\left(x_i - x_j\right)^2 + \left(y_i - y_j\right)^2 + \left(\eta_i\right)^2}} \right) \qquad (2.4.4.9)$$

Then, the integral can be solved remembering that:

$$\frac{d}{d\eta}\left[ln\left(\sqrt{\eta^2 + a^2} + \eta \right) \right] = \frac{1}{\sqrt{\eta^2 + a^2}} \qquad (2.4.4.10)$$

Taking into account Eq. (2.4.4.10) and considering $\left(x_i - x_j\right)^2 + \left(y_i - y_j\right)^2 = a^2$, Eq. (2.4.4.9) can be analytically solved, resulting in:

$$\sum_{j=1}^{N} A_{i,j}(t) = \frac{\mu_0}{4\pi} \sum_{j=1}^{N} Area_j \, J_j(t) \left| \ln \left(\sqrt{(x_i - x_j)^2 + (y_i - y_j)^2 + (\eta_i)^2} + (\eta_i) \right) \right|_{z_i - \frac{L}{2}}^{z_i + \frac{L}{2}} \qquad (2.4.4.11)$$

Inserting Eq. (2.4.4.7) into Eq. (2.4.4.11), the coordinates of the field points (x_i, y_i, z_i) appear again and the final formulation for the term $\sum_j A_{i,j}(t)$ can be expressed as follows:

$$\sum_{j=1}^{N} A_{i,j}(t) = \frac{\mu_0}{4\pi} \sum_{j=1}^{N} Area_j \, J_j(t) \left| \ln \left(\sqrt{(x_i - x_j)^2 + (y_i - y_j)^2 + (z_i - z')^2} + (z_i - z') \right) \right|_{+\frac{L}{2}}^{-\frac{L}{2}} \qquad (2.4.4.12)$$

Then, since the term $\sum_j A_{i,j}(t)$ in Eq. (2.4.4.3) is derived in time, Eq. (2.4.4.12) should be also derived in time. The only term of Eq. (2.4.4.7) affected by this derivation is the term $J_j(x_j, y_j, t)$.

$$\sum_{j=1}^{N} \frac{dA_{i,j}}{dt}(t) = \frac{\mu_0}{4\pi} \sum_{j=1}^{N} Area_j \, \frac{dJ_j(t)}{dt} \left| \ln \left(\sqrt{(x_i - x_j)^2 + (y_i - y_j)^2 + (z_i - z')^2} + (z_i - z') \right) \right|_{+\frac{L}{2}}^{-\frac{L}{2}} \qquad (2.4.4.13)$$

By introducing the term $K_{i,j}$ into Eq. (2.4.4.13), it is possible to rewrite this equation in a compact form as:

$$\sum_{j=1}^{N} \frac{dA_{i,j}}{dt}(t) = \sum_{j=1}^{N} K_{i,j} \, \frac{dJ_j(t)}{dt} \qquad for\ i = 1:N$$

$$(2.4.4.14)$$

$$K_{i,j} = \frac{\mu_0}{4\pi} Area_j \left| \ln \left(\sqrt{(x_i - x_j)^2 + (y_i - y_j)^2 + (z_i - z')^2} + (z_i - z') \right) \right|_{+\frac{L}{2}}^{-\frac{L}{2}}$$

Moreover, the inversion of the matrix K results problematic for the solver, since it contains the terms referred to the case $i = j$, for which the distance between the source and field points results null. To solve this problem, a corrective parameter is introduced, named λ, that avoids divergence errors occurring when a solver inverts the matrix K. The term λ is set through an iterative procedure, by recursively performing the whole analysis while reducing the value of this parameter. The smallest value found which allows convergence of the numerical integration is then retained for the following computations. It yields:

$$K_{i,j\,corrected} = \frac{\mu_0}{4\pi} Area_j \left| \ln \left(\sqrt{(x_i - x_j)^2 + (y_i - y_j)^2 + (z_i - z')^2 + \lambda^2} + (z_i - z') \right) \right|_{+\frac{L}{2}}^{-\frac{L}{2}} \qquad (2.4.4.15)$$

Let consider an external magnetic field $\boldsymbol{B_{ext}}(t)$, sinusoidal in time, which can form any angle θ_{field} with the tape main face (where $\theta_{field} = 0$ corresponds to a perfectly parallel field, and $\theta_{field} = \frac{\pi}{2}$ corresponds to a perfectly perpendicular field). The correlation between the

magnetic field amplitude (B_m) and angle (θ_{field}) with its x and y components (B_{mx} and B_{my}) is expressed by Eq. (2.4.4.15).

$$\boldsymbol{B_{ext}}(t) = \boldsymbol{B_m} \sin(2\pi f t) = B_{mx} \sin(2\pi f t)\,\boldsymbol{i} + B_{my} \sin(2\pi f t)\,\boldsymbol{j} = B_{ax}(t)\,\boldsymbol{i} + B_{ay}(t)\,\boldsymbol{j}$$

$$B_m = \sqrt{B_{mx}{}^2 + B_{my}{}^2} \quad ; \quad \theta_{field} = \arctan\left(\frac{B_{my}}{B_{mx}}\right) \tag{2.4.4.16}$$

The angular velocity ω of the magnetic field can be different from the one to the sinusoidal transport current. Anyway, this work takes into account isofrequential sources only and the two angular velocities are not distinguished.

The simplifying hypothesis of Eq. (2.4.1.1) can be applied also to the A_{ext} term:

$$\boldsymbol{A_{ext}}(x,y,z,t) = A_{ext}(x,y,t)\,\boldsymbol{k} \tag{2.4.4.17}$$

From Gauss' law, the relation between the magnetic field components and the term A_{ext} can be written as:

$$\boldsymbol{B_{ext}}(t) = B_{ax}(t)\,\boldsymbol{i} + B_{ay}(t)\,\boldsymbol{j} = \frac{\partial A_{ext}}{\partial y}(t)\,\boldsymbol{i} - \frac{\partial A_{ext}}{\partial x}(t)\,\boldsymbol{j} \tag{2.4.4.18}$$

If the external field is uniform, the partial derivatives of external vector potentials in Eq. (2.4.4.18) are independent of the spatial coordinates. It is useful to write in separate lines the two components of the magnetic field:

$$B_{ax}(t)\,\boldsymbol{i} = \frac{\partial A_{ext}}{\partial y}(t)\,\boldsymbol{i}$$

$$B_{ay}(t)\,\boldsymbol{j} = -\frac{\partial A_{ext}}{\partial x}(t)\,\boldsymbol{j} \tag{2.4.4.19}$$

In this way, it is possible to integrate the first equation of Eq. (2.4.4.19) along the y-axis and the second equation along the x-axis. It results:

$$A_{ext_i}(t) = A_{ext}(0,0,t) + y_{c_i} B_{ax}(t) - x_{c_i} B_{ay}(t) \tag{2.4.4.20}$$

where x_{c_i} and y_{c_i} are the coordinates of the center of the ith element, meant as the distance of the point (x_i, y_i) from the tape central axis ($x = 0$).

The term $A_{ext}(0,0,t)$ can be considered null for every instant t. Therefore, Eq. (2.4.4.20) can be derived in time, resulting in:

$$\frac{dA_{ext_i}}{dt}(t) = -\frac{dB_{ay}}{dt}(t)x_{c_i} + \frac{dB_{ax}}{dt}(t)y_{c_i} \qquad for\ i = 1:N \tag{2.4.4.21}$$

Inserting Eq.s (2.4.4.14) and (2.4.4.21) into Eq. (2.4.4.3), it lead to:

$$E_i\big(J_i(t)\big) = -\frac{dV}{dz}(t) - \sum_{j=1}^{N} K_{i,j\,corrected} \frac{dJ_j(t)}{dt} + \frac{dB_{ay}}{dt}(t)x_{c_i} - \frac{dB_{ax}}{dt}(t)y_{c_i} \tag{2.4.4.22}$$

For a reason that will be cleared in the following passages, it is convenient to rename the unknowns $J_i(t)$ with the generic term $\psi_i(t)$:

$$E(\psi_i(t)) = -\frac{dV}{dz}(t) - \sum_{j=1}^{N} K_{i,j\,corrected} \frac{d\psi_j(t)}{dt} + \frac{dB_{ay}}{dt}(t)x_{c_i} - \frac{dB_{ax}}{dt}(t)y_{c_i} \qquad (2.4.4.23)$$

The term $\frac{dV}{dz}(t)$ of Eq. (2.4.4.23) is not known. Thus, it is possible to define a $(N+1)$-th unknown as:

$$\psi_{N+1}(t) = \int_0^t \frac{dV}{dz} dt' \qquad (2.4.4.24)$$

In this way, the time derivative of Eq. (2.4.4.24) is equal to:

$$\frac{d\psi_{N+1}(t)}{dt} = \frac{dV}{dz}(t) \qquad (2.4.4.25)$$

To summarize, the system unknowns are renamed as follows:

$$\begin{cases} \psi_i(t) = J_i(t) & for\ i\ =\ 1:N \\ \psi_{N+1}(t) = \int_0^t \frac{dV}{dz} dt' & (N+1)-th\ unknown \end{cases} \qquad (2.4.4.26)$$

Consequently, their time derivatives, which enters in the system of differential equations to be solved, can be summarized as follows:

$$\begin{cases} \dfrac{d\psi_i(t)}{\partial t} = \dfrac{dJ_i(t)}{dt} & for\ i\ =\ 1:N \\ \dfrac{d\psi_{N+1}(t)}{\partial t} = \dfrac{dV}{dz} & (N+1)-th\ unknown \end{cases} \qquad (2.4.4.27)$$

Thus, inserting Eq. (2.4.4.26) into Eq. (2.4.4.22) it results:

$$E(\psi_i(t)) = -\frac{d\psi_{N+1}(t)}{dt} - \sum_{j=1}^{N} K_{i,j\,corrected} \frac{d\psi_j(t)}{dt} + \frac{dB_{ay}}{dt}(t)x_{c_i} - \frac{dB_{ax}}{dt}(t)y_{c_i} \qquad (2.4.4.28)$$

Bringing to the first member all terms of Eq. (2.4.4.28) depending on the unknowns ψ, it results:

$$\frac{d\psi_{N+1}(t)}{dt} + \sum_{j=1}^{N} K_{i,j\,corrected} \frac{d\psi_i(t)}{dt} = -E(\psi_i(t)) + \frac{dB_{ay}}{dt}(t)x_{c_i} - \frac{dB_{ax}}{dt}(t)y_{c_i} \qquad (2.4.4.29)$$

To solve the system of differential equations more easily, it is possible to group all the differential terms due to the $N+1$ unknowns of the system (N current densities + the forcing term due to the scalar potential) into a single term. To do that, the matrix $K_{corrected}$ (formed by the elements $K_{i,j\,corrected}$) has to be modified in order to include a new row and a new column

referred to the term $\frac{d\psi_{N+1}(t)}{dt}$. Thus, it is possible to compose a new matrix, called $Kernel_{corr}$, of dimensions $[N+1 \times N+1]$ as it follows:

$$Kernel_{corr} = \begin{bmatrix} \begin{bmatrix} K_{1,1} & \cdots & K_{1,N} \\ \vdots & \ddots & \vdots \\ K_{N,1} & \cdots & K_{N,N} \end{bmatrix} & \begin{matrix} 1 \\ \vdots \\ 1 \end{matrix} \\ \begin{matrix} Area_1 & \cdots & Area_N \end{matrix} & 0 \end{bmatrix} \tag{2.4.4.30}$$

The first $[N \times N]$ columns and rows of the matrix $Kernel_{corr}$ are equal to the respective columns and rows of the matrix K, as expressed by Eq. (2.4.4.14). The $(N+1)$-th row of the matrix $Kernel_{corr}$ is equal to the area of each element. Moreover, this row corresponds to the Kirchhoff's current balance law. Each element of the $(N+1)$-th column of the matrix $Kernel_{corr}$ is equal to 1, except for the last element (the $N+1 \times N+1$ element) which is equal to 0.

Modifying Eq. (2.4.4.29) as explained above and inserting the matrix $Kernel_{corr}$ of Eq. (2.4.4.30), it results:

$$\sum_{j=1}^{N+1} Kernel_{i,j\,corr} \frac{d\psi_i(t)}{dt} = -E(\psi_i(t)) + \frac{dB_y}{dt}(t)x_{c_i} - \frac{dB_x}{dt}(t)y_{c_i} \tag{2.4.4.31}$$

Eq. (2.4.4.31) is a system of N differential equations for the unknowns $\psi_i(t)$ for $i = 1{:}N$ (the current densities in each element). The existence of an $N+1$ unknown ($\psi_{N+1}(t)$) requires another algebraic equation in order to solve the system. The $(N+1)$-th equation is the conservation of the total current on the tape cross-section, which can be written as follows:

$$\sum_{j=1}^{N} I_j(t) = I_{Tot}(t) \tag{2.4.4.32}$$

The first member of Eq. (2.4.4.32) can be written in terms of current densities as:

$$\sum_{j=1}^{N} Area_j J_j(t) = I_{Tot}(t) \tag{2.4.4.33}$$

Then, Eq. (2.4.4.33) can we derived in time:

$$\sum_{j=1}^{N} Area_j \frac{dJ_j(t)}{dt} = \sum_{j=1}^{N} Area_j \frac{d\psi_j(t)}{dt} = \frac{dI_{Tot}(t)}{dt} \tag{2.4.4.34}$$

Thus, Eq. (2.4.4.32) and Eq. (2.4.4.34) can be combined to form a system of $N+1$ equations in $N+1$ unknown:

$$\begin{cases} \sum_{j=1}^{N+1} Kernel_{i,j_{corr}} \dfrac{d\psi_i(t)}{dt} = -E\big(\psi_i(t)\big) + \dfrac{dB_{ay}}{dt}(t)x_{c_i} - \dfrac{dB_{ax}}{dt}(t)y_{c_i} \quad for\ i\ =\ 1:N \\[4mm] \sum_{j=1}^{N+1} Kernel_{i,j_{corr}} \dfrac{d\psi_j(t)}{dt} = \dfrac{dI_{Tot}(t)}{dt} \qquad\qquad\qquad\qquad\quad for\quad i = N+1 \end{cases} \tag{2.4.4.35}$$

Eq. (2.4.4.35) explains the composition of the $Kernel_{corr}$ matrix as described by Eq. (2.4.4.30). The last row of the matrix $Kernel_{corr}$ is equal to the term $Area_i$ since it appears in the (N+1)-*th* equation of the system (see Eq. (2.4.4.34)). The last column (the (N+1)-*th* column) of the matrix $Kernel_{corr}$ is equal to 1, since this value multiplies the term $\dfrac{d\psi_{N+1}(t)}{dt}$ which appears in the first N equations of the system, as expressed by Eq. (2.4.4.29). The last element of the matrix $Kernel_{corr}$ (the N+1 $\times$ N+1 element) is equal to 0, since in Eq. (2.4.4.29) the summation includes the first N elements only and the term $\dfrac{d\psi_{N+1}(t)}{dt}$ is not present (i.e. is multiplied by 0).

Then, as reported in some studies [127, 128] the formulation of the problem in terms of adimensional unknowns may reveal more accuracy than dimensional analysis when solving a system of differential equations. However, it should be noted that this topic is still debated the scientific community [129].

The following quantities are made dimensionless:

$$\begin{aligned} J^* &= \frac{J}{J_c} \\[3mm] E^* &= \frac{E}{E_c} \\[3mm] \left(\frac{dV}{dz}\right)^* &= \frac{\left(\frac{dV}{dz}\right)}{E_c} \\[3mm] I_{Tot}{}^* &= \frac{I_{Tot}}{I_{Amp}} \end{aligned} \tag{2.4.4.36}$$

Consequently, the time derivatives of the unknowns that appears in the system of differential equations of Eq. (2.4.4.35), previously expressed by Eq. (2.4.4.27) in dimensional form, can be rewritten as:

$$\begin{cases} \dfrac{d\psi_i{}^*(t)}{dt} = \dfrac{1}{J_c}\dfrac{d\psi_i(t)}{dt} = \dfrac{1}{J_c}\dfrac{dJ_i(t)}{dt} \qquad for\ i\ =\ 1:N \\[4mm] \dfrac{d\psi_{N+1}{}^*(t)}{dt} = \dfrac{1}{E_c}\dfrac{d\psi_{N+1}(t)}{dt} = \dfrac{1}{E_c}\dfrac{dV}{dz} \qquad (N+1) - th\ unknow \end{cases} \tag{2.4.4.37}$$

It is possible to introduce the dimensionless derivatives of the unknowns of Eq. (2.4.4.37) in the first term of all the equations presented in Eq. (2.4.4.35), by multiplying by J_c the first N

equations (since $\psi_i(t) = J_i(t)$ for $i = 1:N$) and by E_c the (N+1)-*th* equation (since $\psi_{N+1}(t) = \int_0^t \frac{dV}{dz} dt'$). It results:

$$
\begin{cases}
\sum_{j=1}^{N+1} Kernel_{i,j_{corr}} J_c \frac{d\psi_j^*(t)}{\partial t} + Kernel_{i,N+1_{corr}} E_c \frac{d\psi_{N+1}^*(t)}{dt} = \\
\qquad\qquad = -E\big(\psi_i(t)\big) + \frac{dB_{ay}}{dt}(t)x_{c_i} - \frac{dB_{ax}}{dt}(t)y_{c_i} \quad for \quad i = 1:N \quad (2.4.4.38) \\
\sum_{J=1}^{N+1} Kernel_{i,j_{corr}} J_c \frac{d\psi_J^*(t)}{\partial t} = \frac{dI_{Tot}(t)}{dt} \qquad\qquad\qquad for \quad i = N+1
\end{cases}
$$

Then, the first N equations of the system of equations presented in Eq. (2.4.4.37) can be divided by E_c. At the same time, to obtain the dimensionless quantity I_{Tot}^* in the N+1-*th* differential equation of Eq. (2.4.4.37), both members of this last equation can be divided by the term I_{Amp}:

$$
\begin{cases}
\sum_{j=1}^{N} Kernel_{i,j_{corr}} \frac{J_c}{E_c} \frac{d\psi_j^*(t)}{\partial t} + Kernel_{i,N+1_{corr}} \frac{d\psi_{N+1}^*(t)}{dt} = \\
\qquad\qquad = -\frac{1}{E_c} E\big(\psi_i(t)\big) + \frac{1}{E_c} x_{c_i} \frac{dB_{ay}}{dt}(t) - \frac{1}{E_c} y_{c_i} \frac{dB_{ax}}{dt}(t) \quad for\ i = 1:N \quad (2.4.4.39) \\
\sum_{J=1}^{N} Kernel_{i,j_{corr}} \frac{J_c}{I_{Amp}} \frac{d\psi_J^*(t)}{dt} = \frac{1}{I_{Amp}} \frac{dI_{Tot}(t)}{dt} \qquad\qquad for\ i = N+1
\end{cases}
$$

Inserting the term E^*, as presented in (2.4.4.36), the same system of equations is equivalent to:

$$
\begin{cases}
\sum_{j=1}^{N} Kernel_{i,j_{corr}} \frac{J_c}{E_c} \frac{d\psi_j^*(t)}{\partial t} + Kernel_{i,N+1_{corr}} \frac{d\psi_{N+1}^*(t)}{dt} = \\
\qquad\qquad = -E^*\big(\psi_i(t)\big) + \frac{1}{E_c} x_{c_i} \frac{dB_{ay}}{dt}(t) - \frac{1}{E_c} y_{c_i} \frac{dB_{ax}}{dt}(t) \quad for\ i = 1:N \quad (2.4.4.40) \\
\sum_{J=1}^{N} Kernel_{i,j_{corr}} \frac{J_c}{I_{Amp}} \frac{d\psi_J^*(t)}{dt} = \frac{1}{I_{Amp}} \frac{dI_{Tot}(t)}{dt} \qquad\qquad for\ i = N+1
\end{cases}
$$

It is convenient to rewrite the matrix $Kernel_{corr}$ in order to include the quantities $\frac{J_c}{E_c}$ and $\frac{J_c}{I_{Amp}}$ that appear at first members of Eq. (2.4.4.40) leading to a new matrix named $Kernel_{corr}^*$ (of dimensions $[N+1 \times N+1]$):

$$
\begin{cases}
\sum_{j=1}^{N+1} Kernel_{i,j_{corr}}^* \frac{d\psi_j^*(t)}{dt} = \\
\qquad = -E^*\big(\psi_i(t)\big) + \frac{1}{E_c} x_{c_i} \frac{dB_{ay}}{dt}(t) - \frac{1}{E_c} y_{c_i} \frac{dB_{ax}}{dt}(t) \quad for\ i = 1:N \quad (2.4.4.41) \\
\sum_{J=1}^{N+1} Kernel_{i,j_{corr}}^* \frac{d\psi_J^*(t)}{dt} = \frac{dI_{Tot}^*(t)}{dt} \qquad\qquad for \quad i = N+1
\end{cases}
$$

The matrix $Kernel_{corr}^*$ is written starting from the matrix $Kernel_{corr}$ of Eq. (2.4.4.30) (and its core, expressed in Eq. (2.4.4.15)), and it is equal to:

$$Kernel_{corr}^* = \begin{bmatrix} \begin{bmatrix} K_{1,1,corr}^* & \cdots & K_{1,N}^* \\ \vdots & \ddots & \vdots \\ K_{N,1,corr}^* & \cdots & K_{N,N}^* \end{bmatrix} & \begin{matrix} 1 \\ \vdots \\ 1 \end{matrix} \\ \begin{matrix} \dfrac{J_c}{I_{Amp}} Area_1 & \cdots & \dfrac{J_c}{I_{Amp}} Area_N \end{matrix} & 0 \end{bmatrix} \qquad (2.4.4.42)$$

$$K_{i,j}^*{}_{corr} = \frac{J_c}{E_c} \frac{\mu_0}{4\pi} Area_j \left| \ln\left(\sqrt{(x_i - x_j)^2 + (y_i - y_j)^2 + (z_i - z')^2} + (z_i - z') \right) \right|_{+\frac{L}{2}}^{-\frac{L}{2}}$$

To solve the system of differential equations of Eq. (2.4.4.41), the MATLAB functions *ode15s* ore *ode23t* are chosen; none of them has particular advantages in terms of calculation times compared to the other. The solver requires the definition of the initial values, which are all assumed to be null in this particular problem, at $t = 0$.

$$\psi_i^*(0) = 0 \quad for\ i = 1:(N+1) \qquad (2.4.4.43)$$

Since the Jacobian matrix is critical to reliability and efficiency, it is convenient to compute the *Jacobian* matrix of the problem, not leaving this task to the solver itself. The *Jacobian* matrix is a diagonal matrix of dimensions [$N+1 \times N+1$], and it can be written as follows:

$$Jacobian = \begin{bmatrix} -\dfrac{\partial E(\psi_1(t))}{\partial \psi_1} & & 0 & \cdots & 0 \\ 0 & \ddots & & \ddots & \vdots \\ \vdots & \ddots & -\dfrac{\partial E(\psi_N(t))}{\partial \psi_N} & & 0 \\ 0 & & \cdots & 0 & 0 \end{bmatrix} \qquad (2.4.4.44)$$

The terms $\dfrac{\partial E(\psi_i(t))}{\partial \psi_i}$ are the derivatives of the terms presented in Eq. (2.4.4.4), and their formulation depends on the layer of the tape in which the ith element is located. They can be expressed as:

$$\frac{\partial E(\psi_i(t))}{\partial \psi_i} = \frac{\partial E(J_i(t))}{\partial J_i} = \frac{E_c}{J_c} n \left| \left(\frac{J_i(t)}{J_c} \right) \right|^{n-1} \quad if\ the\ i^{th}\ element \in\ to\ the\ SC\ layer$$

$$\frac{\partial E(\psi_i(t))}{\partial \psi_i} = \frac{\partial E(J_i(t))}{\partial J_i} = \rho_i \qquad\qquad if\ the\ i^{th}\ element \notin\ to\ the\ SC\ layer$$

$$(2.4.4.45)$$

The *Jacobian* matrix can be also made dimensionless. To do that, every element of the matrix (or rather of its main diagonal) has to be multiplied by J_c; in this way the derivatives can be written with respect to the dimensionless term ψ^*. Moreover, every element of the matrix *Jacobian* has to be divided by E_c in order to make the term $E(\psi_i(t))$ adimensional. Note that term $E(\psi_i(t))$ still depends on the variable $\psi_i(t)$, but not on its dimensionless counterpart. It results:

$$Jacobian^* = \begin{bmatrix} -\dfrac{J_c}{E_c}\dfrac{\partial E(\psi_1(t))}{\partial \psi_1^*} & 0 & \cdots & & 0 \\ 0 & \ddots & & \ddots & \vdots \\ \vdots & & \ddots & -\dfrac{J_c}{E_c}\dfrac{\partial E(\psi_N(,t))}{\partial \psi_N^*} & 0 \\ 0 & & \cdots & 0 & 0 \end{bmatrix} \qquad (2.4.4.46)$$

Note that, to use the *ode15s* or the *ode23t* functions in MATLAB, both the *Jacobian* matrix of Eq. (2.4.4.46) and the system of differential equations of Eq. (2.4.4.41) has to be written has *function handles*.

Thus, the values $\psi_i^*(t)$ are obtained. The first N quantities can be therefore multiplied by J_c to retrieve the values $\psi_i(t) = J_i(t)$ (for $i = 1{:}N$). The last value can be therefore multiplied by E_c to retrieve the values $\psi_{N+1}(t) = \int_0^t \frac{dV}{dz} dt'$.

Then, the values $E(\psi_i(t)) = E(J_i(t))$ can be calculated using Eq. (2.4.4.4). Finally, it is possible to calculate the value $\langle p(t) \rangle_{per\,unit}$ by using Eq. (2.4.4.1).

2.4.5. Calculation of the corrective factor in the case without compensation and with voltage taps twisted at a certain distance from the tape middle axis

Once the $\langle p(t) \rangle_{per\,unit}$ value is found, the corrective factor due to the voltage measurement circuit can be calculated with the same solver. In this way, it is possible to estimate the contribution of the configuration of the measurement circuit to the measured AC losses.

First, the case without compensation and with voltage taps twisted at a certain distance from the tape middle axis is considered. In this case, the formulation for the corrective factor is reported in Eq. (2.4.2.23). The $\eta_{per\,unit}$ is found performing the integral of the time derivative of the vector potential over the z-coordinates, in the interval $\left[-\frac{L_0}{2}, \frac{L_0}{2}\right]$. Moreover, in the experimental configuration discussed in *Section 2.4.2*, the voltage taps are twisted at a certain distance from the tape middle axis, in the x direction.

This study aims to understand the dependence of the correction factor $\eta_{per\,unit}$ on the distance α. It is useful to create a discretized map of N_{ext} points at different coordinates $(\alpha, \frac{\delta}{2}, z_k)$, corresponding to the points in which the vector potential is calculated by the integral model (the subscript k is used to differentiate it from i, the subscript that has been previously adopted for field points inside the tape). All these points have the same y-coordinate, equal to $\frac{\delta}{2}$, since the two voltage taps are soldered onto the tape upper surface, and maintained at the same y-coordinate until they are twisted together. Then, the parameter $\eta_{per\,unit}$ is calculated by integrating the term $\frac{\partial A}{\partial t}$ along the line which goes from the point at coordinates $(\alpha, \frac{\delta}{2}, -\frac{L_0}{2})$ to $(\alpha, \frac{\delta}{2}, +\frac{L_0}{2})$.

To compute the vector potential $A_k\left(\alpha,\frac{\delta}{2},z_k,t\right)$ in the N_{ext} points, Eq. (2.4.5.1) can be used. It is worth noting that in this case, $A_k\left(\alpha,\frac{\delta}{2},z_k,t\right)$ is also a function of the z_k coordinate of the kth field points. The term $K_{i,j}$, introduced in Eq. (2.4.4.15) is used into the equation:

$$A_k\left(\alpha,\frac{\delta}{2},z_k,t\right) = \sum_{j=1}^{N} A_{k,j}\left(\alpha,\frac{\delta}{2},z_k,t\right) =$$

$$= \frac{\mu_0}{4\pi}\sum_{j=1}^{N} Area_j\, J_j(t) \left| \ln\left(\sqrt{(\alpha-x_j)^2+\left(\frac{\delta}{2}-y_j\right)^2+(z_k-z')^2}+(z_k-z')\right)\right|_{+\frac{L}{2}}^{-\frac{L}{2}}$$

$$= \sum_{j=1}^{N} K_{k,j\,corrected}\, J_j(t) \qquad for\ k=1:N_{ext} \tag{2.4.5.1}$$

$$K_{k,j\,corrected} = \frac{\mu_0}{4\pi} Area_j \left| \ln\left(\sqrt{(\alpha-x_j)^2+\left(\frac{\delta}{2}-y_j\right)^2+(z_k-z')^2+\lambda^2}+(z_k-z')\right)\right|_{-\frac{L}{2}}^{\frac{L}{2}}$$

It is convenient to introduce in Eq. (2.4.5.1) the dimensionless quantity J^*, expressed in Eq. (2.4.4.36):

$$A_k\left(\alpha,\frac{\delta}{2},z_k,t\right) = \sum_{j=1}^{N} A_{k,j}\left(\alpha,\frac{\delta}{2},z_k,t\right) =$$

$$= \frac{\mu_0}{4\pi}\sum_{j=1}^{N} Area_j\, J_c\, J_j^*(t) \left| \ln\left(\sqrt{(\alpha-x_j)^2+\left(\frac{\delta}{2}-y_j\right)^2+(z_k-z')^2+\lambda^2}+\left(z_k-z'\right)\right)\right|_{+\frac{L}{2}}^{-\frac{L}{2}} \tag{2.4.5.2}$$

It is then possible to multiply and divide the second term of Eq. (2.4.5.2) by the value E_c, in order to introduce the quantity $K_{k,j}{}^*{}_{corr}$, expressed in Eq. (2.4.4.42):

$$A_k\left(\alpha,\frac{\delta}{2},z_k,t\right) = \sum_{j=1}^{N} A_{k,j}\left(\alpha,\frac{\delta}{2},z_k,t\right) = \frac{\mu_0}{4\pi}\sum_{j=1}^{N} \frac{E_c}{E_c} Area_j\, J_c\, J_j^*(x_j,y_j,t)\cdot$$

$$\cdot \left| \ln\left(\sqrt{(\alpha-x_j)^2+\left(\frac{\delta}{2}-y_j\right)^2+(z_k-z')^2+\lambda^2}+\left(z_k-z'\right)\right)\right|_{+\frac{L}{2}}^{-\frac{L}{2}} = \tag{2.4.5.3}$$

$$= \sum_{j=1}^{N} E_c\, K_{k,j}{}^*{}_{corr}\, J_j^*(x_j,y_j,t) \qquad for\ k=1:N_{ext}$$

$$K_{k,j}^{*}{}_{corr} = \frac{J_c}{E_c}\frac{\mu_0}{4\,\pi}\,Area_j\,\left|\ln\left(\sqrt{(\alpha - x_j)^2 + \left(\frac{\delta}{2} - y_j\right)^2 + (z_i - z')^2 + \lambda^2} + (z_i - z')\right)\right|_{+\frac{L}{2}}^{-\frac{L}{2}}$$

Subsequently, the time derivative of Eq. (2.4.5.3) is performed:

$$\frac{dA_k}{dt}\left(\alpha,\frac{\delta}{2},z_k,t\right) = \sum_{j=1}^{N}\frac{dA_{k,j}}{dt}\left(\alpha,\frac{\delta}{2},z_k,t\right) = \sum_{j=1}^{N}E_c\,K_{k,j}^{*}{}_{corr}\,\frac{\partial J_j^*(t)}{\partial t} \qquad for\ k = 1:N_{ext} \quad (2.4.5.4)$$

And then both terms of the Eq. (2.4.5.4) are multiplied by $I_{Tot}(t)$:

$$\frac{dA_k}{dt}\left(\alpha,\frac{\delta}{2},z_k,t\right)I_{Tot}(t) = \left(\sum_{j=1}^{N}E_c\,K_{k,j}^{*}{}_{corr}\,\frac{\partial J_j^*(t)}{\partial t}\right)I_{Tot}(t) \quad for\ k = 1:N_{ext} \quad (2.4.5.5)$$

In this study, the time derivative is performed using the method for the derivative centered in the middle point.

The two operations of mean in time and the integral along the z-coordinate can be performed in the desired order, due to their mathematical properties. It means that Eq. (2.4.2.23) can be written as:

$$\eta_{per\ unit}(\alpha) = -\frac{1}{L_0}\left|\left(\int_{-\frac{L_0}{2}}^{\frac{L_0}{2}}\frac{\partial A_k\left(\alpha,\frac{\delta}{2},z',t\right)}{\partial t}\,dz\right)I_{Tot}(t)\right|_{time} =$$

$$= -\frac{1}{L_0}\left|\left(\int_{-\frac{L_0}{2}}^{\frac{L_0}{2}}\frac{\partial A_k\left(\alpha,\frac{\delta}{2},z',t\right)}{\partial t}I_{Tot}(t)\,dz\right)\right|_{time} = \qquad \left[\frac{W}{m}\right] \qquad (2.4.5.6)$$

$$= -\frac{1}{L_0}\int_{-\frac{L_0}{2}}^{\frac{L_0}{2}}\left(\langle\frac{\partial A_k\left(\alpha,\frac{\delta}{2},z',t\right)}{\partial t}I_{Tot}(t)\,\rangle_{time}\right)dz$$

Finally, the integral in dz of Eq. (2.4.5.6) can be solved. For this study, it is carried out by simply computing the mean of the value $\langle\frac{dA_k}{dt}\left(\alpha,\frac{\delta}{2},z_k,t\right)I_{Tot}(t)\rangle_{time}$, between $z_k = \frac{-L_0}{2}$ and $z_k = \frac{L_0}{2}$, among the N_{ext} discretization points.

Of course, this methodology is valid only if the N_{ext} points are uniformly distributed along the z-coordinate, *i.e.* if dz = *constant*. This can be understood remembering that a definite integral into an interval $[z_{min}, z_{max}]$ can be seen as the area subtended to a curve *f(z)* in that interval. This area can be calculated as the summation of the areas of the rectangles (with a rough approximation) with dimensions $dz_k = (z_k - z_{k-1})$ and $f(z_k)$, where z_k are the N_{ext} points discretizing the interval $[z_{min}, z_{max}]$. This is equivalent to write:

$$\int_{z_{min}}^{z_{max}} f(z)\, dz = \sum_k f(z_k)\, dz_k \qquad (2.4.5.7)$$

If dz_k is a constant (named dz), it can be taken out of the sum.

Moreover, the relation between the length of the interval and dz is:

$$dz = \frac{(z_{max} - z_{min})}{N_{el}} \qquad (2.4.5.8)$$

Thus, Eq. (2.4.5.7) can be written as:

$$\int_{z_{min}}^{z_{max}} f(z)\, dz = dz \sum_k f(z_k) = \frac{(z_{max} - z_{min})}{N_{ext}} \sum_k f(z_k) \qquad (2.4.5.9)$$

Remembering that the operation of mean is equal to $\langle f(z) \rangle = \frac{\sum_k f(z_k)}{N_{ext}}$, Eq. (2.4.5.9) can be written as:

$$\int_{z_{min}}^{z_{max}} f(z)\, dz = \frac{(z_{max} - z_{min})}{N_{ext}} \sum_k f(z_k) = (z_{max} - z_{min}) \langle f(z) \rangle_{z_k \in [z_{min}, \ z_{max}]} \qquad (2.4.5.10)$$

Applying the arguments adopted from Eq. (2.4.5.7) to (2.4.5.10), for the case where $f(z) = \langle \frac{\partial A_k \left(\alpha, \frac{\delta}{2}, z_k, t \right)}{\partial t} I_{Tot}(t) \rangle_{time}$ and $(z_{max} - z_{min}) = \left(\frac{L_0}{2} - \left(-\frac{L_0}{2} \right) \right) = L_0$, Eq. (2.4.5.6) can be written as:

$$\eta_{per\ unit}(\alpha) = -\frac{1}{L_0} \int_{-\frac{L_0}{2}}^{\frac{L_0}{2}} \left(\langle \frac{\partial A_k \left(\alpha, \frac{\delta}{2}, z', t \right)}{\partial t} I_{Tot}(t) \rangle_{time} \right) dz' =$$

$$= -\frac{1}{L_0} \left(L_0 \langle \langle \frac{\partial A_k \left(\alpha, \frac{\delta}{2}, z_k, t \right)}{\partial t} I_{Tot}(t) \rangle_{time} \rangle_{z_k \in \left[\frac{-L_0}{2}, \frac{L_0}{2} \right]} \right) = \qquad \left[\frac{W}{m} \right] \qquad (2.4.5.11)$$

$$= -\langle \langle \frac{\partial A_i \left(\alpha, \frac{\delta}{2}, z_k, t \right)}{\partial t} I_{Tot}(t) \rangle_{time} \rangle_{z_k \in \left[\frac{-L_0}{2}, \frac{L_0}{2} \right]}$$

Eq. (2.4.5.11) allows the calculation of the corrective factor as a function of the geometry of the experimental set-up (varying the value of α).

It is worth noting that, when performing the mean over a period, it is preferable to simulate more than one period and then plot the trend of $p(t)$ by the time, too understand when it reaches the regime condition. Thus, the mean can be performed over a period where the regime conditions have already been reached.

2.4.6. Calculation of the corrective factor in the case with compensation and the minimization of the area of the voltage measurement circuit

The measurement circuit for the voltage signal realized with compensation and the minimization of the area of the voltage measurement circuit is considered in this section. The corrective factor $\gamma_{per\ unit}$ is calculated from Eq. (2.4.3.7).

In this case, the minimization of the area formed by the voltage measuring circuit is considered favourable and ideally the location at which the copper wires are twisted together can be at the same x-coordinate as the voltage taps soldered onto the tape surface (a null area of the circuit). For this reason, the field points can be considered to be placed inside the tape region ($x \in \left[\frac{-w}{2}, \frac{w}{2}\right]$). The dependence of the corrective factor $\gamma_{per\ unit}$ on this distance, called β, is analysed.

It is useful to discretize the line at $y = \frac{\delta}{2}$ (since the voltage taps are twisted on the upper surface of the tape), included between the tape edges, in a finite number of points N_{int}. These points represent the possible locations of the voltage taps (assuming that both voltage taps are soldered at the same x-coordinate at a distance L_0 to each other).

The steps that led to Eq. (2.4.5.11) are valid also for this configuration, noting that in this case $z_k = 0$. Thus, the dependence of the correction factor $\gamma_{per\ unit}$ on β can be calculated using Eq. (2.4.3.7):

$$\gamma_{per\ unit}(\beta) = \left| \frac{\partial A\left(\beta, \frac{\delta}{2}, t\right)}{\partial t} I_{Tot}(t) \right|_{time} \qquad \left[\frac{W}{m}\right] \qquad (2.4.6.1)$$

It is worth noting that, even for this case, it is mandatory to simulate more than one period and then analyse the trend of *p(t)* by the time *t*, to find out when it reaches the regime conditions.

2.4.7. Results of the AC losses calculation with the numerical model based on the A-V formulation

The geometry and the electrical properties of the *SuNAM SCN04* tape are implemented into the model to calculate the AC losses, as a test case. The MATLAB software is used as the solver. The tape geometrical parameters are presented in Fig. 2.4.7.1. Note that the buffer layer is not considered in the geometry, since its influence on the losses is considered negligible compared to the other layers given its small thickness.

The resistivity values of conventional metals used in the simulation are reported in Table. 2.4.7.1, as well as the parameters of superconductor power law, computed from experimental measurements. For the non-ferromagnetic substrate, as well as the other layers, the relative magnetic permeability is taken equal to 1. Table. 2.4.7.1 reports also some geometrical parameters, *i.e.* the length of the tape not covered by the connections with the current leads (*L*) the and the distance between the voltage taps (L_0). These parameters are set in in accordance

with the experimental set-up carried out at the *University of Bologna* and described in *Section 3.1*. In the model, the temperature is considered to be constant and equal to 77 K.
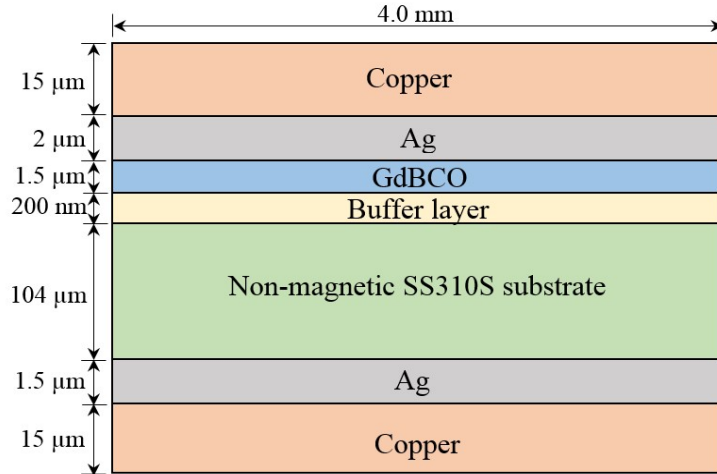

Figure 2.4.7.1. *Geometry of the cross-section of the SuNAM SCN04 tape. The figure is in not in scale.*

Table 2.4.7.1. *Electrical parameters of the SuNAM SCN04 tape and geometrical parameters for the measurement system.*

Parameter	Unit	Value
I_c (77 K , $E_c = 1$ μV/cm)	[A]	242
n- value (77 K , $E_c = 1$ μV/cm)		43
ρ_{Cu}	[Ω m]	$1.97 \cdot 10^{-9}$
ρ_{Ag}	[Ω m]	$2.7 \cdot 10^{-9}$
$\rho_{Sub} = \rho_{AISI310}$	[Ω m]	$7.24 \cdot 10^{-7}$
L	[m]	0.1
L_0	[m]	$5 \cdot 10^{-2}$

The discretization of the tape cross-section is based on rectangular-shaped elements. Due to the high aspect-ratio of the tape, this shape is preferred to square elements that would require a greater number of elements to discretize the same cross-section. Two considerations are made for the discretization of the tape cross-section. Firstly, given that this study is carried out for current amplitudes not higher than I_c, it is supposed that the current flows mostly in the superconducting layer. Secondly, especially for low frequencies, the induced currents flowing in the tape are mainly located at the edges of the tape cross-section. For this reason, a non-homogenous discretization of the superconducting layer is preferred, with wider elements in the central zone of the tape and narrower elements at the tape edges, so as to achieve a better accuracy in the areas where the AC losses are more relevant. As an example, Fig. 2.4.7.2 shows the discretization of the cross-section of the superconducting layer of the tape in the non-

homogenous (a) and homogenous (b) configurations. In both cases, the layer is meshed using the same number of elements. In any case, a homogenous discretization is adopted for the non-superconducting layers of the tape.
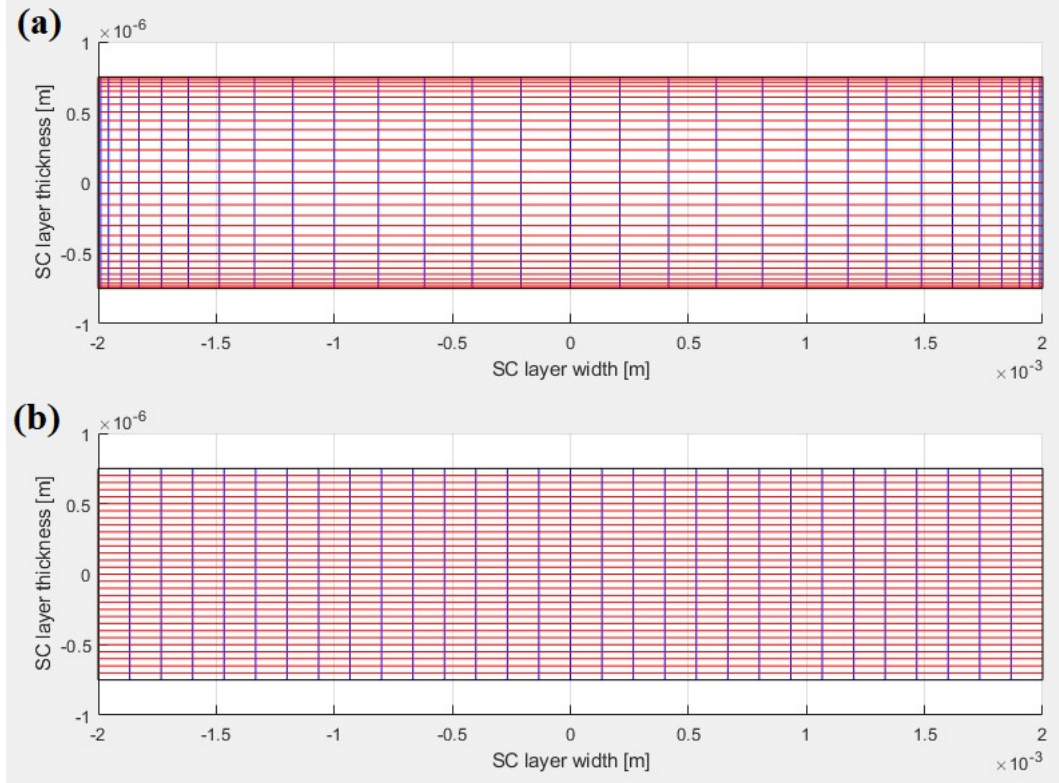
Figure 2.4.7.2. *Examples of discretization of the cross-section of the superconducting layer of a coated conductor with the non-homogeneous (a) and homogeneous (b) configurations. Both configurations presented have the same number of elements. The figure is not in scale.*

Table 2.4.7.2 reports the mesh parameters used in the simulation, which are set after a proper convergence study that is described in *Section 2.4.9*.

Table 2.4.7.2. *Mesh parameters implemented in MATLAB for the integral model based on the A-V formulation.*

	Discretization across the tape thickness	*Discretization across the tape width*	*Total number of elements*
Upper Cu layer	3	15	45
Upper Ag layer	2	15	30
SC layer	4	200	800
Substrate layer	12	20	240
Lower Ag layer	2	15	30
Lower Cu layer	3	15	45
Whole tape	26	/	1190

First, the numerical model is applied to simulate transport AC losses for different current amplitudes and frequencies, without considering any external magnetic field. Then, the magnetization losses are calculated in the case of zero transport current and applying an external magnetic field of different amplitude, frequency and orientation. Finally, the combination of both loss sources is considered. The results are compared with Norris' formula (see Eq. (2.3.5.3)).

Fig. 2.4.7.3 presents the average power dissipation for different current amplitudes (see Eq. (2.1.5) for the expression of I_m). The frequency is set equal to 50 Hz. The non-superconducting layers of the tape do not generate significant power dissipation since the differences between the "*Whole_Tape*" and "*SC_only*" cases are minor (below 0.5 %). The definition of these two cases are described at Page. 26.

The numerical results fit well the analytical trend, although the numerical results are slightly higher at low currents and slightly lower at high currents, compared to the analytical results.
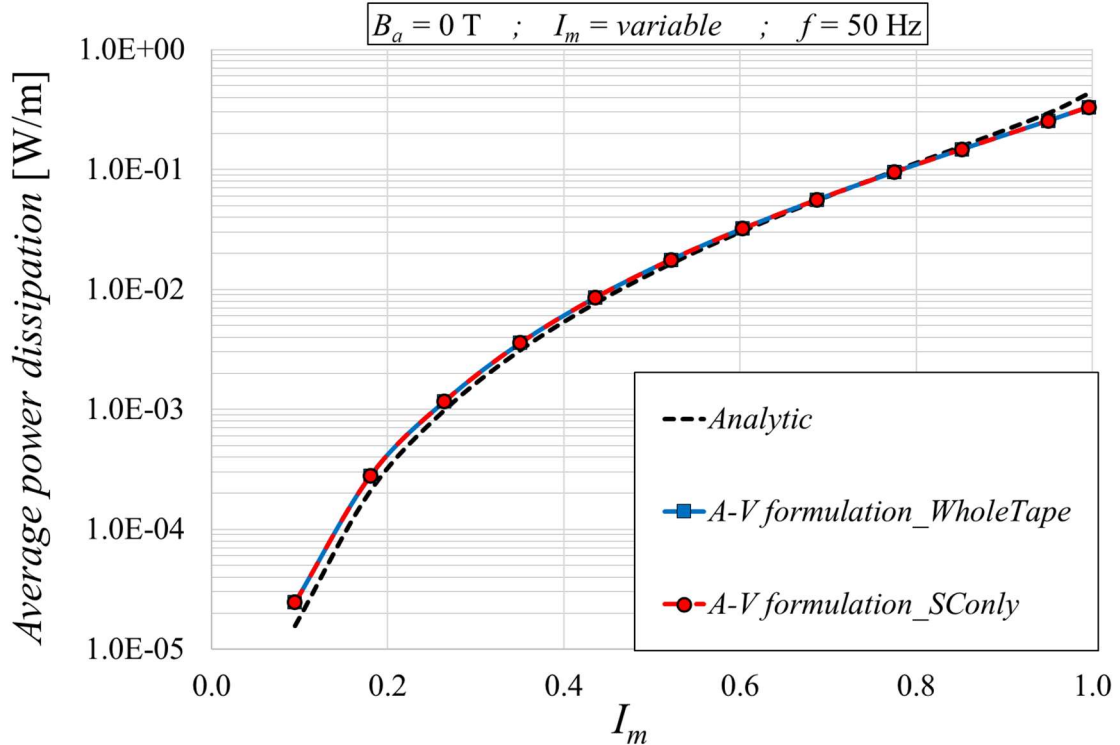
Figure 2.4.7.3. *Average power dissipation for different I_m values and at a frequency set to 50 Hz. The figure is in semi-logarithmic scale.*

Fig. 2.4.7.4 presents the AC losses for different current amplitudes and keeping fixed the current frequency. The trends referred to several frequencies are shown. The curves are consistent with each other; for the same current amplitudes, the losses result greater at low frequencies compared to the higher frequency cases [130]. This pattern does not seem to be influenced by the value of I_m. In fact, the analytical formula adopts the critical state model [131] for the superconductor instead of the power law. A further explanation is reported in *Section 2.4.8*, where the study about the losses dependence on the *n-value* is presented.
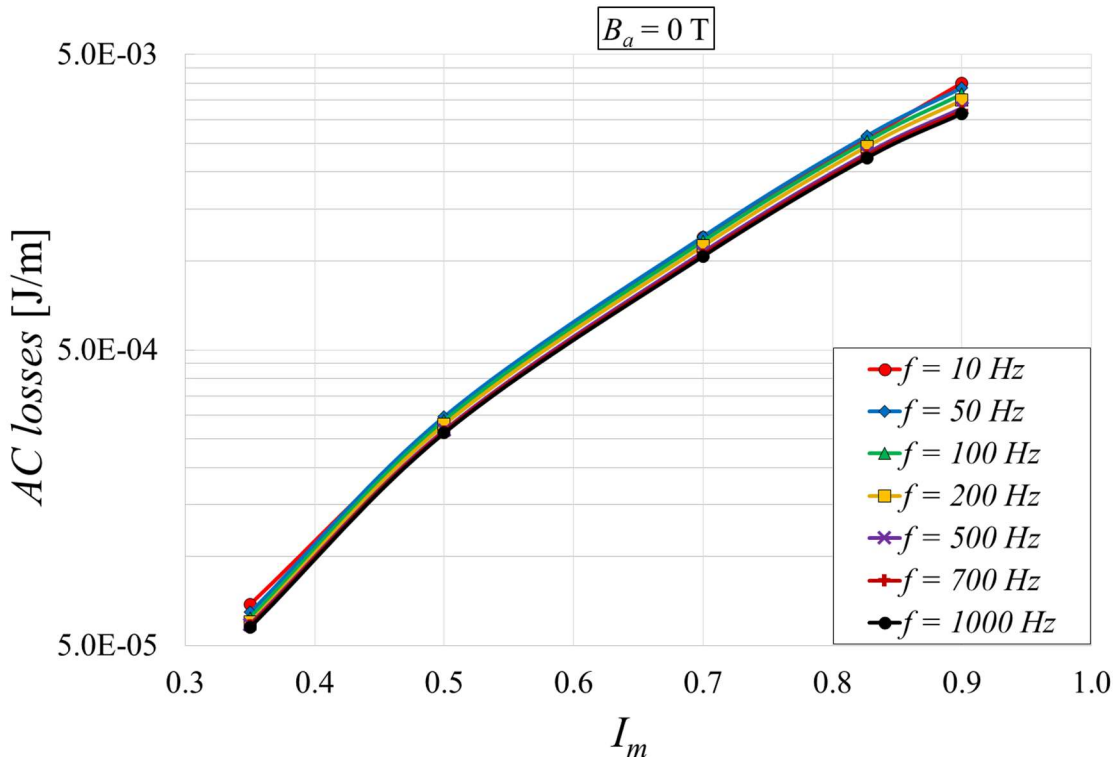
Figure 2.4.7.4. *AC losses for different AC current amplitudes and frequencies. The figure is in semi-logarithmic scale.*

Fig. 2.4.7.5 shows the transport current AC losses for different frequencies at fixed current amplitudes (three I_m values are selected: 0.5, 0.7 and 0.9). At low frequencies, the differences between the "*Whole_tape*" and the "*SC_only*" cases are below 1‰. However, for high frequencies (> 2÷3 kHz) the results of the two approaches start diverging; their difference varies depending on the current amplitude. For f = 10 kHz, the losses in the "*Whole_tape*" case are around 6% lower than in the "*SC_only*" case when I_m = 0.9, while they are around 12% higher when I_m = 0.5.

The numerical curves decrease when the frequency increases. The interpretation of this phenomenon is not trivial, as one could be led to think that the losses in the superconductor should increase with the frequency, as occurs for a normal material, due to the skin effect. However, an opposing mechanism occur in superconductors, since the critical current tends to increase when the frequency rises, as reported in [132 – 134]. This implies that, with the same current amplitude, the resistance offered by the superconductor to the current flow decreases with increasing frequency, and so do the losses. Moreover, it is worth noting a slight increase for the case with I_m = 0.5, for frequencies exceeding 1 kHz. As it will be explained in the next paragraphs, this can be due to the contribution of normal layers, whose transport capacity does not increase with frequency.

Moreover, a good agreement between the analytical and the numerical results is found around a specific frequency which depends on the current amplitude: increasing the current amplitude, the value of this converging frequency reduces. For high values of I_m, this value approaches the standard power frequencies (50 ÷ 60 Hz). This is consistent with the results reported in [132]. It is worth noting how in this work, the quasi-stationary conditions (which allow

neglecting the displacement field in the Ampere's law into the model equations) are assumed to be valid at least for frequencies up to 10 kHz.
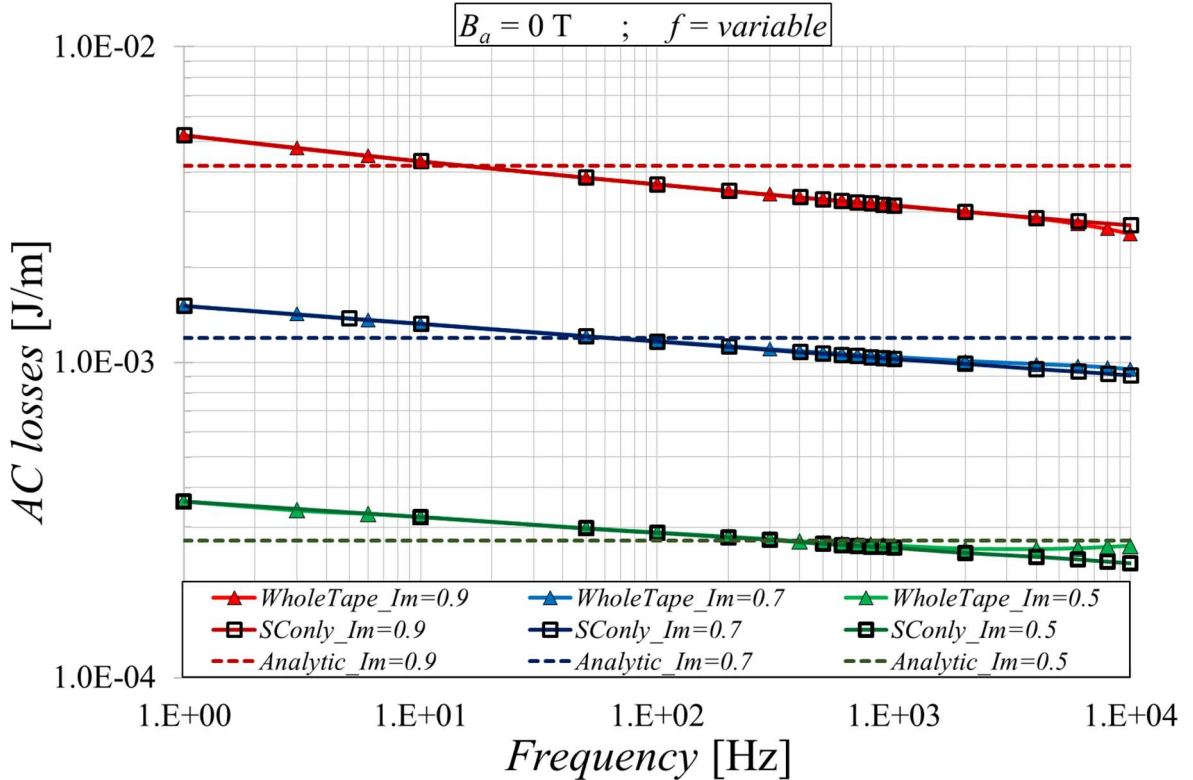

Figure 2.4.7.5. *AC losses for different AC current frequencies and for I_m set to 0.9, 0.7 and 0.5. The figure is in logarithmic scale.*
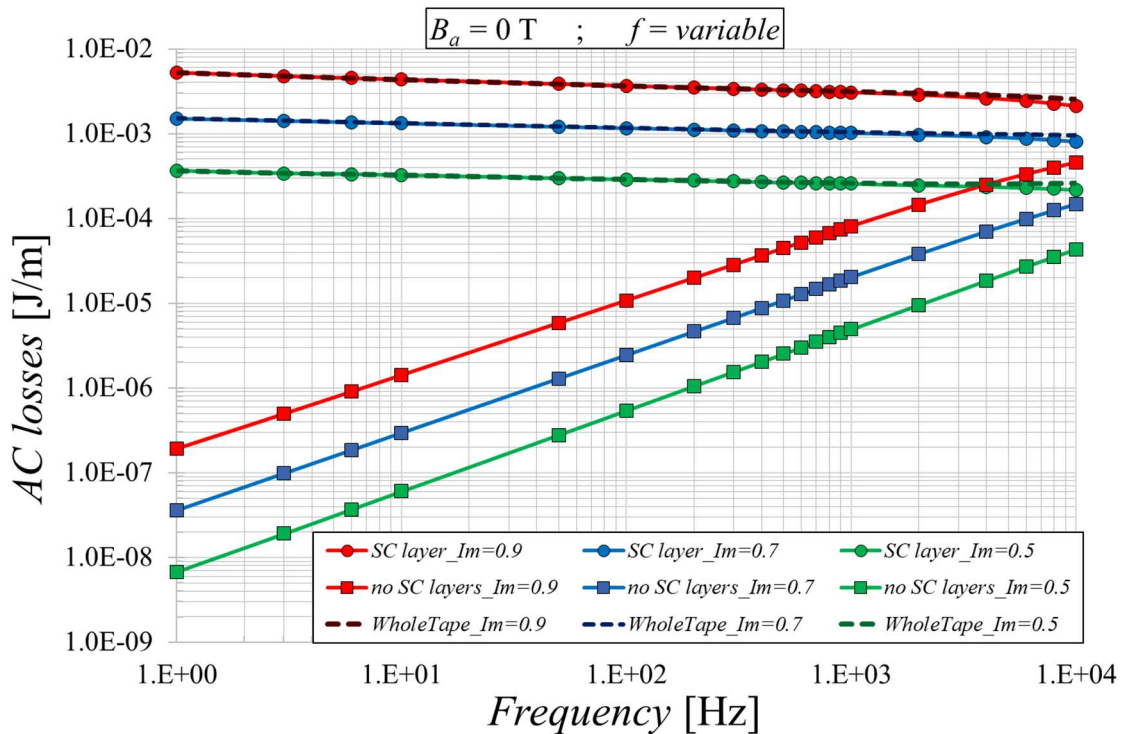
Figure 2.4.7.6. *AC losses for I_m set to 0.9, 0.7 and 0.5, for the superconductor only and for the non-superconducting layers of the tape together. The figure is in logarithmic scale.*

Fig. 2.4.7.6 shows the AC losses generated in the whole tape, those generated in the superconducting layer (extracted from the "*Whole_tape*" model losses, thus they differing from the "*SC_only*" case) and those generated in the other non-superconducting layers altogether. While the losses in the superconducting layer decrease slightly with the frequency, the losses in the other layers increase rapidly, albeit their values remain minor (4 to 5 times lower than the losses in the superconducting layer for f = 10 kHz).
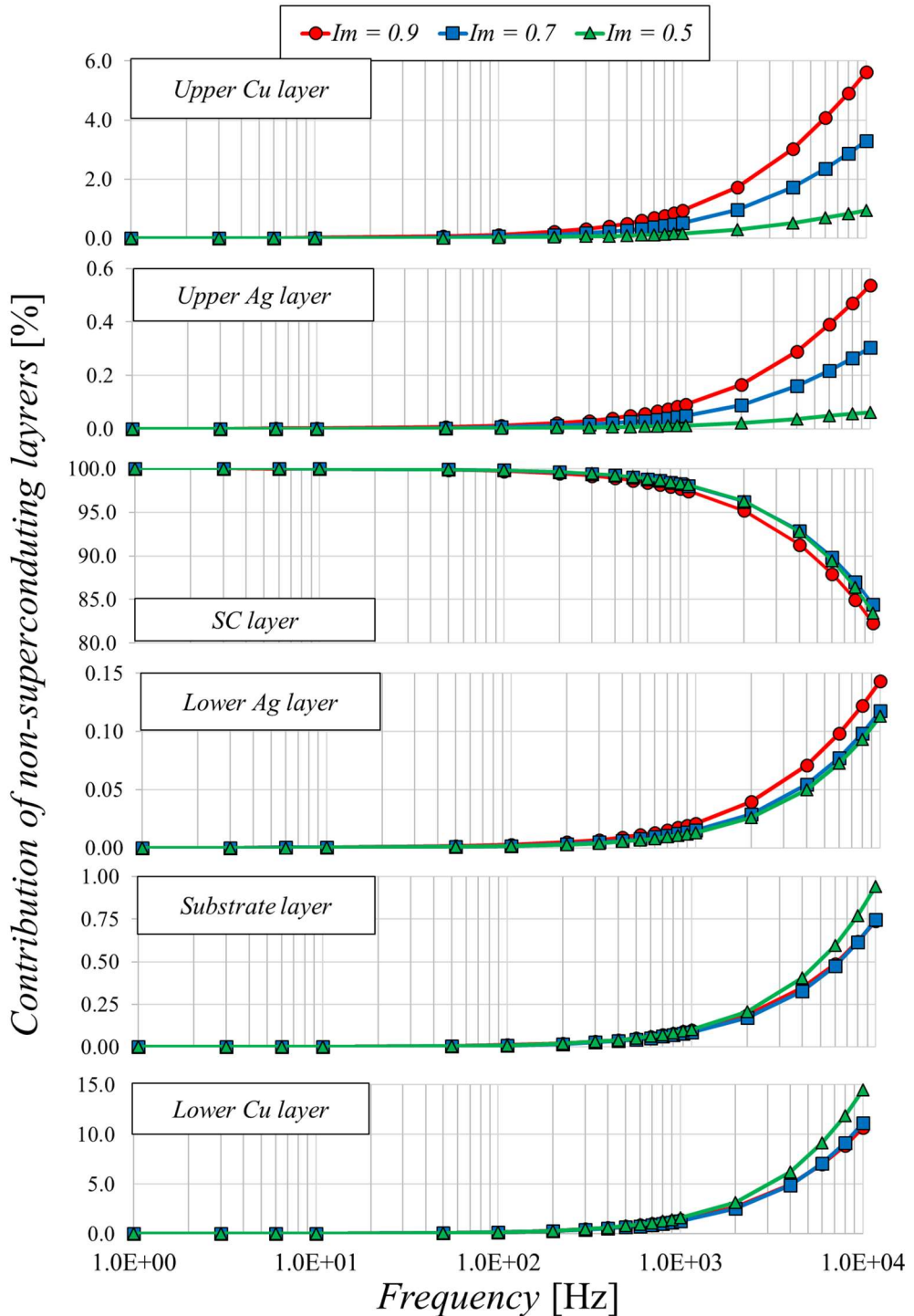
Figure 2.4.7.7. *AC losses contribution of each non-superconducting layer compared to the AC losses of the whole tape, for different AC current frequencies and at I_m equal to 0.9, 0.7 and 0.5. The figure is in semi-logarithmic scale.*

Fig. 2.4.7.7 presents the contribution of each layer to the AC losses of the tape. As expected from the trends shown in Fig. 2.4.7.6, the contribution of the superconducting layer decreases with the frequency. For high frequencies, the contribution of the copper layers becomes predominant, while the contribution of the substrate and silver layers, despite their increase, remains almost negligible. Moreover, the contribution of the lower layers (*Cu* and *Ag* lower layers) is greater compared to the contribution of the upper layers (*Cu* and *Ag* upper layers) notwithstanding the same geometrical dimensions. The contribution of the upper layers strongly depends on the value of I_m: when I_m is higher, their contribution is greater. On the other side, the contribution of the lower layers does not seem significantly affected by the current amplitude.

Then, the model is applied to compute the losses produced in the tape by the presence of an AC external magnetic field, considering null the transport current. Initially, the case of a field perpendicular to the tape main face is considered. For this case, the numerical results are compared with those obtained using the analytical formulation for a thin strip in a perpendicular sinusoidal field, presented in [59]:

$$\langle p(t)\rangle_{Analytic} = f \, 4 \, \mu_0 \, a^2 J_c H_a \left\{ \left[\left(2\frac{H_c}{H_a}\right) ln\left(cosh\left(\frac{H_c}{H_a}\right)\right)\right] - tanh\left(\frac{H_c}{H_a}\right)\right\} \quad \left[\frac{W}{m}\right]$$

(2.4.7.1)

$$H_a = \frac{B_a}{\mu_0} \quad , \quad H_c = \frac{J_c}{\pi} \quad , \quad J_c = \frac{I_c}{2a}$$

where a is the tape half-width, H_a is the amplitude of the external applied magnetic field and H_c is the tape critical field.
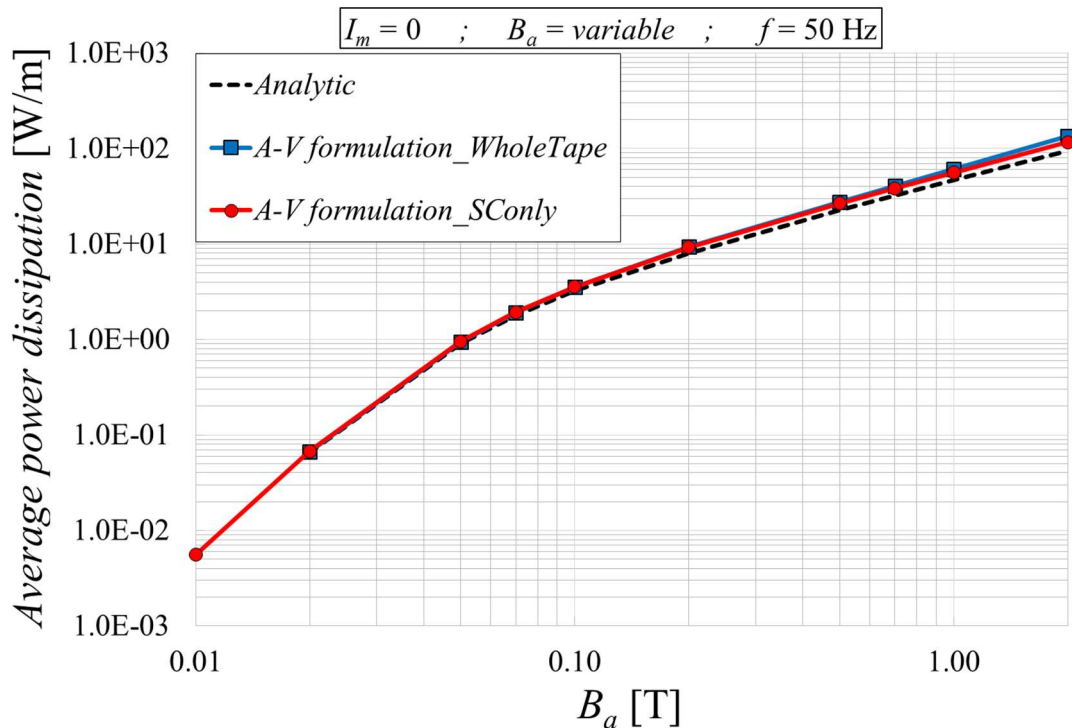
Figure 2.4.7.8. *Average power dissipation for different AC external magnetic field amplitudes and at a frequency equal to 50 Hz. The figure is in logarithmic scale.*

Fig. 2.4.7.8 shows the average power dissipation due to an external magnetic field applied perpendicular to the tape main face, with different amplitudes and a frequency set to 50 Hz. The change in the curve slope for field amplitudes around 50 mT indicates the condition at which the magnetic saturation is reached. The numerical results obtained in the "*Whole_tape*" case indicate slightly larger losses at high fields (13% higher when $B_a = 2$ T) than those obtained in the "*SC_only*" case, which can be explained as an increasing contribution of the non-superconducting layers to the total losses. The numerical and the analytical results are in good agreement, although they start to diverge at high field amplitudes. Some minor discrepancies are unavoidable since the analytical formulation assumes a 1-D approximation [135].

Fig. 2.4.7.9 shows the contribution of non-superconducting layers compared to the power dissipation of the whole tape. The contribution of the non-superconducting layers rises with increasing of the external magnetic field amplitude. This might explain the greater values at higher fields of the "*Whole_tape*" curve of Fig. 2.4.7.8, compared to the "*SC_only*" curve.
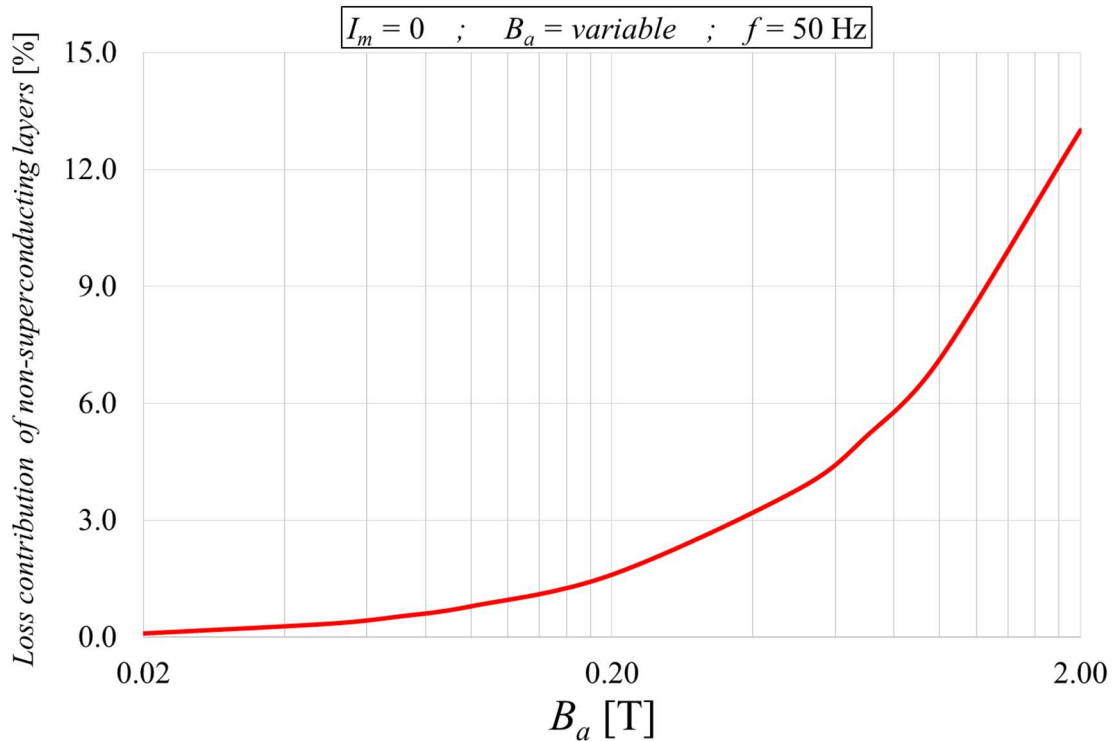
Figure 2.4.7.9. Contribution of the non-superconducting layers to to the magnetization losses of the whole tape, for different external magnetic field amplitudes and at a frequency equal to 50 Hz. The figure is in semi-logarithmic scale.

Fig. 2.4.7.10 presents the magnetization losses computed by varying the perpendicular field frequency with the amplitude set to 0.1 T. The numerical curves overlap at low frequencies appearing to be almost frequency independent, despite the numerical results are higher compared to the analytic values (from 5% to 10% greater, for frequencies below 100 Hz). For frequencies higher than 100 Hz, the "*Whole_tape*" curve increases significantly while the "*SC_only*" curve remains frequency independent. The losses computed in the "*Whole_tape*"

case are around 50% greater than the losses calculated in the "*SC_only*" case when the frequency exceeds 7 kHz.
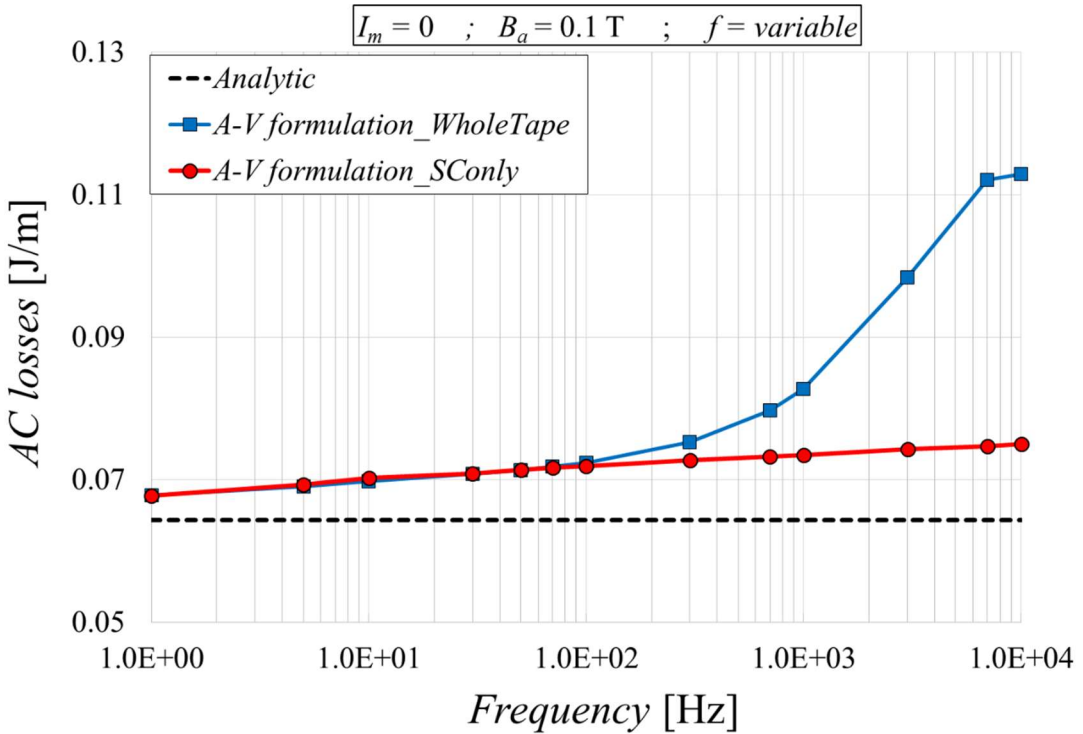
Figure 2.4.7.10. *Magnetization losses for different external magnetic field frequencies and at an amplitude equal to 0.1 T. The figure is in semi-logarithmic scale.*
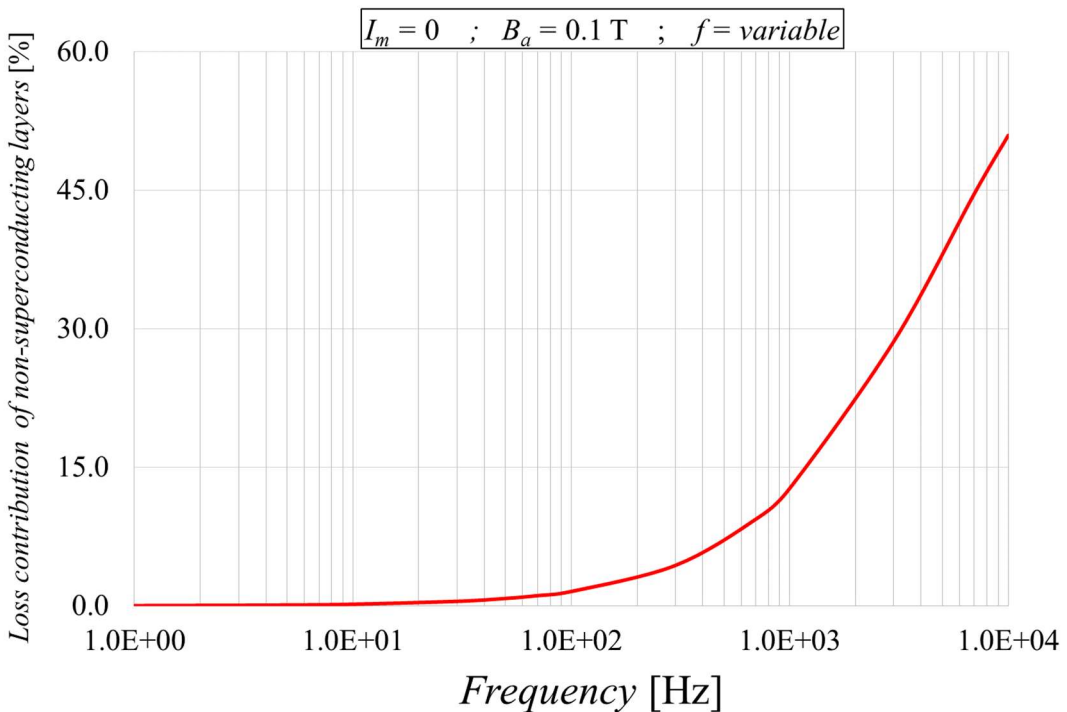
**Figure 2.4.7.11.** *Contribution of the non-superconducting layers to the magnetization losses of the whole tape, for different magnetic field frequencies and for an amplitude equal to 0.1 T. The figure is in semi-logarithmic scale.*

Fig. 2.4.7.11 shows the contribution of the non-superconducting layers to the magnetization losses of the tape. The contribution of the non-superconducting tape becomes predominant (>50% of the total losses) at high frequencies. This corresponds with the discrepancies of the "*Whole_tape*" compared to the "*SC_only*" case at high frequencies, presented in the previous figure. It is worth noting that, for the non-ferromagnetic normal materials composing the tape, the losses are generated by eddy currents. This mechanism differs from the hysteresis phenomenon, but it can be ascribed into the magnetization losses.

Fig. 2.4.7.12 presents the magnetization losses generated in each layer of the tape. The losses in the superconducting layer are frequency independent up to about 1 kHz; passing this threshold value, they start to decrease. On the other side, the losses generated in the other layers increase linearly with frequency.

For a better insight of the underlying physical phenomena, Figure 2.4.7.13 depicts the J/J_c distribution in the cross-section of the superconducting layer, computed for different frequencies (10 Hz, 100 Hz, 1 kHz and 10 kHz) with a perpendicular field amplitude of 0.1 T. Various instants of the field cycle are shown, corresponding to $\omega t = \frac{5}{2}\pi$ (a) and $\omega t = 3\pi$ (b). These instants are included in the second period, since the regime conditions have not yet been reached during the first one. The plots reported on the left side of the figures refer to the "*Whole_tape*" model, although only the current distribution in the superconducting layer is presented. The plots reported on the right correspond to the "*SC_only*" model. The thickness of the superconductor is finely discretized (8 elements) in order to obtain a sufficiently precise representation of the current density fronts at different time instants. However, for the mere AC loss calculation, such fine discretization is not necessary. Both figures show that there are no significant differences between the current density distributions obtained with the two models for frequencies up to 1 kHz. When the induced current distributions are the same for the different cases, the losses obtained are equal. This result is consistent with the frequency independence of the magnetization losses in the superconducting layer at these frequency values, as displayed in Fig. 2.4.7.10. When the frequency overcomes 1 kHz, some discrepancies between the two models can be observed. In particular, the "*Whole_tape*" case results in lower values of the J/J_c ratio (and therefore of the amplitude of induced currents) in the central area of the superconductor as compared to the "*SC only*" case. This indicates that the induced currents can no longer penetrate this layer completely. Since lower induced current amplitudes determine lower values of the losses, the current distributions shown in Fig. 2.4.7.13 prove the losses decrease in the superconducting layer above 1 kHz. Instead, it can be inferred that the induced currents increase in the normal layers, which in turn produces a greater loss contribution. Thus, for the computation of the magnetization losses, neglecting the non-superconducting layers of a tape becomes a too rough approximation when the frequency exceeds 1 kHz. The same outcomes are verified for all the other instants. It is worth noting how the induced currents shift from the outside towards the inside of the conductor during time. The sign of the new induced currents changes according to the field amplitude increasing or decreasing time variations.
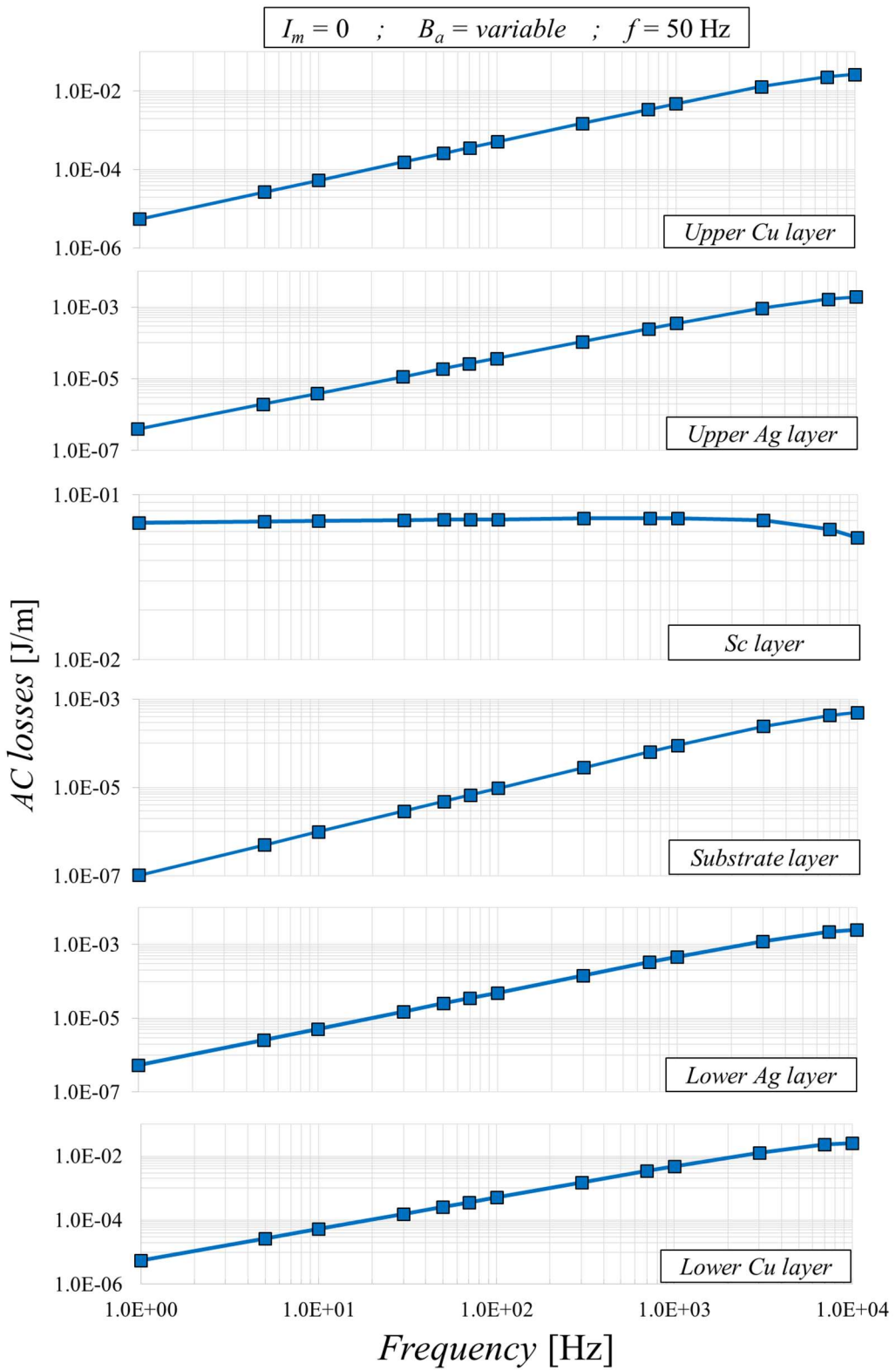
Figure 2.4.7.12. *AC losses generated in every layer of the SuNAM SCN04 tape for different external magnetic field frequencies and at an amplitude equal to 0.1 T. The figure is in semi-logarithmic scale.*
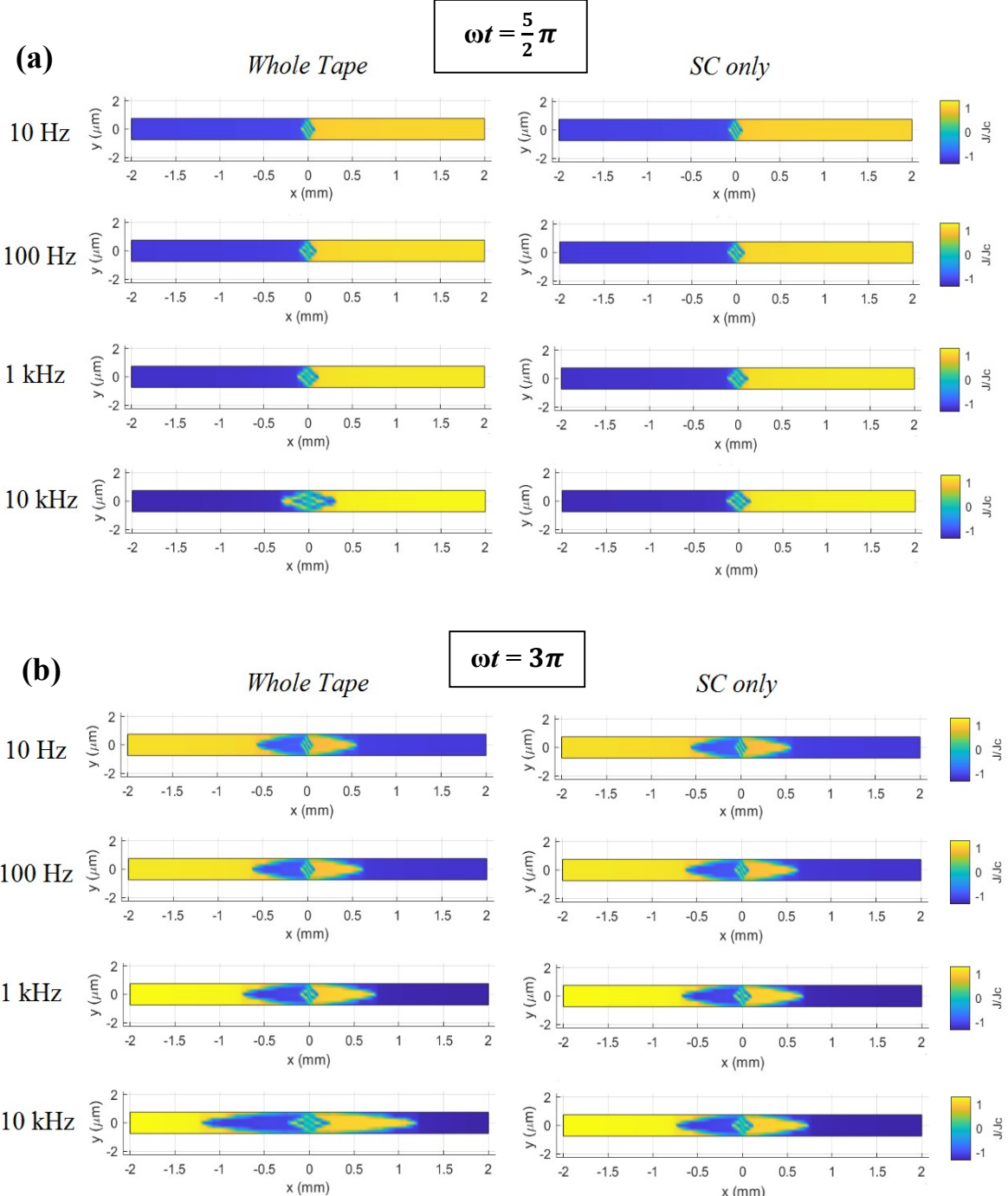
Figure 2.4.7.13. *J/J$_c$ distribution in the superconducting layer of the SuNAM SCN04 tape subjected to a perpendicular magnetic field with an amplitude of 0.1 T and different frequencies, for $\omega t = \frac{5}{2}\pi$ (a) and $\omega t = 3\pi$ (b). In the left side plots, the non-superconducting layers of the tape are implemented, while in the right side plots they are neglected.*

Subsequently, the model is applied to compute the losses due to an AC magnetic field having any orientation. With reference to Eq. (2.4.4.16) and Fig. 2.4.7.14, the θ_{field} angle is the angle formed by the external magnetic field vector and the tape main. When $\theta_{field} = 0°$ the external field is perfectly parallel to the tape main face, while for $\theta_{field} = \frac{\pi}{2} = 90°$ the external field is

perfectly perpendicular to the tape main face. In order to reach convergence also for nearly parallel field orientations, the spatial discretization of the HTS layer is refined to reach 8 elements across its thickness.
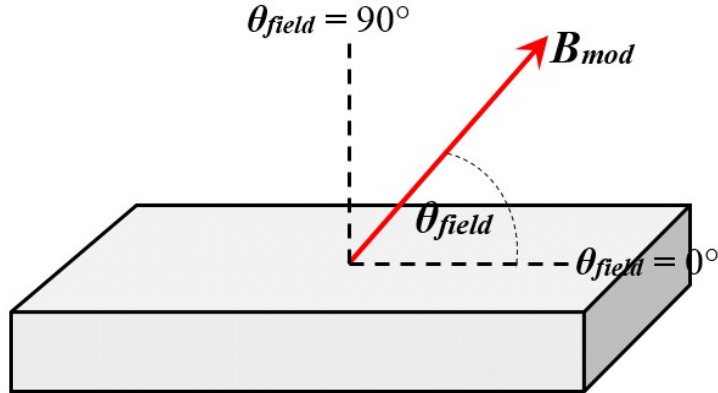
Figure 2.4.7.14. *Parameters used to describe the orientation of the external magnetic field.*
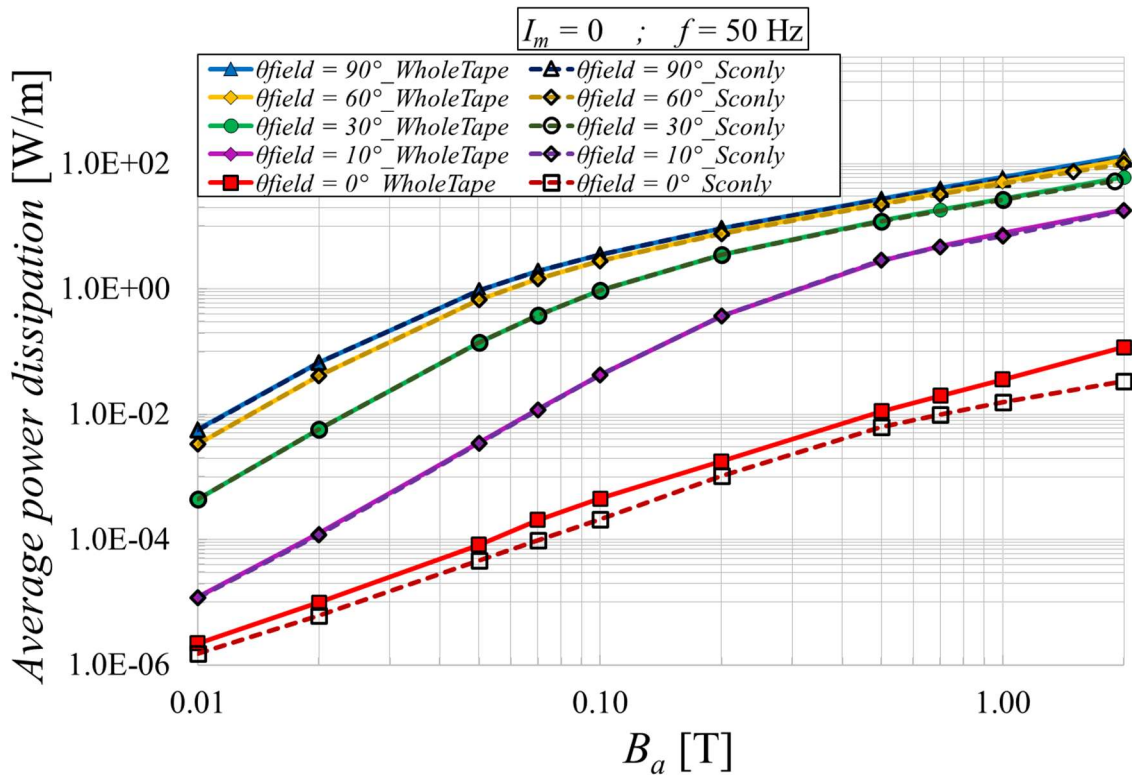
Figure 2.4.7.15. *AC losses generated in the SuNAM SCN04 tape by the presence of an external magnetic field at 50 Hz and for different amplitudes and orientations. The figure is in semi-logarithmic scale.*

Fig. 2.4.7.15 shows the average power dissipation due to an AC external magnetic field forming different angles with the tape main face. The frequency is set to 50 Hz and the field amplitude is varied. As expected, the losses are greater for higher angles, since the perfectly perpendicular case is the most stressing for an HTS tape [104 – 107]. Reducing the incidence angle at constant B_a, the losses are lowered. This reduction is not linear with the θ_{field} angle.

For sufficiently wide angles, the losses do not greatly differ from the perpendicular case; on the contrary, when the angle of incidence approaches the parallel case, the losses are drastically reduced by several orders of magnitude. There is no significant difference in the results obtained with the "*Whole_tape*" or "*SC_only*" models, except for the parallel case. In the latter condition, the discrepancy between the two cases is significant: the contribution of the non-superconducting layers never drops below 50%.

Fig. 2.4.7.16 shows the contribution of the non-superconducting layers of the tape computed for the "*Whole_tape*" model. When θ_{field} = 90°, 60° and 30°, the contribution is negligible for low fields and increases at high fields. When θ_{field} = 10° the contribution at high fields remains limited while it is significant at low fields. Finally, for θ_{field} = 0° the contribution is always relevant. For this last case, the contribution is large at both low and high fields, decreasing at "intermediate fields" where a plateau is present in the range between 0.05 T and 0.5 T.
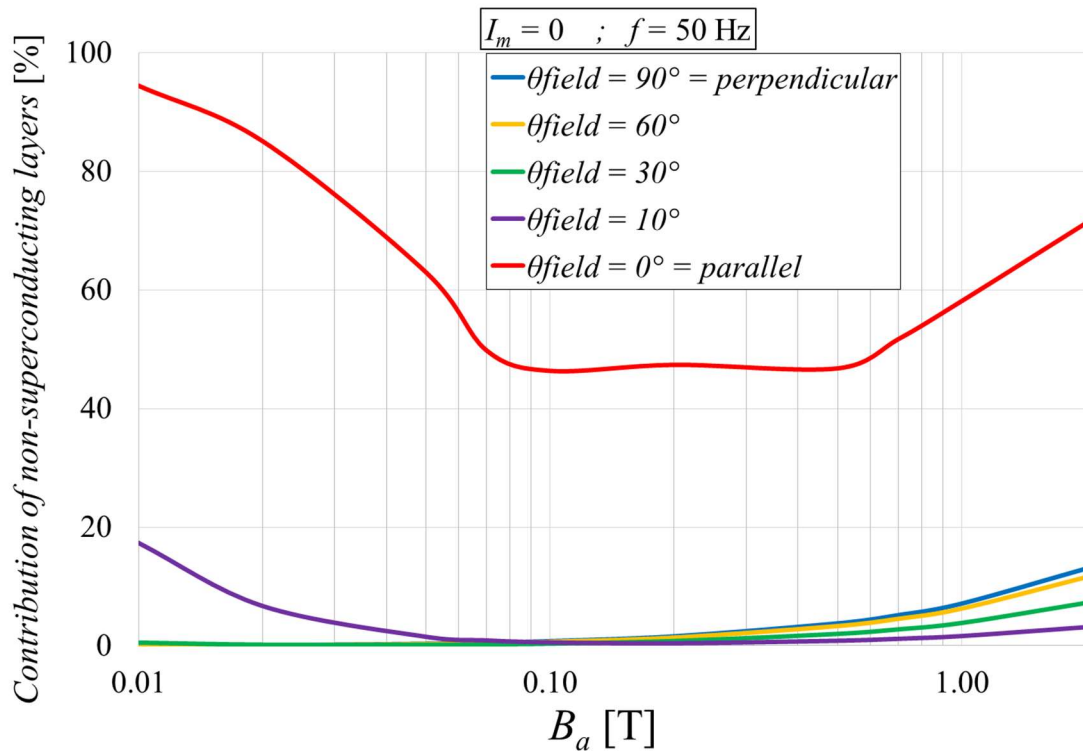
Figure 2.4.7.16. AC losses contribution of the non-superconducting layers compared to the AC losses of the whole tape, due to an external magnetic field at 50 Hz for different amplitudes and orientations. The figure is in semi-logarithmic scale.
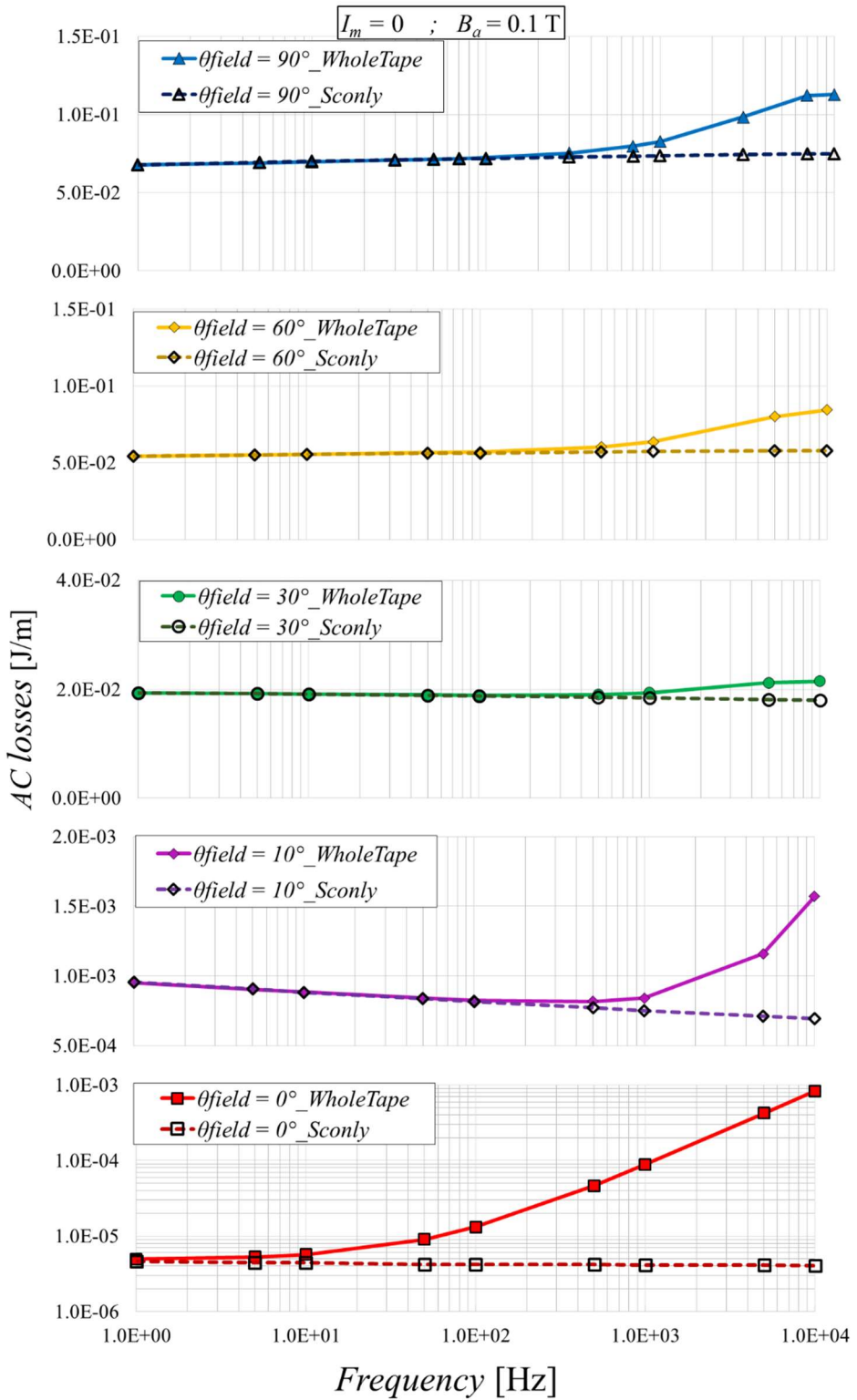
**Figure 2.4.7.17.** *Magnetization losses generated in the tape by the presence of an external magnetic field of amplitude equal to 0.1 T and at different frequencies and orientations. The figure is in semi-logarithmic scale for all cases except for the $\theta_{field} = 0°$, which is in logarithmic scale.*

Fig. 2.4.7.17 presents the magnetization losses due to an AC external magnetic field forming different angles with the tape main face. The amplitude is set to 0.1 T Hz and the frequency is

varied. The losses found with the "*SC_only*" model are almost frequency independent. For the "*Whole_tape*" model instead, all curves converge with the "*SConly*" cases in the low frequencies range but then they start to diverge when the frequency exceeds a threshold value, rising compared to their respective *SConly*" curves. This threshold is in the order of hundreds of Hz for all cases, except for the parallel field case, where the "*WholeTape*" curve diverges already for frequencies of tens of Hz. In this case, the impact of the non-superconducting layers is significant even at low frequencies, becoming predominant (> 50%) around 600 Hz, and approaching 100% of the total losses for frequencies above 1 kHz. Indeed, for parallel field, the thicknesses of the different layers determine the extent of the induced currents, and therefore the losses generated in each layer. Since the metallic layers are thicker than the superconducting one, their contribution is relevant. This phenomenon is enhanced at high frequencies [95]. Therefore, in these conditions it is of great importance to include the non-superconducting layers in the calculation of the magnetization losses due to parallel fields.

Fig. 2.4.7.18 shows the contribution of the non-superconducting layers of the tape. For all the curves except for the $\theta_{field} = 0°$ case, the contribution of non-superconducting layers is negligible until the frequency reaches 1 kHz; then, as the frequency rises, their contribution increases. The $\theta_{field} = 0°$ case is different since the contribution of the non-superconducting layers is significant even at low frequencies, exceeding 50% already below 1 kHz and approaching 100% when the frequency is equal to 10 kHz.
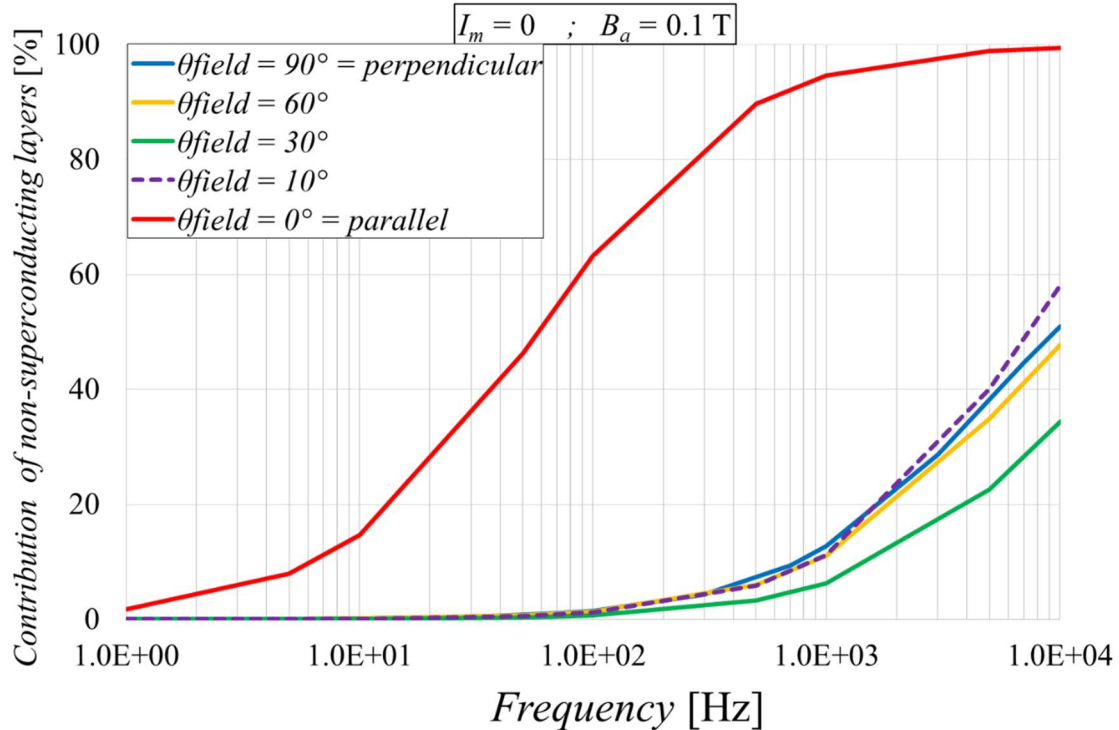
Figure 2.4.7.18. *Magnetization losses contribution of the non-superconducting layers to the losses of the whole tape, due to an external magnetic field of amplitude equal to 0.1 T and for different frequencies and orientations. The figure is in semi-logarithmic scale.*

Finally, the model allows calculating the losses produced in the case of a combination of the two sources: a transport current and an external magnetic field both variable in time with the

same frequency. Fig. 2.4.7.19 presents the average power dissipation generated in the *SuNAM SCN04* tape with a variable current amplitude, while maintaining the perpendicular field amplitude equal to 0.1 T; the frequency of both AC sources is set to 50 Hz. The difference between the results of the *A-V* model obtained in the "*Whole_tape*" and "*SC_only*" cases remains below 1%, which indicates that the losses generated in the non-superconducting layers have a minor impact. As expected, the combination of the two AC sources determines greater losses than those found for their separate application. It is worth noting how the power increases by 2.9 W/m when the current rises from its lower ($I_m = 0.1$) to its higher value ($I_m = 1$). In comparison, the increase obtained between the same amplitudes without considering the contribution of the magnetic field (Fig. 2.4.7.8) is around 0.3 W/m. When both AC sources are considered, the transport current acts in conditions which significantly differ from those obtained for the analyses reported in Fig. 2.4.7.9. In fact, the presence of a magnetic field produces a certain distribution of induced currents within the tape. For a field amplitude of 0.1 T the tape has reached magnetic saturation. Thus, when both AC sources are present, the transport current superimposes to the current distribution generated by the field and its contribution to the dissipated power results greater [136].
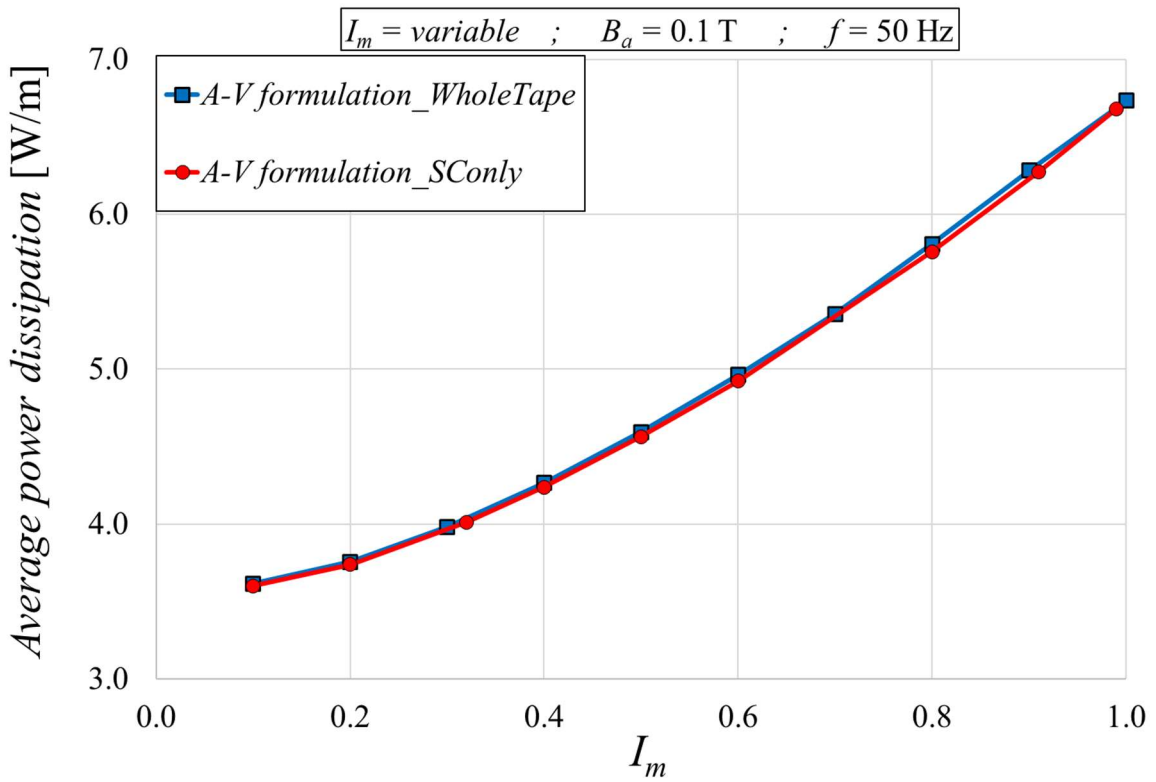
Figure 2.4.7.19. *Average power dissipation in the case of a combination of an AC transport current with different I_m values and an external magnetic field perpendicular to the tape main face with amplitude of 0.1 T. The frequency is set to 50 Hz for both sources. The figure is in semi-logarithmic scale.*

Fig. 2.4.7.20 shows the AC losses generated in the *SuNAM SCN04* tape by the combination of an AC transport current with I_m set to 0.7, and an external AC magnetic field perpendicular to the tape main face with an amplitude of 0.1 T. The frequency of both sources is varied equally in order to maintain the isofrequentiality. The trend is similar to the curves presented in Fig.

2.4.7.10 (magnetic field only). The results of the "*SC_only*" and of the "*Whole_tape*" models converge for low frequencies and they start diverging for frequencies higher than 300 Hz. The curve referred to the "*Whole_tape*" case presents a maximum around 5 kHz; for this peak, the losses computed in the "*Whole_tape*" case are around 26% greater than the losses calculated in the "*SC_only*" case. Then for higher frequencies, the "*Whole_tape*" curve decrease. This could agree well with the fact that Fig. 2.4.7.10 presents a plateau for the high frequencies while the losses shown in Fig. 2.4.7.5 maintain a decreasing profile. The combination of the two effects could lead to the peak in Fig. 2.4.7.20.
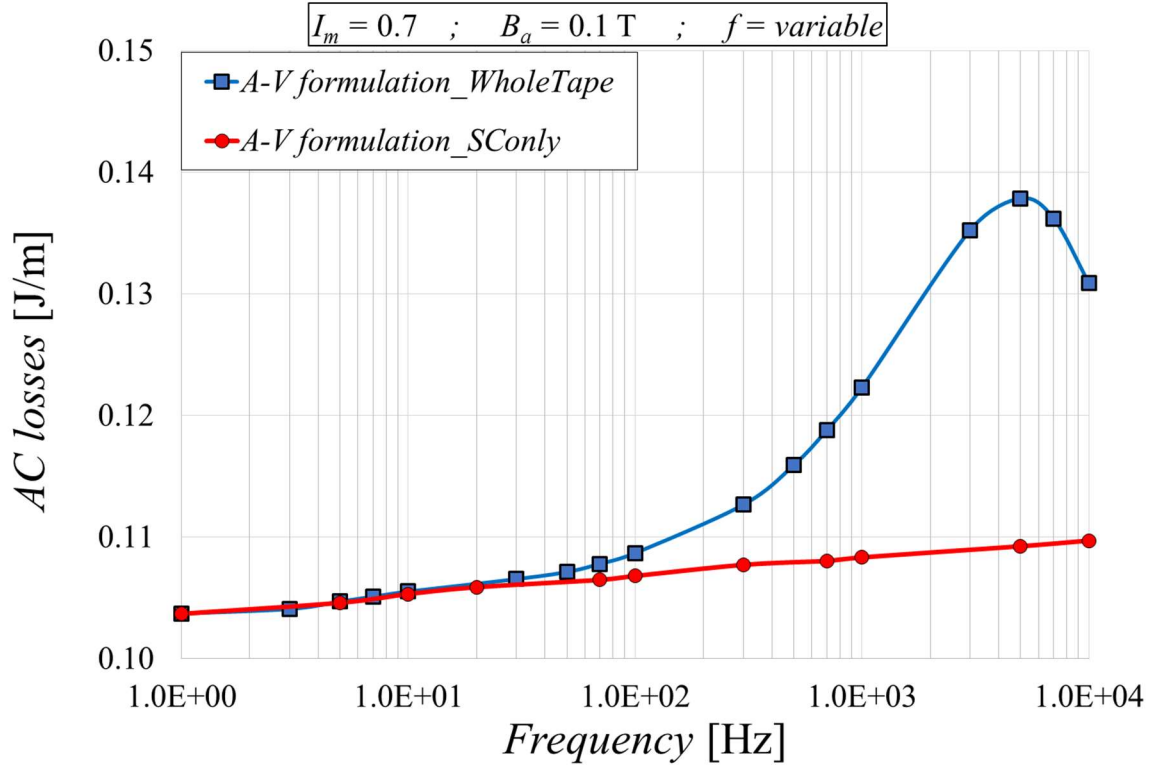
Figure 2.4.7.20. *AC losses in the case of the combination of an AC transport current with I_m set to 0.7 and an AC external magnetic field perpendicular to the tape main face with an amplitude of 0.1 T. The frequency is varied equally for both sources. The figure is in semi-logarithmic scale.*

2.4.8. Parametric study regarding the AC losses dependence on the tape n-value and the superconducting layer thickness

A couple of parametric studies are carried out about the dependence of the AC losses on the electrical and geometric properties of the coated conductor.

First, the dependence of the AC losses on the *n-value* of the tape is analysed. In modern HTS tapes, the *n-value* can be found within a broad range of values. Moreover, it could change during the operations if some damages occur inside the tape [137, 138].

Several studies are reported in the literature about *n-value* dependence [80, 139] and the proposed model allows to draw some conclusion in this regard. Fig. 2.4.8.1 presents the average

power dissipation in the tape due to an AC transport current for different I_m values and for a frequency set equal to 50 Hz. The following *n-values* are analysed: 43 (equal to the one experimentally measured for the *SuNAM SCN04* tape at 77 K in self-field), 30, 20, 10 and 5. Especially the cases with *n-value* equal to 5 and 10 represent the situations in which the tape is heavily damaged and probably unusable. It is worth noting that lower is the *n-value* and the more the curves deviate from the analytical case: for $n = 5$, the losses results 2 times higher at $I_m = 0.1$ and 2.7 times lower at $I_m = 1$ compared to the analytic values. In fact, in Eq. (2.3.5.3) the *n-value* is not present since the critical state model is adopted. At high amplitudes, the AC losses decrease with decreasing *n-value*, while at low amplitudes they increase with decreasing the *n-value*. This explains the curves shown in Fig. 2.4.7.3: if the *n-value* is set to a theoretically infinite value, the numerical and the analytic results should converge. All curves seem to converge for an intermediate I_m value around 0.4. Furthermore, the non-superconducting layers of the coated conductors seem to have a marginal role since there are no significant differences between the "*Whole_tape*" (coloured circles) and the "*SC_only*" (empty squares) cases.
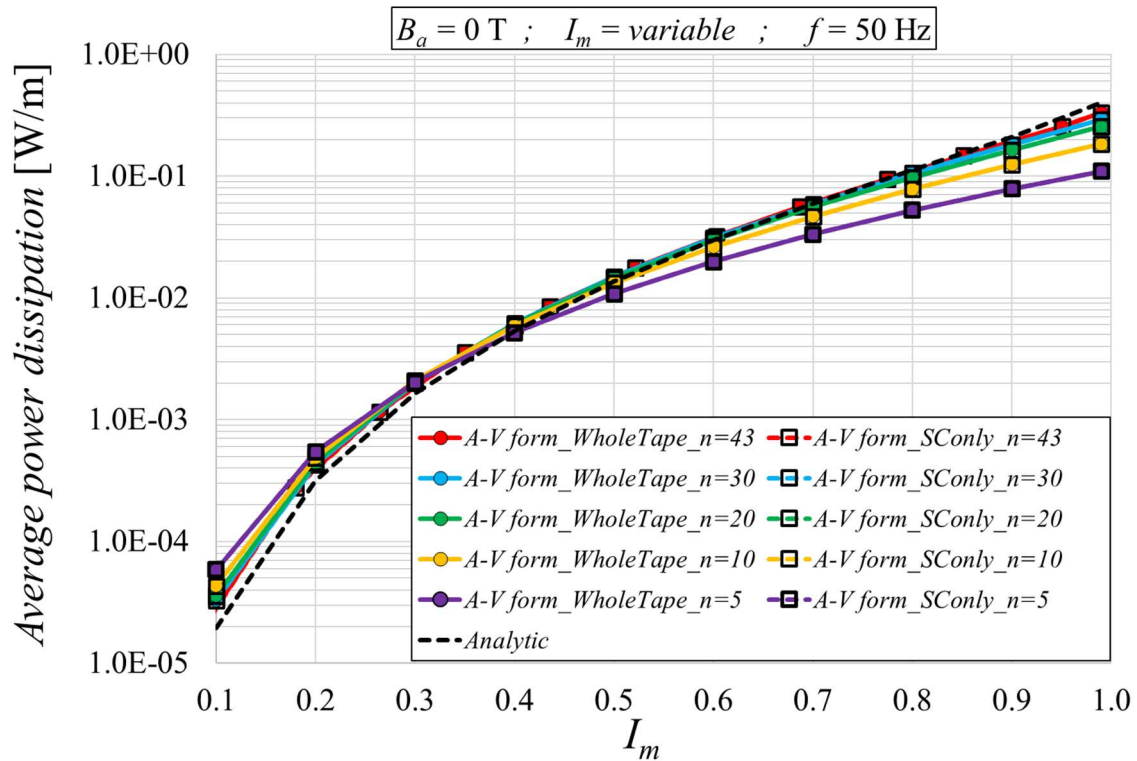
Figure 2.4.8.1. *Average power dissipation in the SuNAM SCN04 tape due to an AC transport current varying I_m and with a frequency set to 50 Hz. Different n-values are tested. The figure is in semi-logarithmic scale.*

Fig. 2.4.8.2 presents the AC losses due to an AC transport current for different frequencies and setting the I_m value to 0.7. It is evident that the greater the *n-value*, the better the agreement with the analytical curve. For low *n-values*, the AC losses dependence on frequency increases. There is a good agreement between the results of the "*Whole_tape*" and "*SC_only*" models for frequencies up to 1 kHz. Above this frequency, the two cases start to diverge. The losses for the "*Whole tape*" case are greater, meaning that the non-superconducting layers of the tape are generating significant losses at high frequencies. This phenomenon enhances the lower the *n-*

value: when $n = 43$, the maximum difference between the two cases at $f = 10$ kHz is around 4%, while when $n = 5$, this difference increases at 51%.
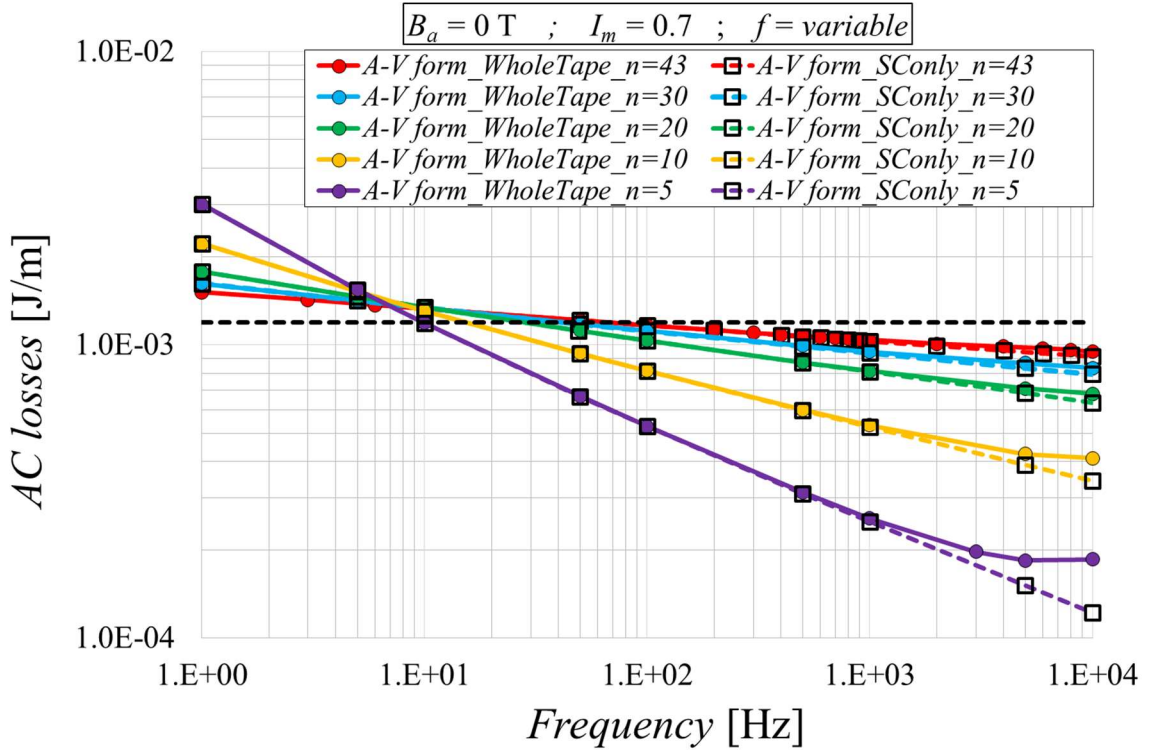
Figure 2.4.8.2. *AC losses in the SuNAM SCN04 tape due to an AC transport current with I_m set to 0.7 and varying the frequency. Different n-values are tested. The figure is in logarithmic scale.*

Fig. 2.4.8.3 shows the average power dissipation due to an AC external magnetic field perpendicular to the tape main face for different amplitudes and frequency at 50 Hz. As for the previous cases, when the *n-value* is higher the convergence with the analytic formulation improves, since Eq. (2.4.7.1) is written adopting the critical state model for the tape. At high fields, the losses are greater when the *n-value* is lower; when $B_a = 2$ T, the losses computed with $n = 5$ are 5 times higher than the analytic case. At the opposite for low fields, the AC losses are greater when the *n-value* are higher but the difference between the various cases is not so evident. All curves converge when the field amplitude is around 0.05 T. The "*Whole_tape*" and the "*SC_only*" curves converge, except for minor differences when the field amplitude is high (> 1 T).
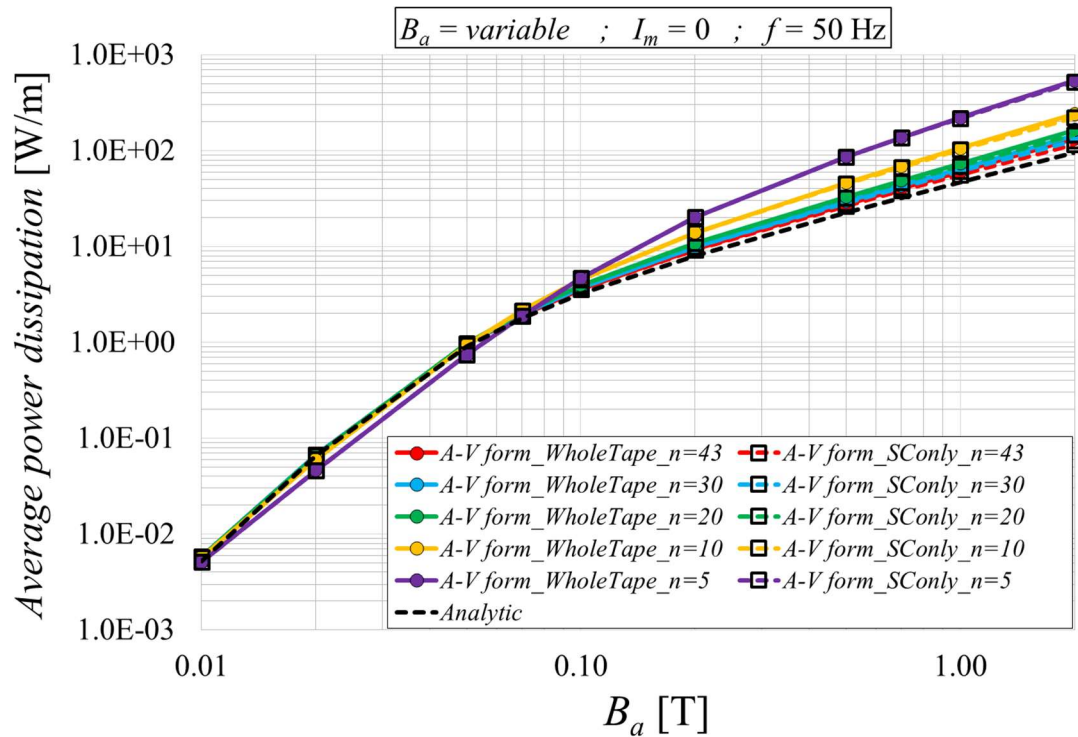
Figure 2.4.8.3. *Average power dissipation in the SuNAM SCN04 tape due to an AC external magnetic field perpendicular to the tape main face with different amplitudes and a frequency set to 50 Hz. Different n-values are tested. The figure is in semi-logarithmic scale.*
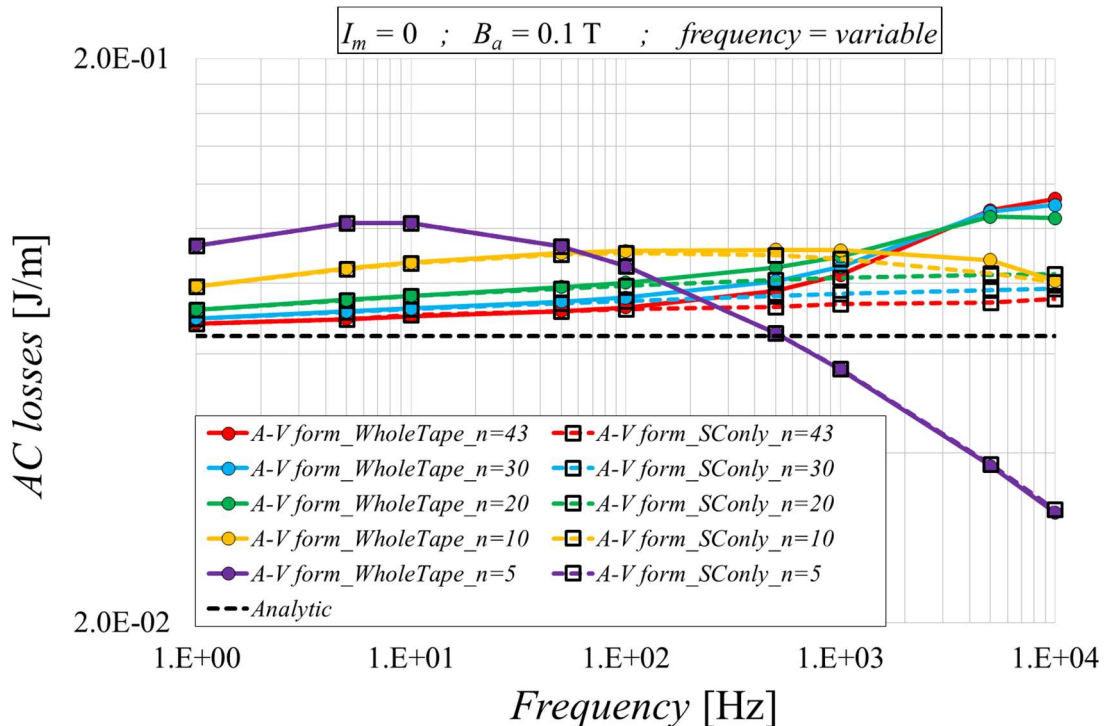
Figure 2.4.8.4. *AC losses in the SuNAM SCN04 tape due to an AC external magnetic field perpendicular to the tape main face with different frequencies and an amplitude set to 0.1 T. Different n-values are tested. The figure is in logarithmic scale.*

Fig. 2.4.8.4 presents the AC losses due to a perpendicular magnetic field for different frequencies and setting the field amplitude to 0.1 T. In this case, the AC losses dependence on the *n-value* is more complex. For high *n-values* ($n = 43$) the numerical losses converge with the analytical values for low frequencies, diverging when the frequency exceeds certain threshold frequencies, as already shown in Fig. 2.4.7.10. When the *n-value* decreases, the curves maximum shifts towards lower frequencies: this means that the losses are higher already at low frequencies, they present a maximum at intermediate frequencies and then they decrease at high frequencies. Furthermore, the agreement between the "*Whole_tape*" and the "*SC_only*" cases improves when the *n-value* reduces. For very low *n-values* ($n = 5$) the two cases are in perfect agreement for every frequency tested.

Secondly, a study is carried out regarding the AC losses dependence on the thickness of the superconducting layer inside the coated conductor. It is interesting to check whether the results of a 2-D model or a 1-D approximation agree when the tape aspect ratio is modified, increasing the tape thickness. In particular, it is proved that the tape critical current density increases as the superconducting layer thickness increases, but there is a limit beyond which no further improvement is achieved [140]. Surely, even if the current density does not vary, an increase in the thickness of superconductor increases the tape critical current. In this sense, many manufactures are developing tapes with incremented superconducting layer thickness to increase the tape electrical performances [141]. For this study, the geometry of the *SuNAM SCN04* tape is implemented in the model, increasing the thickness of the superconducting tape by factors 2 and 3 while leaving all the other geometrical parameters unchanged. The current density of the tape is not modified; therefore, when the thickness of the superconducting layer is doubled the critical current is doubled accordingly.

Fig. 2.4.8.5 shows the average power dissipation produced in the tape by the presence of an AC transport current with different amplitudes and a frequency set to 50 Hz. The geometry of the *SuNAM SCN04* tape is implemented in the model, applying the following multiplication factors to the superconducting layer thickness: 1 (expressed as "*SCthick_x1*", corresponding to the real geometry), 2 (expressed as "*SCthick_x2*") and 3 ("expressed as "*SCthick_x3*"). The tape critical current is changed accordingly in the model: this means that the same I_m values correspond to different current amplitudes in the various cases. For example, $I_m = 0.7$ in the "*SCthick_x1*" case ($I_c = 242$ A) corresponds to an amplitude of 269.4 A, while in the "*SCthick_x2*" case ($I_c = 482$ A) $I_m = 0.7$ corresponds to an amplitude of 338.8 A. As expected, the power dissipation rises as the superconductor thickness increases since also the transport current rises. The discrepancies with the analytical results, representing the 1-D approximation case (thin film), are not particularly influenced by the superconductor thickness: for all cases, the numerical values result around 30% higher when $I_m = 0.1$ and 30% lower when $I_m = 1$, compared to the analytic results and they converge for intermediate amplitudes.
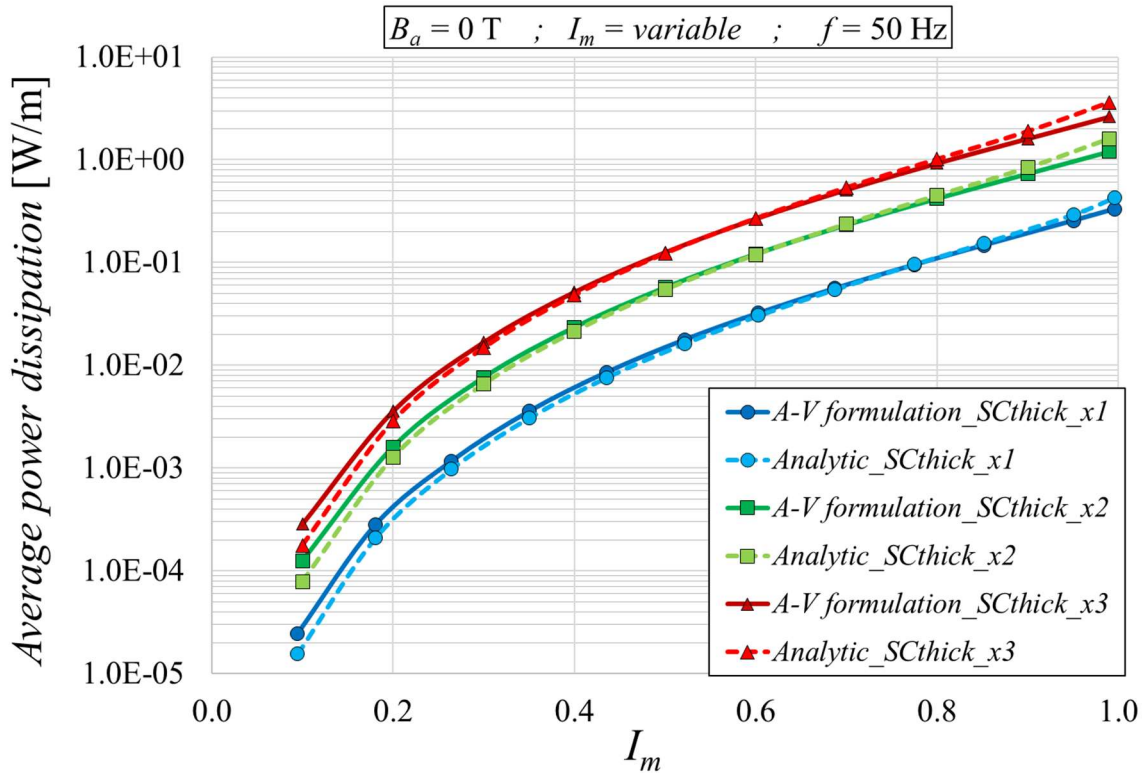
Figure 2.4.8.5. *Average power dissipation due to an AC transport current with different amplitudes and a frequency set to 50 Hz. The geometry of the SuNAM SCN04 tape is implemented, varying the superconducting layer thickness only. The figure is in semi-logarithmic scale.*
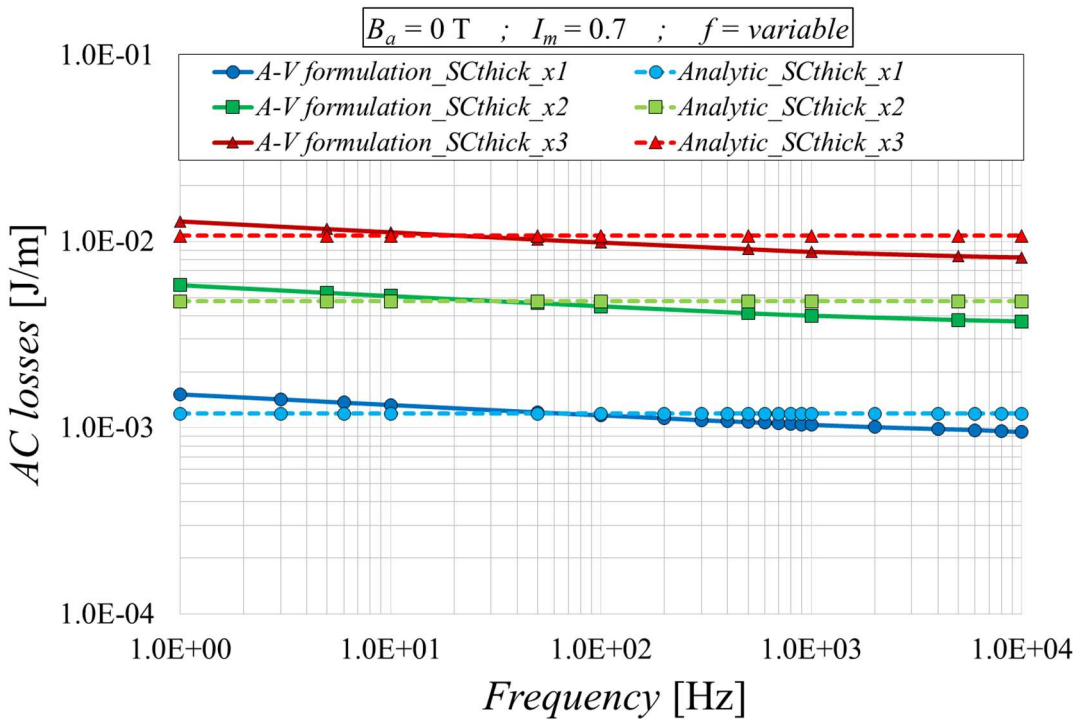

Figure 2.4.8.6. *AC losses due to an AC transport current with $I_m = 0.7$ and with different frequencies. The geometry of the SuNAM SCN04 tape is implemented, varying the superconducting layer thickness only. The figure is in logarithmic scale.*

Fig. 2.4.8.6 presents the AC losses generated in the tape by the presence of an AC transport current with $I_m = 0.7$ and for different frequencies. The losses are greater, the higher is the superconducting layer thickness. The differences between the numerical and analytical results weakly depends on the thickness of the superconducting layer. For $f = 1$ Hz, the numerical values are 1.27, 1.22 and 1.20 times higher than the analytic results going from the thinner to the thicker case, while for $f = 10$ kHz, they are 1.26, 1.28 and 1.31 time lower than the analytic results going from the thinner to the thicker case.
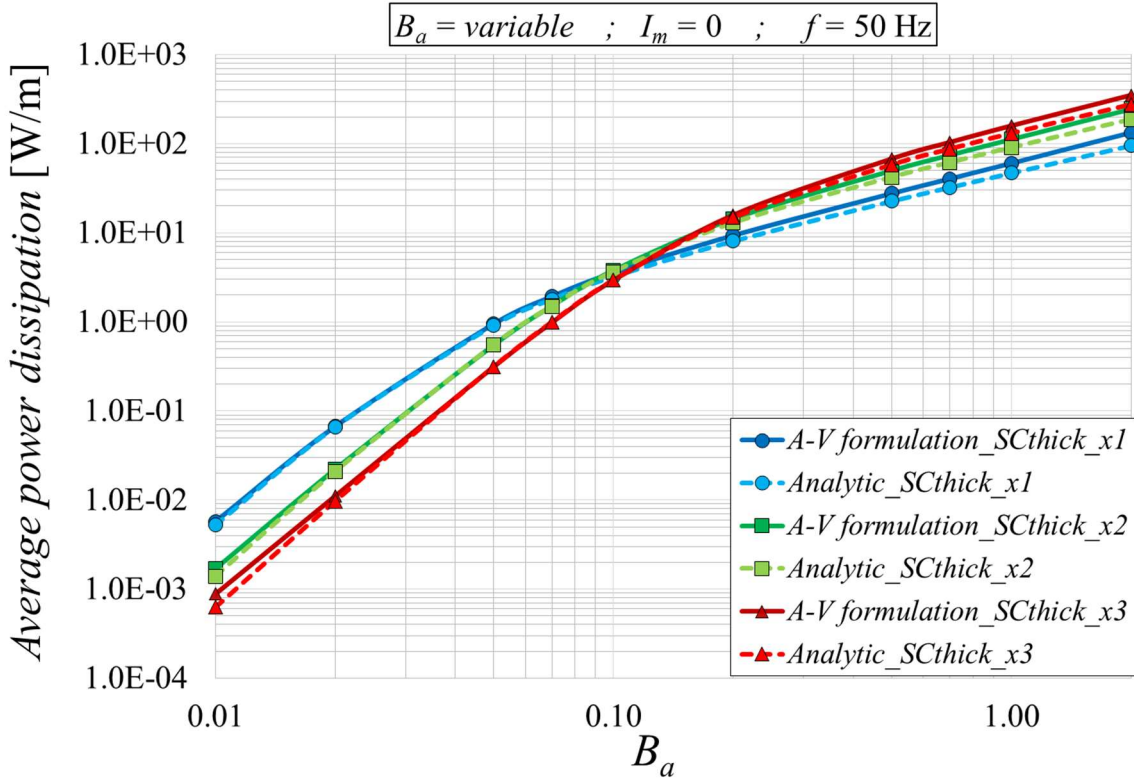
Figure 2.4.8.7. *Average power dissipation due to an AC external magnetic field perpendicular to the tape main face with a frequency set to 50 Hz and for different amplitudes. The geometry of the SuNAM SCN04 tape is implemented, varying the superconducting layer thickness only. The figure is in logarithmic scale.*

Fig. 2.4.8.7 shows the AC losses generated in the tape by the presence of an AC external magnetic field perpendicular to the tape main face, with a frequency of 50 Hz and for different amplitudes. In this case, a thicker superconductor layer does not always correspond to greater losses, since no transport current is involved. At high frequencies, the losses are greater when the thickness of the superconductor is higher, while at low frequencies the losses for smaller thicknesses are greater. However, the difference between the numerical and the analytical results is not very influenced by the thickness of the superconducting layer. For $B_a = 10$ mT, the numerical values are 1.11, 1.22 and 1.41 times higher than the analytic results going from the thinner to the thicker case, while for $B_a = 2$ T, they are 1.40, 1.31 and 1.28 time higher than the analytic results going from the thinner to the thicker case.

Fig. 2.4.8.8 presents the AC losses generated in the tape by the presence of an AC external magnetic field perpendicular to the tape main face, with an amplitude of 0.1 T and a variable

frequency. The dependence of the losses on the thickness of the superconducting layer is more complex in comparison to the previous cases. When the superconductor thickness is doubled compared to the real geometry (*SCthick_x2*), the losses computed with the numerical model are the highest at low frequencies and they better converge with their corresponding analytical curve at high frequencies compared to the real geometry case (*SCthick_x1*). When the superconductor thickness is tripled (*SCthick_x3*), the numerical losses are the lower than in the other cases and the curve decreases going from low to high frequencies.
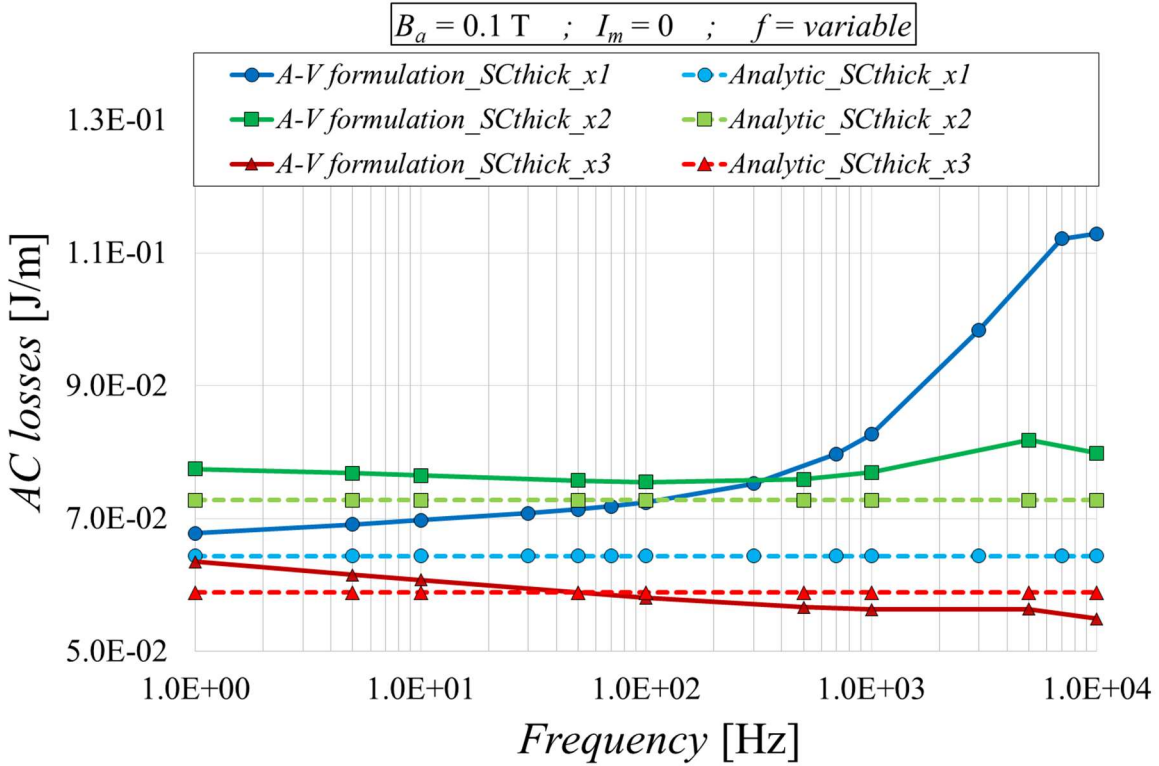
Figure 2.4.8.8. *AC losses due to an AC external magnetic field perpendicular to the tape main face with an amplitude of 0.1 T and a variable frequency. The geometry of the SuNAM SCN04 tape is implemented, varying the superconducting layer thickness only. The figure is in semi-logarithmic scale.*

Understanding the relation between the analytical curves in the three cases is not trivial. Fig. 2.4.8.9 presents the AC losses calculated with the analytic formulation of Eq. (2.4.7.1) for different magnetic field amplitudes. In the abscissa axis, the tape critical current is presented: an increase in the critical current with a fixed current density corresponds to a coated conductor with a thicker superconducting layer. It is evident that the relation between the AC losses and the tape critical current is strongly affected by the amplitude of the magnetic field. For low fields, the losses decrease with increasing the critical current while the trend is opposite for high fields. Following the curve referred to the 0.1 T case, it is possible to understand the relation between the 3 analytical curves of Fig. 2.4.8.8. It is important to remember that, since the analytic formulation considers only the tape width which is kept constant, the sheet critical current density used in the formula (in A/m) increases with increasing the critical current. The formula does not consider any variation in the thickness of the coated conductor and the only way to analyse tapes with different critical currents but constant current densities is to modify

the tape width. On the contrary, with a 2-D approximation it is possible to take into account a constant current density without varying the tape width.
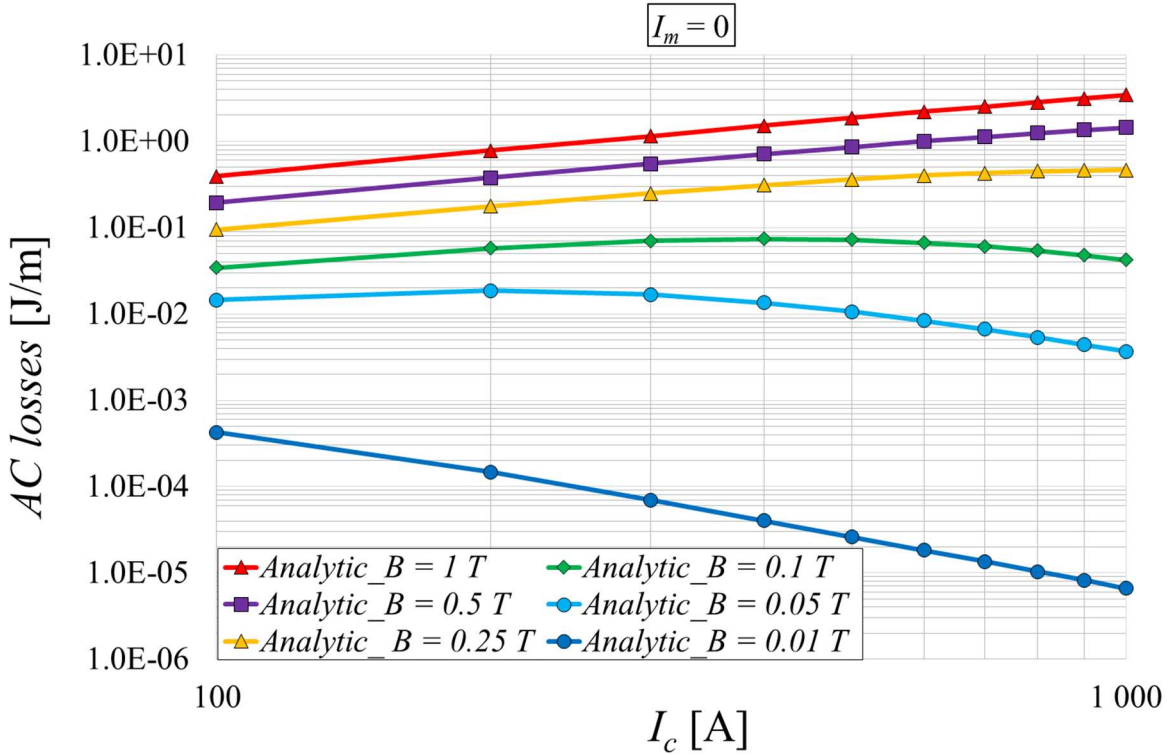
Figure 2.4.8.9. *Analytic trend of the AC losses due to an external magnetic field perpendicular to the tape main face with different amplitudes. The geometry of the SuNAM SCN04 tape is implemented but different critical currents are investigated. The figure is in logarithmic scale.*

The conclusion of this parametric study is that for the analysed cases, the differences between the computation of the transport AC losses using a 1-D or 2-D approximation are minor, since the aspect ratio of the tape remains extremely high even if the superconducting layer thickness is tripled. Further studies should be carried out increasing largely this thickness (maybe more than 10 times), to understand if some discrepancies start to be notable, but these cases have little practical interest. There are no considerable variations even for the magnetization losses varying the field amplitude, while some discrepancies are notable between the 1-D and the 2-D cases when the frequency dependence of the external field is analysed, when the critical current is doubled or tripled. Further studies about this topic might be useful.

2.4.9. Convergence analysis for the calculation of AC losses with the numerical model based on the A-V formulation

This section describes the convergence analysis carried out to set the parameters of the numerical model based on the *A-V* formulation for the calculation of the AC losses.

To reduce the computational burden of the numerical model, it is possible to discretize the tape cross-section with a smaller number of elements N. Anyway, a convergence criterion has to be

reached to ensure an adequate level of accuracy. The comparison with the analytical result is selected in order to present the "normalized" results for different operating conditions, although it should be recalled that the numerical results coincide only for specific operating conditions. In the following, the convergence is assumed to be reached when a further variation of the selected parameter (increasing or decreasing, depending on the study) produces a variation of the value reported on the ordinate axis lower than 5%.

First, a convergence study is performed about the number of elements used to discretize the superconducting layer of the tape. Due to the high aspect ratio of the tape, it makes sense to test separately the discretization across the tape width and thickness. Fig. 2.4.9.1 shows the difference between the numeric and the analytic results, varying the number of points discretizing the superconducting layer across the tape width. The figure reports the results for four different cases: high current and low frequency ($I_m = 0.8$ and $f = 50$ Hz), high current and high frequency ($I_m = 0.8$ and $f = 1$ kHz), low current and low frequency ($I_m = 0.5$ and $f = 50$ Hz) and low current and high frequency ($I_m = 0.5$ and $f = 1$ kHz). These four cases cover a broad range of real operating conditions. A number of elements equal to 200 is chosen (reported in Table 8.2) since it is assumed that for this value the convergence is reached.
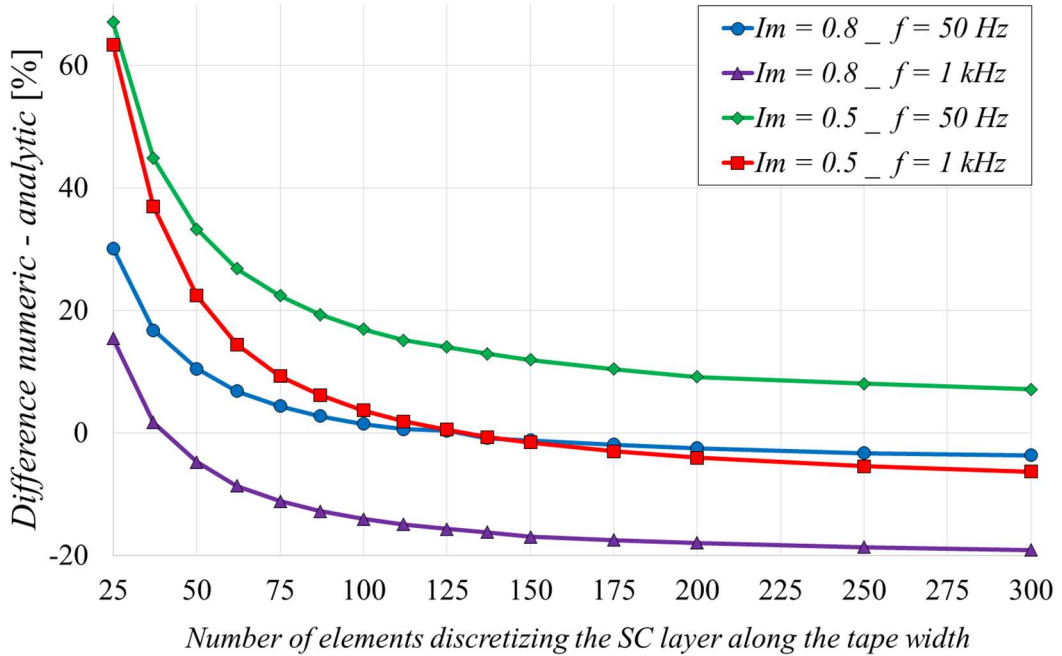
Figure 2.4.9.1. Convergence analysis regarding the number of elements discretizing the superconducting layer across the tape width, for different operating conditions.

Then, the number of elements discretizing the superconducting layer across the tape thickness is considered. Fig. 2.4.9.2 reports the difference between the numeric and the analytic results for the same four cases of Fig. 2.4.9.1. A number of elements equal to 4 is chosen (reported in Table 2.4.7.2) since it is assumed that for this value the convergence is reached.
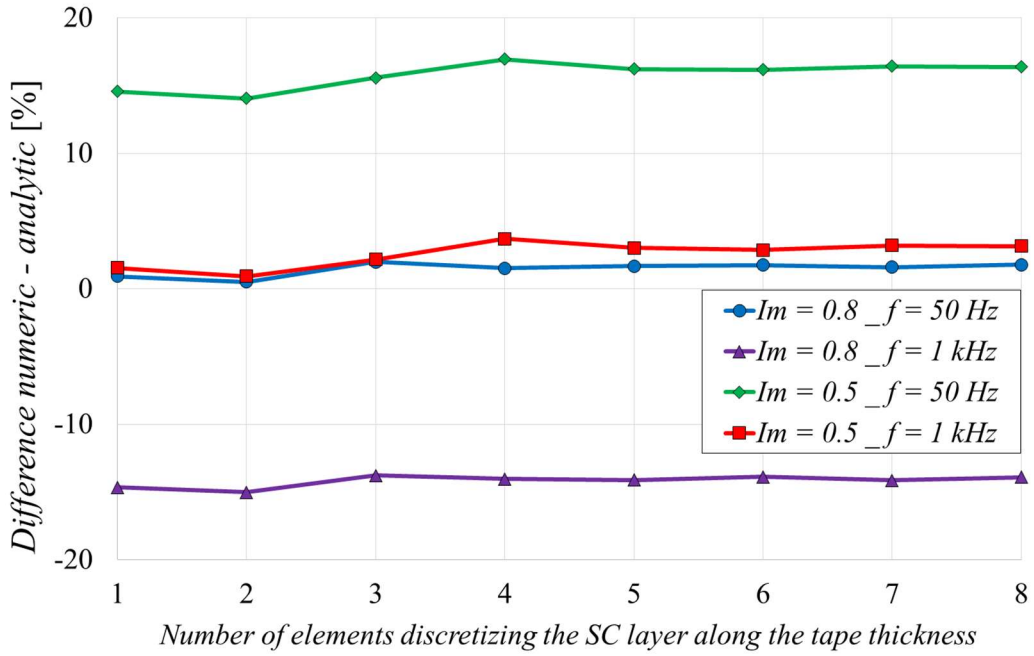
Figure 2.4.9.2. *Convergence analysis regarding the number of elements discretizing the superconducting layer across the tape thickness, for different operating conditions.*
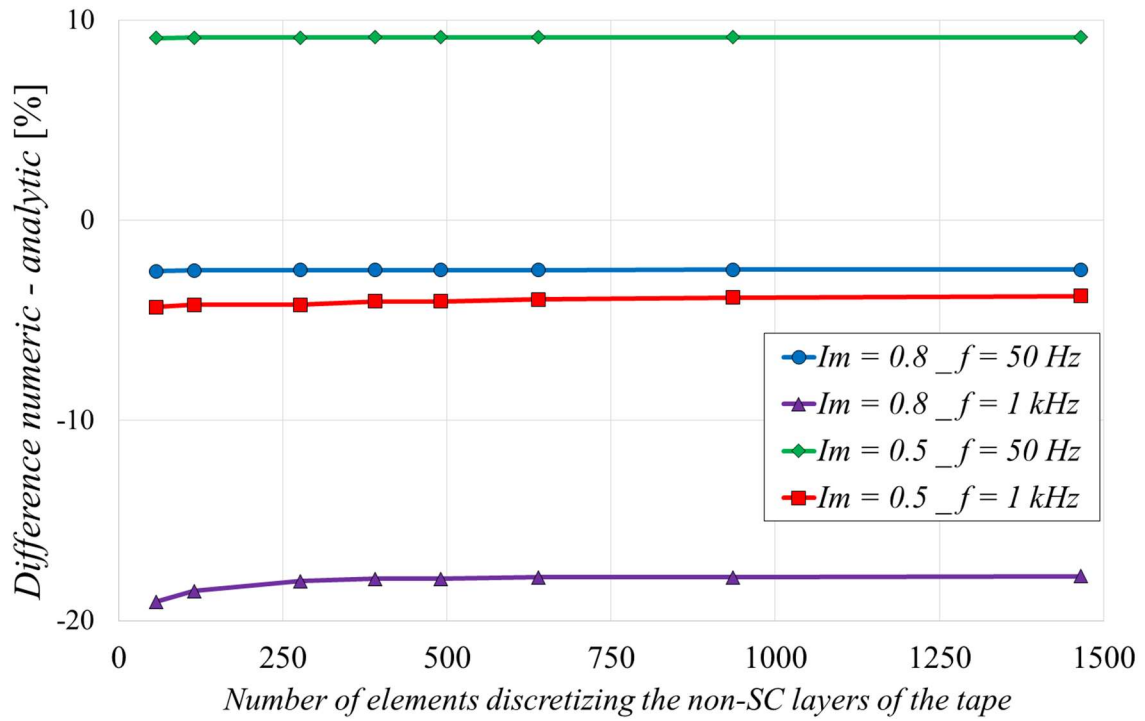
Figure 2.4.9.3. *Convergence analysis regarding the number of elements discretizing the non-superconducting layers of the tape, for different operating conditions.*

Subsequently, a convergence study is performed regarding the number of elements discretizing the non-superconducting layers of the tape. Fig. 2.4.9.3 shows the difference between the numeric and the analytic results for the same four cases of Fig. 2.4.9.1. A number of elements

equal to 390 is chosen (reported in Table 2.4.7.2) since it is assumed that for this value the convergence is already reached. The discretizing elements are distributed among the different layers of the coated conductors dependently on their thickness, but the analysis of convergence for the single non-superconducting layer is not shown in this work.

It is worth noting that A_{int_i} depends on the tape length (see Eq. (2.4.4.5)). An analysis is performed in this regard since if the tape length inserted into the calculations is too short, the convergence might not be reached. Moreover, this length also represents the minimum length of the tape so that the portions close to the current leads, where the induced currents are closing and the system variables are no longer independent of the z-coordinate, can be still considered sufficiently short with respect to the total length of the tape. Therefore, considering valid the simplifying hypotheses of Eq. (2.4.1.1) even in these lateral regions is acceptable, since their contribution to the tape loss is minor. Fig. 2.4.9.4 shows the results of this study, carried out for the same four cases presented above. It is possible to assume that convergence is reached for tapes longer than 10 cm. This value is in accordance with the length set experimentally and presented in the following sections.
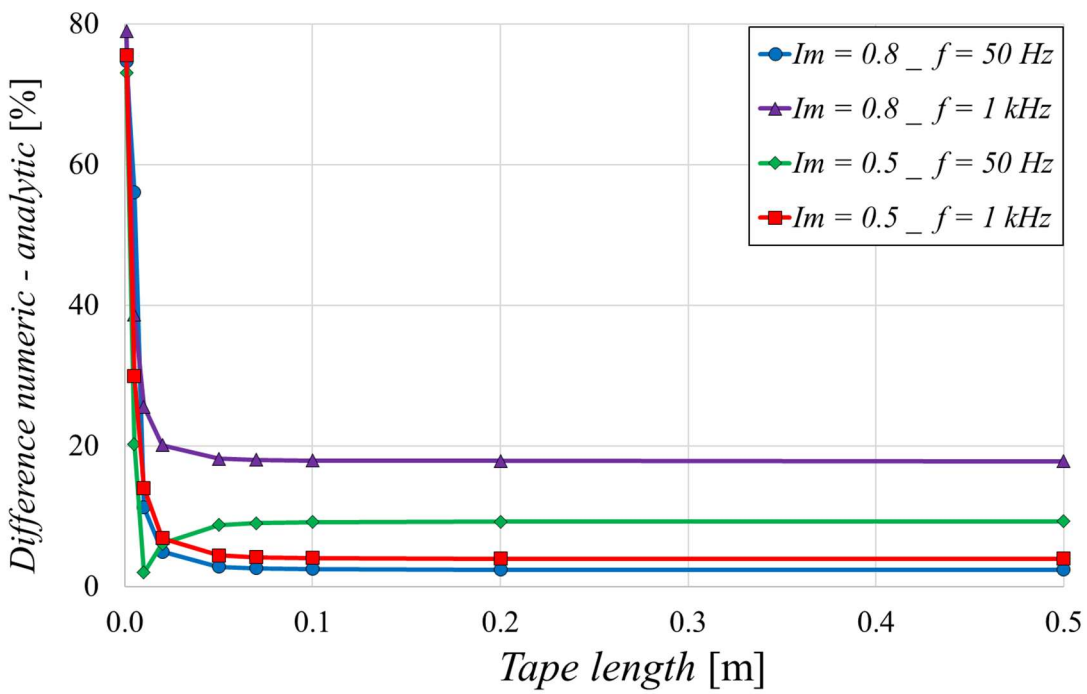
Figure 2.4.9.4. Convergence analysis regarding the tape length, for different operating conditions.

In parallel, the convergence has to be reached also for the time domain. First, reducing the number of simulated periods reduces the calculation time; however, it is necessary to ensure that the system has reached the regime conditions for at least the last period simulated. As an example, Fig. 2.4.9.5 shows the trend of the power $p(t)$ as a function of time (5 periods simulated), for the case with I_m set to 0.8 and frequency set to 50 Hz. It is worth noting that the loss profile is periodic, except for the first period. The first half-period shows considerably lower loss values while its second half-period reaches a slightly higher peak as compared to

the following ones. It is decided to use a total number of periods equal to 2, since the convergence is reached for the second period. The same study was repeated for different frequencies and I_m values, leading to the same conclusion.
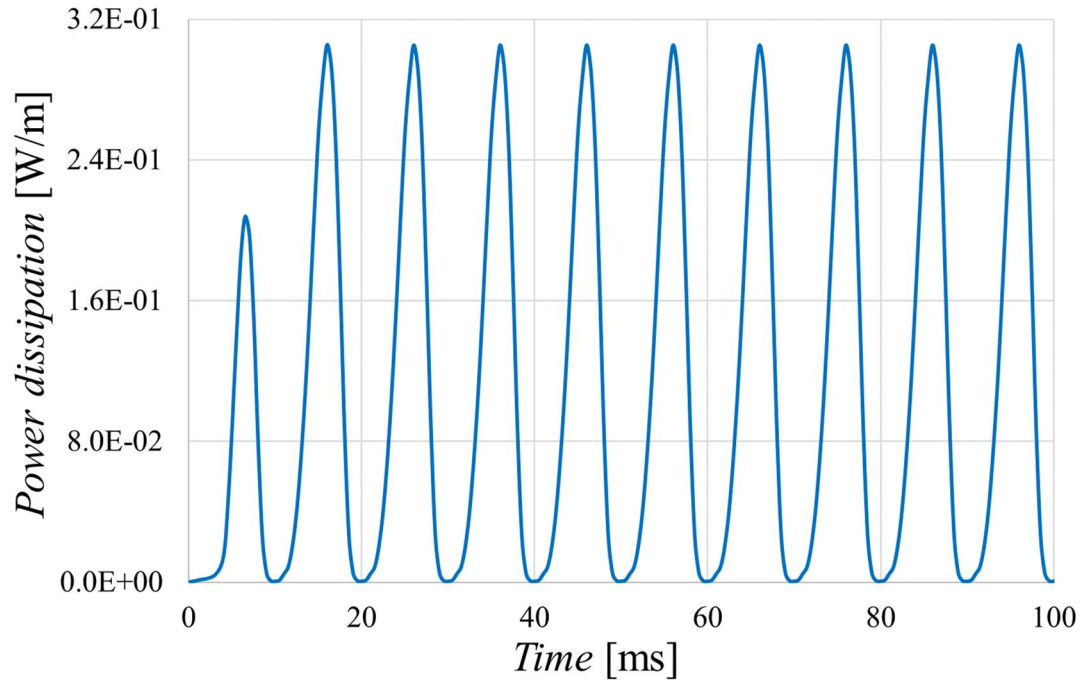
Figure 2.4.9.5. *Power dissipation during time (5 periods simulated) for the case with I_m set to 0.8 and the frequency set to 50 Hz.*
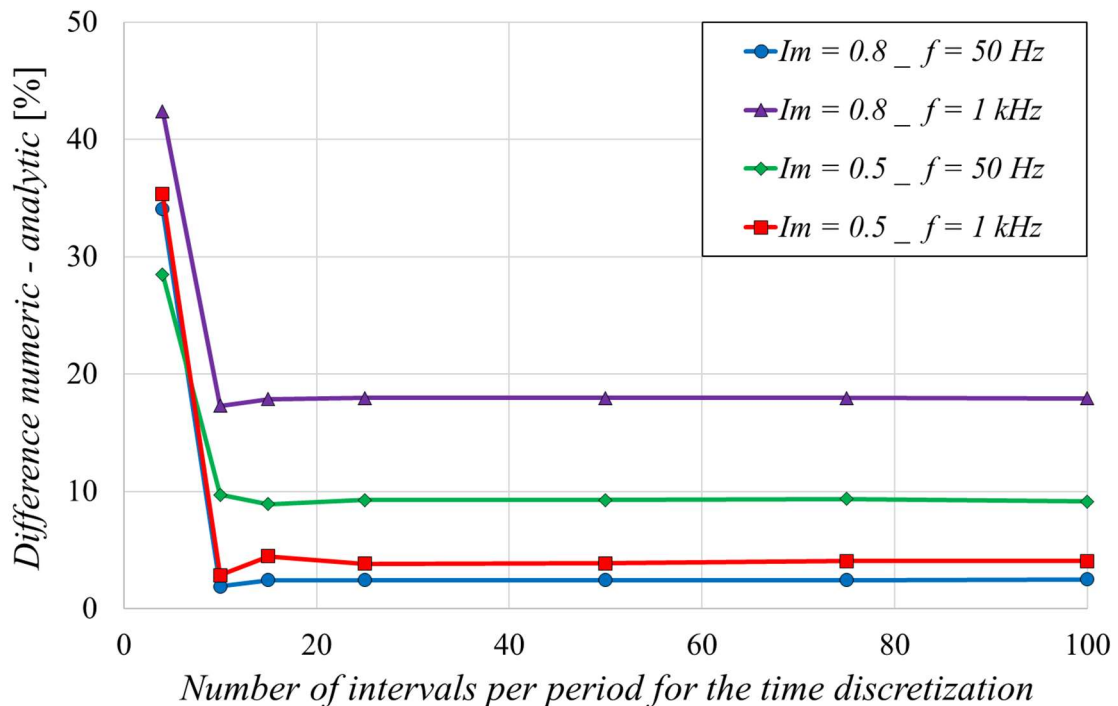
Figure 2.4.9.6. *Convergence analysis regarding the integration time step per period, for different operating conditions.*

Finally, the refinement of the integration time step is analysed since it affects the size of the matrices and the number of iterations. Fig. 2.4.9.6 shows the difference between the numeric and the analytic results, as a function of the number of interval chosen for the time discretization. The integration time step in the simulations is set to a precautionary value of 1/100 of the period, since for that number of intervals the regime conditions are reached. It is worth noting that this parameter applies only for the AC losses calculation. In *Section 2.4.10*, a convergence analysis for the calculation of the corrective factors is presented, showing a different minimum integration time step to reach convergence for this parameters.

2.4.10. Results about the corrective factors due to the experimental set-up configuration

This section presents the results obtained with the numerical model about the corrective factors due to the different measurement configurations for AC losses in coated conductors. The two set-up configurations are described in *Section 2.4.2* (simply referred in the following plots as "*No Compensation*") and *Section 2.4.3* (simply referred in the following plots as "*Compensation*"). Eq. (2.4.5.11) is used to compute the corrective factor for the case without compensation ($\eta_{per\ unit}(\alpha)$) and with the voltage taps twisted together at a certain distance α from the tape middle axis (outside the tape region). Eq. (2.4.6.1) is used to calculate the corrective factor for the case with compensation ($\gamma_{per\ unit}(\beta)$) and the minimization of the area of the voltage measurement circuit as a function of the distance β from the tape middle axis (inside the tape region).

Since the purpose of the corrective factors is precisely to "correct" the experimental results in order to eliminate from the measurement the contribution due to the voltage taps configuration, the analysis described in this section focuses only on operating conditions reproducible at the *University of Bologna*. To date, the application of an AC magnetic field on a sample of HTS tape is not possible in the laboratory, but only the effect of an AC transport current can be investigated. Therefore, the analysis of the corrective factors focuses on operating conditions in which the external magnetic field is null. Future studies may involve a more complex system of AC sources.

From Fig. 2.4.10.1 to Fig. 2.4.10.4, the corrective factor $\eta_{per\ unit}(\alpha)$ is shown (red dashed lines) varying the value of α from $-3w$ to $-\frac{w}{2}$ (the left edge of the tape). The same figures present also the corrective factor $\gamma_{per\ unit}(\beta)$ (blue solid lines) varying the value of β from $-\frac{w}{2}$ (the left edge of the tape) to $+\frac{w}{2}$ (the right edge of the tape). Four different operating conditions are tested: $I_m = 0.9$ and $f = 50$ Hz (high current and low frequency), $I_m = 0.9$ and $f = 1$ kHz (high current and high frequency), $I_m = 0.5$ and $f = 50$ Hz (low current and low frequency), $I_m = 0.5$ and $f = 1$ kHz (low current and high frequency). These cases cover a broad range of operating conditions and give an overall idea of the behaviour of the system.
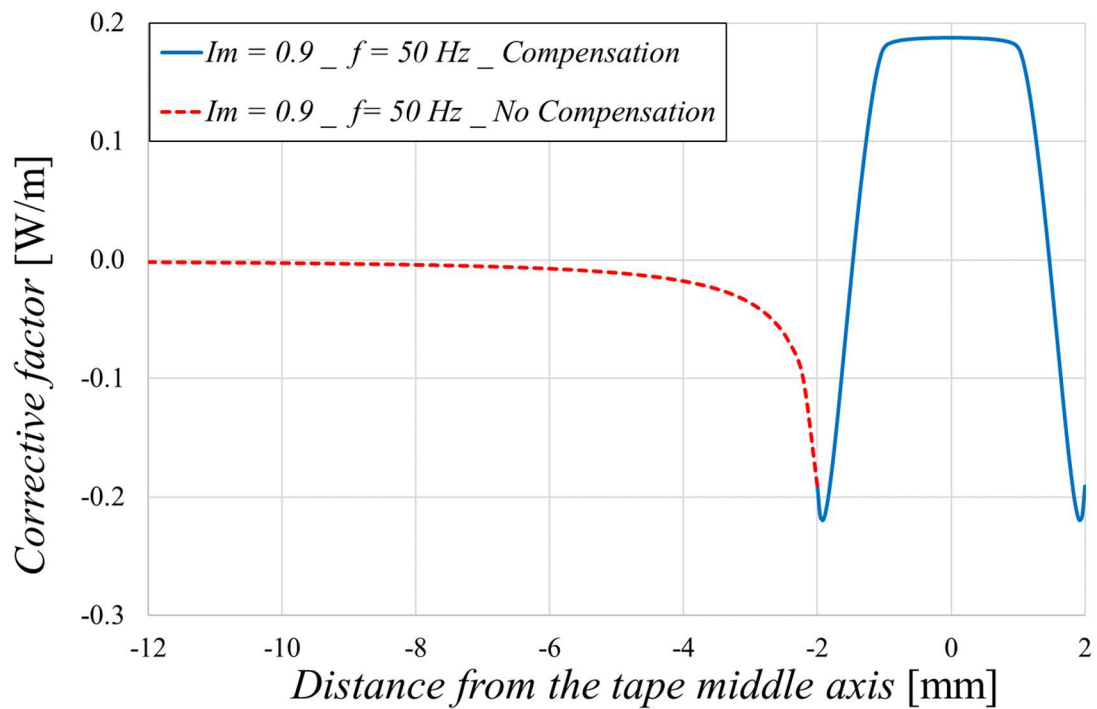
Figure 2.4.10.1. *Corrective factors* $\eta_{per\ unit}(\alpha)$ *(red dashed line) and* $\gamma_{per\ unit}(\beta)$ *(blue solid line), for the case with* I_m *= 0.9 and f = 50 Hz. The values are presented in W/m.*
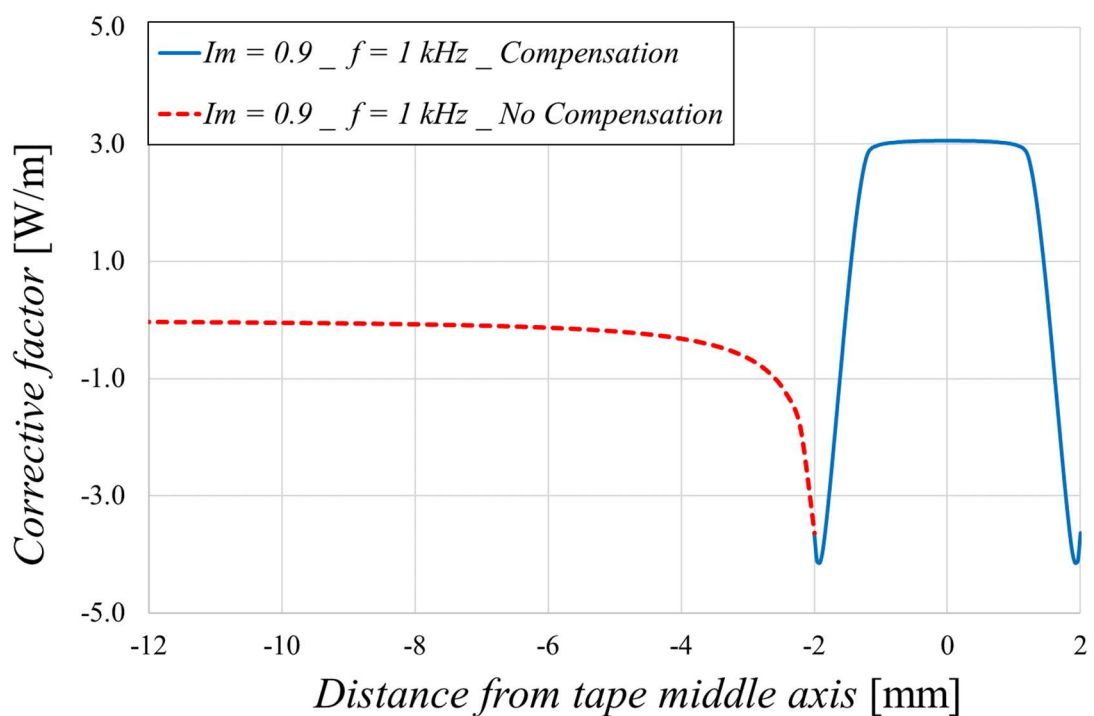
Figure 2.4.10.2. *Corrective factors* $\eta_{per\ unit}(\alpha)$ *(red dashed line) and* $\gamma_{per\ unit}(\beta)$ *(blue solid line), for the case with* I_m *= 0.9 and f = 1 kHz. The values are presented in W/m.*
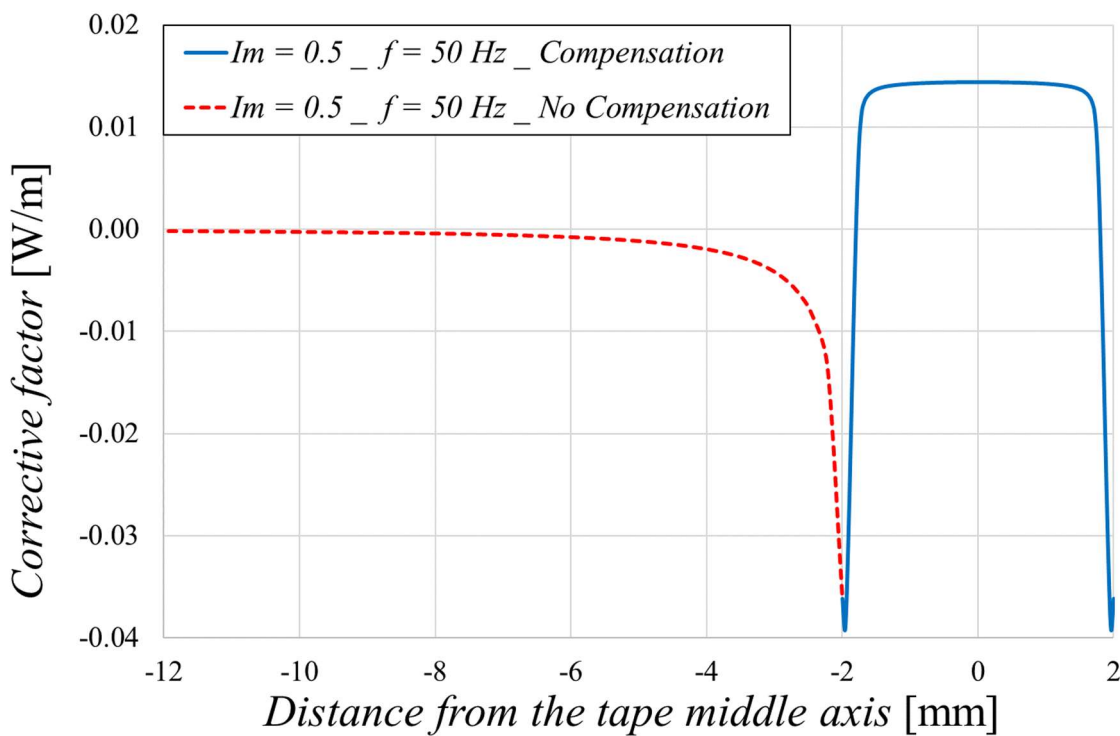
Figure 2.4.10.3. *Corrective factors $\eta_{per\ unit}(\alpha)$ (red dashed line) and $\gamma_{per\ unit}(\beta)$ (blue solid line), for the case with $I_m = 0.5$ and $f = 50$ Hz. The values are presented in W/m.*
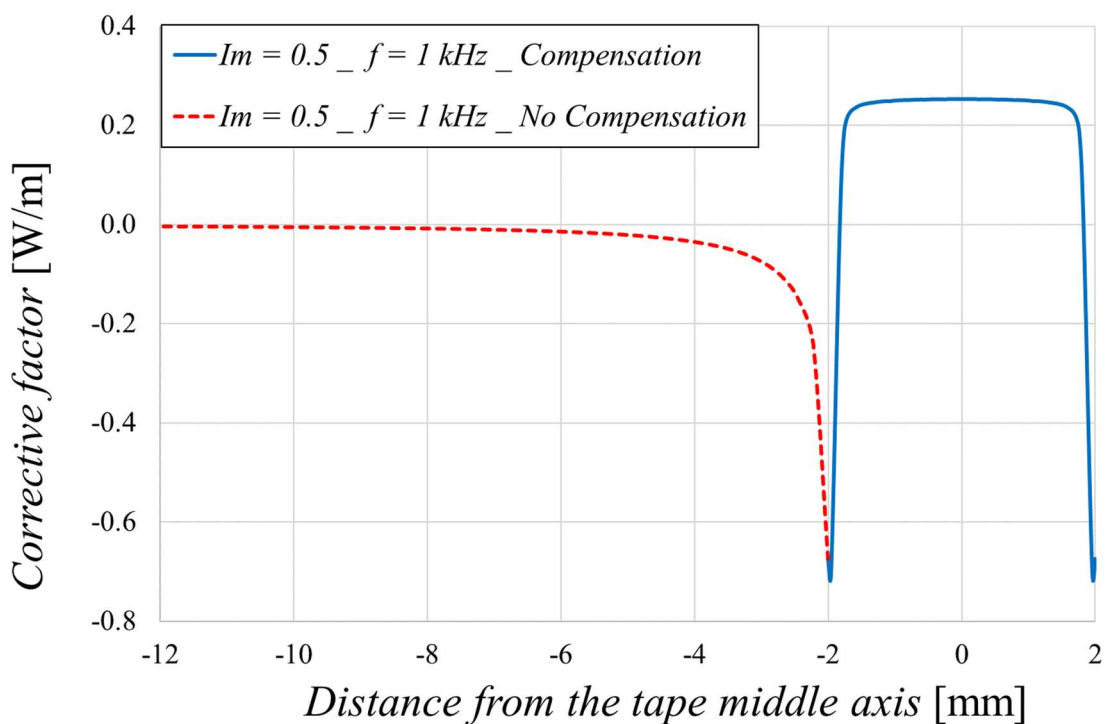
Figure 2.4.10.4. *Corrective factors $\eta_{per\ unit}(\alpha)$ (red dashed line) and $\gamma_{per\ unit}(\beta)$ (blue solid line), for the case with $I_m = 0.5$ and $f = 1$ kHz. The values are presented in W/m.*

Comparing the cases with the same current but different frequencies (Fig.s 2.4.10.1 – 2.4.10.2 and Fig.s 2.4.10.3 – 2.4.10.4), the amplitude of both corrective factors increases when the frequency rises. At the same time, comparing the cases with the same frequency but different current amplitudes (Fig.s 2.4.10.1 – 2.4.10.3 and Fig.s 2.4.10.2 – 2.4.10.4), the amplitude of both correction factors increases when the current rises. These trends reflect the dependencies of AC losses on both current and frequency, as already explained in *Section 2.4.7.*

It is worth noting how the corrective factor $\eta_{per\;unit}$ assume negative values only, as it should be since a sign minus is present at the beginning of Eq. (2.4.5.11). Thus, in this configuration (without compensation) the measured AC losses are higher as compared to the real value and the corrective factor represents how much the measurements should be decreased to converge to the real value. Moreover, the corrective factor $\eta_{per\;unit}$ rises when the distance from the tape edge increases, converging to a null value when the distance is set to infinite. A null value corresponds to the case where no correction is needed and the experimental configuration does not affect the measured losses. The worst condition, intended as the case where the corrective factor $\eta_{per\;unit}$ reaches its maximum, occurs when both voltage taps are twisted at a distance equal to the half-width of the tape.

On the other end, the corrective factor $\gamma_{per\;unit}$ has a different behaviour. It presents a plateau in the middle of the tape, meaning that there are several distances β for which the measurement system influences equally the measured losses. The width of this plateau seems larger for lower currents and poorly influenced by the frequency. A larger plateau allows to relax the precision criteria with which the measuring and compensation circuits are positioned, since even if the taps are soldered at a minimal distance from the tape middle axis, the corrective factor is not particularly influenced. Contrariwise to the case without compensation, the corrective factor $\gamma_{per\;unit}$ assumes positive values in the plateau region. This means that for this voltage taps configuration, the measured AC losses are lower compared to the real value. The corrective factor represents how much this measured value should be increased to converge to the real value. The maximum positive value reached by $\gamma_{per\;unit}$ decreases when the current drops. There might be cases where it reaches negative values, thus the previous assumption should be verified testing cases with even lower current amplitudes. Furthermore, the curves for both corrective factors are perfectly symmetrical compared the tape middle axis, as expected. The right part of the curve for the corrective factor $\eta_{per\;unit}$ is not shown in the figures, but its symmetrical trend is verified.

It is useful to present the same corrective factors as a percentage compared of the real AC losses value calculated with the numerical model. That helps to understand the influence of the experimental measurement system on the measured AC losses. The results are presented from Fig. 2.4.10.5 to 2.4.10.8 for the same four cases tested previously.
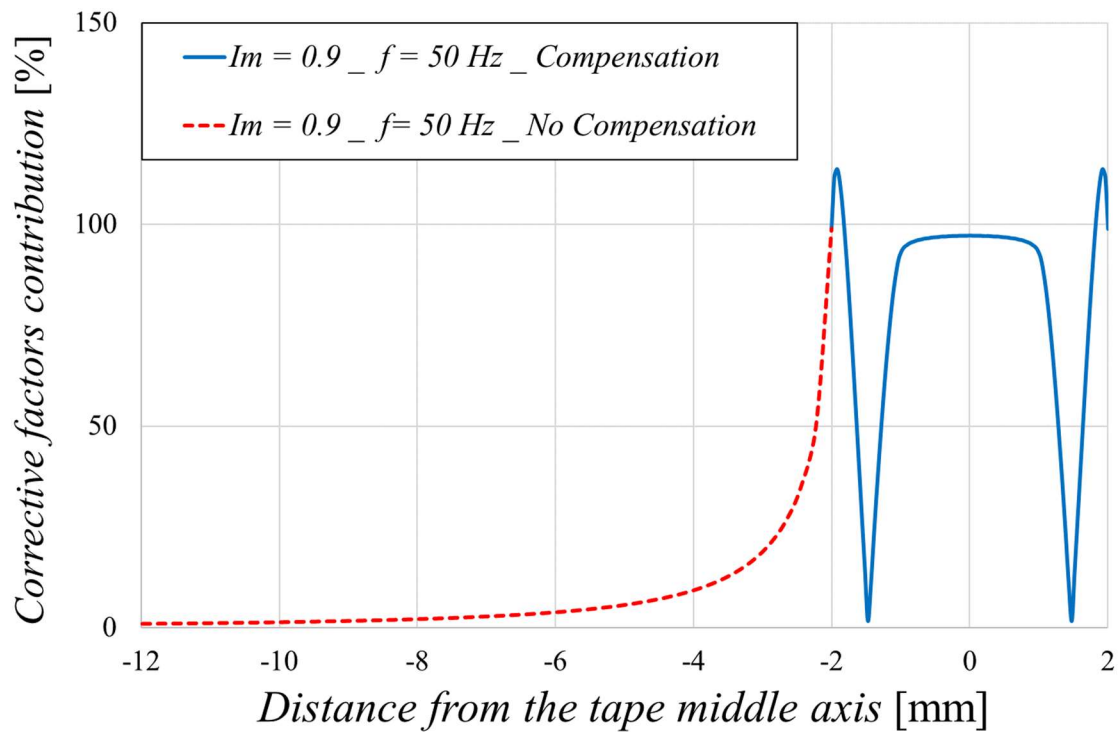
Figure 2.4.10.5. *Corrective factors $\eta_{per\ unit}(\alpha)$ (red dashed line) and $\gamma_{per\ unit}(\beta)$ (blue solid line), for the case with $I_m = 0.9$ and $f = 50$ Hz. The values are presented as a percentage of the desired AC losses value.*
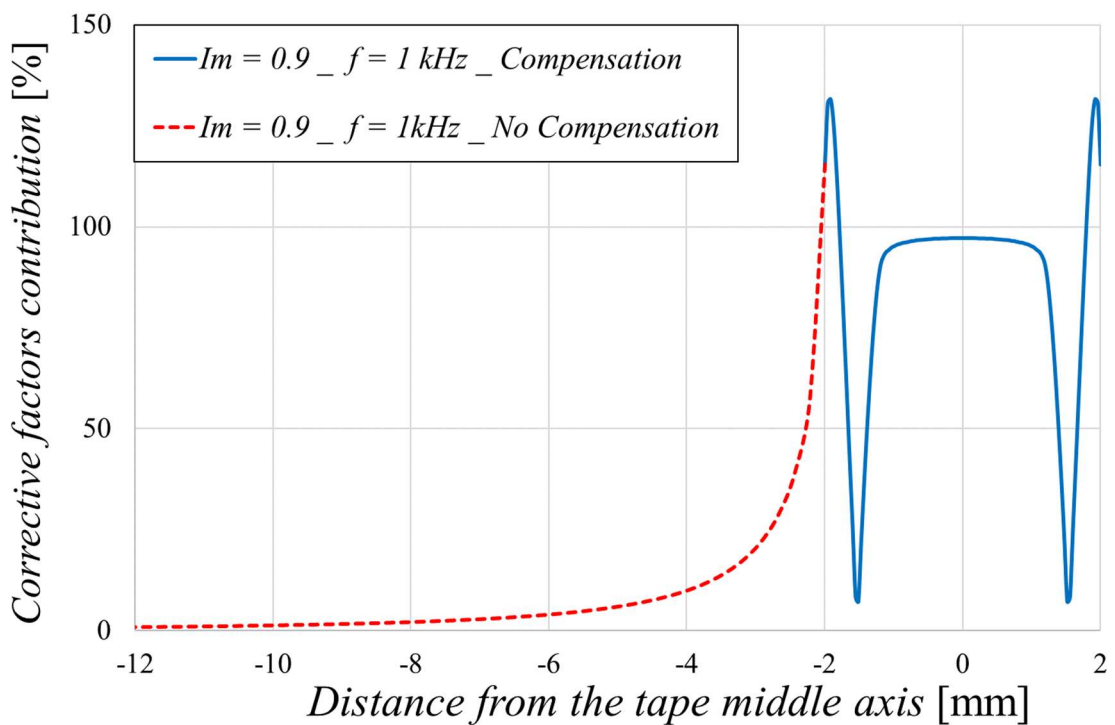

Figure 2.4.10.6. *Corrective factors $\eta_{per\ unit}(\alpha)$ (red dashed line) and $\gamma_{per\ unit}(\beta)$ (blue solid line), for the case with $I_m = 0.9$ and $f = 1$ kHz. The values are presented as a percentage of the desired AC losses value.*
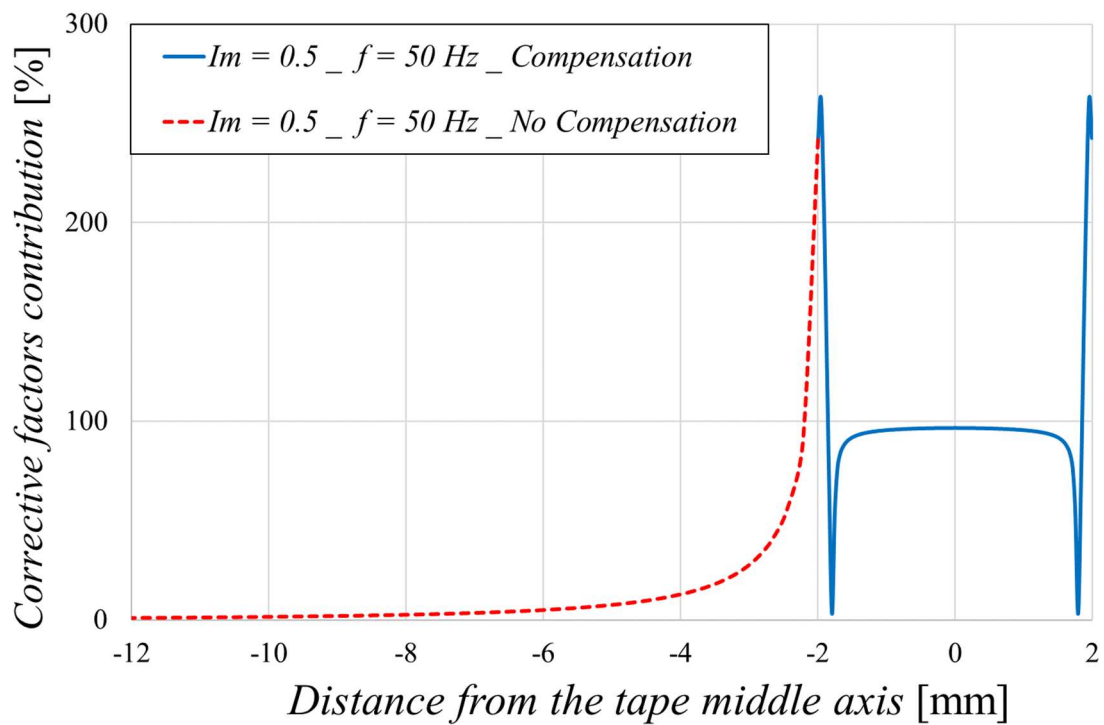
Figure 2.4.10.7. *Corrective factors $\eta_{per\ unit}(\alpha)$ (red dashed line) and $\gamma_{per\ unit}(\beta)$ (blue solid line), for the case with $I_m = 0.5$ and $f = 50$ Hz. The values are presented as a percentage of the desired AC losses value.*
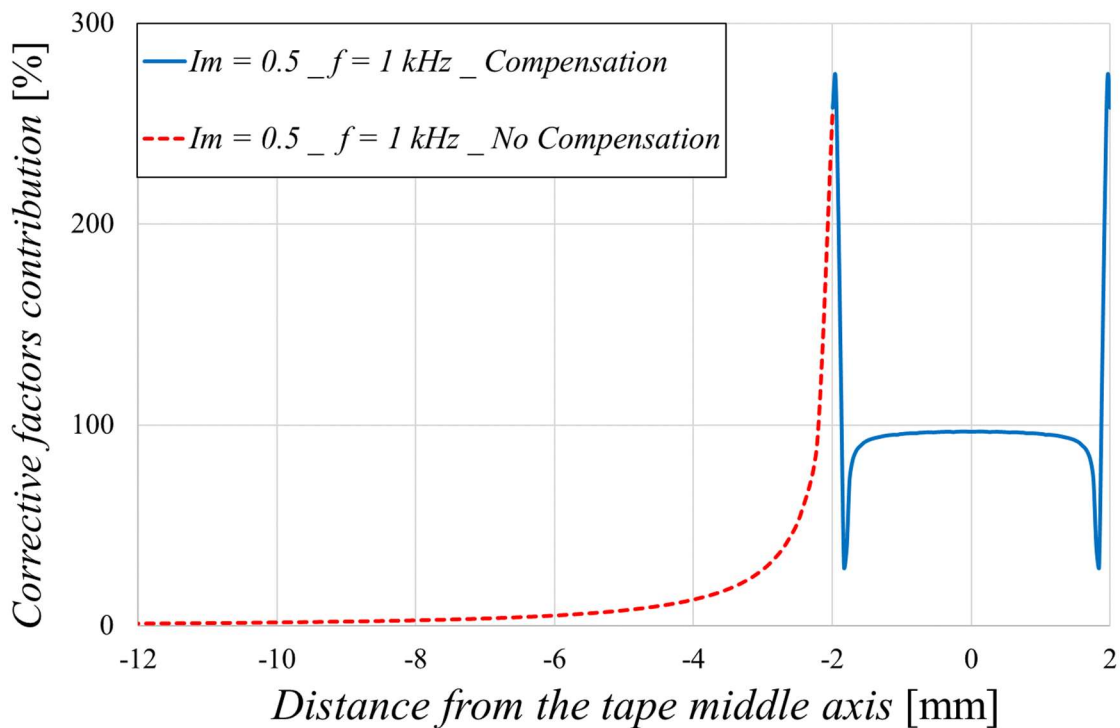
Figure 2.4.10.8. *Corrective factors $\eta_{per\ unit}(\alpha)$ (red dashed line) and $\gamma_{per\ unit}(\beta)$ (blue solid line), for the case with $I_m = 0.5$ and $f = 1$ kHz. The values are presented as a percentage of the desired AC losses value.*

As it can be noticed, the contribution of the corrective factor $\eta_{per\ unit}$ is maximum when both voltage taps are twisted together at one of the tape edges. Then, its influence drops exponentially leading to almost negligible values when $\alpha = 3w$; for larger distances (theoretically infinite), the contribution becomes null. In *Section 3.4*, the experimental results obtained for different α values are shown to confirm that as α increases, the effect of the measurement system is reduced. This trend agrees with the considerations reported in the literature [121 – 126]. In the same papers, it is suggested to set α to $\frac{3}{2}w$. This distance would be a good compromise between a theoretically infinite value (to eliminate completely the dependence on the measurement system) and a very short distance to avoid the creation of a large loop area where the electromagnetic noise can link. With reference to the *SuNAM SCN04* tape ($w = 4$ mm) this compromise value is equal to 6 mm. In the figures presented above, when α is equal to 6 mm the contribution of the experimental set-up on the measured AC losses is in the range between 3.8% and 5.2%. This contribution can be considered minor, but neglect it could be an excessive approximation. A parallel study should be carried out, in which the signals acquired through the voltage measuring circuit at different α values are compared, to understand whether the electromagnetic noise increases with increasing α ($> \frac{3}{2}w$) and when its impact becomes problematic. However, this study is complex and highly dependent on the accuracy of the data acquisition system and the quality of the post-processing technique adopted to eliminate the noise: it would be difficult to draw general conclusions. Therefore, in this work it is simply assumed that twisting the voltage taps farther than $\frac{3}{2}w$ might not lead to a consistent advantage in terms of corrective factor reduction, while it might induce higher electromagnetic noise into the acquisition circuit. $\alpha = \frac{3}{2}w$ is adopted as the correct distance when this specific configuration is selected. This allows a better comparison with the results of other laboratories which use the same value of α.

As previously mentioned, the corrective factor $\gamma_{per\ unit}$ has a different trend. There is a plateau region in the middle of the tape where the influence of the measurement configuration is almost independent of the value of β. The width of the central plateau is larger for lower amplitudes and not affected by the frequency. In this region, the contribution of the set-up is slightly lower than 100%, meaning that the measured losses are almost double compared to the desired value. Then, just outside this region the corrective factor as an abrupt reduction down to 0% for specific values of β, which represents the case where the voltage circuit has no influence on the measured losses. Despite in some plots the blue line does not reach the 0% value, it is proved that refining the spatial discretization (increasing N_{int}), a specific value of β for which the corrective factor is null is found for all cases. Then, getting closer to the tape edges the corrective factor as a steep increase, and its contribution is higher than in the plateau region (more than 2.5 times higher for low currents). Finally, the trend of the $\gamma_{per\ unit}$ contribution has a new drop when β corresponds to the tape edges. When $\alpha = \beta = \pm\frac{w}{2}$ both corrective factors assume the same values, verifying the consistency of their formulations. It is worth noting that $\gamma_{per\ unit}$ contributes the most when the voltage taps are twisted very close to the tape edge but not exactly at $\beta = \pm\frac{w}{2}$, as it happens for $\eta_{per\ unit}$.

Comparing the two configurations described, the following conclusion are drawn. The configuration without compensation and voltage taps twisted together outside the tape is the one that allows to reduce consistently the impact of the measurement system to the total AC losses and to relax the precision criterion regarding the positioning of the voltage taps. If a sufficiently large distance from the tape edge is maintained, the influence of the measurement system is almost negligible, with minimal variations even if α is not measured with great accuracy. But the larger is α and the greater is the area in which external fluxes can link. This would require more precise acquisition systems and post-processing techniques to remove the electromagnetic noises. From the analysis carried out, it results that the value of α proposed in the literature, equal to $\frac{3}{2}w$, is a good compromise. However, the measurement system influences around $4 \div 5\%$ of the measured values (in the case of AC transport losses, depending on the operating conditions); this value should not be totally neglected. Therefore, it is suggested to realize a set-up with α close to $\frac{3}{2}w$, and to include the corrective factor $\eta_{per\ unit}$ in the calculations.

On the other hand, determining the contribution given by the configuration with compensation requires a higher precision in the realization of the set-up and in the measurement of the distance β. There is a central region of the tape where the contribution of the factor $\gamma_{per\ unit}$ is almost constant regardless of the precise location of the voltage taps soldering and twisting. In this region, the contribution is relevant (it influences the measured value by doubling it with respect to the desired value) and it cannot be neglected. Moreover, for narrow tapes, the width of this central region is limited (for the *SuNAM SCN04* tape, it is 3 mm wide for low current amplitudes and 2 mm wide for high amplitudes) and the precision required might be too high. It should be pointed out how, for this configuration, if both voltage taps are soldered and twisted at a specific value of β inside the tape (close to its edges, depending on the operating conditions) and if the compensation circuit is sufficiently similar to the measurement circuit, the contribution of $\gamma_{per\ unit}$ is null. Since this set-up minimizes the area in which the external flows can link, being able to solder the voltage taps at this unique β distance would represent an advantage over the configuration without compensation. However, in this case the measurement circuit should be realized with an extremely high precision. For narrow tapes for example, an error of only 0.2 mm in the soldering leads to an increase in the contribution of the measurement circuit up to 250%, for the tested cases. A too coarse or too extensive soldering could make it difficult to measure the exact point where the voltage taps are located and therefore the calculation of $\gamma_{per\ unit}$ can be misleading. For all these reasons, it is considered preferable to use the configuration without compensation, unless wide tapes are tested (12 mm or greater, for example) and/or the location of the voltage taps in the central region of the tape can be determined with a sufficient precision.
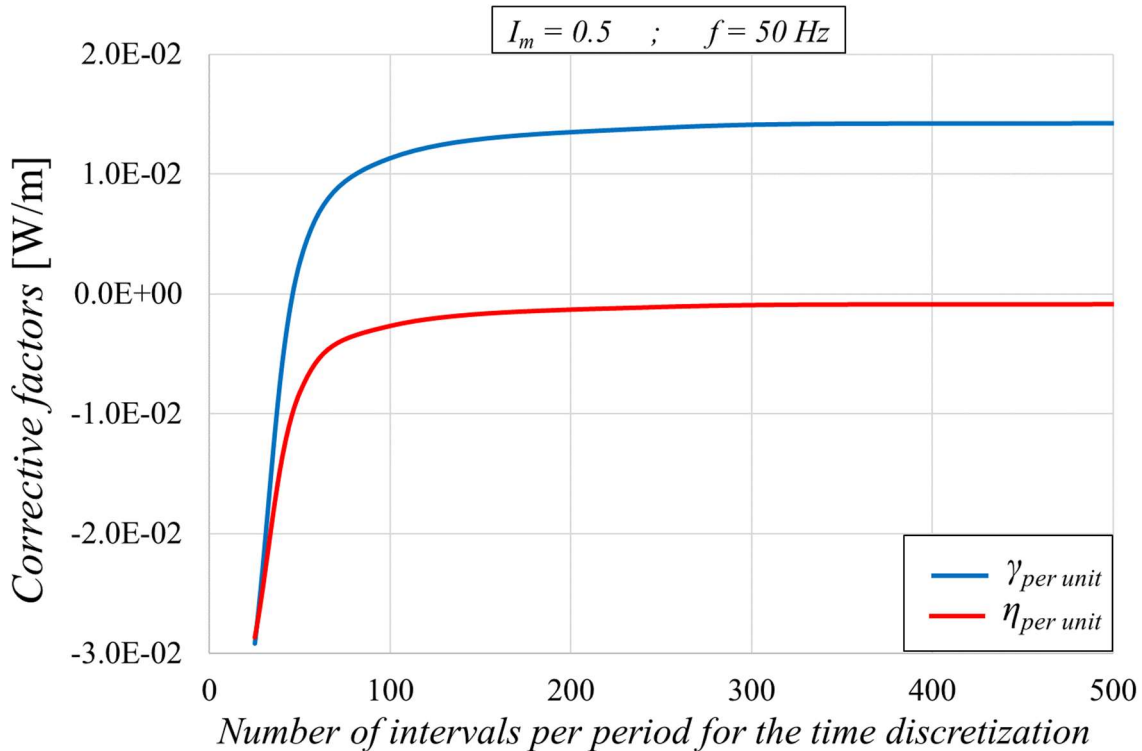
Figure 2.4.10.9. *Convergence analysis regarding the integration time step per period, for the* $\gamma_{per\ unit}$ *factor (with β = 0) and for the* $\eta_{per\ unit}$ *factor (with* $\alpha = \frac{3}{2}w$*).*

Lastly, a convergence analysis is carried out for the calculation of the corrective factors. The analysis for the majority of the parameters involved in their calculation have already been presented *Section 2.4.9*, but some further investigations are required regarding the integration time step per period. Fig. 2.4.10.9 shows the corrective factors varying the number of intervals per period. For the $\gamma_{per\ unit}$ factor, β is set to 0 (the tape middle axis), and for the $\eta_{per\ unit}$ factor, α is set to $\frac{3}{2}$w. For both corrective factors, the regime conditions are reached around 400 ÷ 500 intervals per period. It is worth noting how for the AC losses computation, a number of intervals per period equal to 100 is more than enough, as shown in Fig. 2.4.9.6. Since the increase in calculation time between 100 and 500 intervals per period is limited, it is convenient to use the higher number of intervals per period to ensure convergence for all parameters.

2.5.   *Numerical models comparison*

To compare the results of the numerical models presented in *Section 2.3* and *Section 2.4*, the characteristics of the same reference tape are implemented in both models. The tape selected is the *SuNAM SCN04* tape, already described. In the following, the *A-V* formulation is applied to both the "*Whole_tape*" and the "*SC_only*" cases. The *H*-formulation is applied to the "*Whole_tape*" case only, and this case is hereafter referred as "*H-formulation*" without further specifications.

For the *H*-formulation model, the number of mesh points across the width and thickness of the superconducting layer are set to 90 and 2, respectively. The total number of elements to

discretize the cross-section of the other layers is set to 4320, distributed between the different layers.

In Fig. 2.5.1, the average power dissipation due to an AC transport current computed with the two numerical models are compared. The current amplitude is varied and the frequency is set to 50 Hz. The difference between the results obtained with the two models is below 20% at low current amplitudes, decreasing below 2% when I_m approaches I_c. Fig. 2.5.2 presents a comparison of the power dissipation in each layer of the tape computed with both models. A good agreement is found also at the layer level.
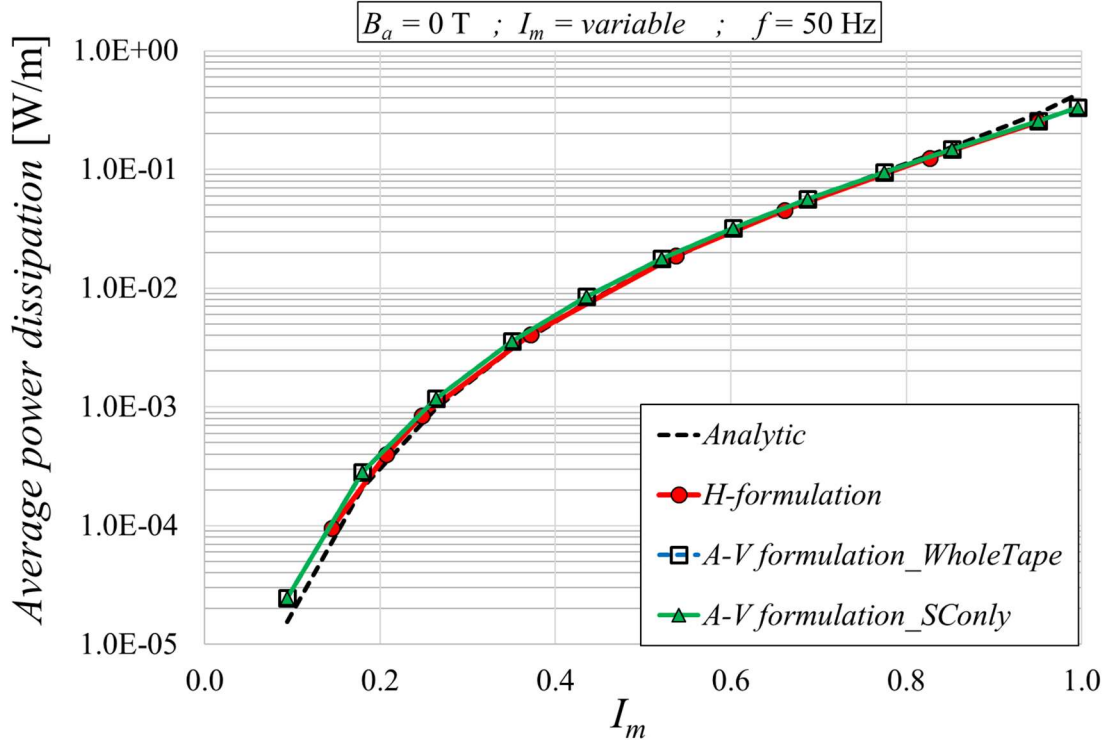
Figure 2.5.1. *Average power dissipation due to an AC transport current, computed with different formulations. The frequency is set to 50 Hz and I_m is varied. The figure is in semi-logarithmic scale.*
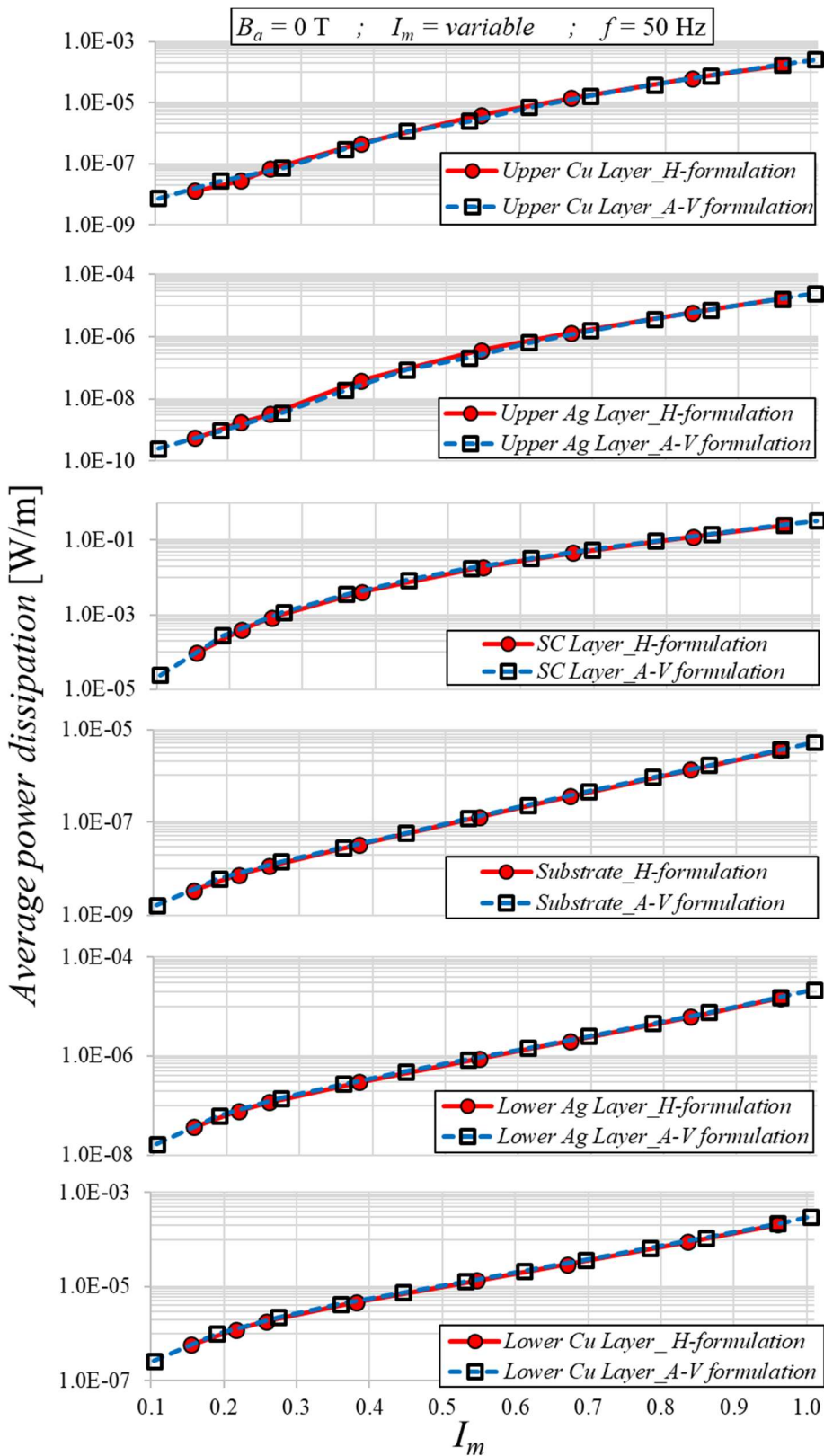
Figure 2.5.2. *Average power dissipation generated in each layer of the tape due to an AC transport current, computed with different formulations. The frequency is set to 50 Hz and I_m is varied. The figure is in semi-logarithmic scale.*

Fig. 2.5.3 shows the transport current AC losses obtained with both models when I_m is set to 0.7 and the frequency is varied. The results of the two models are in good agreement (less than 3% difference at low frequencies, up to less than 10% difference at f = 10 kHz). Moreover, the accordance is confirmed at the layer level, by the results presented in Fig. 2.5.4 in which the losses generated by each layer of the tape are presented.
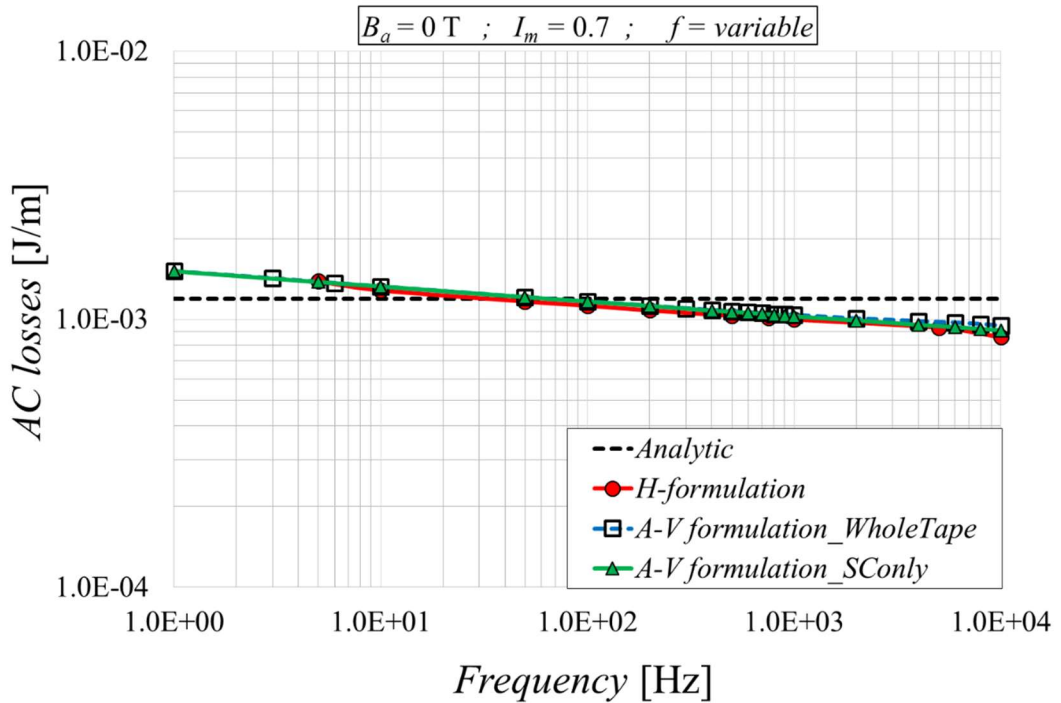
Figure 2.5.3. *Transport current AC losses, computed with different formulations. I_m is set to 0.7 and the frequency is varied. The figure is in logarithmic scale.*
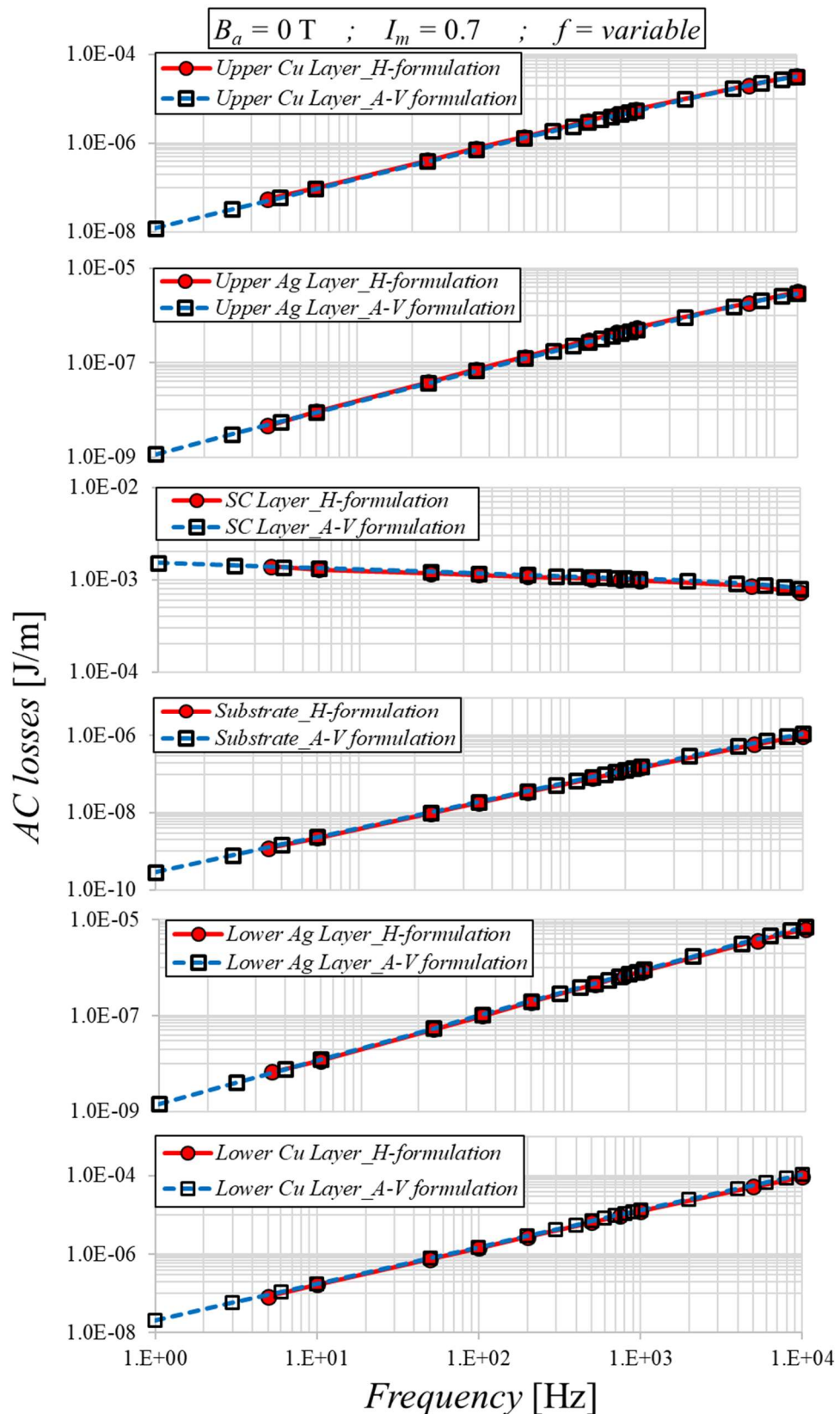
Figure 2.5.4. *Transport current AC losses generated in each layer of the tape computed with different formulations. I_m is set to 0.7 and the frequency is varied. The figure is in logarithmic scale.*

Fig. 2.5.5 presents the average power dissipation due to a perpendicular AC field, setting the field frequency to 50 Hz and varying its amplitude. The discrepancy between the results obtained with the two models is below 15% when B_a = 10 mT, decreasing below 1% already at B_a > 0.1 T. Fig. 2.5.6 shows the power dissipation produced in each layer of the tape. The agreement between the two models is confirmed also at the layer level.
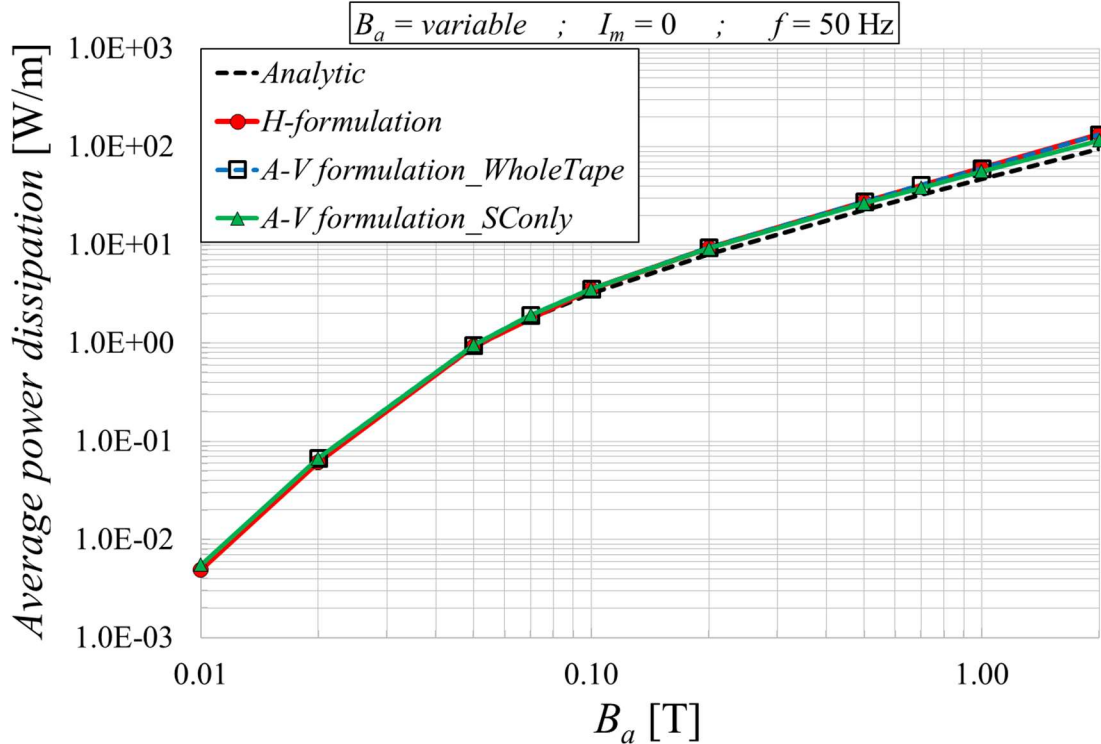
Figure 2.5.5. *Average power dissipation due to a perpendicular AC field, computed with different formulations. The frequency is set to 50 Hz and the field amplitude is varied. The figure is in logarithmic scale.*
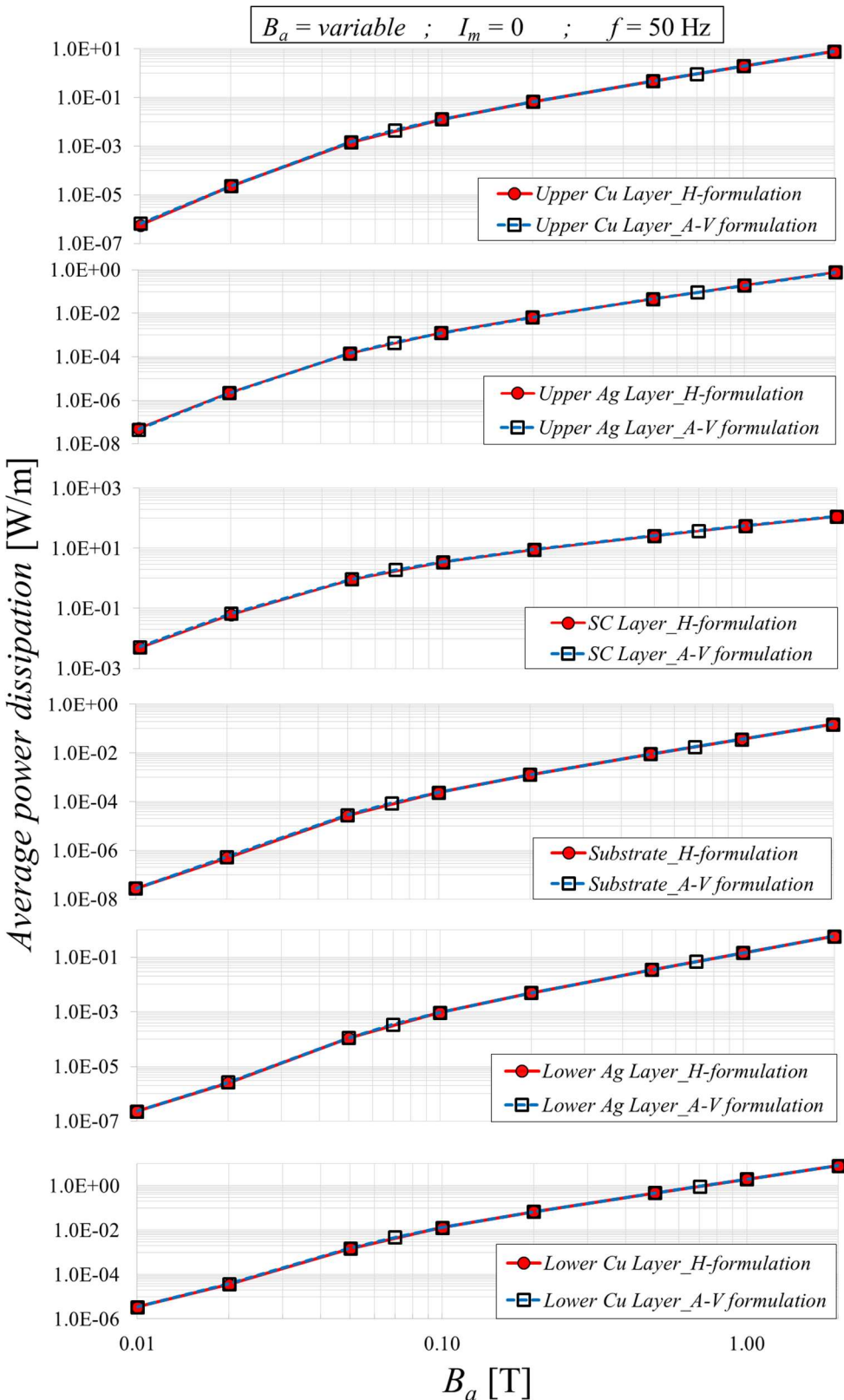
Figure 2.5.6. *Average power dissipation generated in each layer of the tape due to a perpendicular AC field, computed with different formulations. The frequency is set to 50 Hz and the field amplitude is varied. The figure is in logarithmic scale.*

Fig. 2.5.7 presents the magnetization losses due to a perpendicular field, computed with both models, setting the field amplitude to 0.1 T and varying the frequency. Good agreement is found between the results of the two models; for a frequency of 10 kHz, a difference is notable, but it remains below 2.5%. Fig. 2.5.8 shows the magnetization losses in each layer of the tape. Even if the discrepancy at 10 kHz between the two models is less visible in this plot in which the ordinate axis is in logarithmic scale, from the comparative analysis it is concluded that the discrepancy is in the losses generated in the superconducting layer.
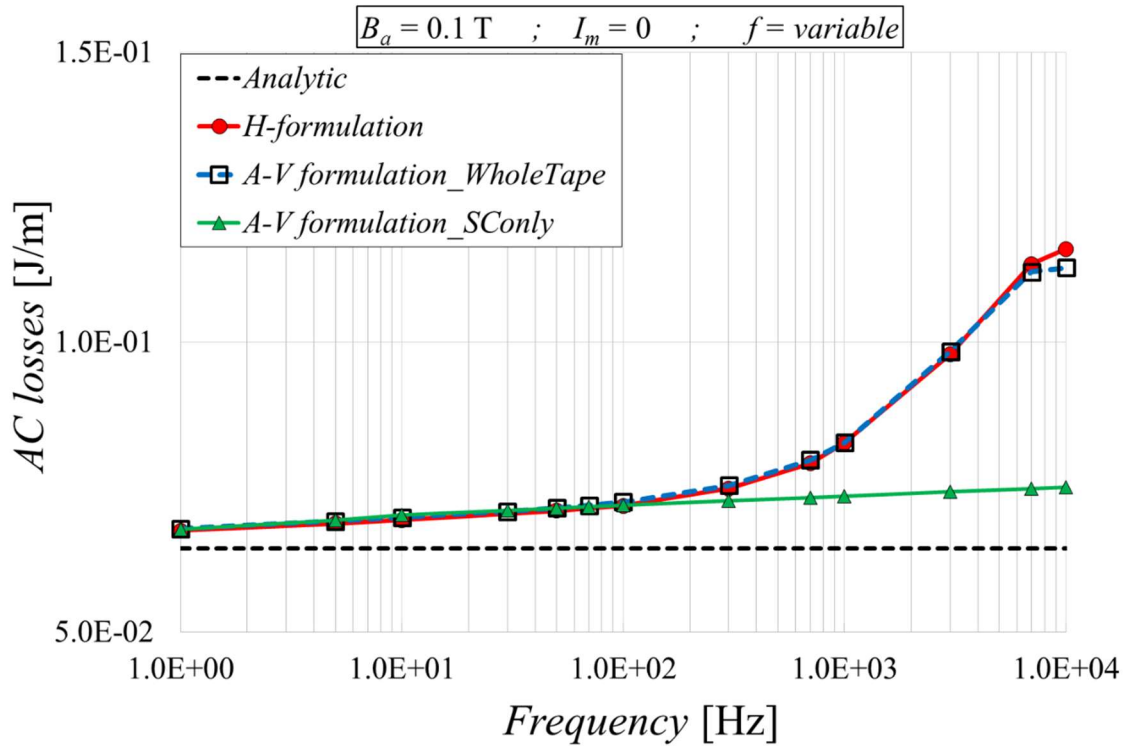
Figure 2.5.7. *Magnetization losses computed with different formulations. The field amplitude is equal to 0.1 T and the frequency is varied. The figure is in semi-logarithmic scale.*
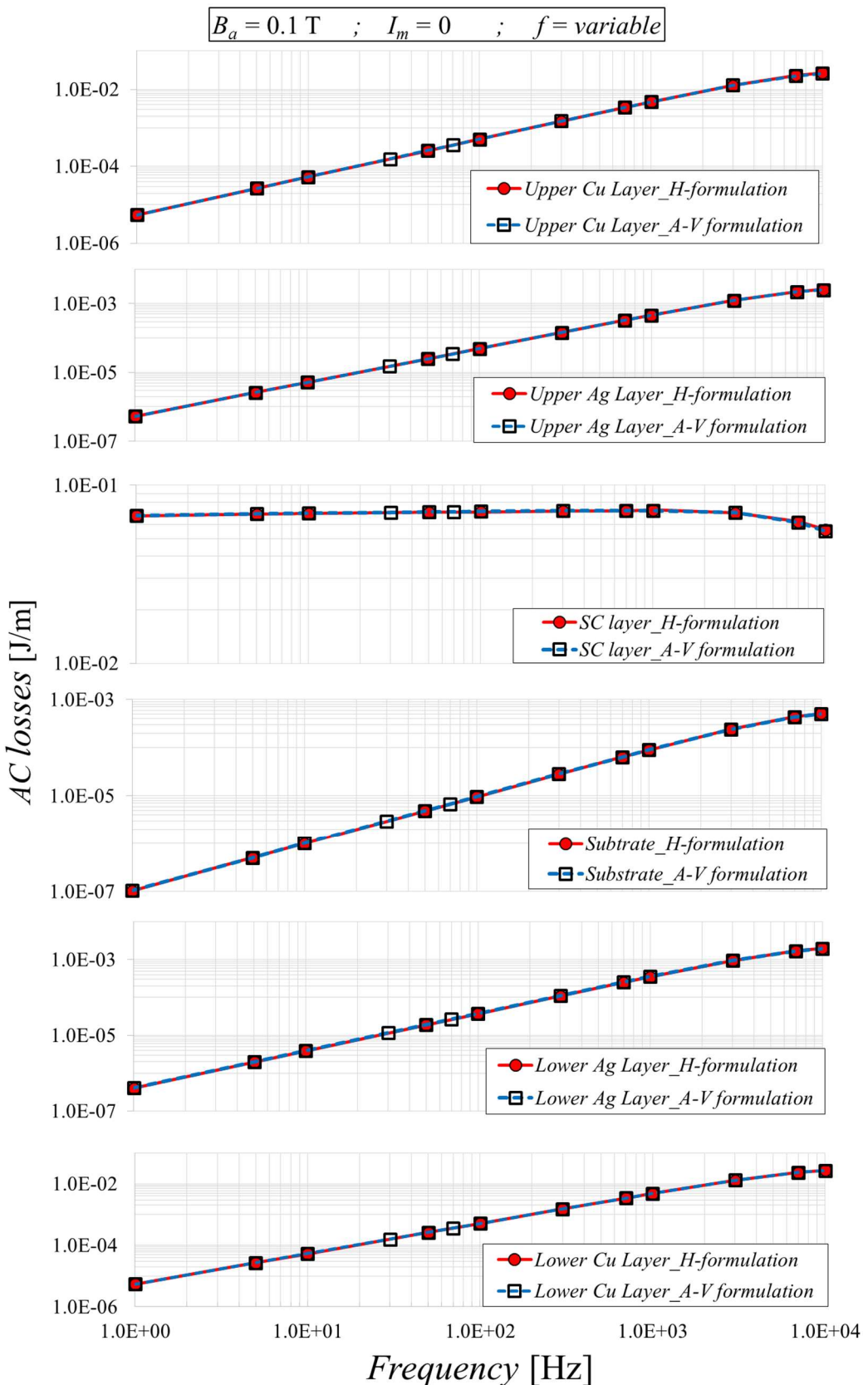
Figure 2.5.8*. Magnetization losses generated in each layer of the tape due to a perpendicular AC field, computed with different formulations. The field amplitude is set to 0.1 T and the frequency is varied. The figure is in logarithmic scale.*

Fig. 2.5.9 presents the average power dissipation generated by the combination of an AC transport current and a perpendicular AC magnetic field. The field amplitude is set to 0.1 T, the frequency of both AC sources is set to 50 Hz and I_m is varied. The results of the two numerical models are in excellent agreement: the discrepancies are below 0.5%. Furthermore, Fig. 2.5.10 shows the power dissipation generated in each layer of the tape, showing a good agreement also at the layer level.
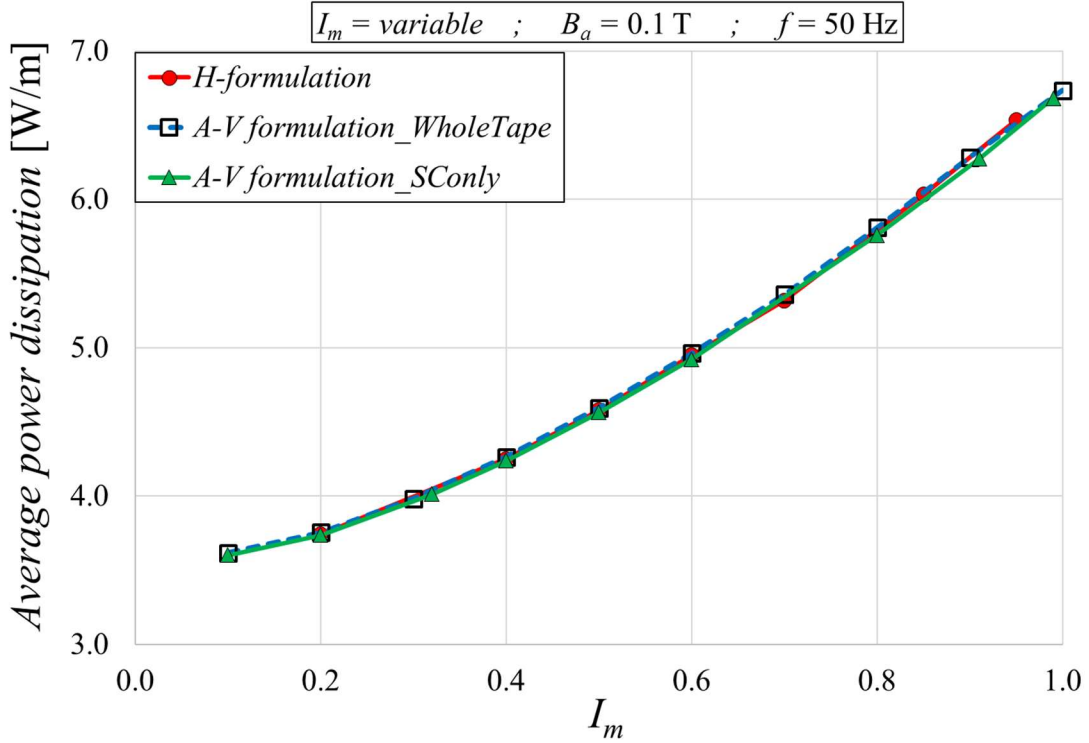
Figure 2.5.9. *Average power dissipation due to a combination of AC transport current and a perpendicular AC magnetic field, computed with different formulations. The field amplitude is set to 0.1 T, the frequency is set to 50 Hz and I_m is varied. The figure is in semi-logarithmic scale.*
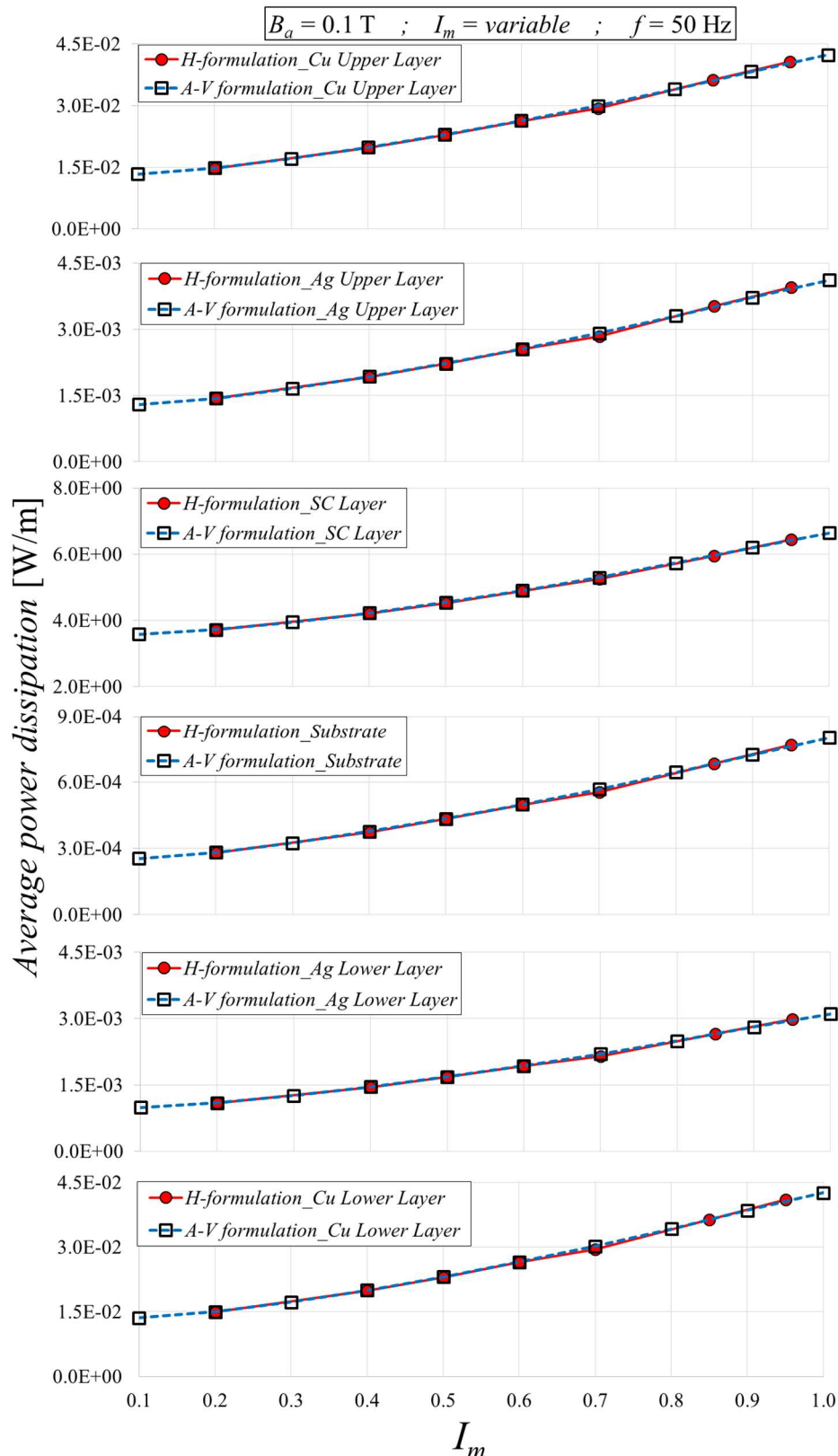
Figure 2.5.10. *Average power dissipation generated in each layer of the tape due to a combination of AC transport current and a perpendicular AC magnetic field, computed with different formulations. The field amplitude is set to 0.1 T, the frequency is set to 50 Hz and I_m is varied. The figure is in semi-logarithmic scale.*

Finally, Fig. 2.5.11 presents the AC losses generated by the simultaneous presence of a magnetic field with an amplitude of 0.1 T, an AC current with I_m is set to 0.7 and varying the frequency of both sources. Both models agree even if the numerical curve calculated with the *H*-formulation exhibits lower values at all frequencies (the maximum discrepancy is around 2%) except for the 10 kHz case, where it shows a higher value (2.5% higher). Furthermore, Fig. 2.5.12 shows the AC losses generated in each layer of the tape, confirming the agreement also at the layer level.
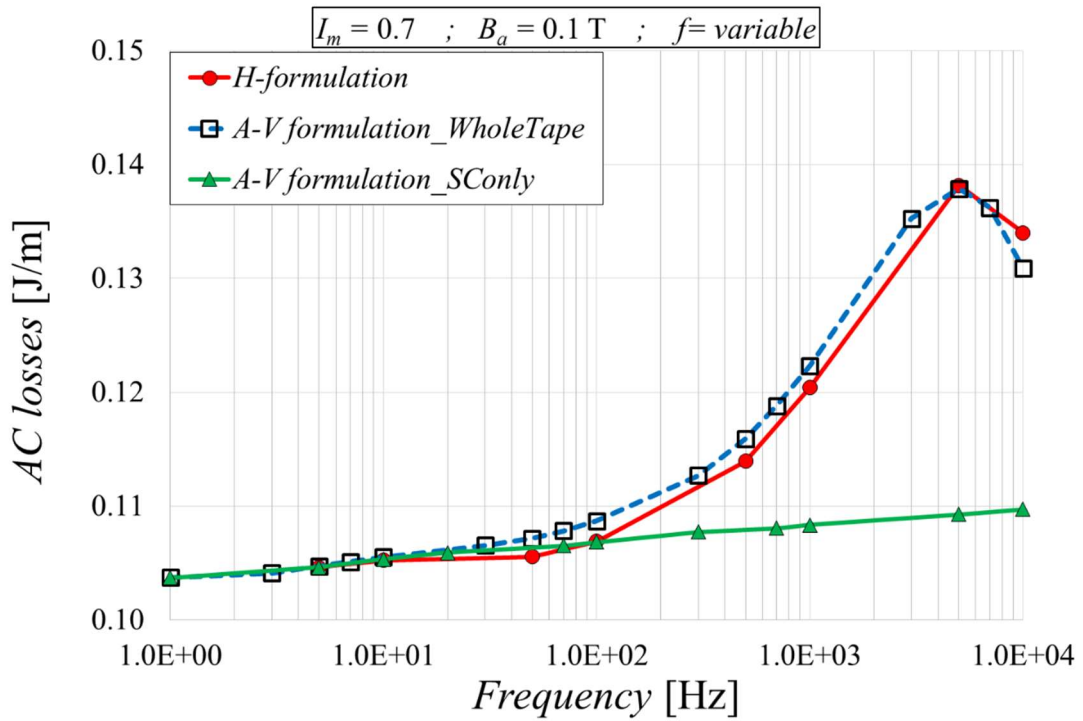
***Figure 2.5.11.** Average power dissipation due to a combination of AC transport current and a perpendicular AC magnetic field, computed with different formulations. The magnetic field amplitude is set to 0.1 T, I_m is set to 0.7 and the frequency of both AC sources is varied. The figure is in semi-logarithmic scale.*
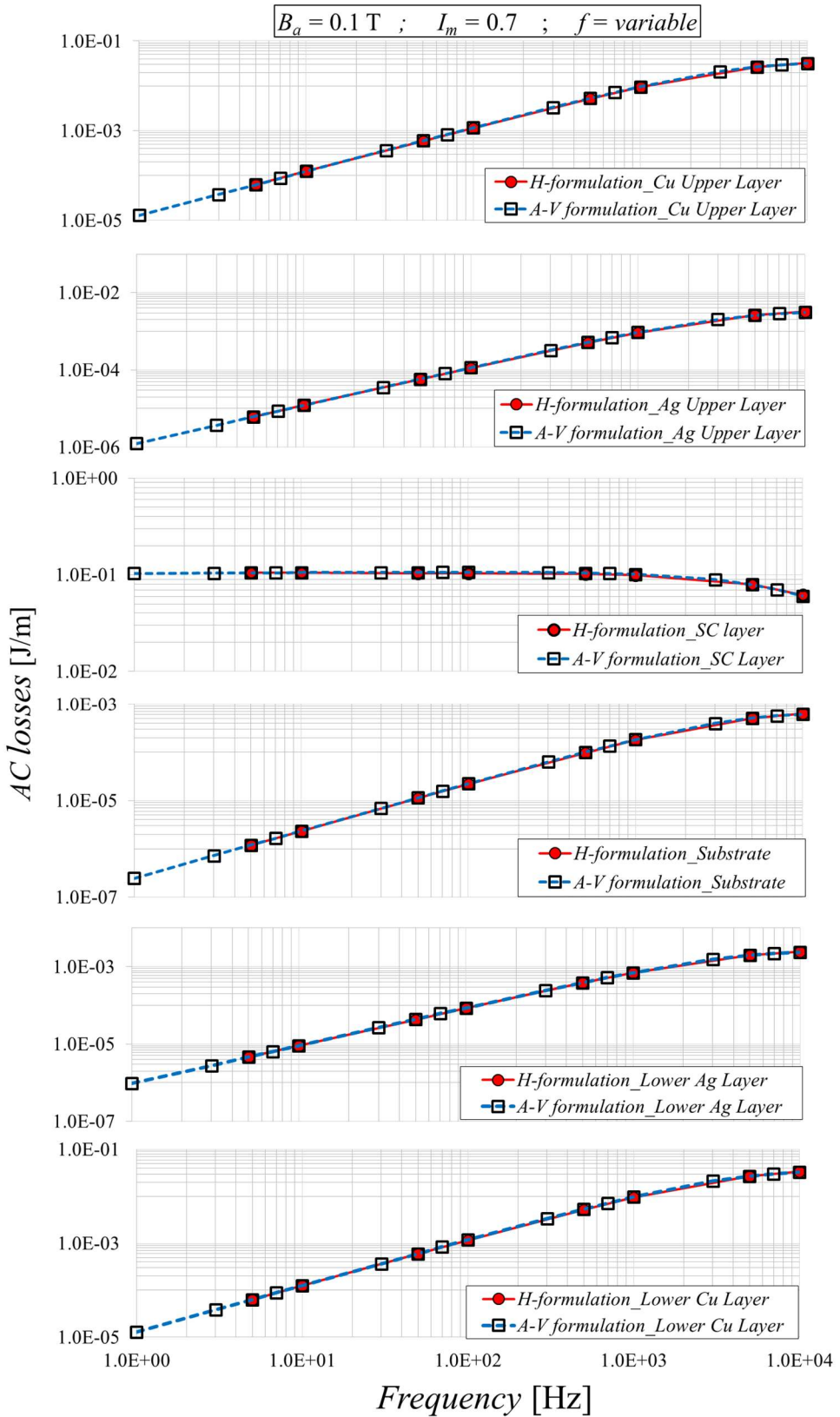
Figure 2.5.12. *Average power dissipation generated in each layer of the tape due to a combination of AC transport current and a perpendicular AC magnetic field, computed with different formulations. The magnetic field amplitude is set to 0.1 T, I_m is set to 0.7 and the frequency of both AC sources is varied. The figure is in semi-logarithmic scale.*

To conclude, the FEM model based on the *H*-formulation and the integral model based on the *A-V* formulation lead to the very similar results in terms of losses, in every conditions tested. This agreement is confirmed also at the layer level. It is worth noting that, since the losses are related to the current density distribution within the tape cross-section, the agreement implies that even these distributions are in accordance between the two models.

Table 2.5.1. Computation times for the AC losses calculation with the two numerical models.

Parameters			Computation time		Speed-up
I_m	B_{ay}	f	*A-V formulation*	*H-formulation*	
	[T]	[Hz]	[s]	[s]	
0.7	0.0	50	158	759	4.8
0.0	0.1	50	320	962	3.0
0.7	0.1	50	375	901	2.4

Finally, Table 2.5.1 shows some examples of computation times for the integral approach, in comparison with those obtained with the *H*-formulation (both found on a computer equipped with an *Intel Xeon E5-2650 v3* CPU and 64 GB of RAM). Three cases are reported, in which the AC sources are either applied separately or act simultaneously. The computations with the *A-V* formulation are 2.4 to 4.8 times faster than those based on the *H*-formulation. However, this comparison is affected by the greater number of degrees of freedom required to achieve convergence in the FEM model. In fact, the stacked configuration requires the spatial discretization across the tape width to be the same for all layers, which does not apply for the integral model. In the model based on the *H*-formulation, the superconducting layer is discretized with 180 elements while all the other layers are discretized with 4320 elements, distributed between the different layers. Moreover, the FEM model requires discretizing the air, which enhances the computation times. Lately, the so-called *H-φ* model has been proposed, which can partially reduce this drawback [142]. Furthermore, it is not excluded that by significantly varying the parameters (simulations of very high or low frequencies or with currents approaching I_c) the speed-up cannot vary considerably.

2.6. Conclusions

This chapter has presented in detail the steps to obtain and to implement in commercial solvers the equations of two numerical models for the calculation of AC losses in the different layers of a coated conductor: a FEM model based on the *H*-formulation and an integral model based on the *A-V* formulation. Both models adopt a 2-D approximation. The FEM model allows an easy implementation of the characteristics of HTS tapes including a ferromagnetic substrate. The integral model contains some elements of innovation compared to similar literature methods, despite in its actual version it does not allow to simulate ferromagnetic layers. The

two models can be implemented into different solvers, which have their pros and cons. For what concerns the model based on the *H*-formulation, it can be easily implemented into COMSOL *Multiphysics*, a software in which the material properties can handily be inserted into the model equations. For example, this allows to consider a non-constant relative permeability in order to account for the ferromagnetic behaviour of a single layer. Therefore, this model is more efficient in calculating the AC losses for different types of tapes. The model based on the *A-V* formulation is a research code implemented in MATLAB which makes use of different optimization algorithms. The code is suitable for an easy implementation into free alternative solvers, such as GNU Octave [143]. Since the user has the possibility to set the solving parameters manually, a research code generally guarantees a greater control over the results. This allows for example a more efficient calculation of the corrective terms due to the configuration of the measurement system and makes this model more suitable for comparisons with electromagnetic measurements. Since the next chapter focuses precisely on the experimental measurement of AC losses in superconducting tapes without ferromagnetic substrate, the model based on *A-V* formulation is selected as a comparison.

Implementing the same tape characteristics and equal operating conditions in both models, their results convergence at the layer level; furthermore, the model based on the *A-V* formulation results faster than the model based on the *H*-formulation.

The method based on the *A-V* formulation has been adopted to conduct two distinct analyses, here summarized.

2.6.1. *Impact of the different layers on the AC losses of a coated conductor under different operating conditions*

The losses computed numerically for the whole tape are similar to the values predicted by the analytical formulae and by methods considering only the superconducting layer of the tape, for a wide range of operating conditions. However, some conditions for which the simulation of the superconducting layer only is not acceptable for a correct evaluation of AC losses exist and are highlighted by the model. In fact, the losses of the non-superconducting layers increase when the frequency of the applied external magnetic field exceeds 1 kHz. If the magnetic field is parallel to the main face of the tape, the impact of the non-superconducting layers is already relevant (and not negligible) at frequencies of tens of hertz.

2.6.2. *Impact of the voltage measurement circuit on the AC losses in coated conductors*

A method has been proposed to numerically determine the impact of the voltage measurement circuit on the electromagnetic measurement of AC losses in HTS tapes. In particular, the trend of the corrective factors to be applied to the experimental results to obtain the real AC losses of the tape is determined at different operating conditions, for two different geometric configurations.

When the voltage taps are twisted together at a given distance from the tape middle axis, without using a compensation signal, increasing the distance lowers the impact of the measurement system (*i.e.* a minor correction is needed). Moreover, it is demonstrated how the

distance of $\frac{3}{2}w$ from the tape middle axis proposed in literature represents a good compromise between reducing the corrective factor and obtaining a not excessive area for the possible linking of external flows.

An alternative configuration has been proposed, in which the two signal wires are twisted near the middle axis of the tape and a second circuit is used for the voltage compensation. In this case, there is a distance by which the correction factor is cancelled out. However, this requires an extreme precision in the positioning of the voltage taps onto the tape surface of the tape.

The numerical analysis described in this chapter is coupled with an experimental study of AC losses in straight tape samples, described in the next chapter, in which the impact of the voltage measurement configuration and the use of the corrective factors is also be experimentally verified.

Experimental measurement of AC losses in HTS tapes

The measurement of AC losses in individual tapes is not a trivial task, due to the very small magnitude of the quantities to detect, which might lead to significant alterations of the results. Experimental methods for AC losses can be divided into two main groups: calorimetric [144 – 146] and electromagnetic [147 – 149]. The first ones are based on the evaporation rate of the coolant when the sample dissipates power (boil-off methods) [150] or by the direct measurement of the sample temperature during the experiment using thermocouples [151]. They are insensitive to electromagnetic noise, but they require precise calibrations of the experimental equipment to achieve the adequate accuracy [152].

The general approach to the electromagnetic measurement of AC losses has already been described in *Section 2.1*. This method is selected for the measurements described in this section; in *Section 3.1* the experimental set-up developed at the *University of Bologna* is presented. Contrariwise to the calorimetric approach, the electromagnetic method is sensitive to electromagnetic noise, and usually rely on the use of lock-in amplifiers, which are suitable devices for the signal processing [153 – 155]. However, these devices have a non-negligible cost and exhibit limitations in the number of harmonics of the measured signal to be filtered which can be obtained. Furthermore, the manufacturers do not usually make available the algorithms implemented in the lock-in amplifier, which might make it more difficult to interpret the results obtained. In *Section 3.2*, a different approach to the electrical measurement of AC losses is illustrated, not involving lock-in amplifiers for the data filtering. In particular, the algorithm adopted for the data processing and the calculation of the AC losses is presented. Then, in *Section 3.3* a comparison between the measurements performed at the *University of Bologna* and by other laboratories worldwide with the same tape is given. Finally, in *Section 3.4* the measurements carried out are compared with the results of the model described in *Section 2.4*, and in particular the corrective factors for the voltage measurement circuit are taken into account in the measurements.

3.1. Experimental set-up for the electromagnetic measurements of AC losses in tapes

The experimental set-up developed at the *University of Bologna* is aimed at applying an AC transport current to the tape and measure the corresponding transport losses. To date, a system for the generation of a time-varying magnetic field is not available at the laboratory, therefore the magnetization losses are not measurable. A photo of the system is presented in Fig. 3.1.1(a), while its basic scheme and connections are displayed in Fig. 3.1.1(b) [147].

(a)

(b)
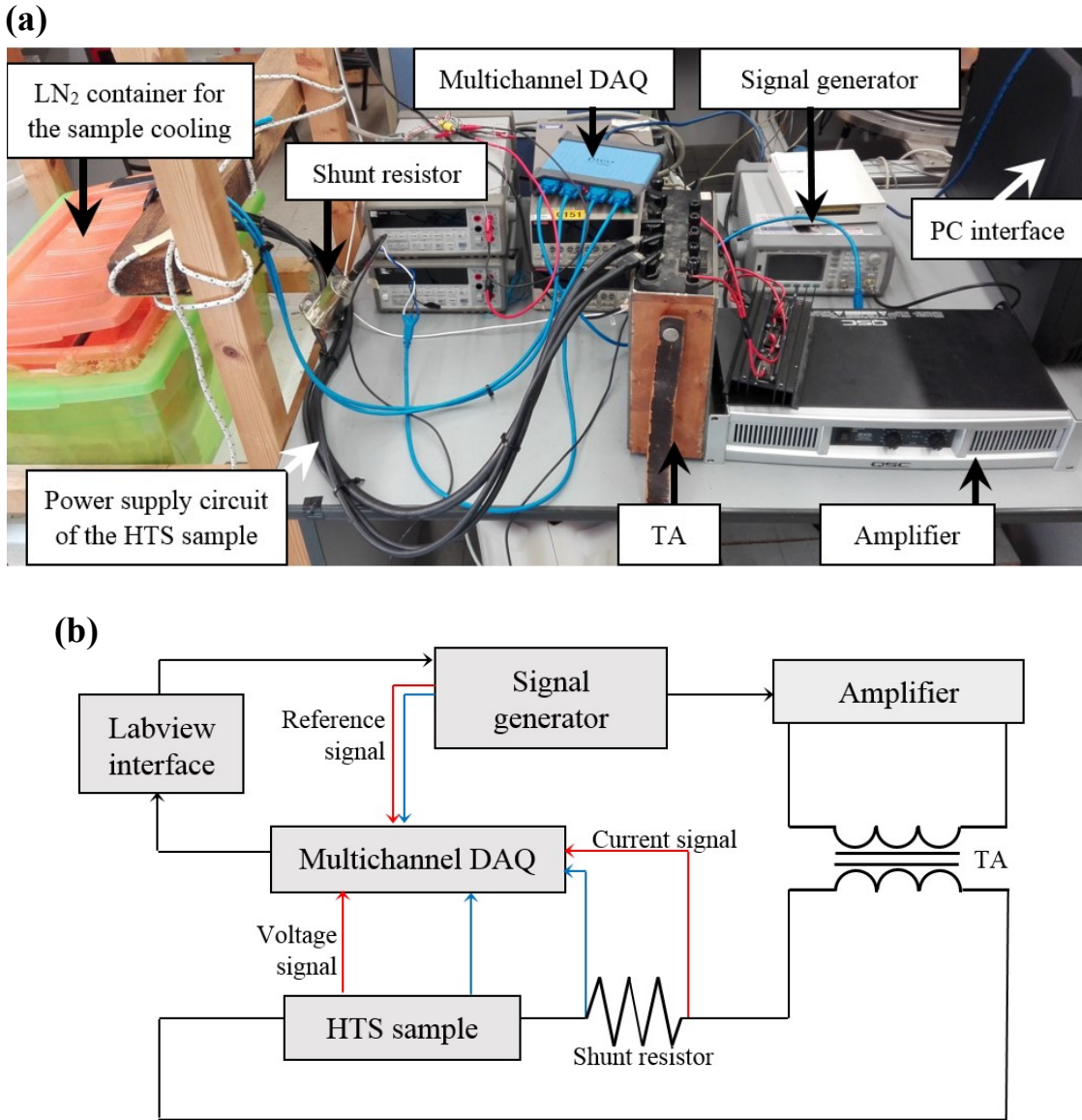
Figure 3.1.1. *(a) Photo (a) and (b) connection scheme of the experimental set-up for AC current generation and data acquisition in tapes developed at the University of Bologna.*

The AC supply circuit initiates from a *Keysight 33500B* waveform generator [156] controlled by the user via *LabVIEW* interface [157], so that the frequency and amplitude of the signal can be varied during the experiment. The generated signal is acquired through a *PicoScope 4444* multichannel oscilloscope [158] and it is henceforth referred as the *reference signal*. The oscilloscope has 4 differential inputs, 14-bit resolution and a full-scale voltage of 10 mV. Applying the reference signal directly on the sample would not achieve a current high enough to generate a detectable voltage drop. Therefore, the signal produced by the waveform generator is amplified by means of a *QSC Audio GX5* power amplifier [159]; as requested by its specification, a 4 Ω resistive load is introduced before the device. The power amplifier has a gain of 34.4 *dB* when operating in a high frequency range from 20 Hz to 1 kHz. The amplification factor is still not sufficient to raise the current adequately and thus a TA transformer is added in series at the circuit, in which the primary and secondary windings are inverted with respect to the normal operation of the device, so as to increase the transport

current intensity. The transformer increases the current by a factor 30 when the frequency is set to 50 Hz, while this ratio reduces to 20 up to 1 kHz. The current is measured through a coaxial shunt resistor and acquired as a voltage signal by the oscilloscope. This type of current transducer minimizes the phase shift between the current flowing in the HTS tape and the obtained signal. Hereafter, this signal is referred as the *current signal*. Finally, the voltage developed along the sample is acquired through voltage taps soldered onto the tape surface at a certain distance from each other. Hereafter, this signal is referred as the *voltage signal*. It is worth noting that, whenever possible, the area of both circuits (measurement or power supply) is minimized to reduce the linked fluxes. For example, the supply and return cables are brought together as much as possible, as shown in Fig. 3.1.1(a).

The scheme displayed in Fig. 3.1.1(b) includes a unique voltage signal coming from the HTS sample, therefore representing the voltage measurement configuration without compensation described in *Section 2.4.2*. However, the implementation of the compensated configuration described in *Section 2.4.3* does not require complex modifications with respect to this scheme (further explanation are given in the next sections).

The duration of the data acquisition is selected to correspond to an integer number of periods. This choice avoids the problems of leakage when performing integral transformations (*e.g.* a *Discrete Fourier Transform*) in the signal processing.

If for a particular analysis it is not required for the frequency of the operating current to be precisely equal to an imposed value, it is preferable to select a frequency corresponding to a prime number (in Hz), close to the desired frequency value (*e.g.* 47 Hz or 51 Hz instead of 50 Hz). This choice partly mitigates the problem arising from the induced electromotive forces due to external electromagnetic fluxes in the measurement circuit, which are responsible for most of the electromagnetic noise. As a matter of fact, these fluxes are characterized by a frequency corresponding to either the network frequency and/or some of its higher order harmonics. When the frequency used in the experiment corresponds to a prime number, the first harmonics affected by a possible superimposition with the harmonics of the network frequency is of a higher order than in case of selecting a non-prime number.

Finally, it should be noted that non-magnetic screws, washers and bolts should be preferred to the classic steel ones to connect the different parts of the circuit or to connect the copper bars with the G-10 support. In fact, these materials could magnetize and increase the flux linked to any circuit loop.

3.2. Signal processing technique

Once the test is concluded, it would be theoretically possible to compute the AC losses by computing the average value of the product between the voltage and current signals acquired. Performing the average in time, the voltage signal component which is not in phase with the current should be automatically cancelled out, thus allowing for the calculation of the active power corresponding to the losses.

However, the intensity of the signals, especially the voltage one, is usually so low that it can easily be covered by the external electromagnetic noise. Furthermore, although a rectilinear tape has a very small inductance, its electrical resistance in the superconducting state is practically negligible. The voltage signal is therefore almost in quadrature with the current signal. This feature makes the system more sensitive to possible phase shifting between the real signal and the acquired signal; the measurement of their in-phase components is therefore more complicated.

Despite the precautions taken during the signal acquisition to reduce the noise, these problems cannot be fully solved and remain relevant. It is therefore important to adopt a proper data post-processing technique to correctly remove the unwanted components of the acquired signals before performing the loss calculation. The procedure adopted in this work is based on the comparison between the current and voltage signals with the reference signal, to identify their harmonic content with respect to the frequency of the reference signal.

Initially, the reference signal is processed by means of an offset removal and normalization. This signal can then be considered as perfectly sinusoidal, *i.e*:

$$\cos(\omega t) \tag{3.2.1}$$

where ω is the pulsation of the reference signal, assumed free of disturbances.

The *Hilbert transform* [160] is then applied, which allows shifting the signal by a phase π/2, resulting in a signal of the type sin*(ωt)*.

The signal is then multiplied by the imaginary unit *–i*, which yields:

$$-i \sin(\omega t) \tag{3.2.2}$$

Finally, Eq.s (3.2.1) and (3.2.2) are summed up to obtain a signal of the type:

$$\cos(\omega t) - i \sin(\omega t) \tag{3.2.3}$$

which is henceforth referred as the *processed reference signal*.

This signal is then processed with the current and voltage signals to obtain their respective harmonic components. The steps described below can be applied separately to either the current or the voltage signals; each of them are singularly referred as the measured signals. If the voltage measurement configuration proposed in *Section 2.4.3* is adopted, a second voltage signal must also be processed (the compensation) following the same steps.

Theoretically, the measured signal should be perfectly sinusoidal; however, it results deformed due to the superimposition with the electromagnetic noise. Thus, it is considered as a generic periodic signal of the type *f(t)*, without reference to the sinusoidal behaviour.

Each harmonic component of the measured signal is calculated separately, in order to express the function *f(t)* as the following sum:

$$f(t) = \sum_{n=1}^{\infty} a_n \cos(n\omega t + \alpha_n) \tag{3.2.4}$$

where a_n and α_n are the amplitude and the phase shift of the nth harmonics.

The calculation of each harmonic component consists in raising the processed reference signal (Eq. (3.2.3)) to the nth power and multiplying it by the measured signal reported in Eq. (3.2.4). Then, the average value of this product in time is computed. It can be demonstrated that every term of the measured signal $f(t)$ that does not correspond to the nth harmonic is cancelled out by this averaging process. In terms of equations, this is equivalent to state that:

$$\langle f(t) \cdot [\cos(\omega t) - i\sin(\omega t)]^n \rangle = \langle a_n \cos(n\omega t + \alpha_n) \cdot [\cos(\omega t) - i\sin(\omega t)]^n \rangle = \quad (3.2.5)$$
$$= \frac{a_n}{2} [(\cos(\alpha_n) + i\sin(\alpha_n)]$$

Eq. (3.2.5) allows one to obtain the amplitude and phase of each harmonics; the process can be repeated for all desired harmonics. A convergence study is carried out regarding the minimum number of harmonics for which the calculation must be repeated to obtain a sufficiently accurate signal filtering. It is found that treating harmonics up to order 20 allows to reach the convergence of the method. However, by repeating the calculation for a higher number of harmonics, the computational burden of the method does not increase significantly. In the results presented in the following, the filtering procedure is repeated up to the harmonics of order 30. It should be noted that the lock-in amplifier typically applies a similar data treatment procedure to one single harmonic only.

Once this procedure is applied to both the current and voltage signals, an *inverse Fourier transform* is computed to retrieve the signals in the time domain. By applying the same process to the current and voltage signals, the filtered signals obtained have the same time scale and do not require further operations to correct for the phase shifts unavoidably related to any data acquisition (DAQ) system.

Finally, the average value of the product of the two processed signals is computed to determine the value of AC losses. Dividing this term by the distance between the voltage taps yields the losses in unit length. If the measurement configuration with compensation is adopted, the processed compensation voltage signal should be previously subtracted from the voltage signal.

Fig. 3.2.1 shows an example of the application of the processing technique to the voltage signal acquired during the test conducted on the *SuNAM SCN04* tape, whose properties are reported in *Section 2.3.5*. In the considered test, I_m is set to 0.88 at a frequency of 50 Hz. The tape length is equal to 30 cm and the distance between the voltage taps is set to 8 cm. The raw signal is affected by a significant amount of noise and it is therefore not possible to use it for the loss measurement. The signal obtained after processing is instead much cleaner from noise and suitable for use in the AC loss assessment. It should be noted that the time evolution of the signal is not perfectly sinusoidal due to the presence of the tape ferromagnetic substrate, which affects the results especially at high values of the ratio between AC transport current and critical current.
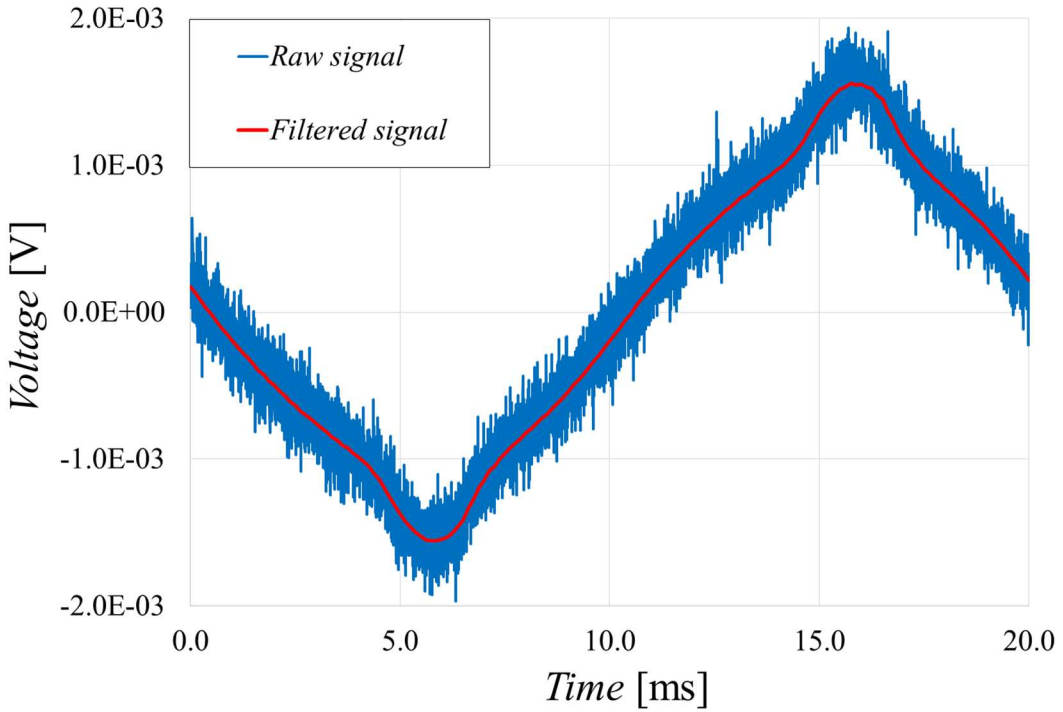
Figure 3.2.1. *Voltage signal acquired before (blue) and after (red) the processing in the time domain. The experimental parameters are: I_m equal to 0.88, frequency set to 50 Hz.*
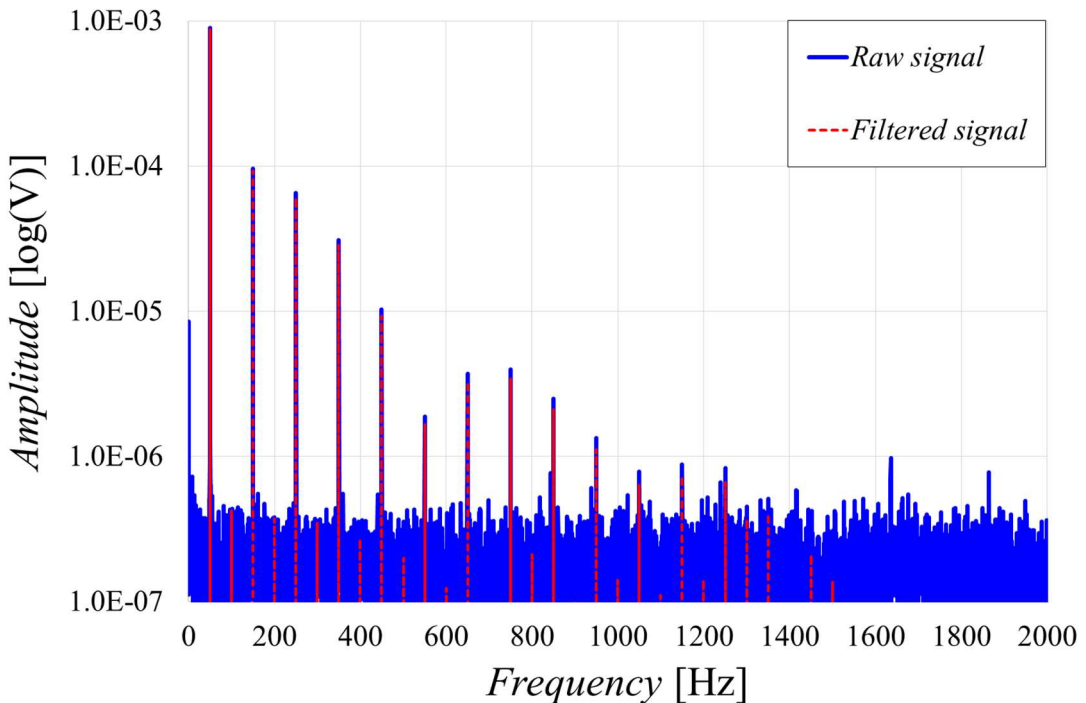
Figure 3.2.2. *Voltage signal acquired before (blue) and after (red dashed) the processing, in the frequency domain. The experimental parameters are: I_m equal to 0.88 and frequency set to 50 Hz. The filtering technique is applied up to the harmonics of order 30. The figure is in semi-logarithmic scale.*

Fig. 3.2.2 shows the same signal presented in Fig. 3.2.1, but in the frequency domain. This highlights the effect of the processing technique on the signal harmonics. There is an evident noise reduction in terms of frequencies of the treated signal compared to the raw signal. In the treated signal, there are no frequencies higher than 1.5 kHz, as the filtering process is repeated up to the harmonics of order 30 of the acquired signal.

3.3. Comparison of the AC losses measurements performed in different laboratories with the same HTS coated conductor

In this section, the AC losses obtained with the developed set-up and processing method are presented and compared with those obtained in other research laboratories by using lock-in amplifiers in the DAQ system. The tape selected for this comparison is the *AMSC 8501* tape, whose parameters have already been described in Fig. 2.3.5.1 and Tab. 2.3.5.1. The tapes tested at the *University of Bologna* (named *lab1* [147]), at the *Southwest Jiaotong University, Chengdu, China* (named *lab2* [96]) and at the *Karlsruhe Institute of Technology, Germany* (named *lab3* [161]) have the same characteristics presented in *Section 2.3.5* and come from the same lot. The tapes analyzed at the *Chinese Academy of Sciences*, *Beijing, China* (named *lab4* [94]) have the same characteristics presented in *Section 2.3.5* but come from a different lot.

All tests were conducted at 77 K, in liquid nitrogen. The experiments were performed by varying the frequency and the I_m value. Only the transport current AC losses are measured, neglecting the presence of any external magnetic field. Since the various laboratories have independently chosen the operating parameters, it is not always possible to present a comparison under the same operating conditions. Nevertheless, the figures are presented so as to make the comparison as clear as possible.

The measurement configuration adopted at *University of Bologna* is the one without compensation described in *Section 2.4.2*, with voltage taps twisted at a distance equal to $\frac{3}{2}w$ from the tape middle axis. The measurements are also compared with the results of the analytic formulation Eq. (2.3.5.3).

Fig. 3.3.1 shows the transport AC losses measured by the different laboratories varying the I_m value. The frequency is not equal for all the cases (therefore, unlike the graphs previously reported in this work, the losses varying I_m are reported in *Joule*), and that should be carefully taken into consideration since the AC losses in the *AMSC 8501* tape are frequency dependent, as shown in Fig. 2.3.5.12. The frequency set at *lab1* (50 Hz) and *lab4* (55 Hz) are very similar. For *lab3*, the tested frequencies immediately after (72 Hz) and before (36 Hz) the 50 Hz value are displayed. The lower frequency tested at *lab2* is equal to 210 Hz and this value is used for the comparison. The trend of all curves is consistent with Fig. 2.3.5.9 (which presented the average power dissipation). The experimental curves are in good agreement with each other and they approach the analytic curve when I_m tends to I_c. The *lab2* curve exhibits values 2 to 4 times higher than the other curves: this is consistent with the losses increase obtained comparing the numerical results shown in Fig. 2.3.5.11 (for $I_m = 0.4$) when $f \approx 50$ Hz and $f \approx$ 210 Hz.
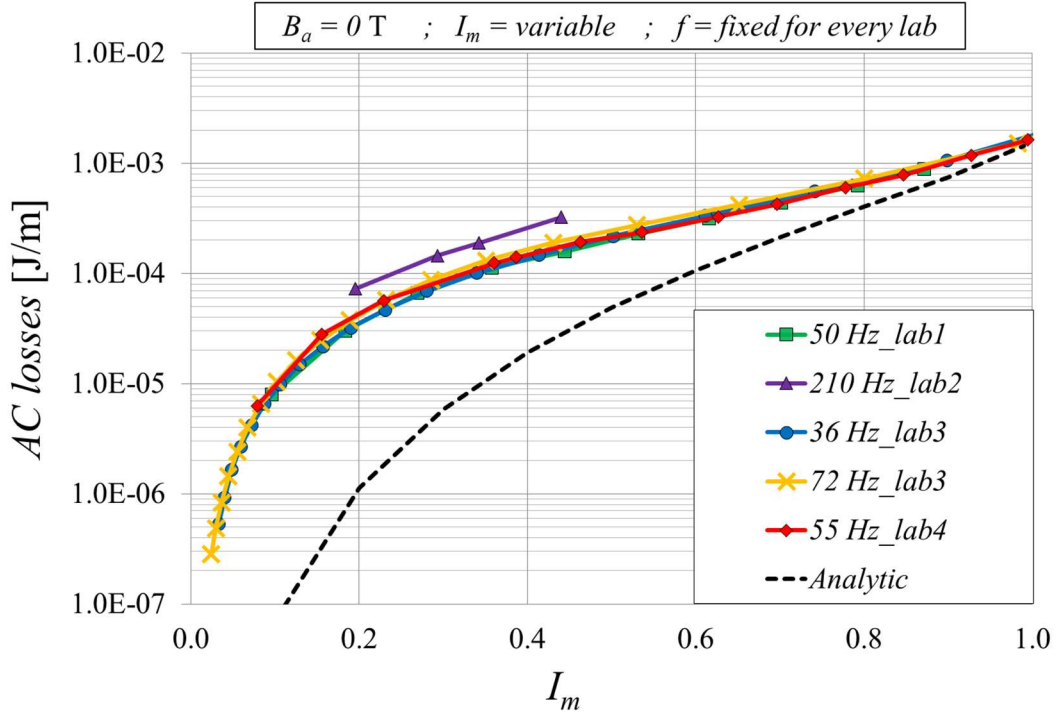
Figure 3.3.1. *Transport current AC losses in the AMSC 8501 tape, measured at lab1 [147], lab2 [96], lab3 [161] and lab4 [94], varying I_m and for similar frequencies. The figure is in semi-logarithmic scale.*

Fig. 3.3.2 presents the transport AC losses measured by the different laboratories varying the frequency. Different I_m values are displayed: $I_m = 0.2$ (a), $I_m = 0.3$ (b), $I_m = 0.4$ (c), $I_m = 0.5$ (d) and $I_m = 0.6$ (e). Note that in this case, the data available from *lab2* and *lab3* do not refer precisely to these I_m values; therefore, the curves referred to these laboratories are the result of interpolations. The trend of all curves is consistent with Fig. 2.3.5.11 and the measurements diverge from the analytic line as the frequency increase. These discrepancies decrease as the current amplitude rises, especially at low frequencies, and this is coherent with the conclusion drawn for Fig. 3.3.1. The trends of the experimental curves are consistent with each other, despite some patterns are distinguishable. The AC losses measured by *lab1* are generally lower than those referred to the other labs, but especially at low amplitudes they tend to converge with the other curves. The AC losses measured by *lab2* are generally greater than those referred to the other laboratories. The curves referred to *lab3* and *lab4* present intermediate values; moreover, the AC losses measured by *lab3* results lower than the losses of *lab4* at low amplitudes ($I_m = 0.2$ and 0.3), while they have a steeper increase at high amplitudes ($I_m = 0.4$, 0.5 and 0.6).

(a)

(b)

(c)
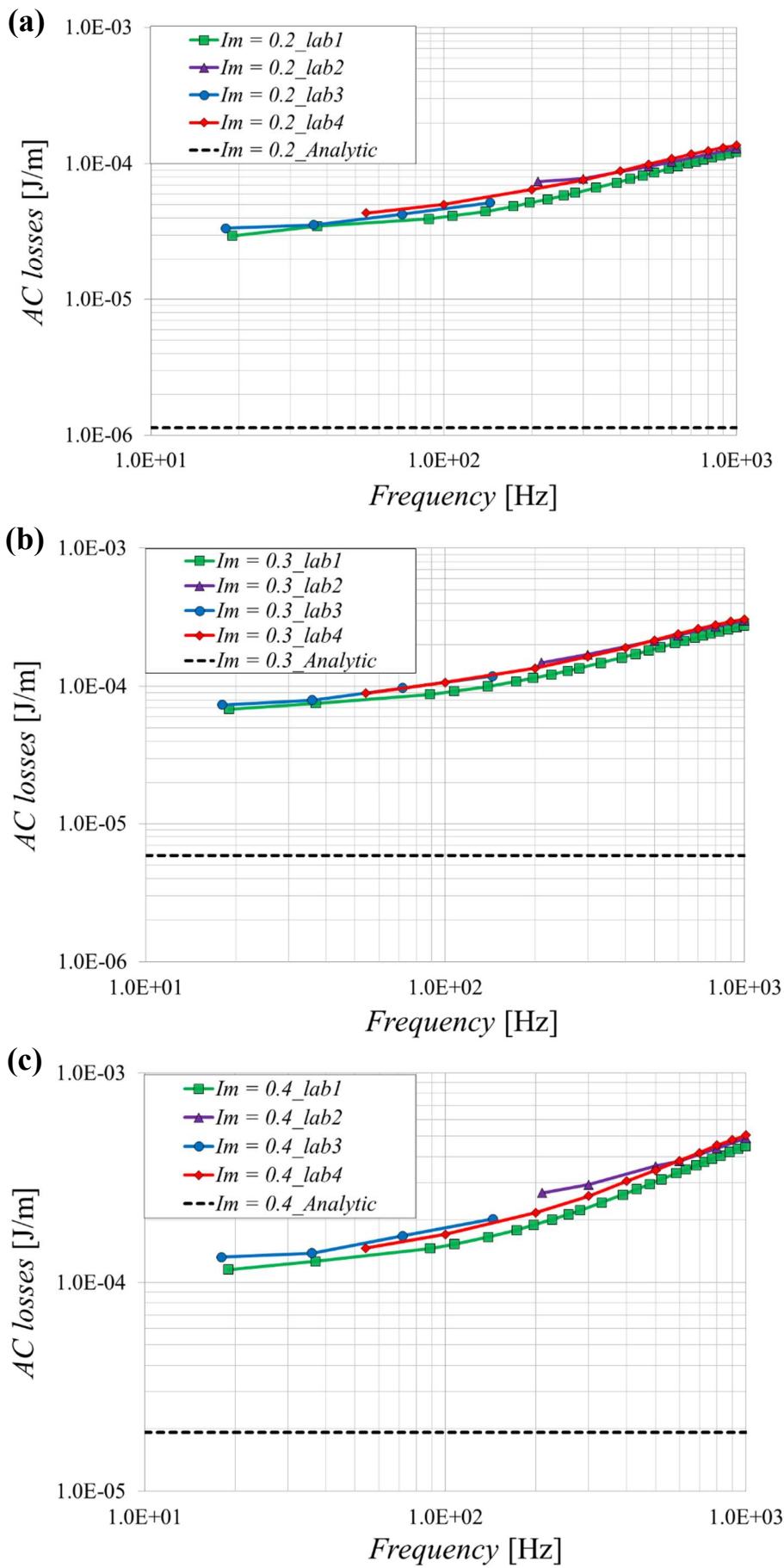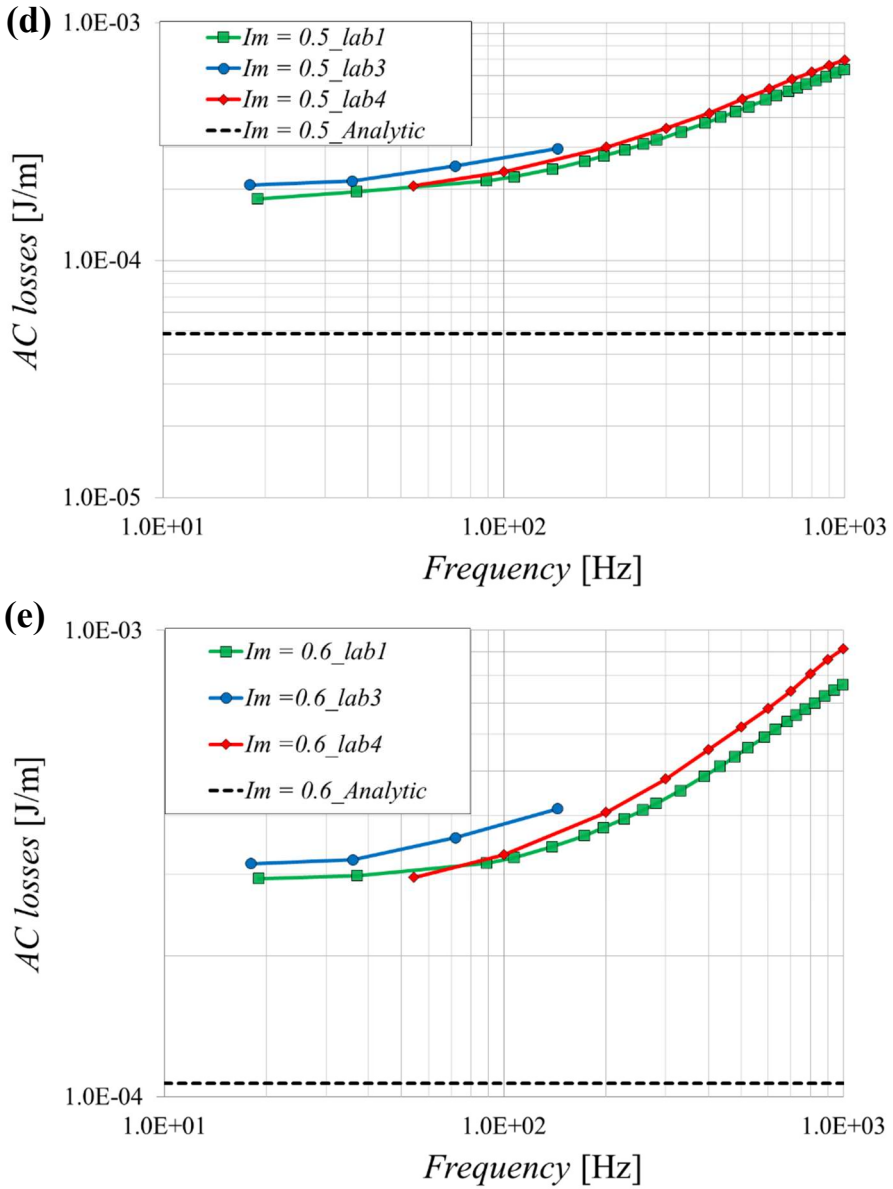
Figure 3.3.2. *Transport current AC losses in the AMSC 8501 tape, measured at lab1 [147], lab2 [96], lab3 [161] and lab4 [94], varying the frequency and for $I_m = 0.2$ (a), $I_m = 0.3$ (b), $I_m = 0.4$ (c), $I_m = 0.5$ (d) and $I_m = 0.6$ (e). The figure is in logarithmic scale.*

It is possible to conclude that, given the good agreement between the results obtained in different laboratories, the effectiveness of the methodology to assess the value of AC losses presented in this work is verified. The advantages of the presented methodology are the possibility to avoid the use of the lock-in amplifiers, to increase the number of signal harmonics treated for the noise reduction, and to have a better control on the reconstructed voltage and current signals.

3.4. Comparison between experimental and numerical results of AC losses in a HTS coated conductor considering different voltage measurement circuit configurations

In this section, a comparison is performed between the AC losses computed with the numerical model proposed in *Section 2.4* and the measurements carried out using the procedure described in *Section 3.1* and *Section 3.2*. For this comparison, the numerical model based on the *A-V* formulation is preferred to the model presented in *Section 2.5*, since it allows to take into account the influence of the voltage measurement circuit and to compare the configurations proposed in *Section 2.4.2* and *Section 2.4.3*.
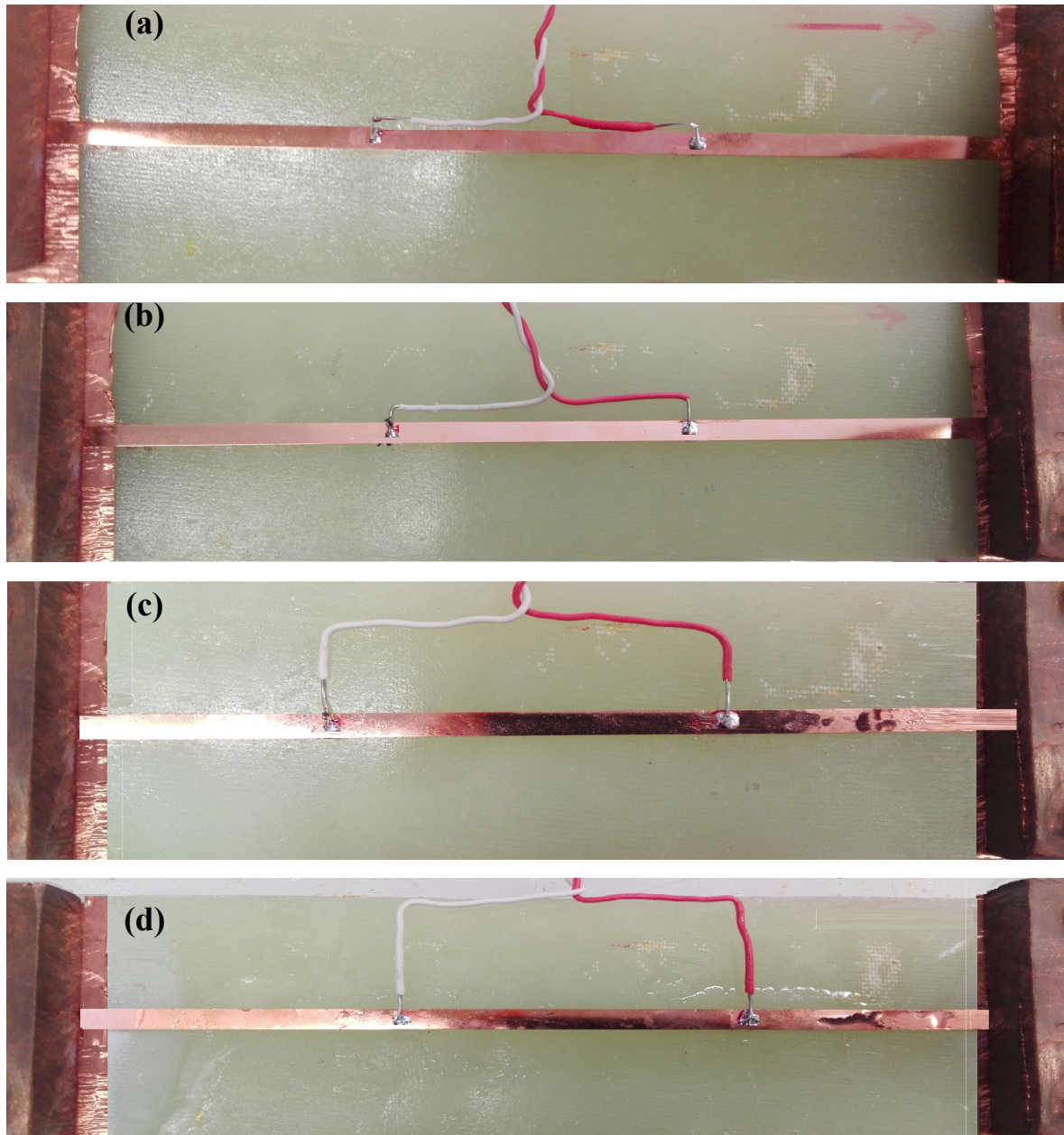
Figure 3.4.1. Photos of the voltage measurement circuit without compensation varying the distance from the tape middle axis at which the voltage taps are twisted together: (a) $\alpha = \frac{3}{4}w$, (b) $\alpha = \frac{3}{2}w$, (c) $\alpha = \frac{7}{2}w$ and (d) $\alpha = \frac{11}{2}w$.

In the following figures, the experimental configuration without compensation and voltage taps twisted at a certain distance from the tape middle axis is referred as *"Exp_Distance"*, followed

by the value of α adopted. Fig. 3.4.1 shows some photos of this configuration, with the different values of α adopted: $\frac{3}{4}w$, $\frac{3}{2}w$, $\frac{7}{2}w$ and $\frac{11}{2}w$. The distance between the voltage taps is set to 7 cm and the tape length is equal to 16 cm. To better visualize the tape in the figures, the Kapton layer used to keep the signal wires adhering to the support during the immersion in the liquid nitrogen bath is removed. As it is possible to notice, the various configurations present some inaccuracies; for example, the shape of the measuring circuit is not perfectly rectangular and the soldering on the tape is not punctual but covers a certain area. These factors affect the accuracy with which the corrective factor is computed; they can be limited but not completely avoided.

The experimental configuration with compensation and the minimization of the area of the voltage measurement circuit is referred as "*Exp_Compensation*"; in this case, both voltage taps are considered to be soldered exactly on the tape middle-axis ($\beta = 0$).

The tape selected for the comparison is the *SuNAM SCN04* tape, with the geometry and the characteristics presented in Fig. 2.4.7.1 and Table 2.4.7.1.

Fig. 3.4.2(a) compares the average power dissipation generated in the tape by an AC transport current with the frequency set to 50 Hz and a variable amplitude. The power dissipation is measured with different configurations, computed numerically and calculated using Norris' analytic formulation. For the *"Exp_Distance"* cases, when α increases the curves tend to converge to each other. The convergence seems to be reached already for $\alpha = \frac{3}{2}w$, as declared in the literature [102 – 107], despite some minor discrepancies with the other curves are visible. It is worth noting that increasing the distance α, the area of the loop widens and the measured signal could be more affected by external fluxes linking (making the acquisition more imprecise). All the *"Exp_Distance"* curves exhibit greater values than the numerical ones, especially for low values of I_m (more than 2 times higher), while they tend to converge with the numerical and analytic curves at high current amplitudes (the differences get lower than 30% when $I_m > 0.6$). The discrepancies between numerical and experimental values at low currents can be ascribed to local variations of the critical current density across the tape width. At low transport current amplitudes, the penetration of the induced currents remains limited to the tape sides, where the current density can be lower. The proposed model does not account for the critical current density inhomogeneities over the tape cross-section, which might be a source of discrepancy with the experimental data, as shown in [162]. Another possible explanation for this discrepancy can be ascribed to the adoption in the model of a field independent Jc value. In practice, the tape self-field can locally modify the J_c within the tape, thus affecting the measured AC losses. Future developments will aim to include a field dependent J_c in the model equations.

Contrariwise, the "*Exp_Compensation*" curve exhibits significantly lower values for all current amplitudes. Compared to the *"Exp_Distance = 11/2 w"* (assuming that this curve represents the case where convergence is surely reached), the power dissipation measured in the case with compensation is 27 times lower when $I_m = 0.35$, 4 times lower when $I_m = 0.45$ and 2 times lower when $I_m = 0.85$. Thus, the difference reduces when the current approaches the tape critical current. It should be noted that for low currents, the amplitude of the measured signals is very

low and it approaches the accuracy limit of the measurement system. In particular, in the compensated measure where a subtraction between two signals is performed, this can lead to misleading results. For the "*Exp_Compensation*" curve, the points with I_m lower than 0.35 are not reported since they could lead to misleading conclusions (some negative values are found, which have physically no meaning).

In Fig. 3.4.2(b), the experimental results presented in Fig. 3.4.2(a) are modified including the corrective factors, as described in *Section 2.4.5* and *Section 2.4.6*. This allows to compare the measurements before and after their correction to take into account the impact of the voltage measurement configuration. The convergence of the *"Exp_Distance_corrected"* curves improves: when $I_m > 0.4$ the experimental curves are in great accordance. The losses at low amplitudes for the *"Exp_Distance = 3/4 w_corrected"* curve remain higher than the other cases, which might be due to an imprecise measurement of the distance α. In fact, as shown in *Section 2.4.10*, when α is close to the tape edge the corrective factor $\eta_{per\ unit}$ is far from the asymptotic zone, and therefore a little imprecision in the measurement of α might lead to an imprecise correction of the measurement. In any case, the action of the corrective factor $\eta_{per\ unit}$ tends to lower down all the *"Exp_Distance"* curves, as already demonstrated in *Section 2.4.10*. Instead, the power values shown in the "*Exp_Compensation_corrected*" curve are considerably enhanced compared to the non-corrected curve (which is also conclusion for the corrective factor $\gamma_{per\ unit}$ presented in *Section 2.4.10*). Compared to the *"Exp_Distance = 11/2 w_corrected"* curve, the power dissipation of the "*Exp_Compensation_corrected*" curve is only 1.25 times lower when $I_m = 0.35$, 1.15 times higher when $I_m = 0.45$ and 1.45 times higher when $I_m = 0.85$. The introduction of the corrective factors greatly improves the convergence of the measurements in the two different configurations. It is worth noting that in this case, the power dissipations reported for the "*Exp_Compensation_corrected*" curve are higher than those reported for the *"Exp_Distance"* curves, when $I_m > 0.4$. The curves slightly diverge when I_m tends to I_c, indicating a possible "excessive" correction by the term $\gamma_{per\ unit}$. This might be due to an incorrect measurement of the value of β, which is considered to correspond precisely to the tape middle-axis. This evaluation could be wrong since the soldering of the voltage taps onto the tape surface are not punctual but quite spread across the tape width, which can lead to an imprecise calculation of the $\gamma_{per\ unit}$ factor, whose impact varies greatly and very rapidly when β approaches the tape edges.
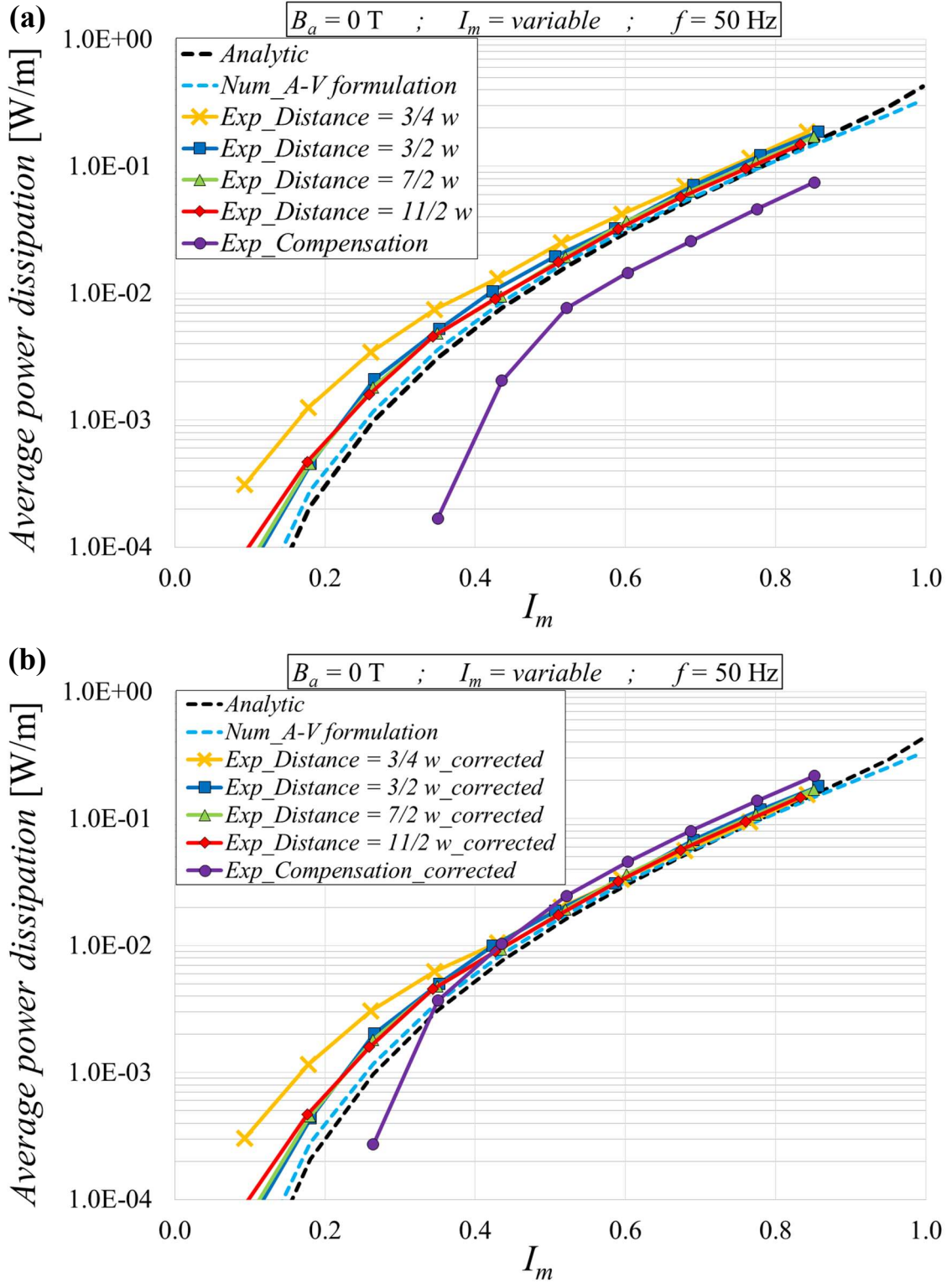
Figure 3.4.2. *Average power dissipation in the SuNAM SCN04 tape due to an AC transport current, measured in different experimental configurations and computed with the numerical model based on the A-V formulation. The frequency is set to 50 Hz and I_m is varied. In (a) the corrective factors are not applied to the measurements, while they are included in the experimental curves in (b). The figures are in semi-logarithmic scale.*

Fig. 3.4.3(a) shows the transport losses measured experimentally, computed numerically and calculated analytically, with I_m set to 0.75 and varying the frequency. As in Fig. 3.4.2(a), the *"Exp_Distance"* curves tend to converge when increasing α. A good convergence seems to be reached for $\alpha = \frac{3}{2}w$, despite some differences are present, especially at high frequencies. However, the ordinate axis of the figure is in linear scale and the discrepancies are minor. Compared to the *"Exp_Distance = 11/2 w"* curve (assuming that this curve represents the case where convergence is surely reached), the losses in the *"Exp_Distance = 3/2 w"* case differ by at most 9% at 479 Hz. The "*Exp_Compensation*" curve is well below the other experimental curves for all frequencies, with losses that are around the half of those displayed in the *"Exp_Distance = 11/2 w"* curve. Compared to the numerical losses, the experimental curves exhibit some discrepancies. They are frequency dependent, decreasing when the frequency increases, but their trend is not linear as it is for the numerical results. The "*Exp_Distance*" curves are higher at low frequencies compared to the numerical curve and they decrease more steeply at high frequencies. Moreover, the range of frequencies for which the crossing point with the analytical curve (which is frequency independent) occurs, moves towards greater values: it passes from a value around 50 Hz for numerical losses, to a value around 200 ÷ 300 Hz for the measured losses. For the "*Exp_Compensation*" curve, this crossing point is not visible in the range tested.

Then, in Fig. 3.4.3(b), the experimental results presented in Fig. 3.4.3(a) are modified by including the corrective factors $\eta_{per\,unit}$ and $\gamma_{per\,unit}$. As expected, the convergence between the experimental curves improves. The *"Exp_Distance_corrected"* curves are closer to each other, in particular the *"Exp_Distance = 3/4 w_corrected"*. In fact, the impact of the corrective factor $\eta_{per\,unit}$ in lowering down the losses is greater as the distance α decreases. At the opposite, when $\alpha = \frac{11}{2}w$, almost no difference is visible before and after performing the correction, as the corrective factor is already in its asymptotic zone, approaching 0% of impact. Even in this case, some doubts arise in the estimation of $\alpha = \frac{3}{4}w$, since the curve moves from being the highest to the lowest of the *"Exp_Distance_corrected"* curves, indicating a possible over-estimation of the corrective factor due to some imprecisions in the assessment of α. The same uncertainty could be referred to the "*Exp_Compensation_corrected*" curve, whose correction greatly improves the convergence with the other experimental measurements (the discrepancies are now included between 7% and 20% compared to the *"Exp_Distance = 11/2 w_corrected"* curve) but it brings this curve to have the higher losses among the other experimental cases. This might be another proof of the difficulties in the correct estimation of β for narrow tapes, which impacts the calculation of $\gamma_{per\,unit}$. In any case, the presence of the corrective factors improves also the convergence between the experimental and the numerical results. Furthermore, the range of frequencies for which the meeting point with the analytical curve occurs is modified, now ranging around 80 ÷ 200 Hz.
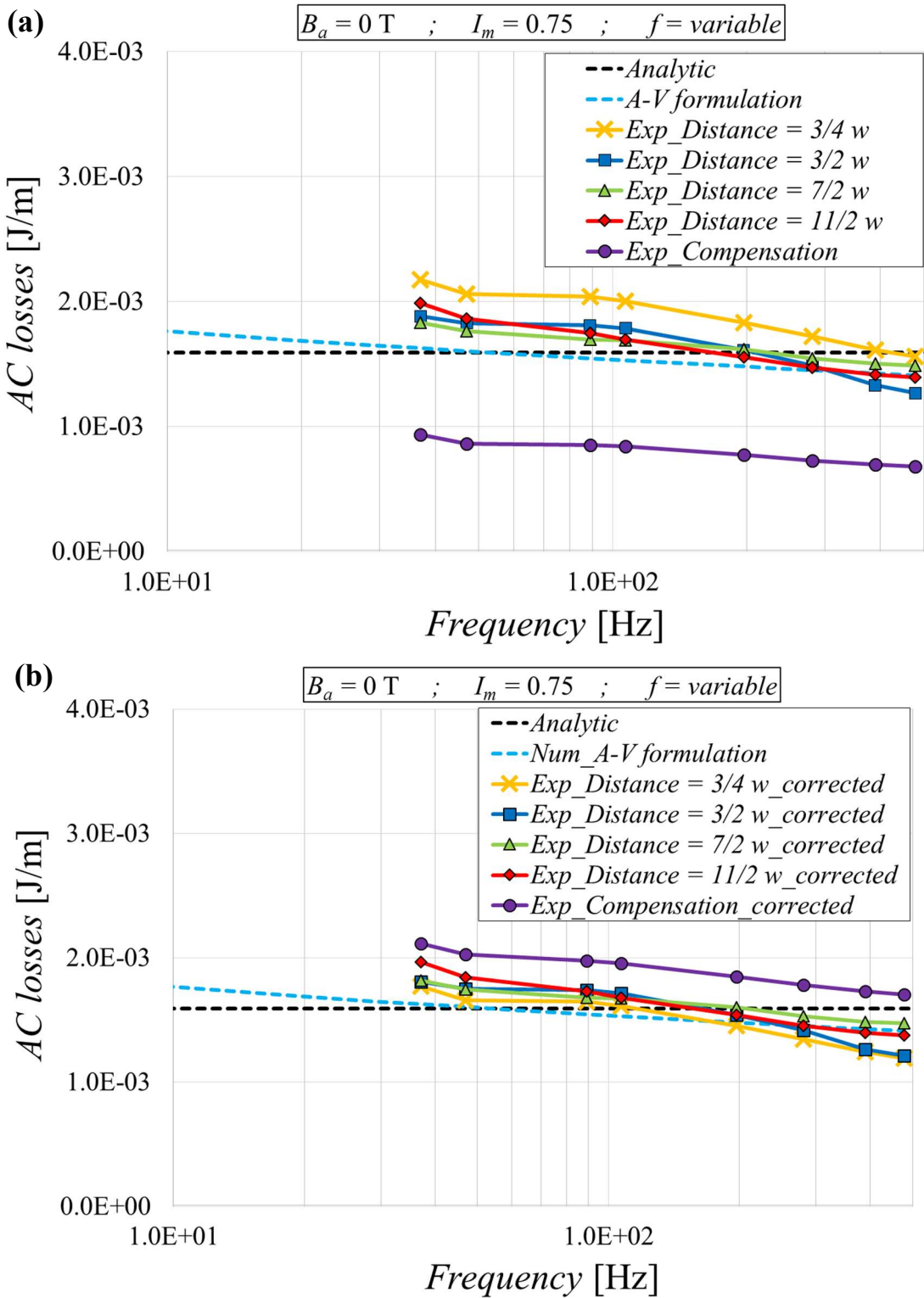
Figure 3.4.3. *Transport current AC losses in the SuNAM SCN04 tape, measured in different experimental configurations and computed with the numerical model based on the A-V formulation. I_m is set to 0.75 and the frequency is varied. In (a) the corrective factors are not applied to the measurements, while they are included in the experimental curves in (b). The figures are in semi-logarithmic scale.*

3.5.   Conclusions

This chapter has illustrated the experimental set-up for the measurement of the electromagnetic signals in a HTS tape subjected to an AC current and the post-processing technique not involving the use of a lock-in amplifier to determine the AC losses. The proposed method allows to increase the number of signal harmonics treated for the noise reduction, and to have a better control on the reconstructed voltage and current signals. The method was verified by comparing the experimental results achieved at the *University of Bologna* with those obtained by other laboratories on the same tape, using the lock-in amplifier.

The method has also been adopted to test the impact of different voltage measurement configurations. By increasing the distance from the tape middle axis at which the voltage taps are twisted together, the experimental measurements converge and approach the numerical results. It has also been verified how the use of the corrective factors obtained in *Chapter 2* improves the convergence between the experimental and the numerical results. Furthermore, despite the measurements performed with the alternative configuration involving a second compensation signal results more problematic, even in this case the experimental results approach the other curves when considering its specific corrective factor.

Future works on this topic would include the possibility to measure the magnetization losses in a HTS tape, taking into account the corrective factors due to the different measurement configurations, and to compare these results with the numerical calculations using the *A-V* formulation model, even for tapes including a ferromagnetic layer.

Concluded the analysis a tape level, in the next chapters the investigation moves to superconducting devices realized with HTS tapes. In particular, the NI configuration of inductive coils is analysed for the two winding techniques illustrated in *Section 1.6.1*: respectively the *pancake-wound* configuration in *Chapter 4* and the *layer-wound* configuration in *Chapter 5*. Before deriving the AC losses in insulated and NI coils, the electric behaviour of these windings is studied in steady-state conditions or in simpler time-varying regimes (current ramps).

Analysis of the impact of multiple superconductive joints inside a no-insulation HTS coil in a pancake-wound configuration

Following a bottom-up methodology, the analysis on coated conductors is followed by the study of HTS devices realized with these tapes, and in particular of their application in NI coils. Before testing these devices in AC conditions, some studies are performed to understand the current distribution and their electrical behaviour in steady-state or linear charge conditions.

With the purpose to investigate the so-called *defect-irrelevant* behaviour of NI coils [40] (introduced in *Section 1.6.2*), this chapter deals with a NI coil in a pancake-wound configuration, realized with a (RE)BCO tape in which some defects are intentionally introduced. A tape with good homogeneity in terms of critical current is selected. Before the winding phase, superconducting joints are inserted at precise locations along the tape length, in order to obtain resistive sections into the winding. The electrical resistance of the joints is measured through tests in liquid nitrogen and it is varied by changing the joint area. The coil is dry-cooled with a Gifford-McMahon (GM) cryocooler at temperatures included between 4.7 K and 80 K and then charged up to various operating currents with increasing ramp-rates. Voltage taps are used to measure the voltage profiles during tests. The measurements acquired at specific conditions (when the current is maintained constant for a sufficient long time to reach the regime conditions, and during the subsequent shut-down of the power supply), are used to derive the parameters of an equivalent lumped parameter circuit for the coil. The aim is to understand whether and how the insertion of faulty sections affects the electromagnetic performance of the winding.

The activity is carried out in collaboration with the *Applied Superconductivity Laboratory* (*ASL*) group directed by Prof. Seungyong Hahn at the *Seoul National University* (Seoul, South Korea). To Prof. Hahn and his collaborators go the sincerest thanks for their fundamental contribution.

4.1. *Preparatory phases for the NI pancake-wound coil*

Before the winding realization, it is necessary to select the HTS tape to be used and to set some geometric parameters of the coil.

4.1.1. *HTS tape homogeneity test*

The tape selected for the coil is the *SuNAM SCN04* tape, whose geometrical properties have already been presented in *Section 2.4.7*. The data about the homogeneity of the critical

current (at 77 K) along the tape length are provided by the manufacturer and kindly made available by the *ASL* group. Fig. 4.1.1.1 presents the critical current along the length of the lot acquired at *ASL* (108 m long). The red vertical lines represent the portion of tape used in this study, obtained by cutting from the lot a segment included between the 24 m position the 35.5 m position along the tape length. In this portion, the critical current variations are below 1.5%; therefore, the homogeneity of the virgin tape can be considered sufficiently high for this study. This is fundamental for the purposes of the analysis, since the only "desired" defects within the tape are those inserted intentionally through joints.
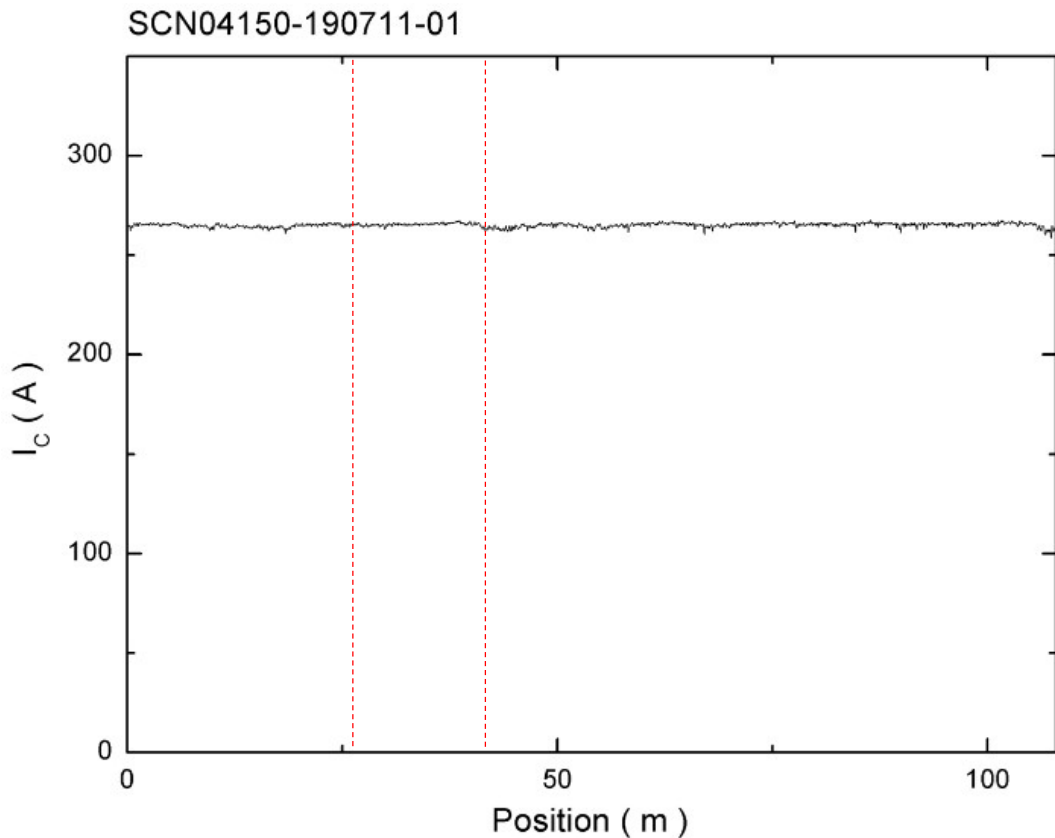
Figure 4.1.1.1. Critical current along the SuNAM SCN04 tape lot used in the study, provided by the manufacturer. The red lines highlight the extremities of the section used to wind the coil.

To confirm the data reported by the manufacturer and to verify whether the tape has been accidentally damaged during the manipulations occurred before the winding phase, the critical current is measured in a liquid nitrogen bath. The measurement is performed on a limited portion of the tape. A central section of the tape used for the winding, 30 cm long, is straightened on a rigid support and connected to the power supply using copper bars, while the remaining parts at both ends are carefully wound around two mandrels, also cooled in the nitrogen bath and kept in position to avoid exposing the tape to undesired stresses.

Two voltage taps are soldered at 10 cm from each other, and used to acquire the electric field signal. The signal wires are not perfectly twisted together and they do not follow exactly the same path inside the nitrogen container, therefore, they have slightly different temperatures. In order to reduce the *Seebeck effect* due to the configuration of the voltage taps [163], which can

affect the quality of the measure, the test is repeated twice reversing the polarity of the transport current generated by the power supply. The acquired data are depurated from the offset of the measurement device. Then, summing the signals with inverse polarity and halving the result (*i.e.* performing the mean value) the *Seebeck effect* can be reduced from measurements.

The critical current measured at the lower and the upper critical fields are respectively equal to 255.0 A and 268.5 A. The average I_c along the tape length displayed in Fig. 4.1.1.1 corresponds to 265.0 A; it is not known whether this value is calculated at the lower or upper critical field. However, it is in accordance with the values measured at *ASL* and this is considered sufficient to confirm that the tape has not been damaged. Thus, the data of Fig. 4.1.1.1 are assumed to be valid also for this study.
Lastly, the *n-value* measured is equal to 46.1.

4.1.2. NI pancake-wound coil design

The main parameters of the NI project coil are presented in Table 4.1.2.1. The table shows both the design parameters and those measured or recalculated after the winding phase.

Table 4.1.2.1. *Project and measured parameters of the NI pancake-wound coil.*

Parameter	Unit	Project value (before winding)	Measured/estimated value (after winding)
Inner radius (R_{int})	[mm]	20.0	20.0
Outer radius (R_{ext})	[mm]	25.9	26.7
Turn thickness (average between all the coil turns)	[μm]	130.0	145.6
Coil height (H_{coil})	[mm]	4.1	4.1
Number of turns		46	46
Tape length (neglecting the extra segments used in the winding phase)	[cm]	66.6	67.1
Inductance (estimated)	[μH]	151.0	150.0
Lowest J_c at 77 K inside the coil when I_{op} = 70 A (estimated)	[A/m^2]	$1.72 \cdot 10^8$	$1.76 \cdot 10^8$
B_z (0,0,0) at 77 K when I_{op} = 70 A (estimated)	[mT]	88.1	86.9

The single-pancake technique is used; thus, the tape height corresponds to the coil height. The number of turns is selected in order to maintain the tape length around 6 ÷ 7 m, for practical reasons, without considering the extra segments needed during the winding process and that are discarded when the coil is completely wound. It is worth noting that these extra sections, whose purpose is described in *Section 4.2.2*, do not serve the purpose of carrying current and

thus even low-quality tape can be used. The coil outer radius results larger than the project one, due to the presence of superconducting joints which increase the turn thickness in some sections. Moreover, the voltage taps technique adopted (described in *Section 2.4.3*) also affects the winding dimensions. Since the average thickness is enhanced, a longer tape is needed to wind the whole coil, kept fixed the number of turns.

Table 4.1.2.1 reports also the coil inductance, computed analytically by approximating the sum of all turns as a single conductor with a rectangular cross-section included between the inner and the outer radius of the winding.

When designing a superconducting coil, it is of great importance to estimate its operating margins, especially regarding the operating current (I_{op}), which should not exceed the safety margin selected in the design phase. In this study, I_{op} must not exceed the 70% of the coil I_c at a reference temperature (meant as the I_c computed for the turn having the lowest critical current density among all the turns of the winding, during the whole charging phase). This limit is relatively precautionary. In fact, it is calculated for an ideal coil without inhomogeneity, but it is then applied to a coil having low I_c sections. Furthermore, in an NI coil the hypothesis of uniform current distribution is less reasonable given the possibility for the current to flow radially. Thus, since the possibilities that the I_{op}/I_c safety margin could be practically exceed are greater in the project coil, the limit is set precautionary low.

The coil is tested at different temperatures, corresponding to different I_c values and maximum I_{op} during the experiments. However, to study the coil behaviour with temperature, the same current profiles are adopted during tests at the various temperatures. Therefore, in the design phase the calculation of the maximum I_{op} is carried out for the reference temperature of 77 K, which is close to the highest value adopted during tests (80 K) and at which the J_c (B_{mod}, θ_{field}) function of the tape, provided by the manufacturer, is computed.

To find the I_{op} limit to adopt for the test phase, an iterative computation is performed. Firstly, the self-field distribution inside the coil cross-section must be estimated, since the tape J_c strongly depends on its local value. In this work, the self-field is computed using a FEM code implemented in the MATLAB software and developed at the *University of Bologna*. The model solves the problem on the *x-z* plane of the Cartesian reference system shown in Fig. 4.1.2.1. The coil has a double symmetry: both along the central *z*-axis and along the median *x-y* plane. Thus, it is sufficient to simulate a quarter of the cross-section (the upper right quarter is selected), thus reducing the number of elements in the model. Moreover, the whole winding pack is approximated as a single conductor, in which a uniform current flows. These assumptions are valid if any inhomogeneity in the tape, included the presence of joints, is neglected.
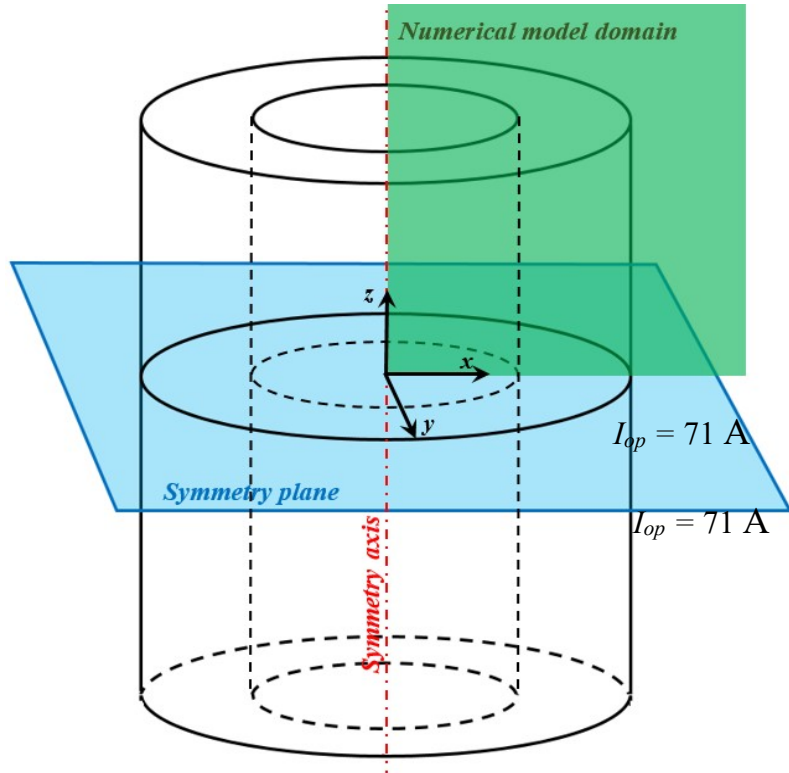
Figure 4.1.2.1. *Symmetry axis and plane for a NI pancake-wound coil. The green rectangle represents the portion of the coil cross-section used in the model.*

Secondly, it should be remembered that the tape self-field depends on the operating current. I_{op} affects the local critical current density into the coil and consequently, the current limit during the coil charging. It follows that the calculation must be iterated to obtain the maximum I_{op} at which the electromagnet can be charged without exceeding the safety criterion and, at the same time, to generate the project magnetic field amplitude. In this study, a target magnetic field is not imposed, but the scope is to maximize the field produced by the single-pancake coil in which the inner radius and the tape length are set within certain limits (consequently, all the geometric parameters are fixed). The I_{op} selected as a conservative limit at which the coil can be charged, corresponds to 70 A. It can be useful to the reader, to present the graphs about the final steps of the iterative process.

Fig. 4.1.2.2 shows the map of the coil self-field computed numerically at I_{op} equal to 70 A (left side) and 71 A (right side). The figure displays only the upper right quarter of the coil cross-section and its proximities. Fig. 4.1.2.2(a) and Fig. 4.1.2.2(c) present the field module (B_{mod}) maps. As expected, the field is greater at the inner surface of the coil and it decreases as the axial distance from the coil center increases. Comparing the scales of the two plots, the field peak is greater at 71 A, despite the difference between the two cases seems minor. Fig. 4.1.2.2(b) and Fig. 4.1.2.2(d) show the field orientation map, using arrows of normalized length. The field is parallel to the tape main face near the inner and outer surfaces of the coil (with opposite directions), while in the middle of the coil cross-section θ_{field} get closer to 90° (Fig. 2.4.7.14). The graphs are almost identical for both I_{op} cases.
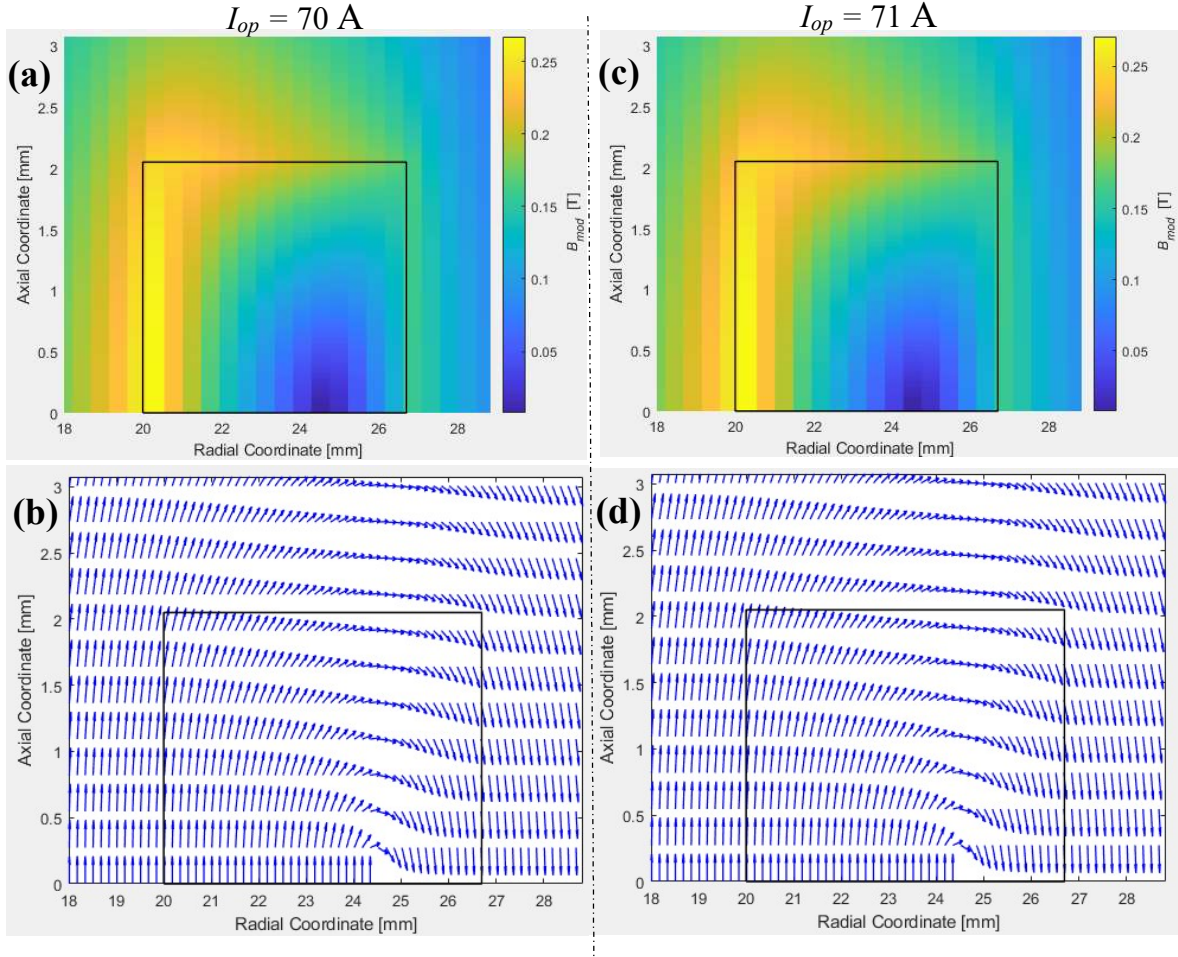
Figure 4.1.2.2. *Map of (a)-(c) the magnetic field module and (b)-(d) the magnetic field orientation generated by the NI pancake-wound coil at I_{op} = 70 A (left side) and I_{op} = 71 A (right side), computed numerically. The geometrical parameters are set accordingly to those measured after the winding phase. The black rectangle represents the contour of the upper quarter of the coil cross-section. The axes are not in scale.*

Then, supposing a uniform current distribution into the cross-section of the whole coil and knowing the J_c (B_{mod}, θ_{field}) function at 77 K [164], a map of the J/J_c ratio is obtained. Fig. 4.1.2.3 presents this map at (a) I_{op} = 70 A and at (b) I_{op} = 71 A, highlighting the position of each turn (considering an ideally uniform winding sequence). Labelling the turns from 1st to 46th, going from the inner to the outer radius of the coil, it results that the 31st and 32nd turns have the lowest J/J_c ratio. This is mainly due to the local transverse component of the magnetic field. While at I_{op} = 70 A the J/J_c ratio remains always below 0.8, at I_{op} = 71 A it locally exceeds this threshold. This indicates that at some locations the current passes the limit of 80% of I_c when I_{op} = 71 A, if the hypothesis of a uniformly distributed current in the tape is adopted. Therefore, to satisfy the design safety margins, I_{op} should not exceed 70 A during the charging phase of the coil.
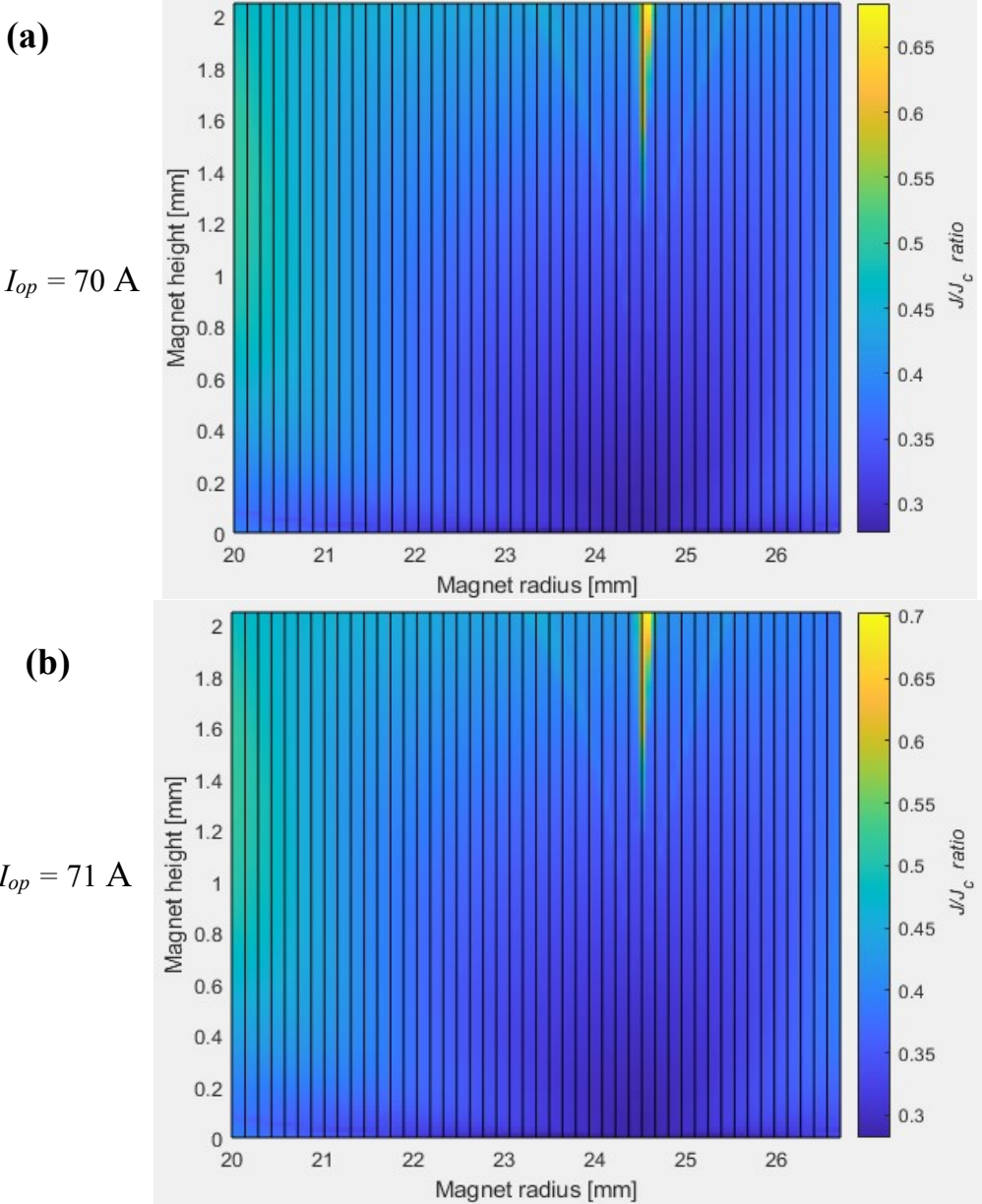
Figure 4.1.2.3. *Map of the J/J$_c$ ratio in the NI pancake-wound coil at (a) I$_{op}$ = 70 A and (b) I$_{op}$ = 71, computed numerically. The geometrical parameters are set accordingly to those measured after the winding phase. Each rectangle represents the contour of the cross-section of the turns belonging to the upper quarter of the coil. The axes are not in scale.*

Tab. 4.1.2.1 displays the lowest J_c at 77 K inside the coil when I_{op} = 70 A, using in model both the geometric parameters estimated before the winding and those measured after the winding. For the same I_{op} value, since the real coil is thicker than the design coil, it can sustain a higher current. However, this assumption is valid only if the winding pack is represented as a single conductor. In reality, the thickness of the superconducting layer of the tape is constant and the cross-section in which the current can flow does not vary. Thus, the J_c can give only a qualitative indication about the difference between the real and the design coil,

Furthermore, the coil parameters are set to maximize the magnetic field produced in its bore. Indicatively, the higher are both the operating current and the number of layers and the greater is the field.

Then, to investigate the *defect-irrelevant* behaviour in terms of magnetic field, the field amplitude computed numerically in the design phase for a defect-free coil is compared with the measurements performed in the project coil during the test phase. To carry out the measures, a uniaxial Hall sensor (directed along the z-axis of the coil) is used. The sensor could not be placed perfectly at the center of the winding bore during the instrumentation phase, thus the calculation of the field only at the center of the reference system ($B_z (0,0,0)$) may not be sufficient. It follows that at each iteration, the z-component of the magnetic field along the z-axis of the coil ($B_z (0,0,z)$) has to be computed.
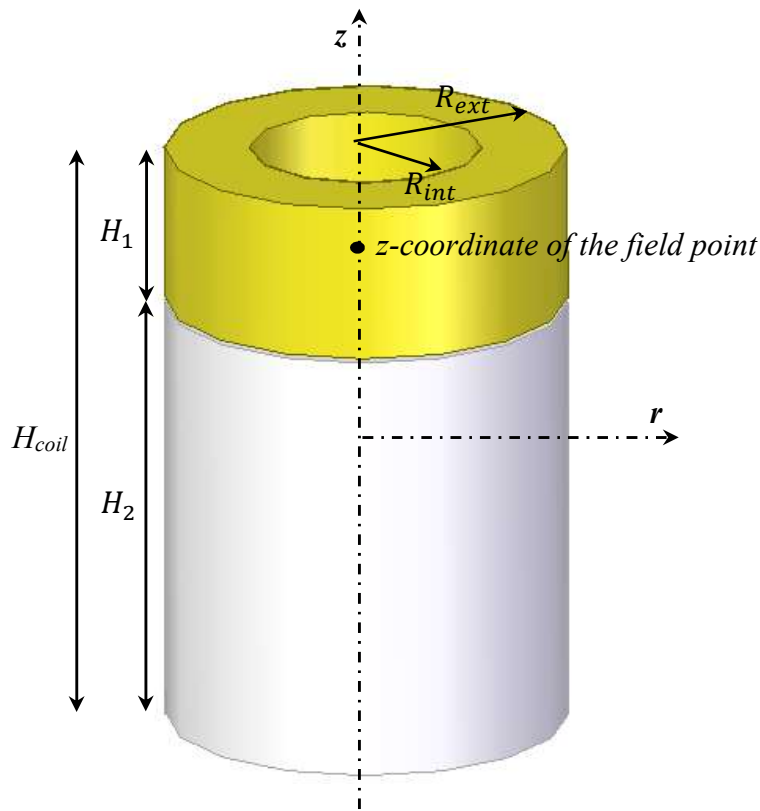
***Figure 4.1.2.4.** Schematic drawing of the coil with the parameter used to calculate the magnetic field generated in a generic field point of the central axis.*

The field generated by a coil in a generic point of the domain (*field point*) can be determined by dividing the winding into two sections, as shown in Fig. 4.1.2.4. The upper section has a height (H_1) included between the z-coordinate of the field point and the top of the coil. The lower section has a height (H_2) included between the bottom of the coil and the z-coordinate of the field point. In this way, $H_1 + H_2 = H_{coil}$ (the height of the whole coil). For the symmetry of the system, the field generated in the field point by the upper part of the coil is equal to half of the field produced there by a coil of double height having the field point as its center. Similarly, the field generated at the field point by the lower part corresponds to half of the field produced there by a coil of double height having the field point as its center. In the field point, the

magnetic field generated by both coil sections is acting. To compute $B_z(0,0,z)$ at a certain I_{op}, the following equation is implemented:

$$B_z(0,0,z) = \frac{1}{2}\,\mu_0\,J_{op}\,R_{int}\left[\beta_1\,ln\left(\frac{\alpha+\sqrt{\alpha^2+\beta_1^2}}{1+\sqrt{1+\beta_1^2}}\right) + \beta_2\,ln\left(\frac{\alpha+\sqrt{\alpha^2+\beta_2^2}}{1+\sqrt{1+\beta_2^2}}\right)\right] \qquad (4.1.2.1)$$

$$\alpha = \frac{R_{ext}}{R_{int}} \quad,\quad J_{op} = \frac{I_{op}\,N_{turns}}{H_{coil}\,(R_{ext}-R_{int})} \quad,\quad \beta_1 = \frac{z}{R_{int}} \quad,\quad \beta_2 = \frac{z}{R_{int}}$$

where N_{turns} is the number of turns in the single-pancake coil.

Fig. 4.1.2.5 shows $B_z(0,0,z)$ computed at I_{op} = 70 A. As expected, the field is maximum at the coil center and it decreases with the distance, although within the height of the coil (from -2.0 mm to 2.0 mm) the variations are less than 1%. The peak field obtainable without exceeding the safety margins (*i.e.* at I_{op} = 70 A), is reported in Tab. 4.1.2.1, using both the geometrical parameter estimated before the winding and those measured after the winding phase.
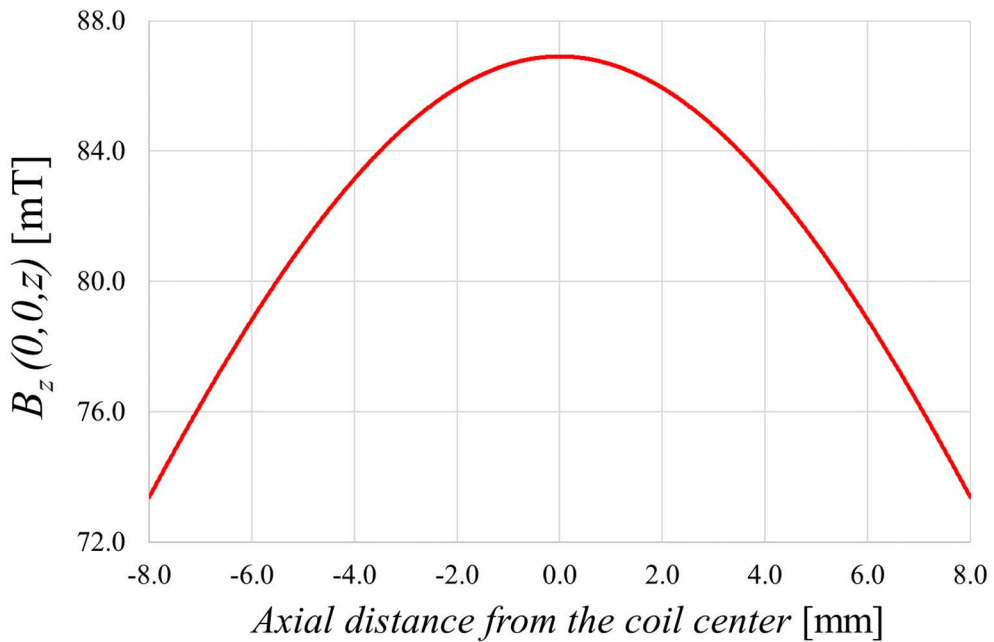
Figure 4.1.2.5. *Numerical calculation of the z-component of the magnetic field produced in the central z- axis of the single-pancake coil at I_{op} = 70 A. The geometrical parameters are set accordingly to those measured after the winding phase.*

4.2. NI pancake-wound coil realization

To realize the project coil, superconductive joints are firstly realized in the tape; then, after the winding phase around the mandrel, the coil is instrumented. All passages are described in the following sections.

4.2.1. Superconducting joints

As anticipated, the insertion of defective areas in the coil is performed by jointing several tape segments to obtain the spool used in the winding phase. For the project coil, 3 joints are realized, thus requiring 4 tape sections to be jointed together. In the design phase, the length of each section is selected with the following criteria.

First, once the sections are jointed together, the tape should not result shorter than the length reported in Table 4.1.2.1. The design length of the last section is increased by 30 cm, to take into account for the additional length required for the connection with the current lead.

Second, the lengths of the sections affect the position of each joint within the coil. In the design phase, it is settled to avoid placing the joints close to the 31st and 32nd turns of the coil, the areas with the lower critical current density, as shown in Fig. 4.1.2.3. Moreover, it is aimed to locate the center of each joint (*i.e.* the half of their lengths) at an angle equal to $\frac{2}{3}\pi$ with respect to the others. This should reduce the possibility of the defective areas to affect each other, and would allow the current to bypass a defective region without being strongly affected by the presence of a second joint. The length of the 1st, 2nd, 3rd and 4th sections jointed together are respectively equal to: 200 cm, 138 cm, 240 cm and 141 cm. These sections are labelled from the one in direct contact with the mandrel up to the outermost one.

Then, the superconducting joint configuration to be used for HTS tape is examined. Two different configurations are examined: lap joints and bridge joints [165].
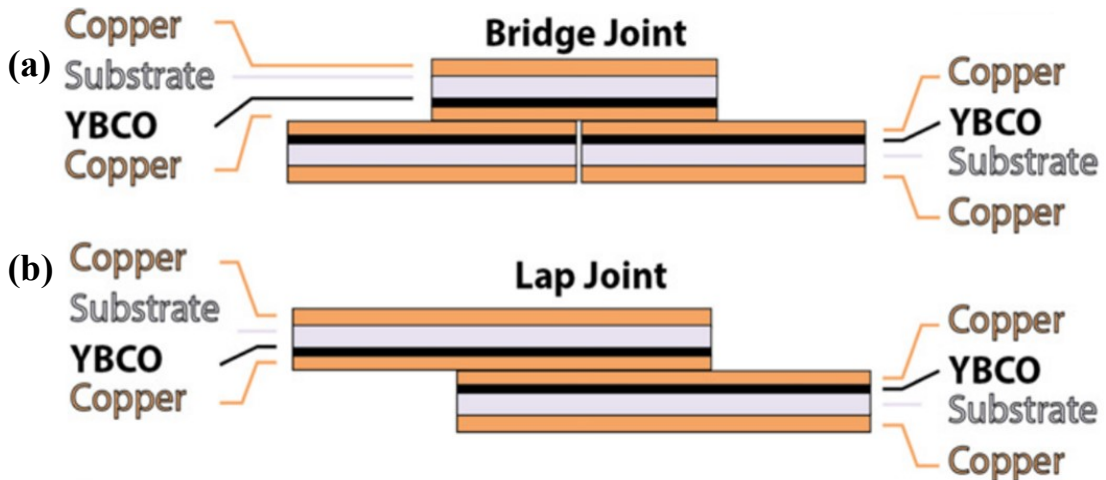
***Figure 4.2.1.1**. (a) Bridge joint and (b) lap joint configurations [165].*

In the bridge joint configuration, two tape sections are aligned along their narrowest side, as displayed in Fig. 4.2.1.1(a). Then, a third shorter segment of tape, usually coming from the same lot, is soldered on top of both sections so as the current can flow from one section to the other by crossing this third segment. Fig. 4.2.1.2 shows a bridge joint realized using two segments of the *SuNAM SCN04150* with a bridge section of length equal to 3 cm.
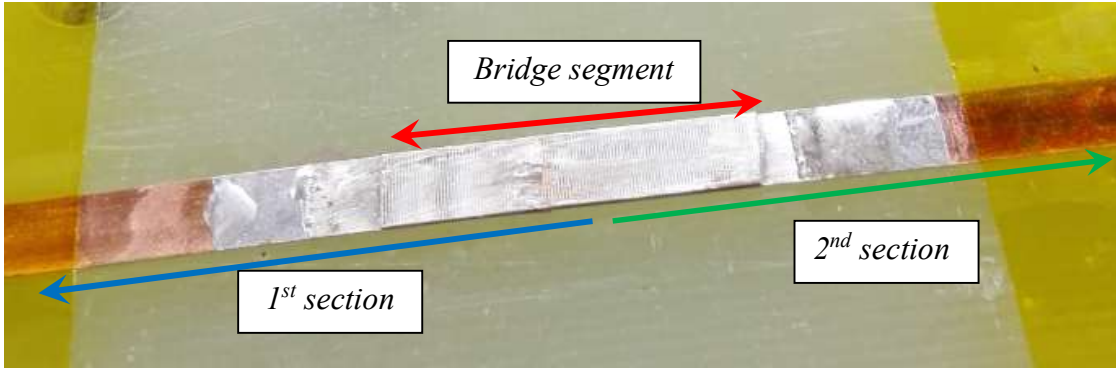
Figure 4.2.1.2. Bridge joint realized using the SuNAM SCN04 tape.

Despite this configuration is widely used for HTS windings [166 – 169], some problems have arisen during the preliminary tests carried in this study. Fig. 4.2.1.3 shows two photos taken after the manual winding of two distinct tapes around the mandrel of the coil (2 cm of radius) in which a bridge joint of length equal to (a) 5 cm and (b) 3 cm is inserted. Due to the small bending radius, the bridge joints appears to be damaged during the winding phase. In particular, the ends of the bridge joints are not perfectly folded around the mandrel (some light is visible between the mandrel and the winding). This can lead to poor electrical performance of the joint, to the tape delamination and to damage to the turns wound above them. For these reasons, it is decided to avoid the use of the bridge joint configuration.
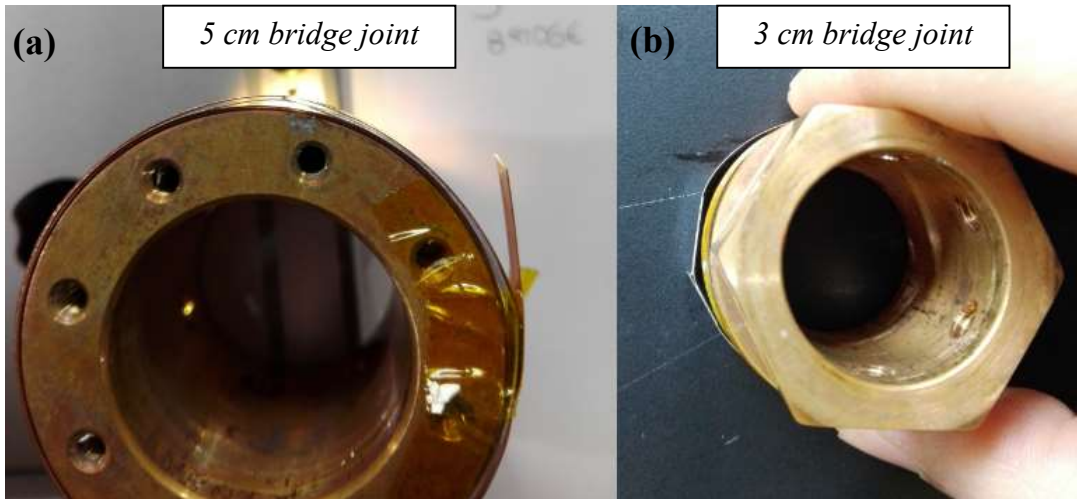
Figure 4.2.1.3. SuNAM SCN04 tape with bridge joints of length equal to (a) 5 cm (b) and 3 cm (right) wound around a mandrel having an outer radius of 2 cm.

In the lap joints configuration instead, two tape sections are connected to each other without using a third segment, but overlapping and soldering the sections along their length, as presented in Fig. 4.2.1.1(b). Fig. 4.2.1.4 shows two photos taken before and after realizing a lap joint between two sections of the *SuNAM SCN04150* tape. It is verified that the lap joint configuration suits better with the mandrel dimensions used in this study.
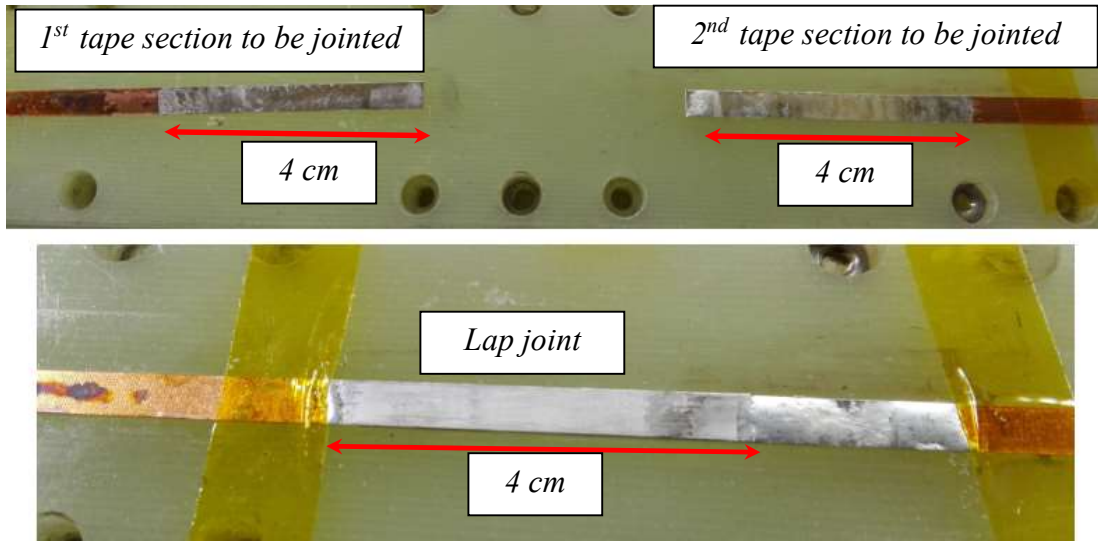
Figure 4.2.1.4. *Lap joint realized using the SuNAM SCN04 tape.*

However, when realizing lap joints, care should be taken regarding which surface of each tape section should face the joint area, since it affects the contact electrical resistance. In fact, the cross-section of a HTS tape is generally not symmetrical (see Fig. 2.4.7.1 for the *SuNAM SCN04* tape), and two different surfaces can be identified: one closer to the superconducting layer and one closer to the substrate. Usually, the lowest contact resistance in a joint is achieved by assuring that both tapes are facing the surfaces closer to their superconducting layer (*SC-SC* case). This prevents current from flowing through the substrate of one of the two tape, which has usually a higher resistivity and thickness compared to the other layers. Thus, when sectioning a common lap joint, the cross-sections of the two sections are mirrored, as shown in Fig. 4.2.1.5(a).
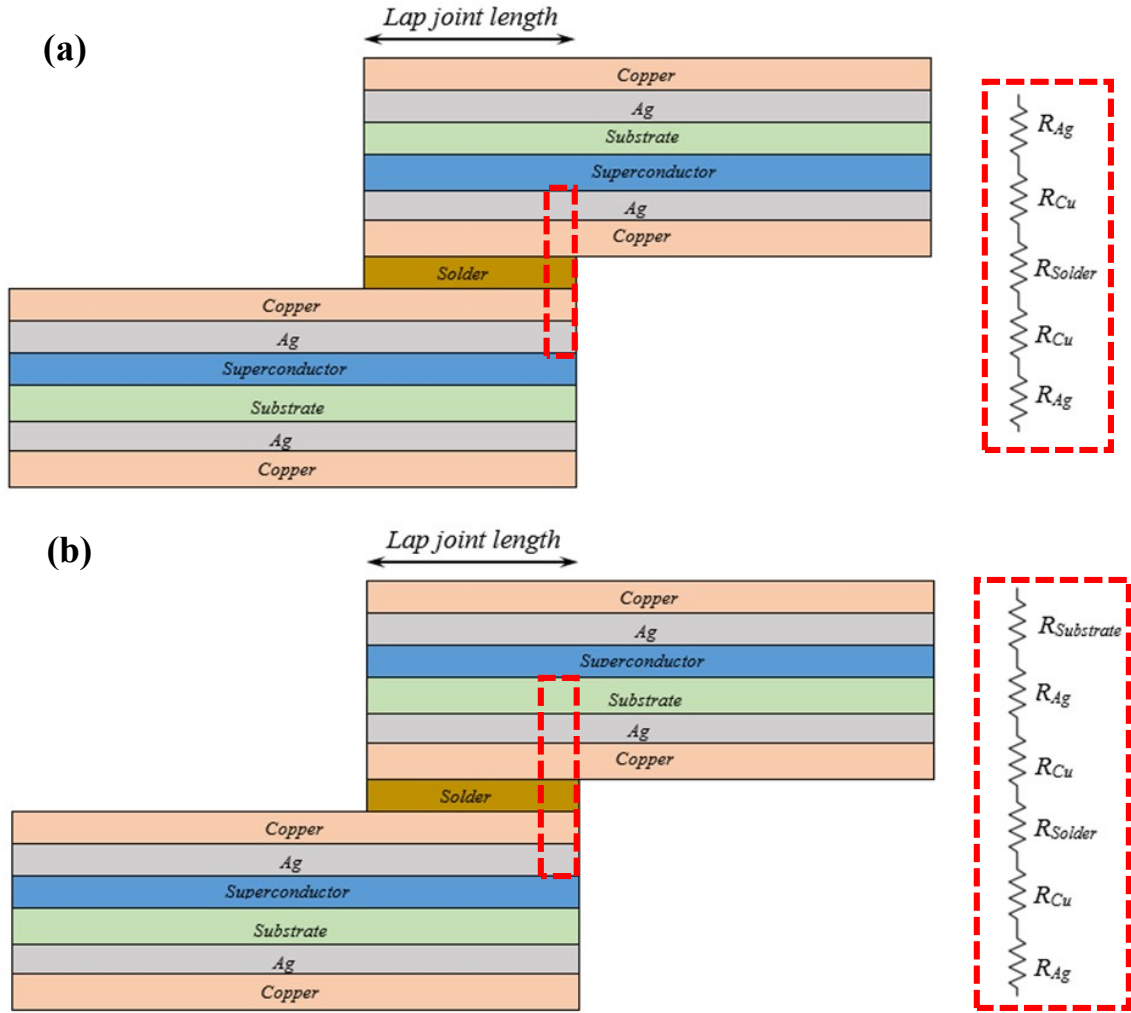
Figure 4.2.1.5*. Cross-section of a lap joint realized with two sections of the SuNAM SCN04 tape in (a) the S-SC case and (b) in the SC-Sub case. The electrical resistances involved in each case are shown, neglecting the contact resistances.*

However, this mirroring can increase the level of complexity when analysing a coil using 2-D or 3-D models. In fact, it is necessary to take into account that the stacking sequence of the tape is inverted at each joint in the winding. To avoid this problem, lap joints can be realized facing the superconductive side of one section towards the substrate side of the other section (*SC-Sub* case), as in Fig. 4.2.1.5(b). This alternative configuration enhances the electrical resistance of the joint since the current has to flow through at least one additional resistance ($R_{substrate}$) to flow from one tape to the other. In order to quantify the resistance enhancement, a preliminary test is carried out to measure the electrical resistance of two lap joints in the *SC-SC* and the *SC-Sub* cases, both having a joint length of 4 cm. Since the superconductive face of the *SuNAM SCN04* tape is not easily identifiable (the tape was remove from its original spool and its original bending was lost), a limited segment at the end of each tape section is delaminated using a cutter. This segment is then discarded. The superconducting layer differs from the substrate since it has a darker and easily identifiable colouring, as shown in Figure 4.2.1.6. The resistance tests are performed in liquid nitrogen bath, increasing I_{op} up to 220 A and measuring the resistance with the 4-terminal technique.
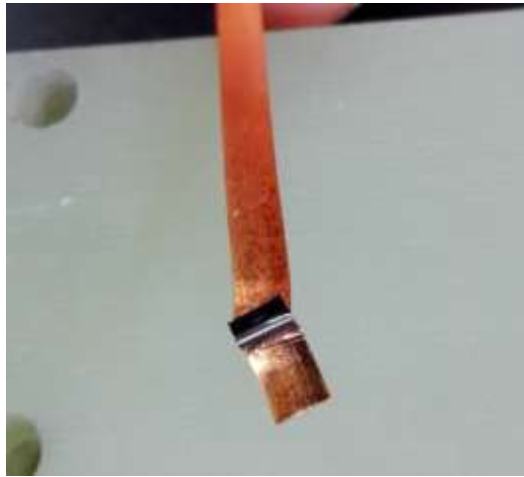
Figure 4.2.1.6. *Delamination test to identify the superconducting layer location inside the SuNAM SCN04150 tape.*

Fig. 4.2.1.7 presents the electrical resistance measured in the two cases. The electrical resistance in the *SC-Sub* case is 3 times higher compared to the *SC-SC* case (2.1 μΩ and 0.7 μΩ, respectively). Since this work does not focus on the realization of high quality joints, their difference is considered tolerable. Therefore, it is decided to realize lap joints in the *SC-Sub* configuration. This facilitates the comparison between the experimental measurements and the model results.
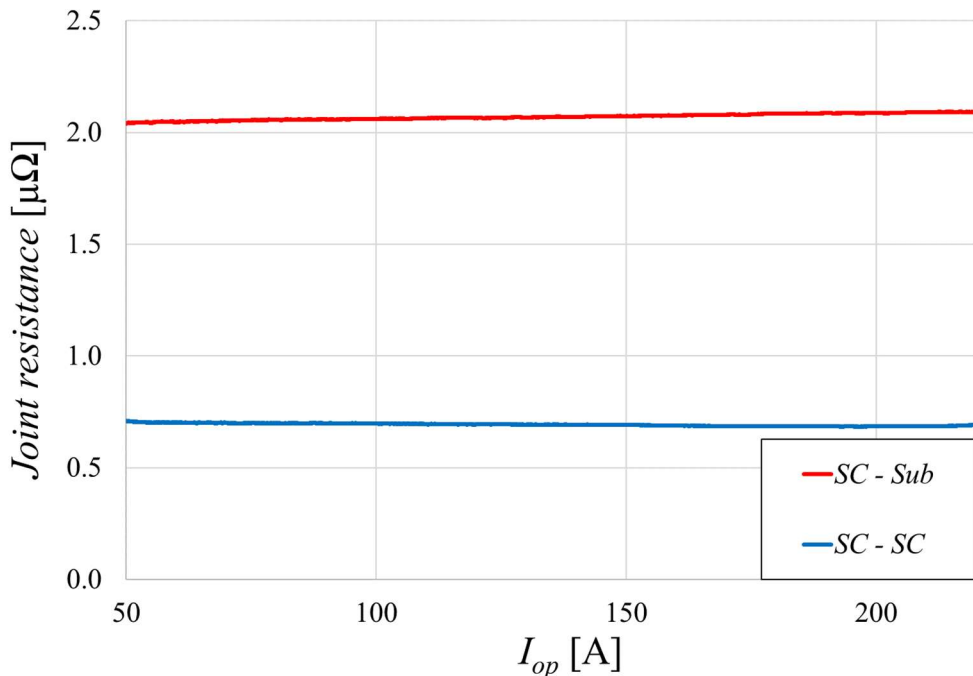
Figure 4.2.1.7. *Lap joint resistance measured in the SC-SC and the SC-Sub cases varying I_{op}.*

It is possible to resume the steps performed to realize a lap joint as follows:

➤ Identification of the superconductive side of both tape sections;

➤ Cleaning the contact surfaces using a cloth soaked in alcohol;

- ➢ Spreading a layer of flux agent to facilitate the soldering;

- ➢ Spreading a layer of indium onto both contact surfaces using a welding machine with a flat tip, up to a temperature of 473 K (low enough to melt the indium block without damaging the tape);

- ➢ Cleaning of the contact surfaces with a cloth soaked in alcohol;

- ➢ Overlapping the two surfaces for a given length, with particular care of their alignment;

- ➢ Spreading a layer of indium onto both sides of the joint area, applying homogenous pressure in order to melt the indium layer deposited inside the joint.

For the work, it is considered interesting to insert defects of different entity into the coil. The defects/joints are labelled as 1st, 2nd and 3rd joint going from the innermost to the outermost locations inside the pancake coil. The contact area between each couple of sections (*i.e.* the joint length) is set to 4 cm, 6 cm and 8 cm, as reported in Tab. 4.2.1.1. Since the joint resistance is inversely proportional to the contact area, 3 different resistances are obtained. Theoretically, when doubling the soldering area, the joint resistance should be halved. Anyway, the electrical resistivity can vary due to several inhomogeneity factors, such as the pressure during soldering, the solder thickness and the surface cleanliness. Thus, it is preferable to measure directly the resistance of each joint. Fig. 4.1.2.8 shows the experimental set-up used for this measurement. A portion of the tape near to the joint is straightened on a flat surface and connected to the power supply using copper bars. A 4-terminal technique is adopted. The measures are performed at 77 K in liquid nitrogen bath.
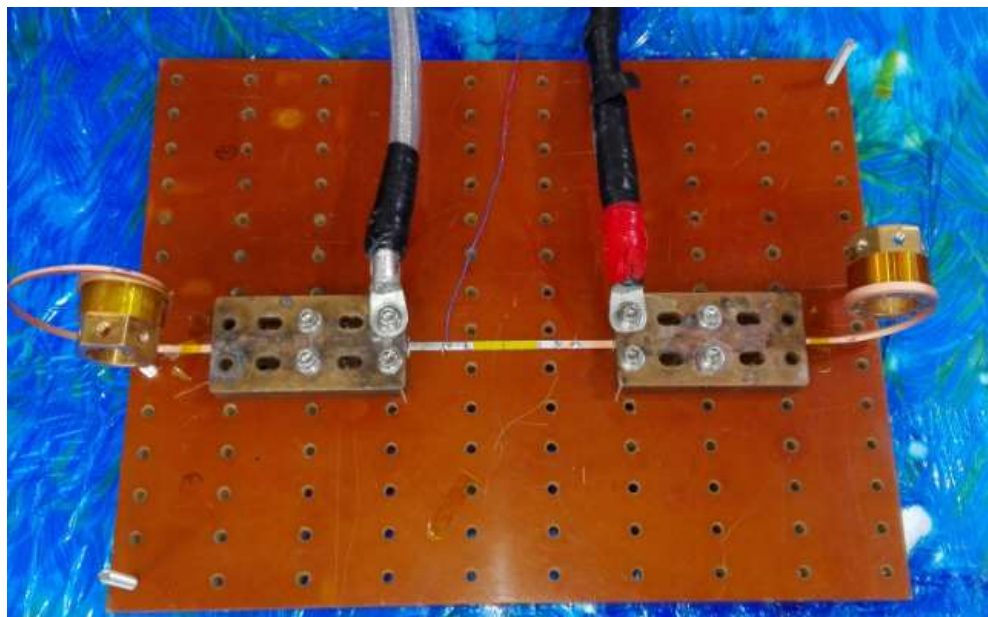
Figure 4.2.1.8. Experimental set-up for the measurement of the electrical resistance of one of the lap joint inserted into the tape.

Fig. 4.2.1.9 presents the experimental results for (a) the 1st and 2nd joints together and (b) the 3rd joint alone, varying I_{op}. The 3rd joint resistance is presented in a separate plot since the scale is logarithmic. The resistances are measured before the coil winding and at end of the whole

study, when the coil is unwound and the tape can be straightened again to perform resistance measurements. The average values of each resistance at different I_{op} is displayed in Tab. 4.2.1.1.
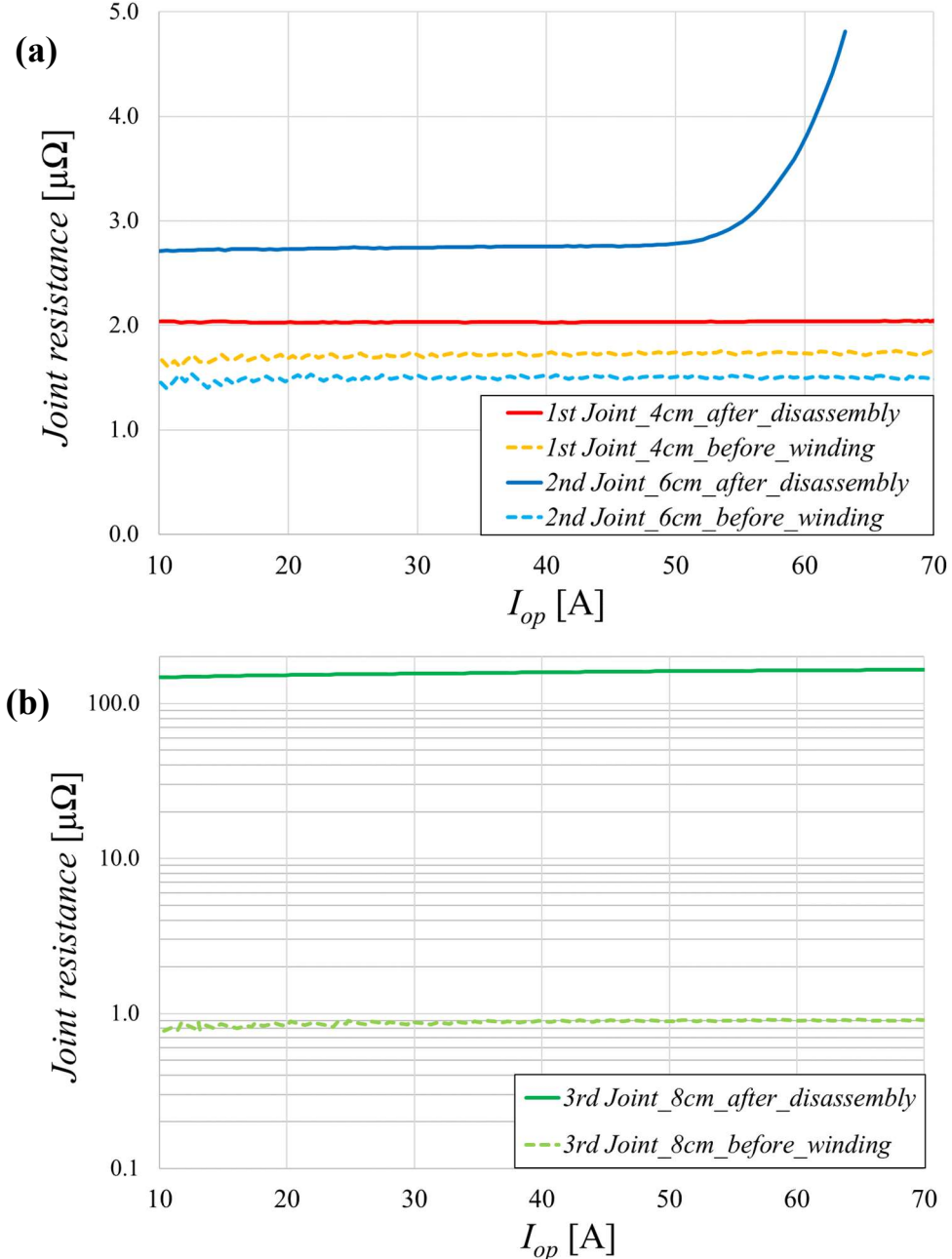
Figure 4.2.1.9. *Lap joint resistance at 77 K varying I_{op} before the coil winding and after the coil disassembly, for (a) the 1st and 2nd joints and (b) for the 3rd joint. Note that the scale in (b) is logarithmic.*

With the exception of the resistance measured for the 2nd joint after the coil disassembly, for which the average operation is performed up to 50 A only, the resistances are almost constant with the current. The slight reduction at low I_{op} amplitudes could be due to the sensitivity of the DAQ system, since to a small I_{op} corresponds a small voltage signal. As expected, the resistances measured before the coil winding are greater for shorter joint lengths. To better compare the 3 joints, Tab. 4.2.1.1 reports the product between the measured resistance and the

length of each joint, a parameter which should be theoretically identical if none of the aforementioned homogeneity problems would arise during the jointing procedure. Before the coil winding, this parameter is similar for all joints (it goes from 7 to 9 $\mu\Omega$ cm), which proves the good homogeneity maintained during the jointing procedure. However, the resistances measured after disassembling the coil are greater compared to those measured in the previous phase. In particular, compared to the pre-winding measurements, the resistance of the 1st joint increases by 17%, that of the 2nd joint by 83%, while that of 3rd joint increases by 173 times. It is suggested that these sections have been damaged during the winding or the test phases. Since it has not been possible to measure directly the joint resistances during the coil tests, the values measured after the coil disassembly are considered valid for the whole test phase.

It is worth noting how the resistance of the 3rd joint undergoes a very substantial increase compared to the pre-winding measurements. Normally, in an insulated coil, it would be necessary to replace this section or the entire coil. However, the presence of a damaged section of such extent does not affect the quality of the study, but represents the case study of an NI coil in which the performances of the inner section are compromised during the coil operations. Finally, it is worth noting that, after the coil disassembly, the resistance of the 2nd joint is no longer linear with the current, but has a typically superconducting transition when I_{op} exceeds 50 A of amplitude. It can be deduced that in the 2nd joint, in addition to a damaging occurred to the joint of a verifiable but not remarkable entity, a damaging has also occurred in at least one of the superconducting layers of the two jointed tapes, since its critical current has significantly degraded. Again, while for an insulated coil such problem would force to replace the section involved, this additional defect could be useful to verify the *defect-irrelevant* behaviour of a NI coil.

Table 4.2.1.1. Parameters of the lap joints inserted in the NI project coil.

| | Length | Before coil winding | | After coil disassembly | |
| | | Resistance | Resistance · length | Resistance | Resistance · length |
	[cm]	[$\mu\Omega$]	[$\mu\Omega \cdot$ cm]	[$\mu\Omega$]	[$\mu\Omega \cdot$ cm]
1st joint	4.0	1.74	6.96	2.04	8.16
2nd joint	6.0	1.50	9.00	2.75	16.50
3rd joint	8.0	0.91	7.28	157.35	1258.80

4.2.2. Winding phase

Since the project coil is realized in a single-pancake configuration, the tape end located in the innermost turn cannot be connected directly with the current leads (see *Section 1.6.1*). Thus, the current lead is screwed to the mandrel itself, made of highly conductive copper, while the superconducting tape is soldered to the mandrel outer surface, ensuring a regular current flow. Fig. 4.2.2.1 shows a picture of the mandrel and its connection zones.

First, to solder the HTS tape into the mandrel, an indium layer is spread on both the HTS tape connection surface and on the mandrel outer surface. Then, the whole mandrel is heat up to a temperature equal to 523 K using a heating plate. In fact, a regular welding machine would not be sufficient to melt homogeneously the indium layer, since the great thermal diffusivity of the copper mandrel would draw away the heat very quickly from the locally heated area. Immediately after turning off the heating plate, the innermost turn of the winding is tightly wound around the heated mandrel and kept in contact manually with its surface for long enough to solder. The length of the soldered section covers almost the whole inner turn.

Connection zone with a current lead.

Connection zone with the HTS tape.
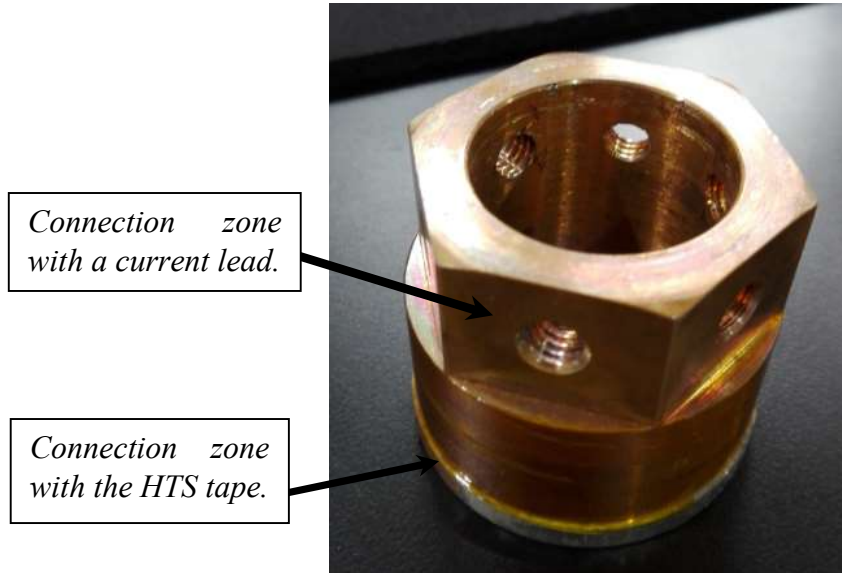
Figure 4.2.2.1. Copper mandrel and its connection with the current lead and the HTS tape.

Figure 4.2.2.2. Winding machine available at ASL, used in the study.

Then, the whole coil is wound using the winding machine shown in Fig. 4.2.2.2. The machine exerts a weight on the tape equal to 1.5 Kg, which corresponds to a winding force of 14.7 N. This value is considered sufficiently high to ensure a good contact between the turns and

guarantee a low turn-to-turn resistivity [170], but not excessive to prevent damaging the joint sections. The winding speed is equal to 5 rpm.

As anticipated in *Section 4.1.2*, the winding machine requires some additional length for the outermost end of the coil. This is necessary to maintain constant the tension on the tape while it is wound around the mandrel and simultaneously unwound from its original bobbin. This extra section serves only a mechanical purpose and is not used to transport current. Therefore, a low-quality tape can be used. It comes from the same lot but it is already manipulated during previous tests. The extra section is jointed to the outermost end of the tape (sized in the design phase to consider this additional joint length), and then cut off at the end of the winding phase, before connecting the tape with the current lead.
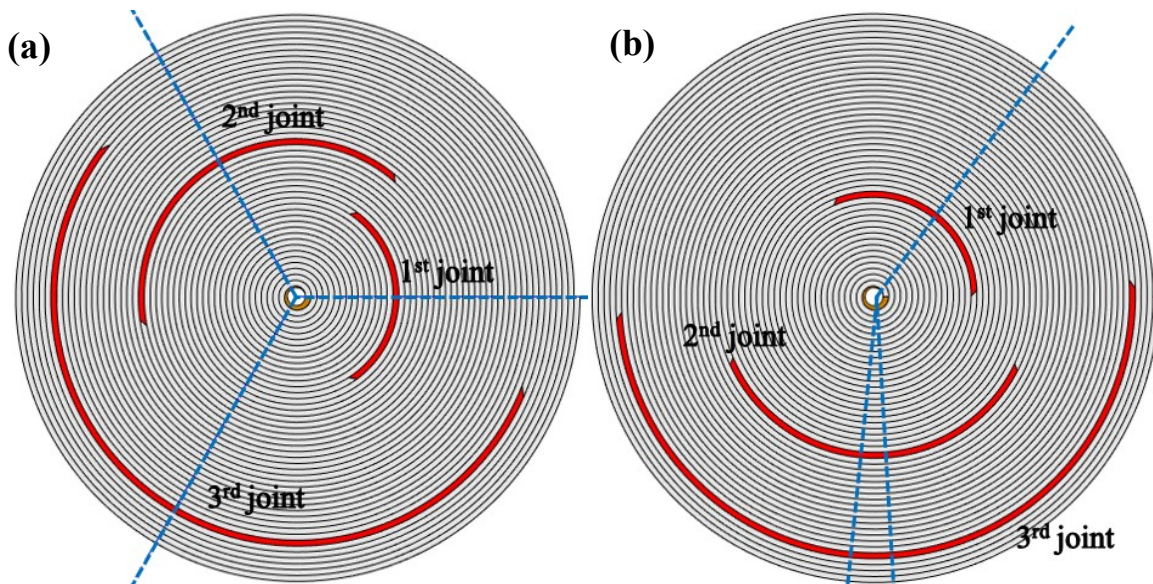
Figure 4.2.2.3*. Scheme of the joints location (in red) within the project coil, (a) as estimated in the design phase and (b) as obtained after the winding phase. The blue lines connect the coil center with the center of each joint. The coil dimensions are not in scale.*

Moreover, the winding machine is able to calculate the length of conductor used and the number of turns realized. This feature is used to establish the joints location inside the coil, to verify if their arrangement matches with that estimated in the design phase. Fig. 4.2.2.3 presents a scheme of the joints location within the coil, (a) as estimated in the design phase and (b) as obtained after the winding phase. To improve the figure readability, the tape thickness is scaled up by 10 times compared to the other geometrical parameters. As visible, the measured joints location does not match the design one. This is due to the coil inhomogeneities which are very difficult to quantify correctly in the design phase. For example, in the design phase the fact that the joints thickness is more than double the thickness of a single tape is neglected, as well as the presence of voltage taps creating unwanted spacing between turns. Therefore, the lengths selected for the 4 sections is slightly inaccurate. Fig. 2.2.2.4 shows a photo of the project coil at the end of the winding phase. The outermost turns shown are not part of the project coil but are only used in the winding phase. They are manually wound around the winding to maintain compactness, and they are removed to connect one coil end to the current supply.

In Fig. 4.2.2.4, empty spaces are evident inside the coil, as well as thicker areas due to joints and the voltage taps. These inaccuracies cause also the joints not to be equally angular spaced,

i.e. the angle included between the center of each couple of joints does not correspond to $\frac{2}{3}\pi$. In particular, the 2nd and 3rd joints are quite close to each other in angular terms. However, several turns of distance are maintained between the two joints, a condition that is considered sufficient to avoid that, in the area of the coil included between the two joints, the current distribution can be affected by the proximity of both defects. Furthermore, it is verified that none of the joints is located in the 31st and 32nd turns, the most critical areas in terms of transport current. In fact, the locations of the 1st, 2nd and 3rd joints correspond respectively to the 15th, 24th and 39th turn inside the coil.
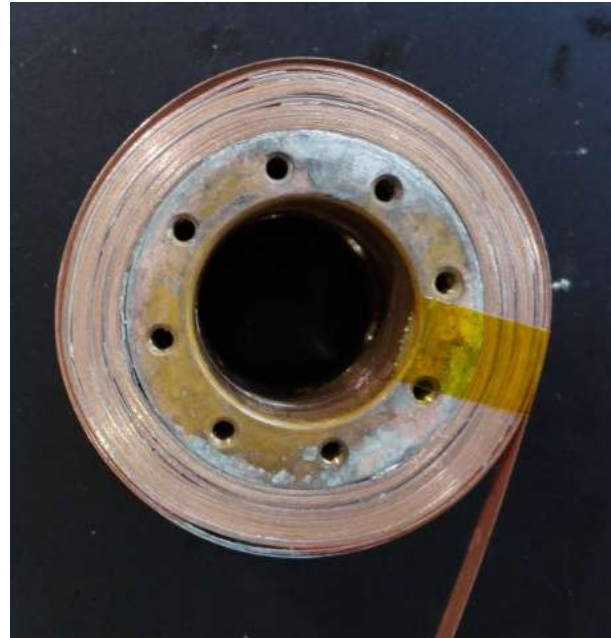
Figure 4.2.2.4*. Lower view of the project coil at the end of the winding phase.*

4.2.3. Instrumentation phase

The coil behaviour during tests is monitored by voltage taps, placed inside the coil during the winding phase. First, an investigation is carried out on how to arrange the voltage taps. Two main voltage taps configurations are considered, reported in Fig. 4.2.3.1.

The commonly used voltage tap configuration (Fig.4.2.3.1(a)) consists in a signal wire soldered directly onto the tape surface inside the coil. The technique adopted in this work is slightly different. During winding, a short tape segment at the same is placed at the same location designed for the soldering of a "usual" voltage tap. The tape segment is cut from the same lot of the winding tape. The segment is positioned transversely with respect to the winding direction and with its superconducting side facing the turn where the voltage signal is intended to be measured (see Fig.4.2.3.1(b)). An indium sheet is placed in the insertion area inside the coil, to homogenize the electrical contact. The whole superconducting face of the additional segment is considered equipotential with respect to the turn surface at the *reference position* inside the winding. Subsequently, a signal wire is soldered at the top of the short segment, outside the coil. Compared to the commonly used voltage taps configuration, this alternative

technique avoids the presence of soldered wires inside the coil. In fact, wires unsoldering can occur when the coil is rapidly cooled down at cryogenic temperatures. If the wire is soldered outside the coil, it can be easily repositioned without requiring any unwinding. Moreover, the alternative configuration allows soldering all the wires after the winding phase, preventing them from being a potential obstacle for the proper functioning of the winding machine.
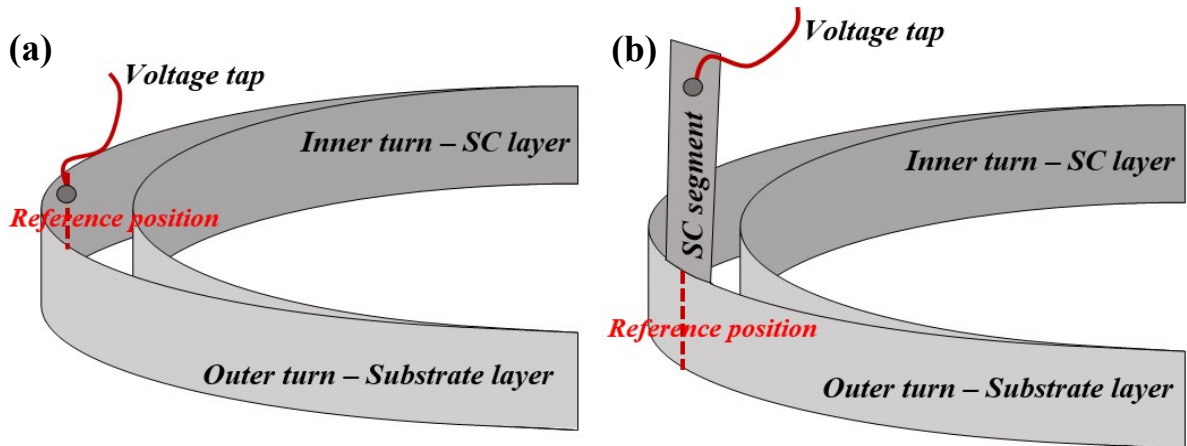
Figure 4.2.3.1. Voltage tap configuration with (a) the wire directly soldered onto the tape surface inside the coil or (b) with the wire soldered onto the surface of an additional tape segment inserted into the coil.
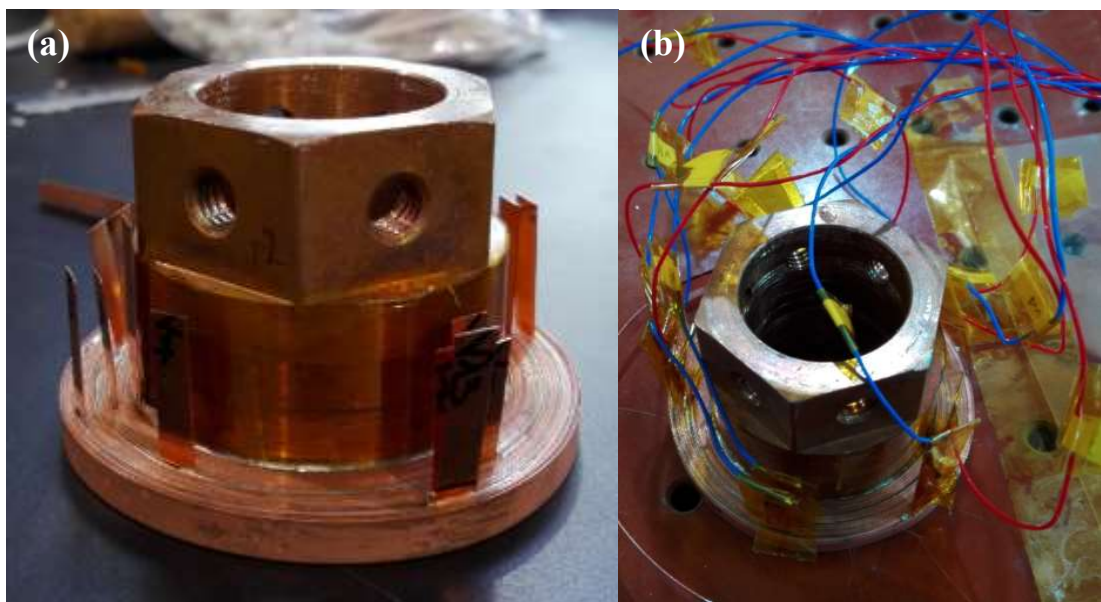
Figure 4.2.3.2. Project coil (a) before and (b) after the signal wires are soldered on each tape segment inserted into the winding.

14 voltage taps are inserted into the project coil with the abovementioned technique, at locations set during the design phase. However, the purpose of the study described in this section is not the detailed analysis of the coil but its macroscopic behaviour, therefore the signals coming from the voltage taps placed in the internal turns of the winding are not considered (but they will be used for future analyses). In this study, only the two voltage taps located at the end of the innermost and the outermost turns are used. Fig. 4.2.3.2(a) shows the

project coil at the end of the winding phase, in which all the tape segments are inserted. Fig. 4.2.3.2(b) presents the project coil after the signal wires are soldered to each segment and insulated with a Kapton tape to prevent undesired electric contacts between adjacent segments.

Whereupon, the two voltage wires are connected to one channel of the DAQ system, a *PXI-e4309* acquisition card, manufactured by *National Instruments* [171]. Given the small amplitude of the signals which are expected to be handled, the DAQ system full-scale is set to its minimum amplitude, equal to 2.5 mV.

Then, the coil mandrel is screwed to a rigid support to ensure its positioning during the test phase. The support, made of stainless steel, is electrically insulated from the mandrel by means of a Kapton tape.

Subsequently, a uniaxial cryogenic Hall sensor series *LHP-NA* manufactured by *AREPOC spol. s.r.o.* [172], is placed into the coil bore and fixed to the support, so as to monitor the coil magnetic field during tests. The sensor has a nominal control current of 50 mA and a sensitivity of 26.9 mV/T at 77 K. The active face of the Hall sensor is maintained parallel to the *x-y* plane of the coil. Thus, the sensor is able to detect the *z*-component of the magnetic field only. For practical reasons, the sensor is placed in the central axis of the coil, but shifted upwards from the middle *x-y* plane of the coil by 7 mm. It follows that, for a correct comparison between the measured and the estimated magnetic fields, the calculation of B_z (0,0,z) presented in *Section 4.1.2* is necessary. The relative position of the Hall sensor and of the various supports used is shown in Fig. 4.2.3.3.
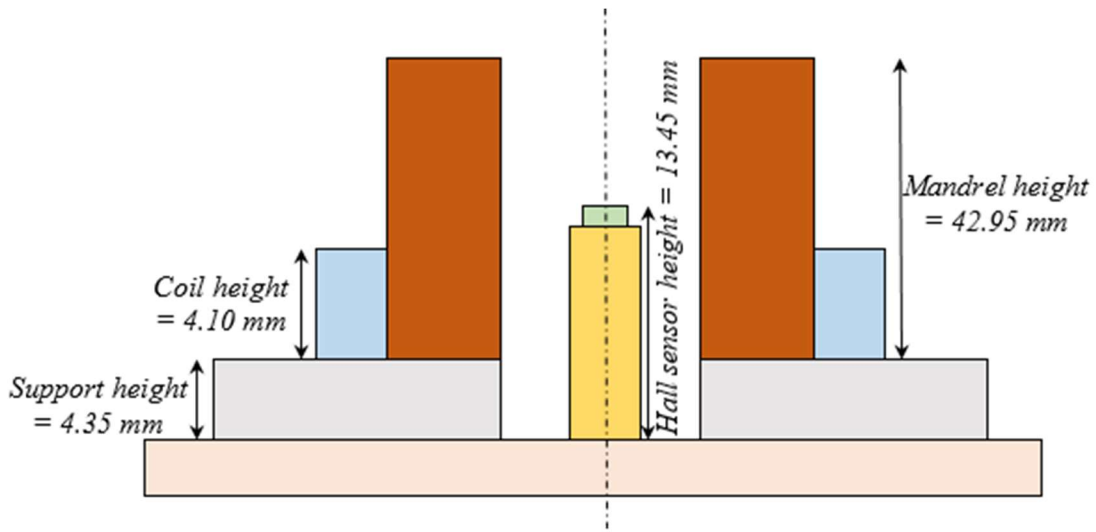
Figure 4.2.3.3. *Relative position of the Hall sensor and the project coil positioning system.*

4.3. NI pancake-wound coil tests

The test phase is carried out using the cryostat facility available at *ASL*, the cryogenic temperatures are reached with a GM cryocooler. The coil support is fixed to the cryocooler 2nd stage. To ensure a better thermal contact, a circular metal plate is pressed above the coil and thermally connected to the cryocooler 2nd stage. The plate is shaped with a central hole of the

same size of the mandrel, so that its upper part can be connected with the first superconducting current lead. The plate has lateral opening, allowing to pull out the outermost tape end and connecting it to the second superconducting current lead as well as conducting the voltage wires to the DAQ system. Fig. 4.3.1 displays the different connecting components described.
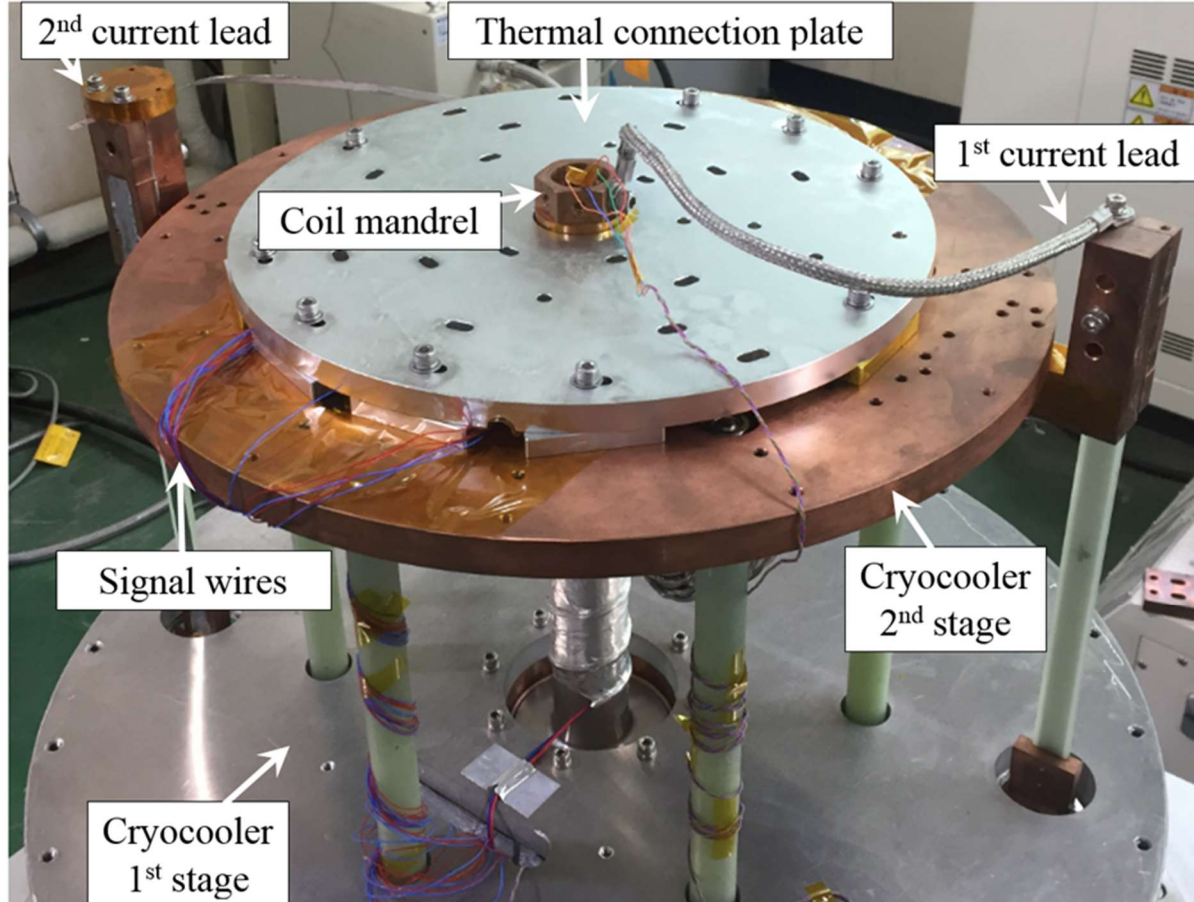
Figure 4.3.1. Coil connections with the cryogenic system, the power supply and the DAQ system.

Figure 4.3.2. Mechanical and electrical strengthening of the terminal section of the tape connected to the current lead, obtained by soldering an additional superconducting tape segment.

It is worth noting that the outermost end of the tape is connected to the cold source by conduction with the rest of the coil, which is located at a certain distance. Moreover, it has to be twisted by 90° when connected to the current lead in the cryostat (operation done with extreme caution to prevent damaging the tape). These factors make this specific ending zone very delicate. Thus, to improve the mechanical performance and the transport current capacity

of the connecting area, a 30 cm long tape segment cut from the same lot is soldered onto the surface of the tape, as shown in Fig. 4.3.2. The procedure adopted is the same performed for the lap joints.

Then, the thermal shield (Fig. 4.3.3(a)) is lowered on the 1st and 2nd stages of the crycooler and the vessel of the cryostat (Fig. 4.3.3(b)) finally seals the cryogenic system.
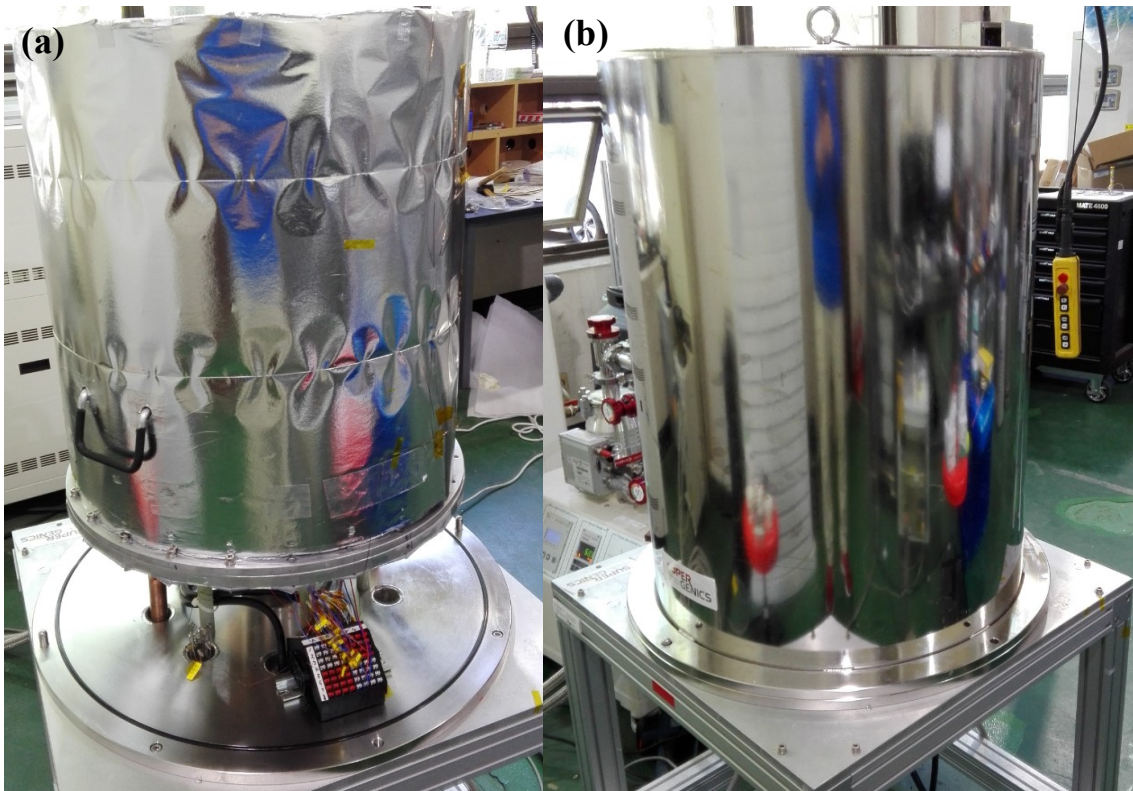
Figure 4.3.3. (a) Thermal shield and (b) cryostat vessel of the cryogenic system.

Consequently, both current leads are connected to the external power supply system. The system consists of 4 *Mercury iPS-M* power supplies connected in series [173]. Each device is able to generate a DC current of a maximum amplitude equal to 60 A, thus, the maximum I_{op} for the whole system corresponds to 240 A. The current is acquired during tests from the voltage signal coming from a 100 µΩ shunt resistor, placed in series with the coil. A manual switch can be used to rapidly switch off the current during tests.

Lastly, vacuum is realized inside the cryostat by means of a pumping station. Once the design pressure is reached, the cryocooler can be turned on. The cryocooler available at *ASL* is designed to cool down its 2nd stage to 4 K (depending on the heat load). To perform experiments at higher temperatures, a heater is fixed to the 2nd stage, whose current control system has been implemented by *ASL* group in *LabVIEW* environment. The heater current, and consequently the power dissipated by the Joule effect, is automatically varied during the cool down, following an iterative procedure, until the regime condition at the project temperature is reached. The temperatures of the 1st and 2nd stage are controlled by means of thermocouples. No thermocouple is instrumented on the coil surface, but its temperature during each test is considered equal with the temperature of the 2nd stage.

4.3.1. Charging/discharging tests at different ramp-rates

The first tests campaign conducted with the project coil consists in charging the coil up to a certain current amplitude with a ramp-rate of 0.1 A/s, maintaining the current for a sufficient amount of time to ensure reaching the regime conditions and then discharging the coil by reducing I_{op} to zero with the same ramp-rate. The test is repeated for the following maximum I_{op}: 10 A, 20 A, 30 A, 40 A, 50 A, 60 A and 70 A. The sequence of the amplitudes is maintained in this order so as to check that the coil behaviour remains stable and there are no unexpected transition phenomena. Then, the experiments are reiterated for different temperatures: 4.7 K (the lowest temperature achievable by the 2nd stage of the cryocooler with a null heater current), 10 K, 20 K, 30 K, 40 K, 50 K, 60 K, 70 K and 80 K. Finally, all tests are repeated twice to ensure the reproducibility of the acquired signals. The time dependent profiles presented in the following figures refer to a single test, while the parameters extrapolated from the curves are obtained by averaging the parameters extrapolated from both reproducibility tests.

Fig. 4.3.1.1 shows the (a) current and (b) voltage profiles acquired during tests, at a temperature of 70 K (chosen as an example). The voltage profiles do not present any critical elements; they vary over time following I_{op}, remaining stable during the current plateau. The increase during charging is due both an inductive signal and, mostly, a resistive signal due to the turn-to-turn and longitudinal resistances in the winding, Comparing the voltage values during the different current plateaus, it is possible to note a weak non-linear increase with the current, when I_{op} exceeds 50 A. This could be explained by the presence of defective areas in the coil, as in the case of the 24th turn, whose properties has already been presented in Fig. 4.2.1.9(a), referred to the resistance of the 2nd joint after the coil disassembly. In fact, the solid blue curve of Fig. 4.2.19(a) exhibits the initiation of a sharp superconducting transition starting from 50 A. However, that test is carried out on a straight tape having no contact with other conductors (moreover, that test is carried out at liquid nitrogen temperature). In Fig. 4.3.1.1(b) instead, the transition appears smoother; this could prove that in the project coil the currents redistribute radially avoiding partially to flow in the 24th turn (and probably in other damaged areas not predicted in the design phase) thus preventing a rapid increase of the voltage of the whole winding.
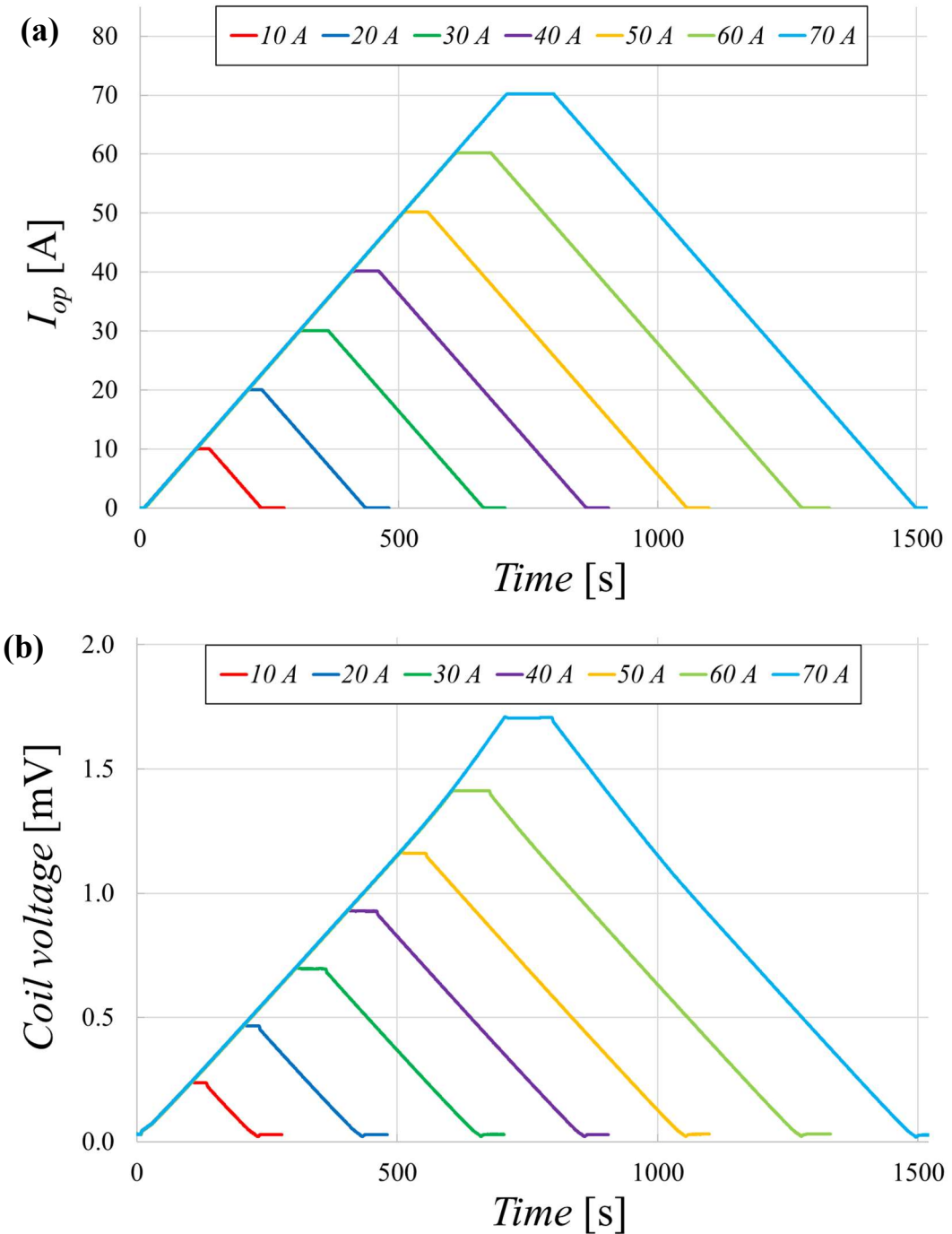
Figure 4.3.1.1. *(a) Current and (b) voltage profiles during the charging/discharging tests at 70 K with a ramp-rate of 0.1 A/s.*

After that, the coil behaviour during charging/discharging tests with different ramp-rates is investigated. NI coils usually require to be charged slowly, due to the radial currents which can flow even at low operating currents [38, 45, 53, 174 – 178]. These currents hinder the proper coil charging as well as generating high resistive voltage drops. Moreover, the inductance of the coil drives the currents to flow radially, with an action that is the greater the faster the charge/discharge transients. Thus, it is essential to estimate how rapidly a NI coil can be safely charged. The coil is consecutively charged and discharged up to I_{op} = 50 A, with the following

ramp-rates: 0.1 A/s, 0.5 A/s, 1 A/s, 2 A/s and 5 A/s. The test is repeated for different temperatures: 4.7 K, 10 K, 20 K, 30 K, 40 K, 50 K, 60 K and 70 K; test at 80 K are considered risky and thus avoided. Fig. 4.3.1.2 presents the voltage profiles acquired during the experiments. To improve readability, the discharges at 0.1 A/s are cut from the figure in correspondence with the coloured dashed lines. Moreover, for each temperature a grey horizontal dashed-line is inserted in correspondence of the voltage value at the end of the transient, after the first charge. It is noted that even for fast charges at 5 A/s, the voltage signal at regime remains the same. What clearly changes are the inductive peaks at the end of the charge and discharge phases, whose amplitude and duration increases with increasing the ramp-rate. Although these peaks reach considerable values, the coil shows works properly (no quench signs) and it can be charged correctly. However, increasing the ramp-rate above 5 A/s can be risky and therefore this is imposed as the charging limit of the project coil.
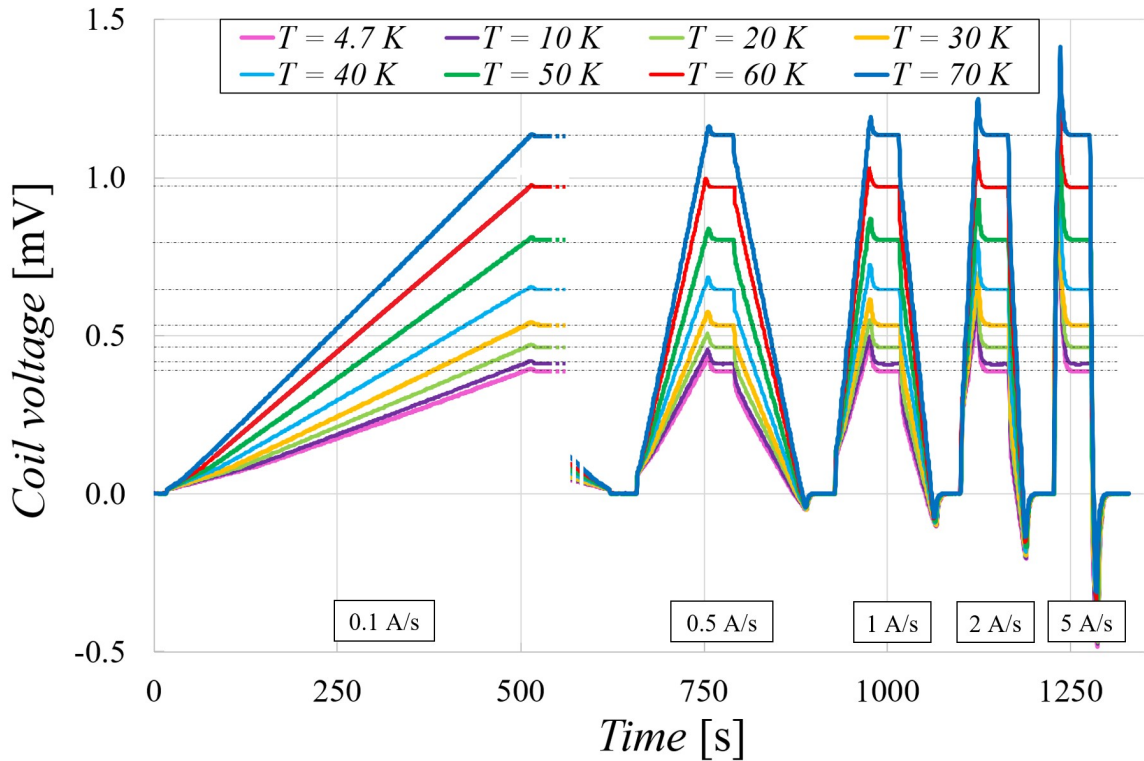
Figure 4.3.1.2. Charging/discharging up to I_{op} = 50 A with various ramp-rates and at different temperatures.

The analysis of the magnetic field performance of the project coil can give useful indications regarding the *defect-irrelevant* behaviour of the NI coil. The magnetic field profile acquired from the Hall sensor during tests is compared to the field computed numerically for a defect-free coil, with the simplifying assumptions described in *Section 4.1.2*. The numerical field is calculated taking into account the sensor position, which lies in the *z*-axis of the coil bore and it is shifted upwards by 7 mm from the coil center. Fig. 4.3.1.3 presents the comparison for a charging/discharging test performed at 70 K and up to I_{op} = 70 A, with a ramp-rate of 0.1 A/s. These parameters are chosen as examples, but the same conclusions are verified for all the other conditions. I_{op} is reported in the secondary ordinate axis. The experimental field results 16.6% lower than the field expected from the model. This difference can be due to several

factors. First, even a little imprecision in the measurement of the Hall sensor position with respect to the coil center may lead to errors in the numerical evaluation of the field. Furthermore, the numerical model is based on simplifying assumptions (insulated coil, uniform current distribution, use of the engineering current density rather than the current density in the superconducting layer only) which introduces some level of imprecision. Finally, the project coil contains defect, not accounted in the model. The model adopted in the design phase does not consider the presence of radial currents bypassing the defective regions of the winding. These currents do not produce a field along the z-axis, but they modify the current distribution by reducing the current flowing longitudinally in some turns. Therefore, the discrepancy of the measured magnetic field compared to the numerical one can be considered acceptable to declare the proper functioning of the coil.

Moreover, the field profile measured results stable during time and the charging and discharging phases are almost identical.
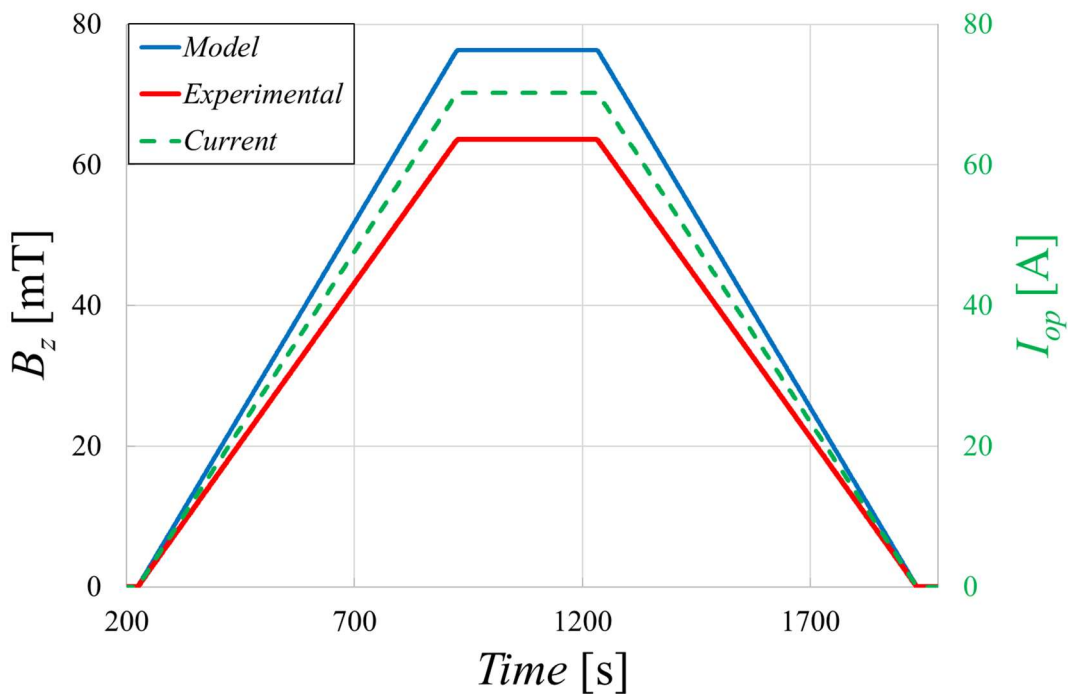
Figure 4.3.1.3. Experimental and numerical profiles of the magnetic field generated by the project coil in correspondence of the location of the Hall sensor during a charging/discharging test up to I_{op} = 70 A and at a temperature of 70 K.

Fig. 4.3.1.4 shows the trend of the maximum magnetic field measured during the coil charging tests performed up to the same maximum I_{op} and varying the operating temperature. At a temperature of 80 K, it is preferred to not carry out tests at currents greater than 50 A. The magnetic field appears stable with the temperature and proportional to the current supplied, a sign that the coil is working properly despite the presence of defects.
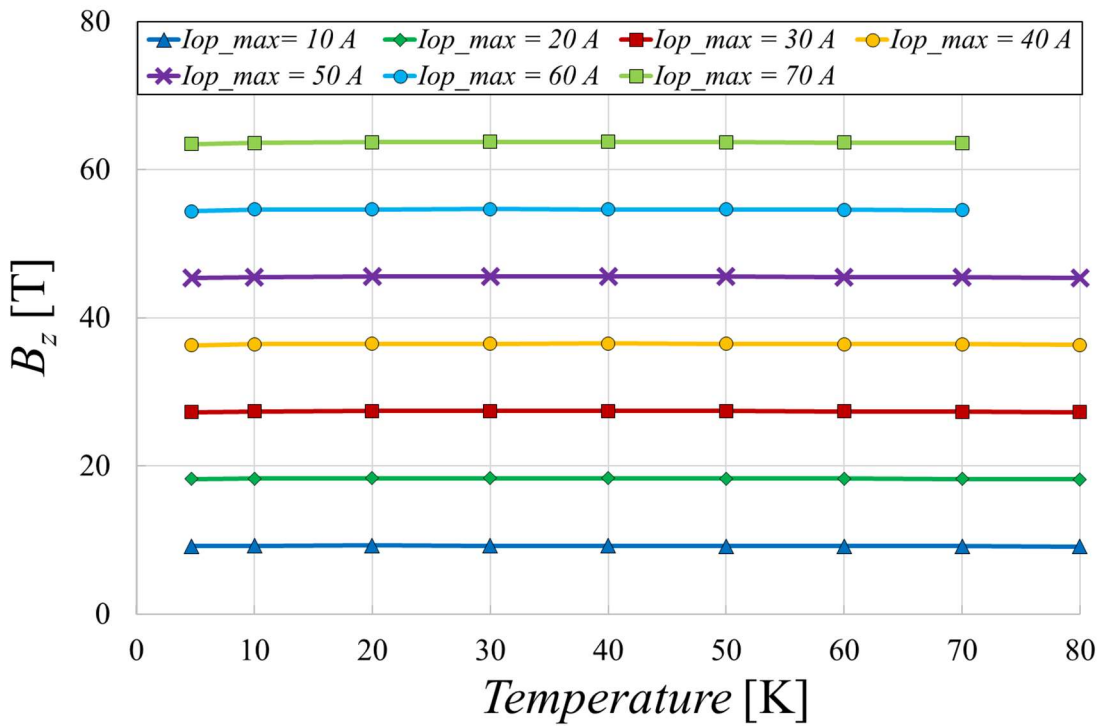
Figure 4.3.1.4. *Maximum magnetic field measured during the coil charging test up to different maximum I_{op} and at various operating temperatures.*
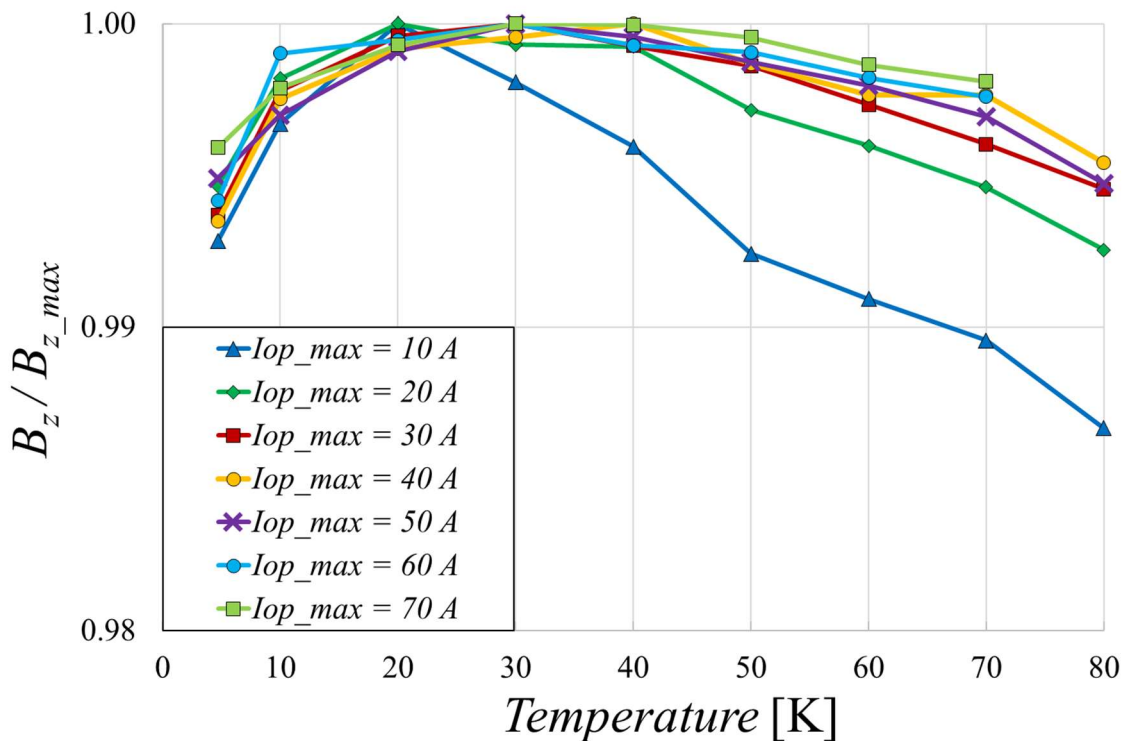
Figure 4.3.1.5. *Ratio between the magnetic field measured during each coil charging test up to a certain maximum I_{op} and the highest field measured during all charging tests conducted up to the same maximum I_{op}. Various operating temperatures are tested.*

Indeed, minimal fluctuations with temperature are present, as visible in Fig. 4.3.1.5. The figure shows the ratio between the magnetic field measured during each coil charging test up to a certain maximum I_{op} and the highest field measured during all charging tests conducted up to the same maximum I_{op}. The field has a peak (*i.e.* the ratio is equal to 1) in the temperature range of 20 ÷ 40 K, and then it decreases. The decrease is expected since higher the temperature the lower is the coil critical current, thus the probability that a fraction of I_{op} flows radially without contributing to the field increases. Then, the field rises from 4.7 K to 20 K; this phenomenon can be attributed to a different sensitivity of the Hall sensor at these temperatures, even if this consideration needs to be further investigated. Nevertheless, the fluctuations are minimal, generally below 0.5%. Differences of 1.3% are reached only for the case of maximum I_{op} equal to 10 A; however, low currents correspond to low amplitudes of the voltage signal, which can approach the sensitivity of the DAQ system and therefore be affected by a certain level of imprecision.

4.3.2. Charging/shut-down tests

The second tests campaign conducted with the project coil consists in charging the coil up to a certain current amplitude with a ramp-rate of 0.1 A/s, maintaining the current for a sufficient amount of time to ensure reaching the regime conditions and then shut-down the power supply. The test is repeated up to the same maximum current amplitudes and for the same operating temperatures of the first test campaign. As in the first test campaign, all tests are performed twice and the agreement between the signal profiles obtained in both cases is checked, to ensure the reproducibility.

Fig. 4.3.2.1 presents the (a) current and (b) voltage profiles acquired during tests, at a temperature of 70 K, chosen as an example. The voltage signals during the current plateaus are the same as those shown in Fig. 4.3.1.1(b). Then, the voltage drops once the power supply is shut-down, reaching negative values which should be greater the higher the maximum I_{op}. In the figure, the voltage drop is to not exactly proportional to the current drop. This is due to the DAQ system. Since it is not possible to synchronize the sampling rate with the exact instant at which the power supply is turned off, it is likely that the negative peaks are not correctly recorded.

The coil characteristic time (τ) can be obtained from the voltage signal acquired during the shut-down phase. In fact, the voltage drops during time with a negative exponential trend, proportional to $e^{-\frac{t}{\tau}}$. A numerical exponential fitting of the voltage profile is performed using the MATLAB software, then τ is easily found as the inverse of the fitting function exponent. Alternatively, τ can be computed as the crossing point between the time axis and the line tangent to the voltage curve during the exponential decay. This second approach is less precise but it is used as a check for the results obtained with the fitting exponential method.
Fig. 4.3.2.2 shows the τ values for each experiment, at different temperatures and current amplitudes. τ varies from 832 ms to 259 ms going from the lowest to the highest temperature. As expected, the characteristic time reduces as the temperature rises, since it corresponds to the ratio between the coil inductance and the coil equivalent resistance. The inductance depends

poorly on the temperature, while the coil resistance could rise consistently increasing the temperature, thus determining faster transients. At the analysed current amplitudes, the transient dynamics of the winding does not seem to be significantly affected by the maximum I_{op} before the shut-down. However, the uncertainty in the calculation of τ could lead to misleading conclusions in this regard, as it is based on a best fitting method and on the precision of the DAQ system. For particularly rapid transients, for example, the number of samples acquired during the shut-down affects the quality of the fitting function. In the following sections, a more precise method to interpret these dependences is investigated.
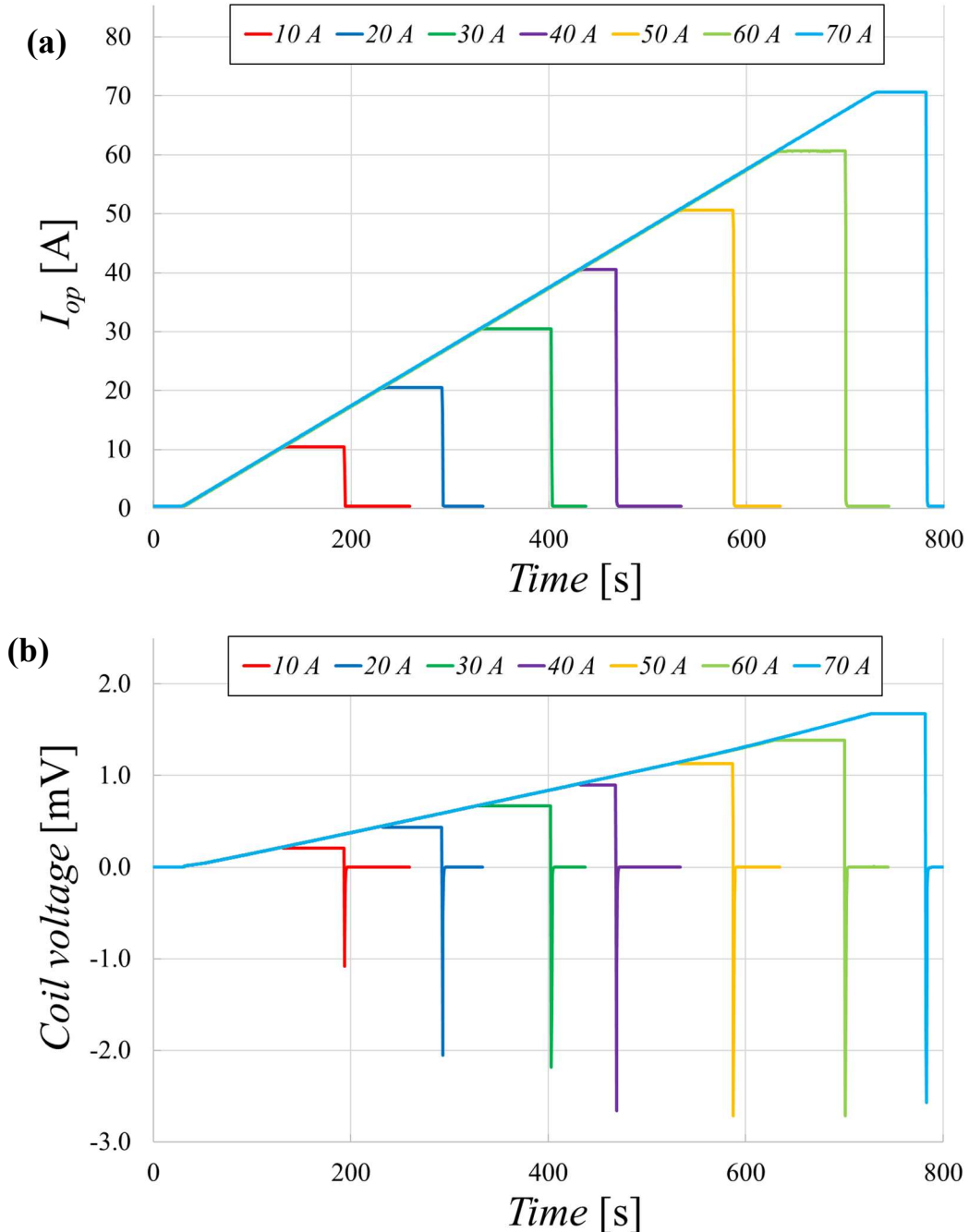
Figure 4.3.2.1. *(a) Current and (b) voltage profiles during the charging/shut-down tests at 70 K with a ramp-rate of 0.1 A/s.*
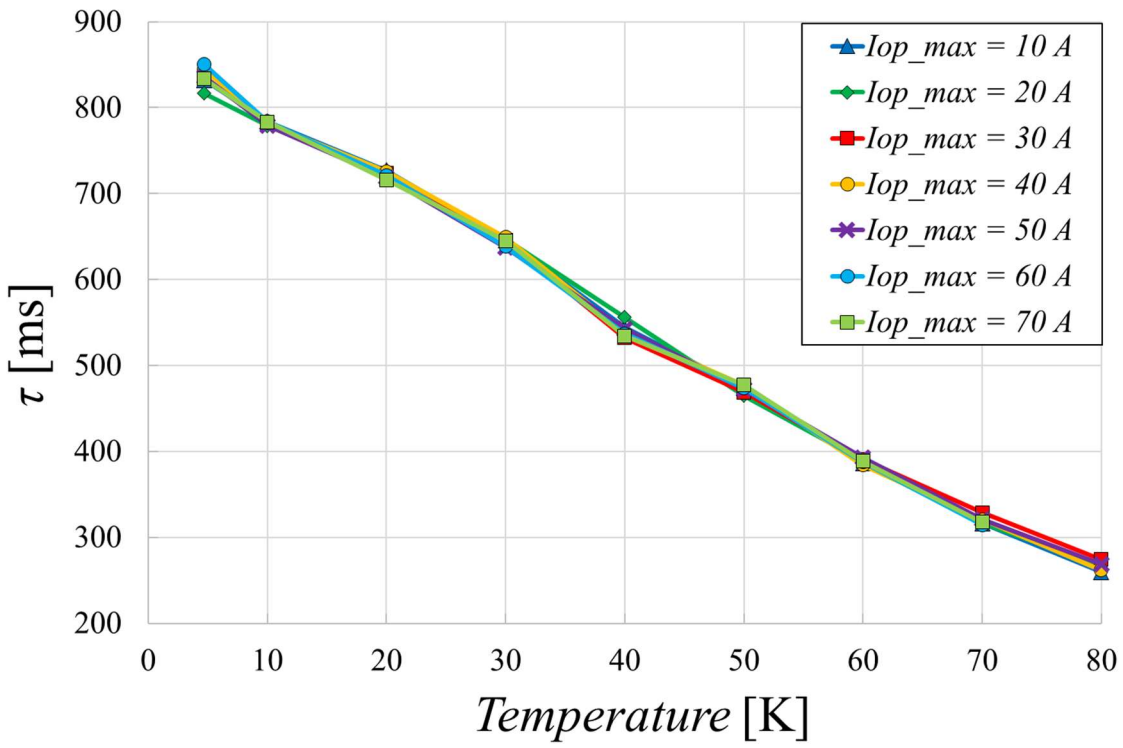
Figure 4.3.2.2. *Coil characteristic time computed during the coil charging/shut-down tests to a certain maximum I_{op} and at different operating temperatures.*

4.4. Equivalent lumped parameter circuit for a NI pancake-wound coil

The NI pancake-wound coil can be characterized using the simple equivalent lumped parameter circuit shown in Fig. 4.4.1.
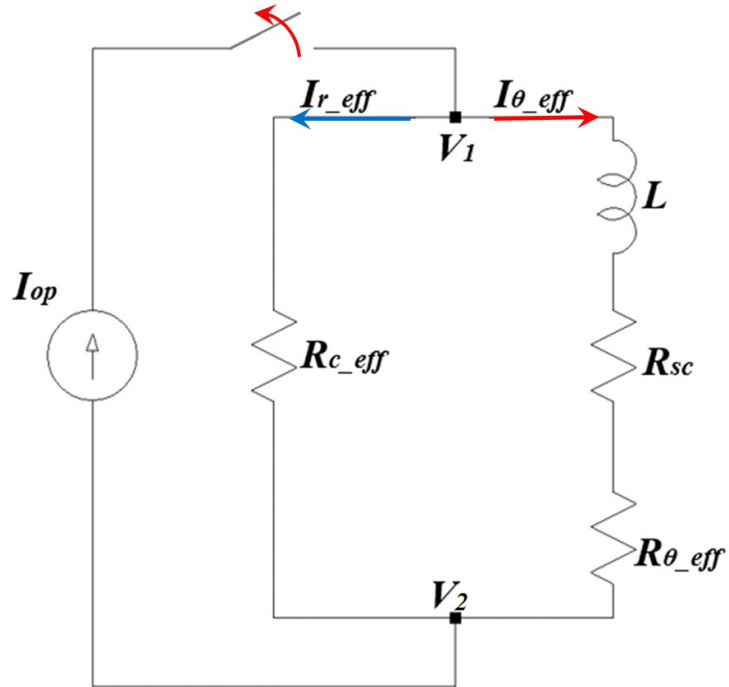
Figure 4.4.1. *Equivalent lumped parameter circuit for a NI pancake-wound coil.*

I_{θ_eff} represents the effective current flowing longitudinally in the turns of the coil and I_{r_eff} represents the effective current flowing radially from one turn to the adjacent ones. In the right branch of the circuit, the longitudinal current flows through the coil inductance L and the resistances R_{θ_eff} and R_{sc}. R_{θ_eff} represents the effective longitudinal resistance of the tape due to the presence of defects, intentionally or unintentionally inserted in the coil. R_{sc} represents the non-linear resistance of the superconducting layer. On the other branch, the radial current flows through the resistance R_{c_eff}, which represents the effective turn-to-turn resistance of the coil. The circuit parameters are referred as *effective* values, since they describe the macroscopic coil behaviour and not local conditions within the coil. As an example, the parameter R_{θ_eff} does not exactly correspond to the sum of the resistances of the defective regions in the winding, but it represents an average value for the entire coil length. The lumped parameter equivalent circuits presented in the literature to describe the behaviour of NI coils [49, 55, 179] usually offer a greater level of detail, but also require higher computation times and accurate coil instrumentations to be experimentally validated. Instead, the simple equivalent circuit proposed in this work can be useful a tool to compare different coils with or without defects of different extent, and its parameters can be rapidly found analytically from the test results.

Since I_{op} varies, the circuit can be solved in time. In fact, the parameters could be *current dependant* and not just *temperature dependant* (even if within a single test, the temperature is considered constant). However, to compare the different tests, it is preferred to pick a single instant at which to calculate the circuit parameters. It is chosen to compute their values at regime conditions, during the current plateau. This allows to simplify the solving equations. The coil inductance can be short-circuited and thus neglected, despite its computation is however necessary to solve system It is obtained using the calculations reported in *Section 4.1.2*. Moreover, R_{sc} is considered negligible compared to the other resistance at the operating currents adopted in this work.

It follows that, at regime ($t = t_{reg}$), the unknowns of the equivalent circuit are the terms I_{θ_eff} (t_{reg}), I_{r_eff} (t_{reg}), R_{θ_eff} (t_{reg}), and R_{c_eff} (t_{reg}). These parameters can be computed by solving the following system of equations:

$$\begin{cases} V_{coil}(t_{reg}) = R_{c\_eff}(t_{reg}) \cdot I_{r\_eff}(t_{reg}) \\ V_{coil}(t_{reg}) = R_{\theta\_eff}(t_{reg}) \cdot I_{\theta\_eff}(t_{reg}) \\ I_{op}(t_{reg}) = I_{\theta\_eff}(t_{reg}) + I_{r\_eff}(t_{reg}) \\ \tau = \dfrac{L}{R_{c\_eff}(t_{reg}) + R_{\theta\_eff}(t_{reg})} \end{cases} \qquad (4.4.1)$$

The first two equations are found by applying Ohm's Law to both circuit branches and equal it to the voltage signal measured at regime, V_{coil} (t_{reg}). The third equation corresponds to the current conservation equation. The fourth equation corresponds to the definition of the coil characteristic time, already introduced in *Section 4.3.2*, and it is necessary to close the system of equations.

When solving Eq. (4.4.1), a quadratic equation appears. However, one of the two solutions can be discarded since it would lead to a radial current higher than the operating current, which has no physical meaning. Therefore, the system parameters can be found as follows:

$$
\begin{cases}
I_{r\_eff}(t_{reg}) = \dfrac{I_{op}(t_{reg}) - \sqrt{[I_{op}(t_{reg})]^2 - 4\dfrac{\tau\, V_{coil}(t_{reg})\, I_{op}(t_{reg})}{L}}}{2} \\[2em]
I_{\theta\_eff}(t_{reg}) = I_{op}(t_{reg}) - I_{r\_eff}(t_{reg}) \\[1em]
R_{c\_eff}(t_{reg}) = \dfrac{V_{coil}(t_{reg})}{I_{r\_eff}(t_{reg})} \\[1.5em]
R_{\theta\_eff}(t_{reg}) = \dfrac{V_{coil}(t_{reg})}{I_{\theta\_eff}(t_{reg})}
\end{cases}
\qquad (4.4.2)
$$

Using the methodology proposed to solve the circuit of Fig. 4.4.1, it is required the experimental acquisition of the operating current and the voltage signals, as well as the coil inductance measurement or estimation.

4.4.1. Equivalent circuit parameters calculation from the experimental results

In this section, an analysis is performed about the parameters of the equivalent circuit obtained through the experimental signals of the various tests.
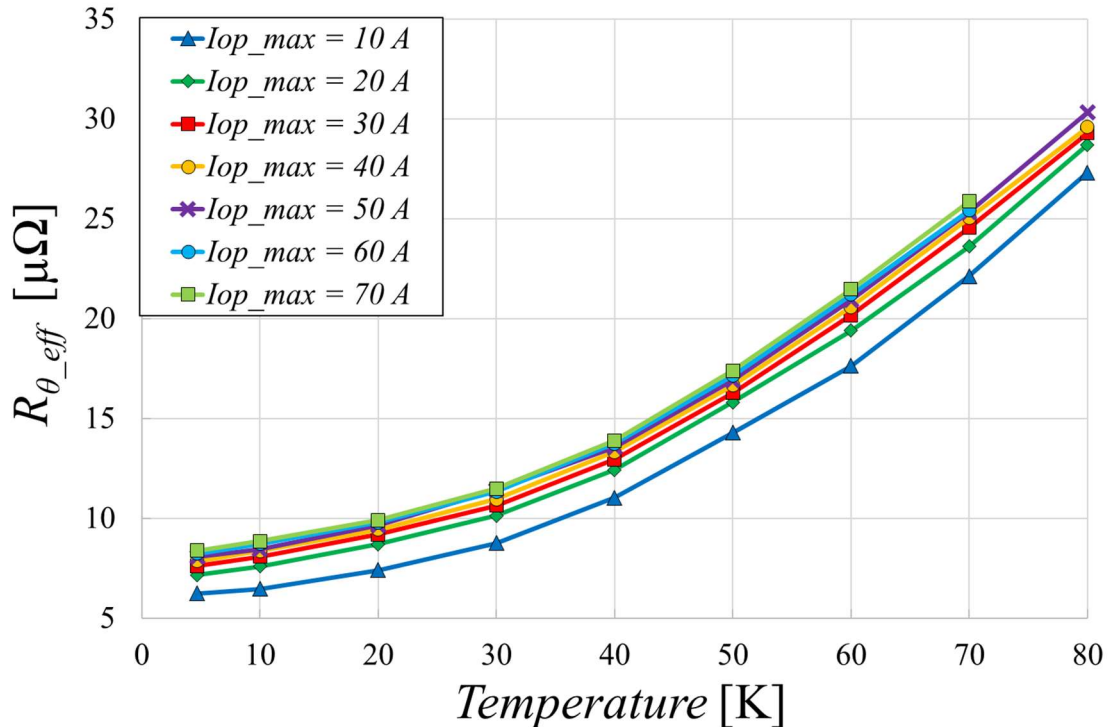
***Figure 4.4.1.1**. Effective longitudinal resistance in the equivalent circuit of the NI project coil for the charging tests up to a certain maximum I_{op} and varying the operating temperature. The parameter is computed at regime conditions.*

Fig. 4.4.1.1 shows the R_{θ_eff} parameter computed at regime, for the charging tests performed up to a certain maximum I_{op} and varying the operating temperature. Comparing the values at

higher temperatures with the measurements reported in Tab. 4.2.1.1 (at 77 K), it can be seen that R_{θ_eff} does not correspond to the sum of the 3 joints in the project coil (as it would be in an insulated coil), despite the order of magnitude being respected. R_{θ_eff} appears to increase exponentially with the temperature, with a very low exponent. This might indicate an approach to the critical current of the superconductor at the defective locations. However, the increase is substantial even at low current amplitudes, which makes it unlikely to be caused by the superconducting transition only. It is more probable that the increase of resistance with temperature is due to a combination of two different phenomena: an approach to the tape critical current in specific sections as well as a linear increase in the resistance of the joints. Furthermore, comparing the values at the same operating temperature, R_{θ_eff} rises with the current amplitude. This is reasonable because as I_{op} increases, more current flows longitudinally (and radially) enhancing the resistance of the superconducting sections eventually damaged during the winding phase.

After that, Fig. 4.4.1.2(a) presents the R_{c_eff} parameter computed for the same tests. The turn-to-turn resistance is one order of magnitude greater than the longitudinal resistance. This is valid despite the presence of defects. Therefore, I_{op} encounters less obstacles flowing longitudinally through the turns and the coil results properly charged. The R_{c_eff} trend seems slightly exponential, similar to the resistivity curve of copper [180], which constitutes the layers of tape through which the current I_{r_eff} must flow at the joints locations. Unlike the longitudinal resistance, the R_{c_eff} curves computed for different maximum I_{op} do not differ from each other considerably, and the discrepancies seem to be due mostly to inaccuracies in the measurements. This is reasonable, as the turn-to-turn resistance is not affected by the amount of current flowing through it, unless this leads to a heating of that section. However, this does not seem the case given the data acquired by the thermocouple are almost constant during tests.

Then, it is useful to introduce another parameter, called R_{ct_eff}, representing the *effective* turn-to-turn surface resistivity of the coil, measured in $\mu\Omega$ cm^2. It allows to estimate the quality of the electrical contact between adjacent turns in the winding. It is an average over the entire coil and it depends heavily on the winding conditions. It can be computed as in [53]:

$$R_{c\_eff} = \sum_{i=1}^{Nturn} \frac{R_{ct\_eff}}{2\,\pi\,r_i\,w} \qquad (4.4.4.1)$$

where r_i is the inner radius of each turn and w is the tape width.
Fig. 4.4.1.2(b) shows the R_{ct_eff} parameter; as expected, it is proportional to R_{c_eff} and their trends are the same. The R_{ct_eff} range obtained in this study ($22 \div 72\ \mu\Omega$ cm^2) is in agreement with the values calculated in other works on NI coils wound with (RE)BCO tapes with similar properties [53, 164, 181]. Yet, this parameter is highly dependent on the winding tension and a comparison with other experimental results can give only qualitative indications. It can be concluded that the winding conditions of this project are in line with the criteria adopted in the literature for similar coils.
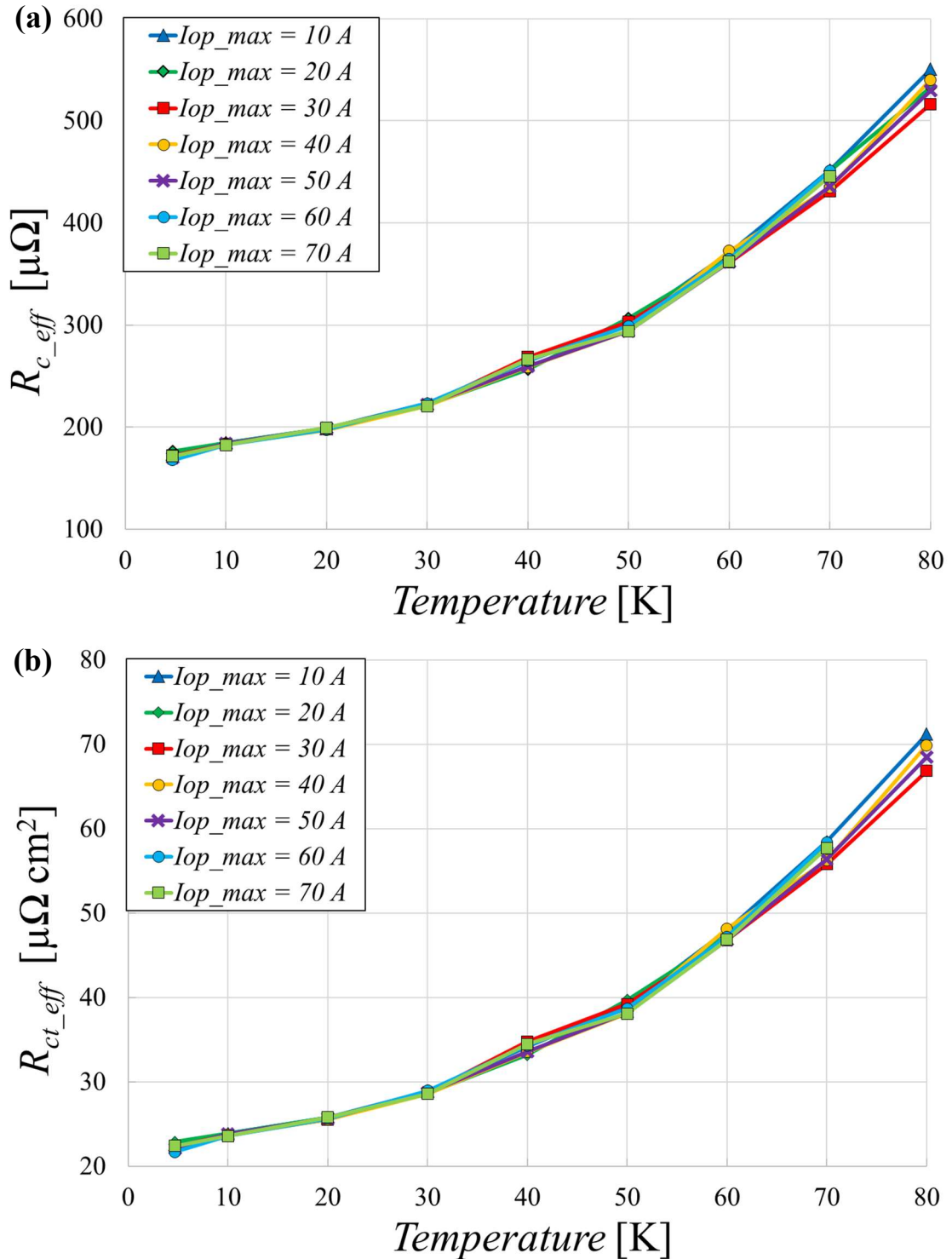
Figure 4.4.1.2. *Effective turn-to-turn (a) resistance and (b) resistivity in the equivalent circuit of the NI project coil for the charging tests up to a certain maximum I_{op} and varying the operating temperature. The parameters are computed at regime conditions.*

Furthermore, it is useful to compare the temperature dependence of the two resistive parameters of the equivalent circuit. Fig. 4.1.1.3 shows the increase of both R_{θ_eff} and R_{c_eff} during tests at different temperatures compared to the parameters obtained at the lowest temperature, 4.7 K. Each point in the figure is the average of the tests carried out at different maximum I_{op} and at

the same temperature, since the current dependence of both resistive parameters is minor. It results that the longitudinal resistance, which is due to the defective regions, has a steeper increase with the temperature, compared to the turn-to-turn resistance.
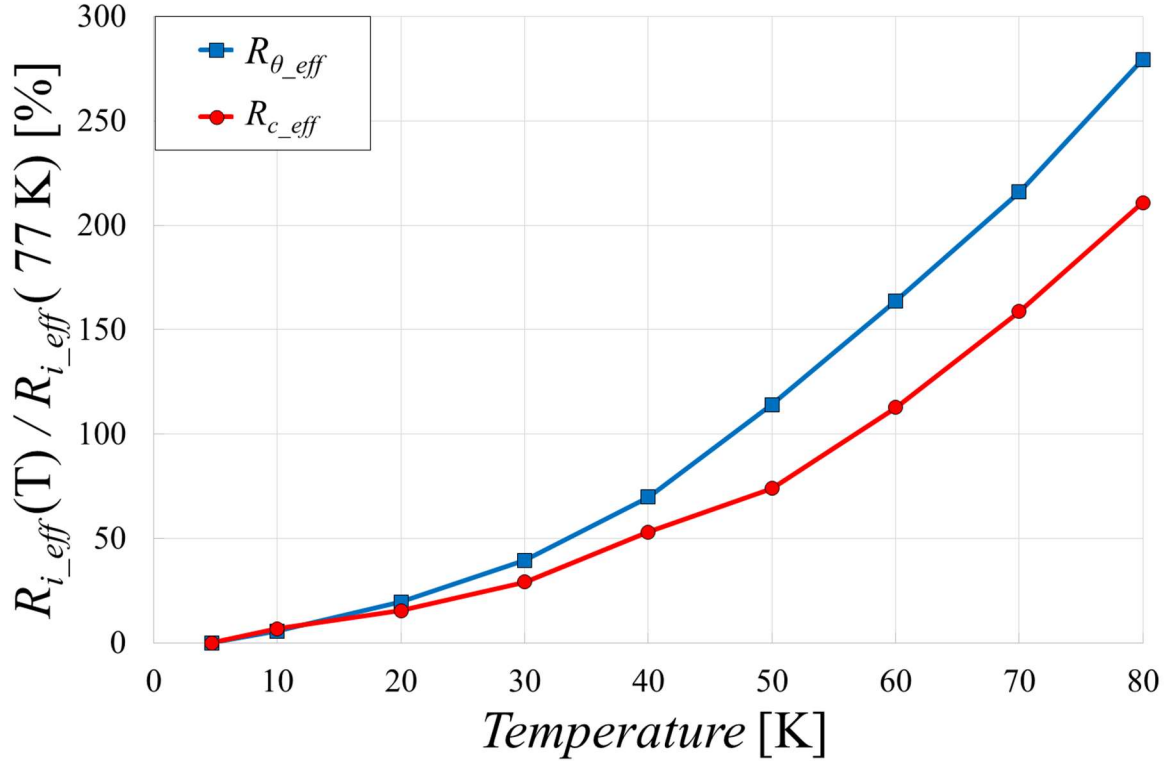
Figure 4.4.1.3. *Increase with temperature of the R_{θ_eff} and R_{c_eff} parameters compared to the 4.7 K case. Each point is the average of the tests carried out at different maximum I_{op} and with the same temperature. All parameters are computed at regime conditions.*

Finally, the parameters proportional to the longitudinal and radial currents of the coil (I_{θ_eff} and I_{r_eff}) are determined. Fig. 4.4.1.4 reports the ratio I_{r_eff}/I_{op}, corresponding to the percentage of current flowing radially in the coil, compared to the I_{op} supplied. The value of I_{θ_eff}/I_{op} (the percentage of current flowing longitudinally in the coil), can be obtained as its complement. The same tests conditions as in the previous figures are investigated. The general trend indicates an increase of the current flowing radially in the coil, despite the curves are not monotonic as for the other parameters. The effective radial current in the coil increases (and therefore the effective longitudinal current is reduced) since, as shown in Fig. 4.1.1.3, the resistance of the defective areas rises more steeply than the turn-to-turn resistance with temperature. This is in line with the behaviour expected from an NI coil, which favours the passage of radial currents when the longitudinal resistance increases (locally or globally) thus reducing the coil stability risks.

Moreover, comparing the values at the same operating temperature, I_{r_eff}/I_{op} rises with the current amplitude, although there are some exceptions, probably due to imprecise measurements. This reflects the proportionality of the R_{θ_eff} parameter with the current, reported in Fig. 4.4.1.1. At very low currents ($I_{op} = 10$ A), the resistance of the damaged superconducting sections remains limited and the normal layers of tape can contribute significantly despite their

poor transport capacity. Then, since the increase in the longitudinal resistance is not proportional to the increase in I_{op} and a greater percentage of current is forced to flow radially.
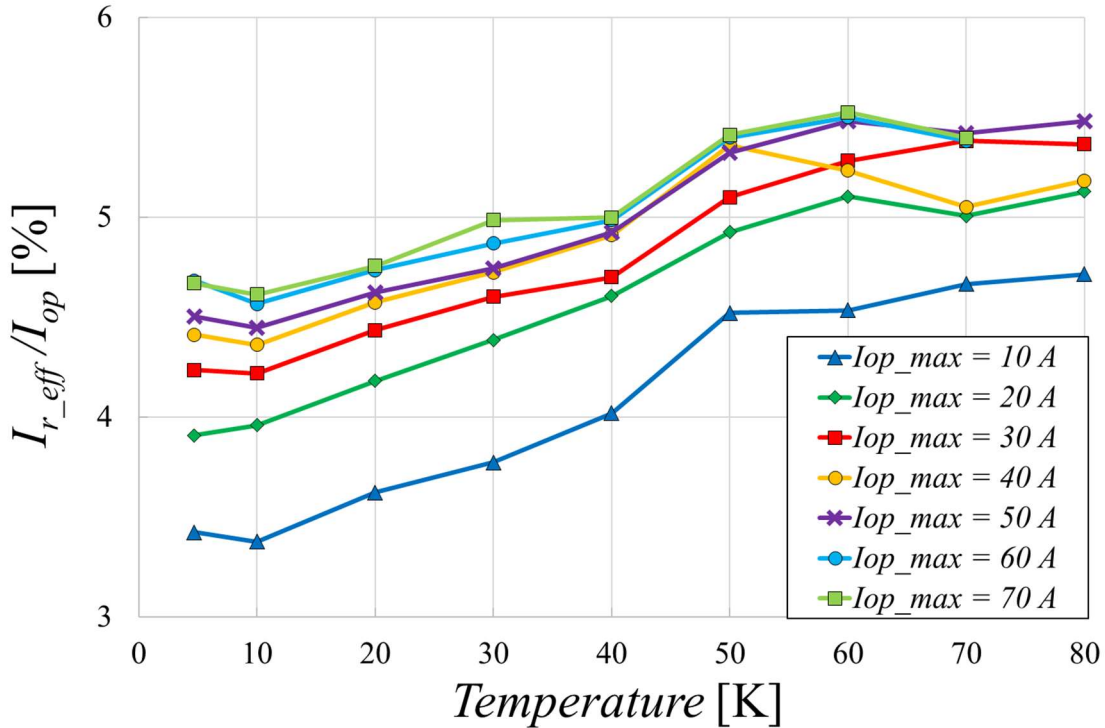
Figure 4.4.1.4. Temperature dependence of the I_{r_eff}/I_{op} ratio in the equivalent circuit of the NI project coil for the charging tests up to a certain maximum I_{op}. The parameters are computed at regime conditions.

Overall, the NI project coil behaves properly under the testing conditions, despite the presence of defects of remarkable extent. The voltage profiles do not show significant irregularities, and the magnetic field generated is just slightly lower than that expected from the design phase. An effective radial current of limited entity (4.3% to 5.5% of I_{op} from the lowest to the highest temperature tested) is sufficient to allow a correct functioning of the coil despite the presence of defects which, in an insulated configuration, would affect the electrical performance of the winding and require partial or total replacements. Therefore, the *defect-irrelevant* behaviour of the project coil can be considered verified.

4.5. Conclusions

In this chapter, an experimental study has been conducted on the *defect-irrelevant* behaviour of an NI coil in pancake-wound configuration, in which some defects have been intentionally introduced in the form of lap joints. The coil has been charged (and suddenly discharged) up to a maximum current chosen with an appropriate safety criterion, varying the operating temperature from 4.7 K to 80 K using a dry cooling method. The coil charges correctly with ramp-rates up to 5 A/s, generating a magnetic field which is slightly lower than that expected from a defect-free winding.

Furthermore, a simple equivalent circuit has been implemented to quickly derive the effective parameters of the coil, *i.e.* its longitudinal and turn-to-turn effective resistances and the amount of effective current flowing radially to avoid the damaged areas. This last parameter in particular, corresponds to the 4.3% ÷ 5.5% of I_{op} from the lowest to the highest temperature tested, which is considered limited and thus an evidence of the proper functioning of the NI coil.

The next chapter investigates at the alternative winding technique for NI coils: the layer-wound configuration.

Electrical characteristics of HTS coils with and without insulation in a layer-wound configuration

With the purpose of analyzing the behaviour of NI coils wound with different techniques, this chapter deals with the layer-wound configuration, the alternative configuration to the one described in the previous chapter (the pancake-wound configuration).

In general, superconducting coils are designed to operate with the same current along each turn, which allows generating the design magnetic field. In insulated windings, the currents have no alternative paths than flowing longitudinally in each turn of the coil, thus their proper charging is not problematic in this sense. Conversely in NI coils, transverse currents flowing in radial direction can also arise in the absence of quenches, caused by rapid transients, or an increase in superconducting resistance when the current supplied approaches I_c or the presence of local defects, as analyzed in *Chapter 4*. Although the no-insulation configuration improves the overall thermal stability of the coil compared to the insulated technique, NI coils requires a more detailed investigation regarding their electrical characteristic during the charging (or discharging) phase. In fact, it is important to establish the operating conditions at which transverse currents arise and to determine their intensity, in order to ensure the proper charging of a NI coil.

For complementarity with respect to the work described in *Chapter 4*, this chapter deals with the layer-wound configuration, considering that this technique is not investigated extensively in the literature for NI coils [34, 45 – 48], differently from the pancake-wound technique [49 – 56]. In this study, measurements of the *V-I* electrical characteristic are carried out on two windings, with and without electrical insulation between turns, of almost identical geometry. To interpret the experimental results obtained, with special reference to the peculiar behaviour of the voltages recorded across different layers of the winding, an electrodynamic model based on a non-linear lumped parameter circuit of the coil is proposed. The model results are compared to the experimental ones, thus giving an insight in the distribution of current and dissipated power inside the winding and a representation of the charging performance of an NI coil.

The activity is carried out in collaboration with the *Superconductors Laboratory* at *R.S.E. S.p.A.* (Milan, Italy), and to all the colleagues of the research group go the warmest thanks for their precious contribution.

5.1. *Experimental set-up for the layer-wound coils*

Two coils are realized using the layer-wound technique, with and without insulation. A *High Strength Plus* BSCCO tape manufactured by *American Superconductor Corp.* [182], cut from the same lot is used for both windings. The coils are wound on two identical G-10 mandrels, with the same number of layers (N_L) and turns per layer (N_T). The mandrel outer

diameter (81.5 mm) is selected so as not to degrade the tape critical current due to bending [183]. The main coils parameters are reported in Tab. 5.1.1.

Table 5.1.1. *Parameters of the tape and the layer-wound coils used in the project.*

General parameters	Unit	Value
Tape thickness [μm]	[μm]	300.0
Tape width [mm]	[mm]	4.1
Inner radius	[mm]	41.0
Number of layers (N_L)		3
Number of turns per layer (N_T)		10
Insulated coil / NI coil	**Unit**	**Value**
Outer radius	[mm]	41.9 / 42.1
Length of each layer	[cm]	258.8 / 259.1 ; 260.6 / 261.4 ; 262.5 / 263.6
I_c of each layer	[A]	109.5 / 109.5 ; 109.5 / 109.5 ; 113.4 / 109.5
n-value of all layers		13.5 / 13.5
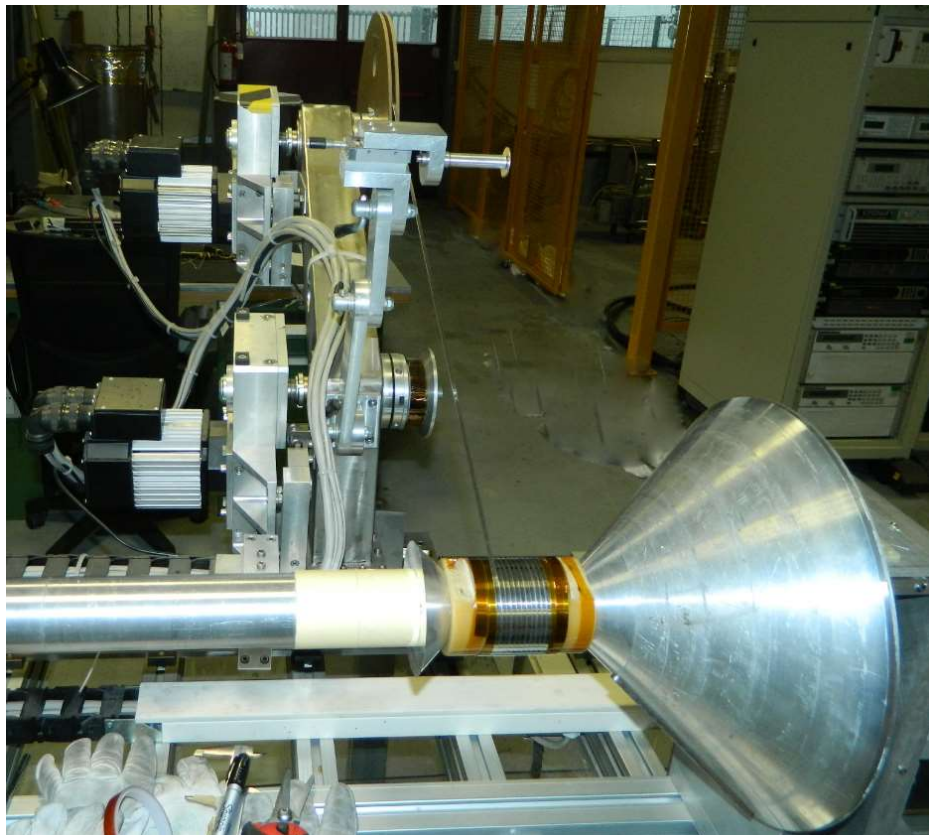
Figure 5.1.1. *Winding machine available at the Superconductors Laboratory at R.S.E. S.p.A, used in the study*

The critical current and the *n-value* for the tape composing each layer of the insulated coil are calculated from the voltage signals acquired during the charging tests. For the NI coil instead, these values can only be estimated; this is cleared in the next sections. Considering a tape with a good homogeneity, the critical current and the *n-value* of each layer of the NI coil are set equal to the values computed for the 1st and 2nd layers of the insulated coil.

The coils are wound using the winding machine available at the *Superconductors Laboratory* at *R.S.E. S.p.A.*, presented in Fig. 5.1.1. The machine can impose the rotation of the coil mandrel around its central axis, as well as a longitudinal translation thereof, thus ensuring the proper winding angle and the eventual pitch between turns. The direction of the longitudinal translation of the mandrel is reversed in correspondence of each layer change.

In the NI coil, the layers are wound on top of each other without inserting any insulation. In the insulated coil, each layer is separated from the adjacent ones by a Kapton layer of 50 µm thickness, positioned during the winding phase. This creates a difference between the outer radius of the two coils (41.9 mm and 42.1 mm for the insulated and the NI coils, respectively), which however can be considered negligible. In the insulated coil, a minimum pitch is kept to avoid uninsulated electrical contacts between turns of the same layer. Fig. 5.1.2 shows two photos taken during the winding phase of the coils. For the insulated coil (Fig. 5.1.2(a)), the interlayer Kapton insulation is visible, as well as the pitch kept between turns.
At the end of the winding phase, a layer of Kapton tape is wound tightly around the coils, to ensure better compression of the layers.
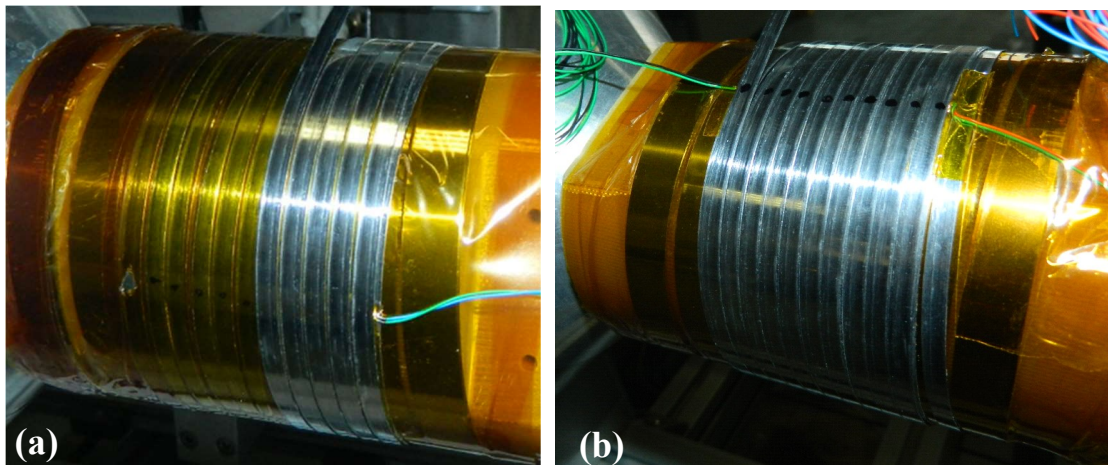
Figure 5.1.2. Winding phase for the (a) insulated and (b) NI coils

Both coils are instrumented with voltage taps soldered on the tape surface at the ends of each layer. Compared to the pancake-wound coil presented in *Chapter 4*, the voltage tap configuration shown in Fig.4.2.3.1(a) is adopted for the layer-wound coils. No voltage taps are introduced between the layers to avoid deforming the winding. The voltage wire pairs soldered to the ends of each layer are connected to different channels of the DAQ system, a *PXI-e4309* acquisition card, manufactured by *National Instruments* [171].

At the end of the winding phase, a pair of custom made removable G-10 bars are screwed into the casings realized at the mandrel ends, as displayed in Fig. 5.1.3. The two tape ends of the

coil are positioned on these bars. Since the number of layers is odd, the tape ends are located at opposite ends of the mandrel. Then, a copper plate is screwed on each G-10 bar, allowing the connection with the current leads. The current leads are connected to the current supply system, realized with two *HP/Agilent 6680A* power supplies [184], connected in parallel. The system can generate both current ramps and step profiles of variable amplitude and duration. The current signal during tests is acquired through a *Danisense DS600UB-1V* current Transducer [185].
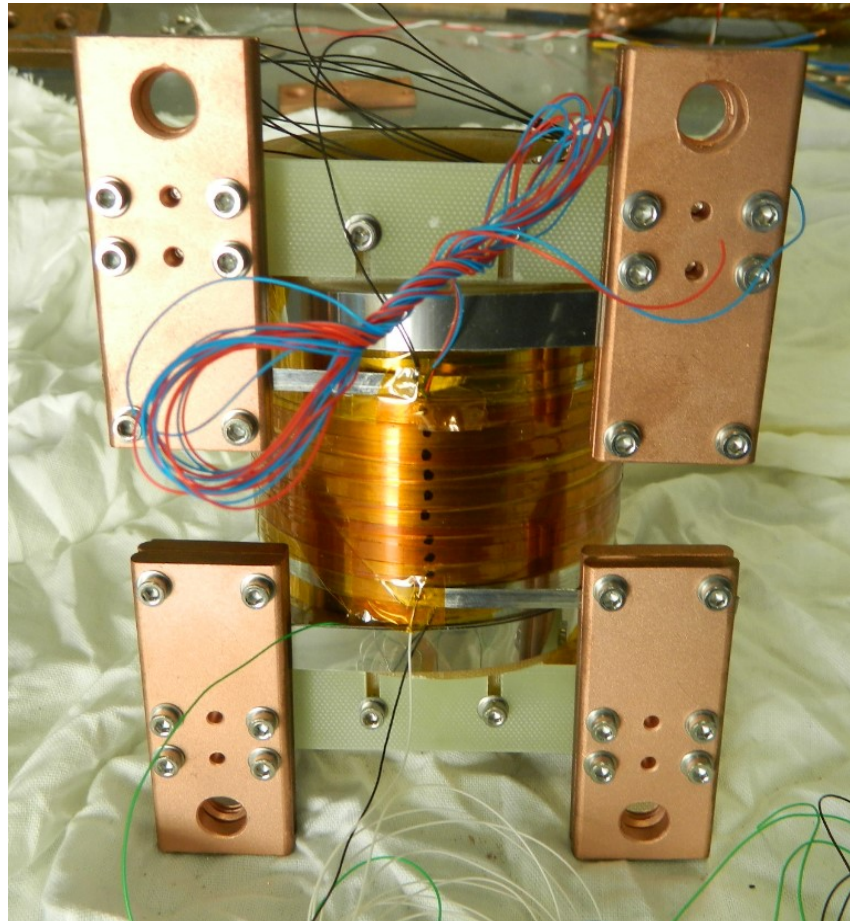
Figure 5.1.3. *NI layer-wound coil with voltage taps and the connecting bars with current leads.*

Figure 5.1.3 shows a second wider tape, wound as a single layer around the outer diameter of the mandrel, below the superconducting winding. This is a stainless steel tape to be used as a heater, and it can be connected separately to a second power supply system with the same G-10 bars used for the superconducting tape. However, no current is supplied to the heater in this specific study. The inner diameter of the HTS windings is measured considering the presence of this inner tape.

Finally, the tests on both coils are carried out in a liquid nitrogen bath, charging each coil up to 130 A with a ramp-rate of 1 A/s. Then, both coils are discharged with the same ramp-rate. Both the charging ramp-rate and the maximum operating current set during tests are considered suitable in order not to damage the coils.

5.2.   Equivalent lumped parameter circuit for a layer-wound coil

The electrical characteristics of the layer-wound coils is analyzed through the equivalent lumped parameter circuit presented in Fig. 5.2.1. The double bars indicate that the circuit branches can be replicated for a generic number of layers and turns.
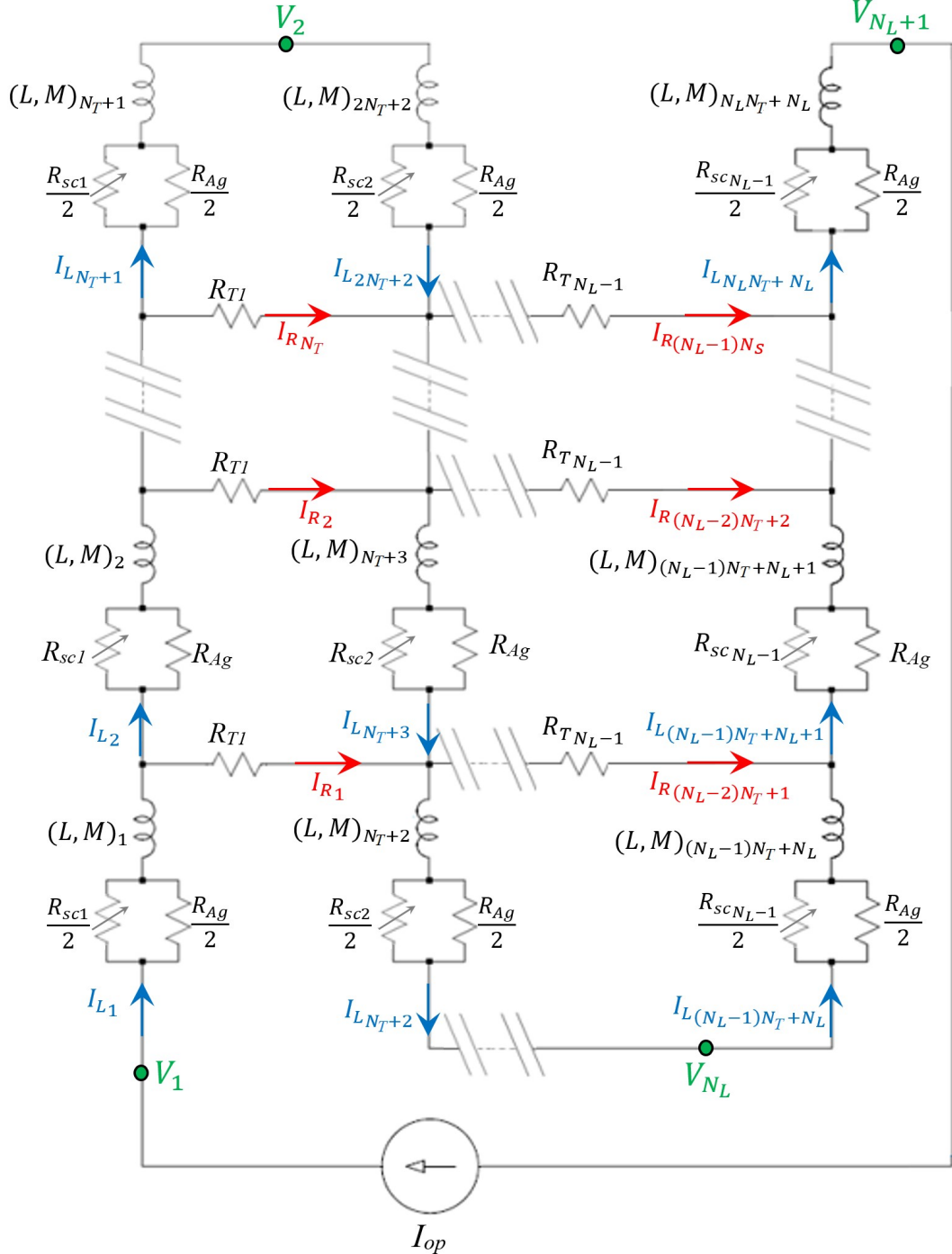
Figure 5.2.1. *Equivalent non-linear lumped parameters electric circuit of a layer-wound coil with a generic number of turns and layers.*

The current source imposing the operation current is connected to the first turn of the inner layer and to the last turn of the outer layer of the coil. In the circuit, each half turn of the winding is represented as the series between a linear inductor and a non-linear resistor. The terms $(L,M)_i$

correspond to the self-inductances of each longitudinal branch and the mutual-inductances between each other. To better reproduce the electrical properties of the BSCCO tape, each longitudinal resistor is given by the parallel connection between the non-linear resistance of the superconductor ($R_{sc,i}$) and the linear resistance of the silver matrix (R_{Ag}). The power law is adopted for the superconductor electric characteristics, with the properties reported in Tab 5.1.1. The resistivity of silver at 77 K is taken equal to 2.7 n$\Omega \cdot$ m [94] and the fill-factor of the tape is set to 30%. To consider the possible inhomogeneity of the superconductor, the critical current and the *n-value* can be varied between the layers. Then, from the tape geometrical dimensions and the length of each half turn, considered identical for the turns belonging to the same layer, the resistances $R_{sc,i}$ and R_{Ag} are computed.

To account for the current flowing radially between layers, transversal resistances ($R_{T,i}$) are introduced. By varying these parameters, it is possible to include the presence of an electrical insulation. Each turn is considered to be in contact with the turns of the adjacent layers at its same height (*i.e.* on the left and right sides) by means of a resistance $R_{T,i}$ which is lumped in the middle of the turn length. Therefore, it is assumed that all layers perfectly overlap at the same height. This approximation neglects the different winding angle of each layer, due to which the turns that can be in direct contact with only one turn of the adjacent layer.

Lumping the transversal resistances in the middle of each turn allows one reducing the number of elements in the circuit. Since there are no branches connected between the second half of a turn and the first half of the subsequent turn, their longitudinal resistances and inductances are in series and can be represented as a single electric component. The electric components representing the first and last half turns of each layer are instead kept separate, in order to keep the various layers distinct in the circuit representation. Thus, the corresponding resistances and inductances are halved with respect to those of the other branches of the same layer. Each layer is therefore described with N_T+1 longitudinal branches, each connected to the previous or subsequent layer with N_T transverse branches.
The transverse contacts between turns belonging to the same layer (*i.e.* across their thickness) is assumed negligible.

The currents flowing in the longitudinal ($I_{L,i}$) and transverse ($I_{R,i}$) branches are highlighted in Fig. 5.2.1 with different labels, colors and the corresponding numbering. For a coil with a generic number of turns and layers, the number of longitudinal currents is (N_T+1)$\cdot N_L$, while the number of transverse currents is (N_L-1)$\cdot N_T$. The positive reference direction of the longitudinal currents is in agreement with the path followed by the tape during the winding phase. In the first layer, the positive orientation is directed from bottom to top, and is then inverted at each subsequent layer. The positive direction of the transverse currents is taken from left to right.

The loop analysis is adopted to solve the circuit [186]. The number of problem unknowns, namely the loop currents, is equal to $N_L \cdot N_T$. Once the system is solved, the branch currents can be computed as the algebraic sums of the currents of the loops adjacent to the branch considered. Since I_{op} can vary in time, a system of differential equations has to be solved. The numerical method adopted to solve this system is the Cash-Karp Embedded Runge-Kutta of 5th order [187].

Finally, from the branch currents it is possible to compute the voltage differences between each pair of nodes of the circuit. The green dots in Fig. 5.2.1 represent the locations of the N_L+1 voltage taps inserted in the coils, from which the values of the average electric fields are computed, dividing by the length of each layer.

5.3. Experimental and numerical results from tests performed with the layer-wound coils

The measurements carried out during the charging tests are compared with the numerical results obtained with the equivalent circuit, simulating the same testing conditions.

5.3.1. Electrical characteristics of the layer-wound coils

The measured electric characteristics of the insulated and the NI coils are plotted in Fig. 5.3.1.1(a) and Fig. 5.3.1.1(b), respectively. The insets magnify the curves up to 1 µV/cm (corresponding to the lower critical field).

For the insulated coil, the different profile of the 3rd layer as compared to the others is ascribed to a higher I_c value of the tape in this layer, as reported in Table 5.1.1. The discrepancy (3.5%, as compared to the other layers), is due to a non-uniformity of the tape, and can be considered as acceptable.

In the simulations with the equivalent circuit, both resistances between the turns of the 1st and the 2nd layers ($R_{T,1}$) and the turns of the 2nd and the 3rd layers ($R_{T,2}$) are set to 30.0 mΩ. It was verified that this is the minimum value that guarantees obtaining transverse currents of negligible amplitude ($I_{R,1} < 1‰\ I_{op}$) for the charging ramp-rate adopted in this project, as it is described in the following paragraphs. If a lower value is selected, the difference between the voltage curves increases and the coil electrical behaviour gradually shifts towards that of a NI one. If a greater value is selected, the results do not differ from those reported in 5.3.1.1(a).

The NI coil exhibits a peculiar behaviour, since the electric fields in the first and the last layers have a practically identical growth, while that in the central layer increases more slowly. In particular, the electric field in the three layers remains the same up to $I_{op} < 0.8·I_c$, while for higher amplitudes the curves diverge. The experimental curves can be well reproduced with the numerical model, by using the transverse resistances between layers as fitting parameters. In particular, the resistance $R_{T,1}$ between the 1st and 2nd layers is set to 2.0 mΩ while $R_{T,2}$ between the 2nd and 3rd layers is set to 0.5 mΩ. This non-uniformity of the contact between layers could be due to the winding phase, where a different tensional state could have been applied to the tape. The different simulated behaviour of the outer layers is related to the different values of $R_{T,1}$ and $R_{T,2}$; it was verified, by setting these two parameters equal, that the outer layers exhibit the same V-I curve.
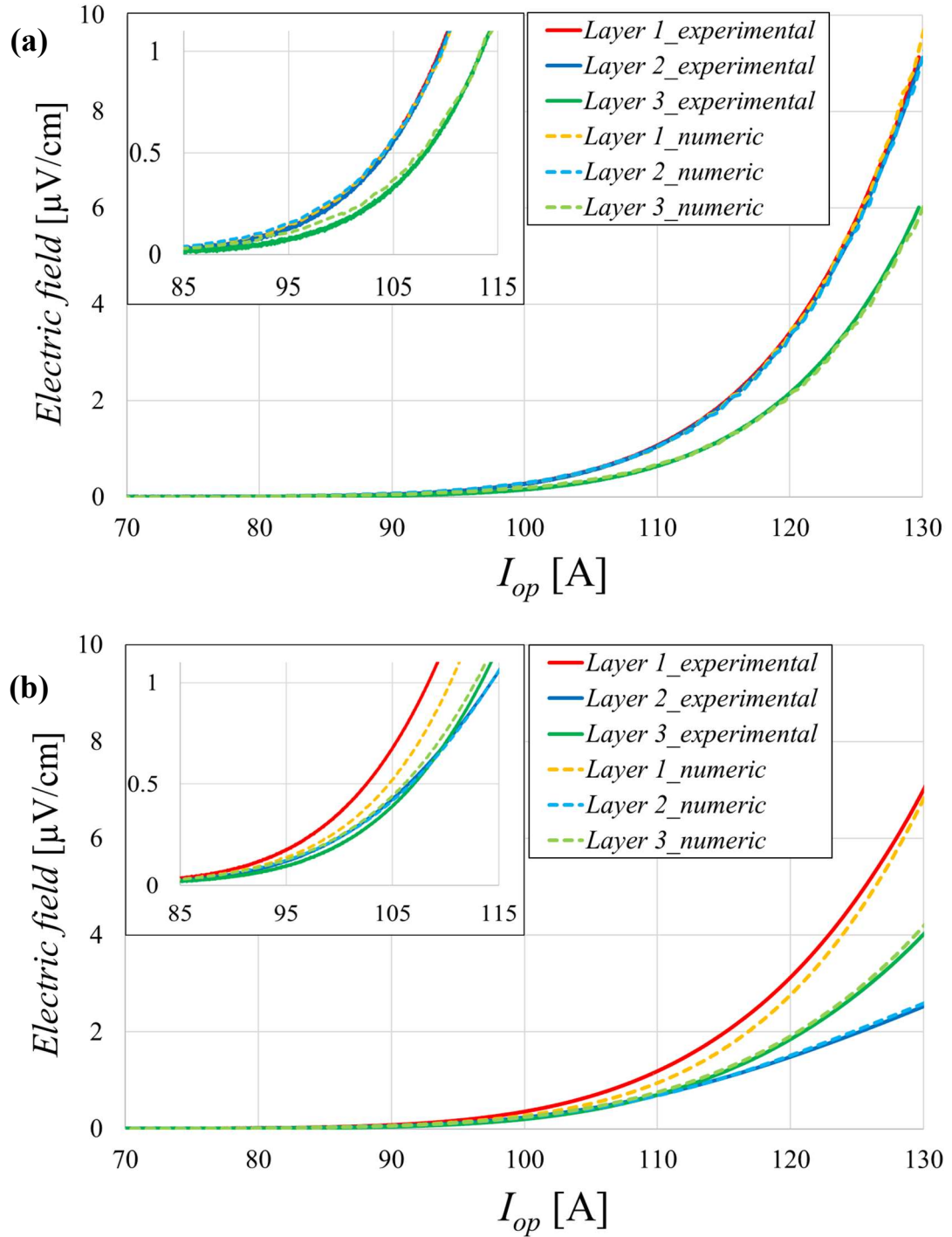
Figure 5.3.1.1. *Comparison of the electric field measured during tests and computed numerically for the 3 layers of the (a) insulated and (b) NI coils. The insets magnify the curves up to 1 μV/cm.*

5.3.2. Current distribution in the layer-wound coils

Fig. 5.3.2.1(a) presents the ratio between the longitudinal currents and I_{op}, in three branches of each layer of the NI coil, located at the same height ($I_{L,2}$, $I_{L,13}$ and $I_{L,24}$ at the bottom, $I_{L,6}$, $I_{L,17}$ and $I_{L,28}$ in the middle, $I_{L,10}$, $I_{L,21}$ and $I_{L,32}$ at the top) during the coil energization

(expressed as the ratio with I_c). Fig. 5.3.2.1(b) shows the ratio between the transverse currents and I_{op}, in four branches between each pair of layers of the coil, located at the same height ($I_{R,1}$ and $I_{R,11}$ at the bottom, $I_{R,4}$ and $I_{R,14}$ in the middle-lower part, $I_{R,7}$ and $I_{R,17}$ in the middle-upper part, $I_{R,10}$ and $I_{R,20}$ at the top) during the coil charging.
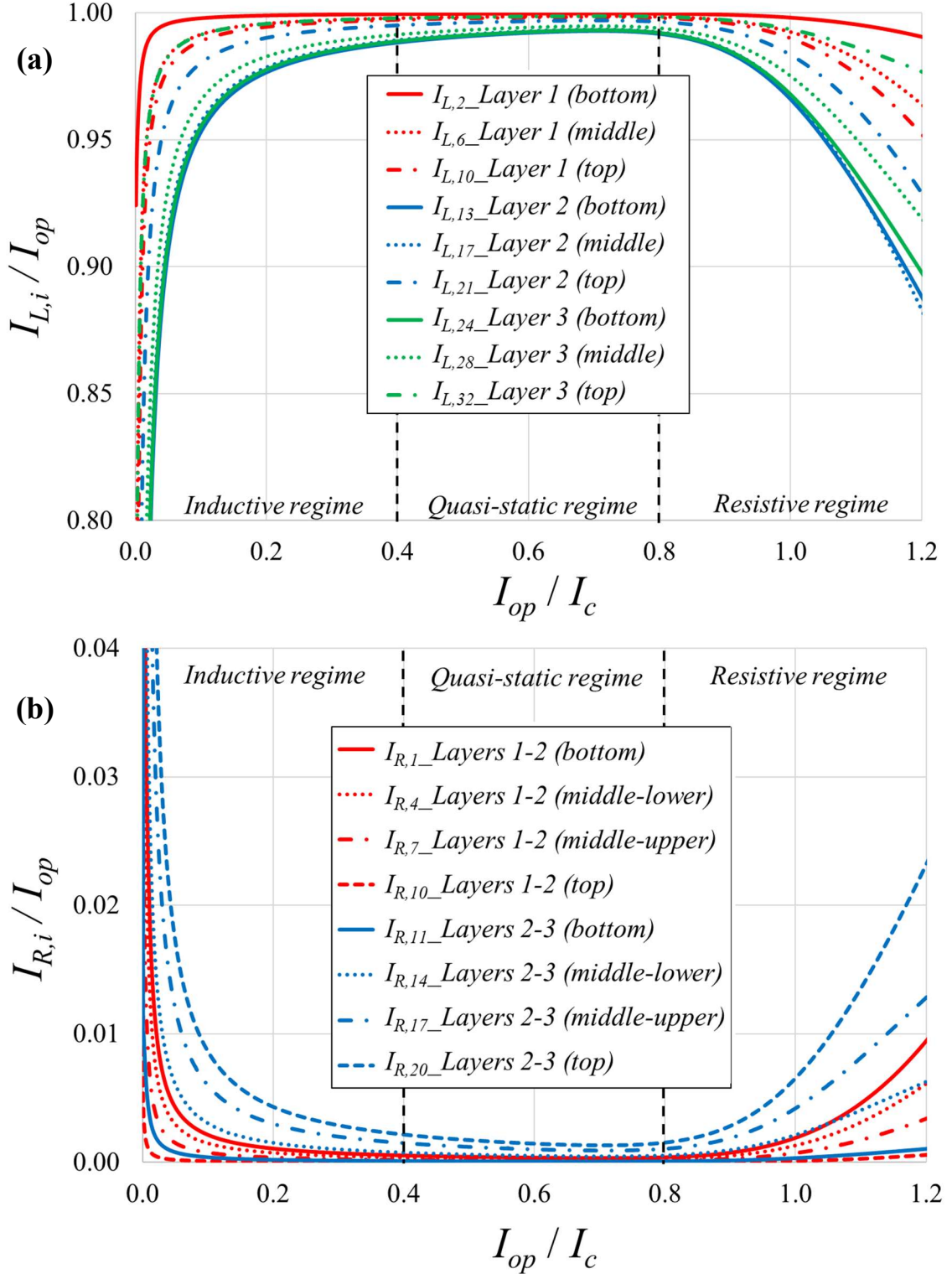
Figure 5.3.2.1. *(a) Longitudinal and (b) transverse currents flowing in selected branches of the equivalent circuit during the charging phase of the NI coil.*

At $I_{op}/I_c < 0.4$, the current distribution is mainly driven by the inductances of the circuit (*inductive regime*). The time constants of this electrodynamic transient range from 5 s to 50 s. During the transient, the current in each branch evolves differently, depending on its location in the circuit. At $0.4 < I_{op}/I_c < 0.8$, an almost steady-state condition is reached (*quasi-static regime*), in which all the longitudinal branches are almost evenly loaded. At $I_{op}/I_c > 0.8$, the longitudinal currents start to spread again due to the transition from superconducting to normal state (*resistive regime*). This is particularly evident for the longitudinal branches located in the 2nd and 3rd layers, in the middle-lower section of the circuit. At $I_{op}/I_c = 1.2$, the current flowing in these branches is about 88% of I_{op}; correspondingly, a certain amount of current flows in the transverse paths. The transverse currents start to rise at $I_{op}/I_c > 0.8$, reaching a maximum amplitude about 2.4% of I_{op} when $I_{op}/I_c = 1.2$. The transverse currents are greater between the 2nd and 3rd layers since $R_{T,2} < R_{T,1}$, while they are smaller at the bottom of the coil between the 2nd and 3rd layer, and at the top of the coil between the 1st and 2nd layers.

It can be concluded that the NI coil is not loaded uniformly during the charging-phase. For the ramp-rate used in this work, the inhomogeneity due to the resistive transition occurs when I_{op} exceeds amplitudes higher than the safety margin usually adopted for a superconducting device, generally not greater than 80% of I_c [188 – 190]. If the resistances $R_{T,i}$ are lowered, the threshold at which the longitudinal currents become inhomogeneous due to the resistive transition is reduced.

For completeness, Fig. 5.3.2.2 presents the ratio between the longitudinal currents and I_{op} (a) and the ratio between the transverse currents and I_{op} (b), for the insulated coil. The results for the same circuit branches of Fig. 5.3.2.1 are displayed. Both in the *inductive regime* and in the *resistive regime*, the difference between the longitudinal currents is minimal (less than 1%), therefore the coil charges properly and there are no relevant differences in the electrical characteristics of the various layers (except for that due to an inhomogeneous critical current). In this case, the time constants of this electrodynamic transient range from 25 s to 30 s. Concerning the transverse currents, they are almost negligible; they reach 1‰ when $I_{op}/I_c = 1.2$.
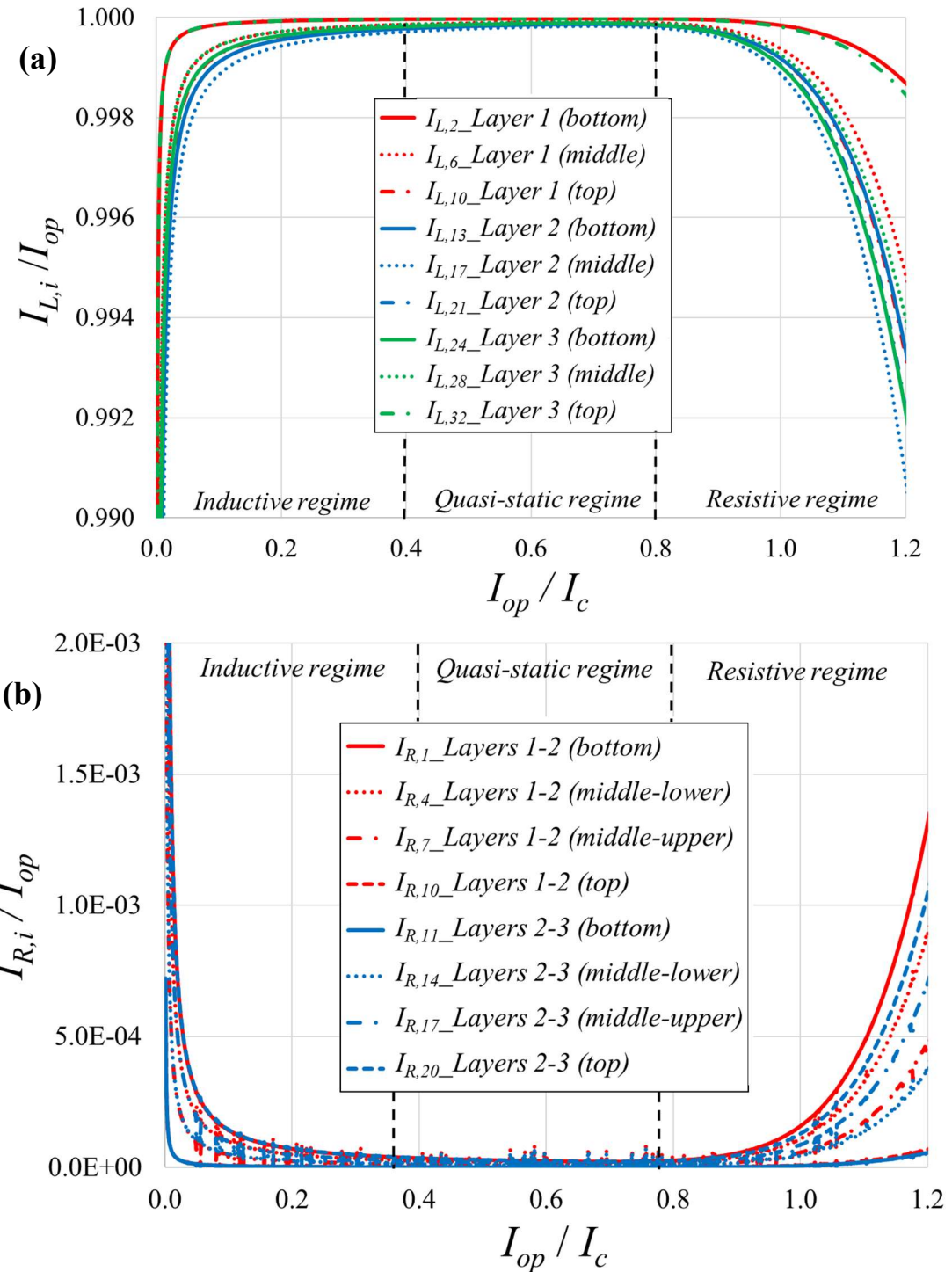
Figure 5.3.2.2. *(a) Longitudinal and (b) transverse currents flowing in selected branches of the equivalent circuit during the charging phase of the insulated coil.*

5.3.3. Dissipated power distribution in the layer-wound coils

Once the branch currents of the equivalent circuit are computed, the power dissipated by Joule effect in each branch can be determined as $R \cdot I^2$, where R is the branch resistance (longitudinal or transverse).

Fig. 5.3.3.1 presents the dissipated power in the longitudinal branches ($P_{L,i}$) of the equivalent circuit of the NI coil, at (a) I_{op}/I_c = 0.9 and at (b) I_{op}/I_c = 1.19. Each bar indicates the amplitude of the power computed in a longitudinal branch. The branches are organized according to their position along the circuit height. In the project coil (N_T = 10), the positions n°1 and n°11 corresponds respectively to the branches located at the bottom and at the top of each layer. To account for the different tape length corresponding to each longitudinal branch, the power is shown per unit of length.

At I_{op}/I_c = 0.9, all longitudinal branches dissipate a similar amount of power. Conversely, at I_{op}/I_c = 1.19, the Joule heat differs considerably according to the branch. In the 1st layer, the power gradually decreases moving from the bottom to the top of the circuit, while in the 3rd layer, the power decreases moving from the top to the bottom of the circuit. In both cases, the power converges asymptotically towards low amplitudes moving far from the branches that are directly connected to the current leads. Finally, in the 2nd layer the power dissipation is lower than in the outer layers, decreasing slightly from position n°1 to n°5, and then increasing more consistently from position n°5 to n°11.

As expected, the losses computed in Fig. 5.3.3.2(b) are much higher than those of Fig. 5.3.3.1(a), since an increase in operating current corresponds to an increase in longitudinal current, albeit not proportional in all branches.

Fig. 5.3.3.2 shows the dissipated power in the transverse branches ($P_{T,i}$) of the equivalent circuit of the NI coil, at (a) I_{op}/I_c = 0.9 and at (b) I_{op}/I_c = 1.19. The powers are not reported per unit of length, as the length of the transverse branches of the circuit is not a well identifiable value. The bars corresponding the transverse branches are organized as in Fig. 5.3.3.1. In this case, the colours identify the branches located between different pairs of layers.

In this case, a strong dependence of the transverse Joule heat on the branch position inside the circuit is already visible at I_{op}/I_c = 0.9. The power dissipated in the transverse branches placed between the 1st and 2nd layers decreases going from the bottom to the top of the circuit, while power dissipated in the transverse branches placed between the 2nd and 3rd layers increases greatly going from the bottom to the top of the circuit.

Despite $R_{T,1}$ is greater than $R_{T,2}$, the power produced between the 1st and 2nd layers is generally lower than the power generated between the 2nd and 3rd layers. This depends on the transverse current values, which are consistently lower in the branches between the 1st and 2nd layers since the high resistance in these branches obstacles the transverse current flow.

As the I_{op}/I_c ratio increases, the power dissipation on the transverse branches rises. Differently from Fig. 5.3.3.1, the trends shown in Fig.s 5.3.3.2(a) and 5.3.3.2(b) do not differ significantly from each other. This is due to the fact that the transverse resistances are linear. However, the distribution of the transverse currents also depends on the non-linear resistance of the longitudinal branches. It is worth noting that Fig. 5.3.3.2(b) appears more symmetrical than Fig. 5.3.3.2(a). In fact, as shown in Fig. 5.3.2.1(b), at I_{op}/I_c = 1.19 the transverse currents flowing in the branches at the same height of the circuit are more similar to each other.
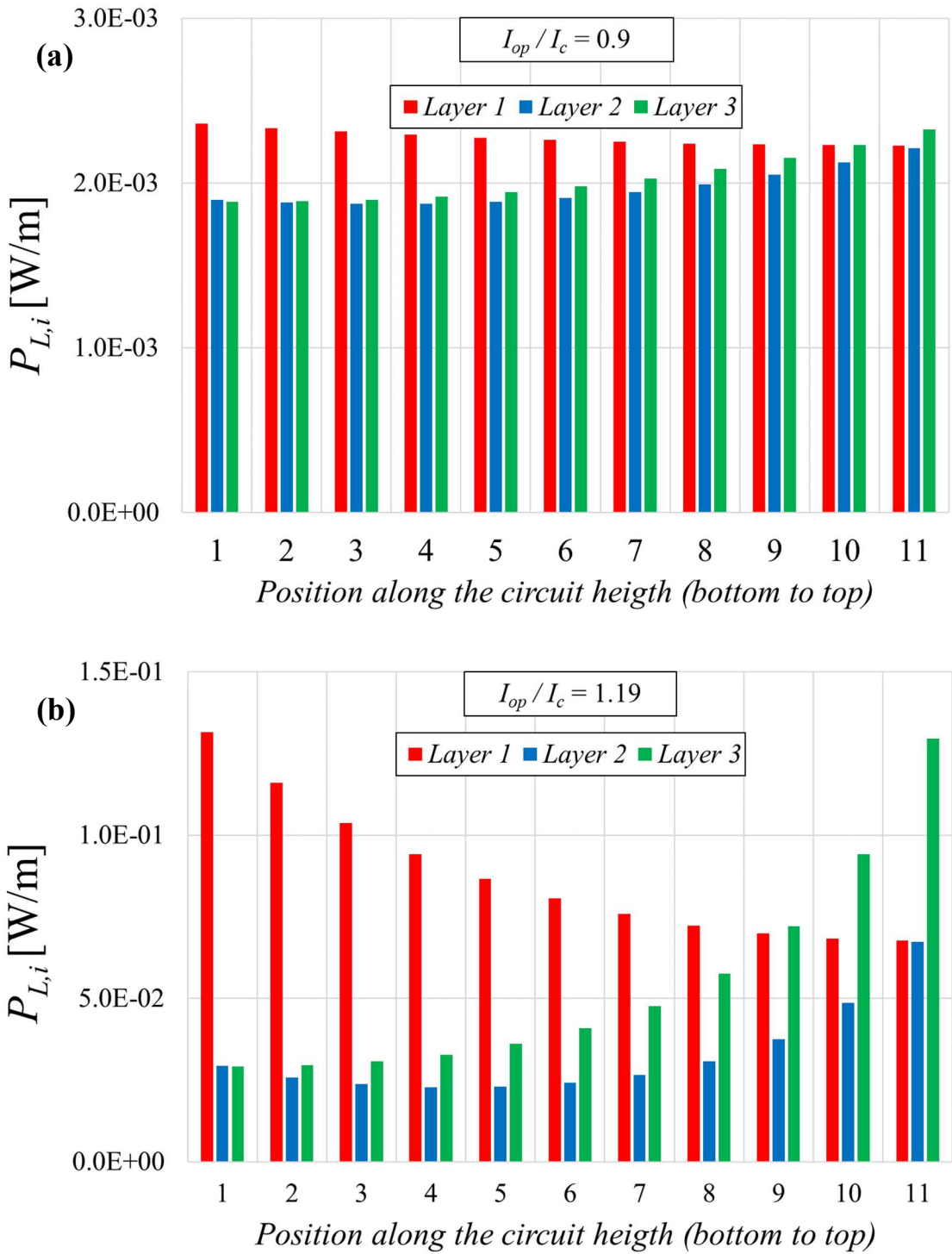
Figure 5.3.3.1. *Dissipated power computed for the longitudinal branches of the equivalent circuit of the NI coil during the charging phase, at (a) $I_{op}/I_c = 0.9$ and at (b) $I_{op}/I_c = 1.19$.*

Therefore, the most stressed branches of the circuit in terms of power dissipation, both longitudinal and transverse, are those in the proximity of the connections with the current generator. The power generated in the other branches decreases moving away from these regions, both radially and longitudinally.
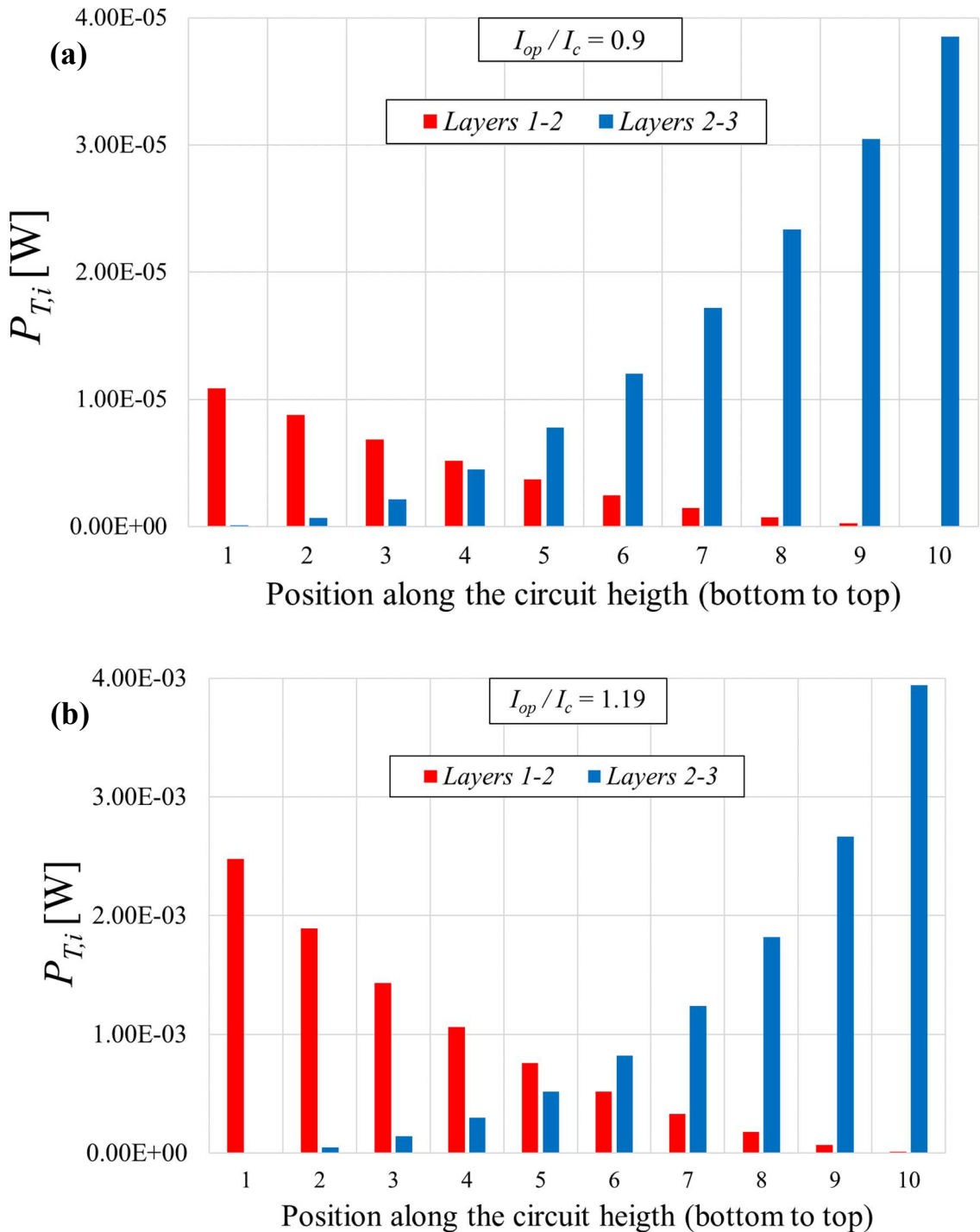
Figure 5.3.3.2. Dissipated power computed for the longitudinal branches of the equivalent circuit of the NI coil during the charging phase, at (a) I_{op}/I_c = 0.9 and at (b) I_{op}/I_c = 1.19.

These conclusions can also be verified by computing the heat generated in each turn of the winding represented by the equivalent circuit. Since each longitudinal branch represents either half turn or the sum of two half turns, half of the power generated by two consecutive longitudinal branches is assigned to each turn (or the whole power, if the branches are the first or the last of a given layer, see Fig. 5.2.1). As for the power dissipated in the transverse

branches, this is equally subdivided between the two longitudinal branches it connects. At the end of the process, the heat generated in the $N_L \cdot N_T$ turns of the winding is retrieved.

Fig. 5.3.3.3 shows the dissipated power distribution within the NI coil during the charging phase, at (a) $I_{op}/I_c = 0.5$, (b) $I_{op}/I_c = 0.9$ and at (c) $I_{op}/I_c = 1.19$. Each square in the 2-D representation of the cylindrical coordinate system represents a turn of the winding. Only one value of power is assigned to each turn at a given I_{op}; for the sake of representation, a shading color plot is obtained via 2-D interpolation. At $I_{op}/I_c = 0.5$, the heat generation is concentrated in the 3rd layer, at the upper part of the coil, with remarkable variations included between 0.2 µW and 2.3 µW. At $I_{op}/I_c = 0.9$, the heat peak is still located in the upper part of the 3rd layer, but the distribution of dissipated power appears to shift throughout the 1st layer, especially in its lower part. In this case, the inhomogeneities are limited below 20%. At $I_{op}/I_c = 1.2$, the heat generation mainly occurs in the regions close to the connections of the coil to the current leads, thus confirming the deductions obtained through the histograms. In these regions, the power per unit length is more than 3 times greater than that generated in the turns of the 3rd layer at the bottom of the winding.
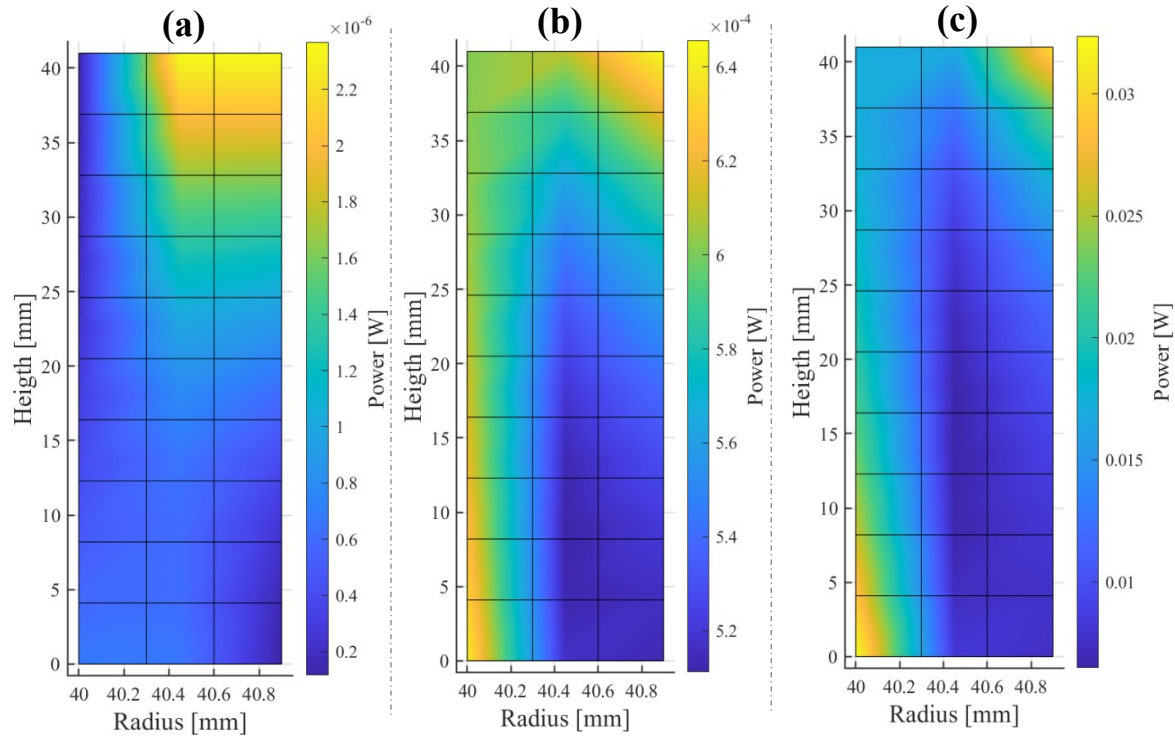
Figure 5.3.3.3. *Dissipated power generated in the turns of the NI coil during the charging phase, at (a) $I_{op}/I_c = 0.5$, at (b) $I_{op}/I_c = 0.9$ and at (c) $I_{op}/I_c = 1.19$, obtained with the numerical model.*

The dissipated power distribution in the insulated coil are not reported. Simply, since in this case the transverse currents are negligible and the turns results evenly loaded, also the dissipated power is uniformly distributed in the coil cross-section during the whole charging phase.

5.4.   Conclusions

This section has highlighted the different electrical characteristics of a NI coil in a layer-wound configuration, compared to its insulated counterparts. While the insulated coil charges as expected, exhibiting similar voltage traces in the various layers, the voltages measured on the NI coil reveal instead a clear difference in the time evolution of the voltage of the outer layers with respect to the inner one. The proposed lumped parameter non-linear electric circuit model of the coil allows interpreting the voltage development in the various layers in terms of the current redistribution inside the winding during the transport current ramp. At the ramp-rate level adopted (1 A/s), the currents flowing in radial direction in the NI coil are driven by inductive effects for transport currents up to 40% of the critical current, and by resistive effects for transport currents above 80 % of the critical one. This means that if the DC operating current in an NI coil is kept below the safety margin usually adopted for a superconducting device, it is uniformly redistributed in the turns of each layer and the coil proper charging is guaranteed. However, these limits strongly depend on the charging rate.

Lastly, as the current distribution in the charging phase of an NI coil differs from that of an insulated coil, the distribution of dissipated power is also different, revealing areas of particular stress in correspondence with the turns in direct contact with the current leads.

In the following chapter, the AC losses in NI coils are investigated. In particular, the layer-wound configuration is selected as it is possible to compare the behaviour under AC conditions of the pair of coils with very similar geometric characteristics, with or without insulation, presented in this chapter. This allows to extend some of the considerations presented at the tape level in *Chapter 2* and *Chapter 3* to HTS coils, and to complete the analysis of AC losses.

AC losses in HTS coils with and without insulation in a layer-wound configuration

On the one hand, HTS coils wound without electrical insulation between turns have great quench stability and are able to work properly even in the presence of local defects when designed to work in DC conditions or with slow transients, as analyzed in *Chapter 4*. On the other hand, the performance of NI coils in time-varying regime are poorer compared to their insulated counterpart, especially for fast transients, as reported in *Chapter 5*. Normally, the use of NI coils for AC applications is avoided, as in these conditions their proper charging is problematic and the intensity of the transverse currents in the inductive and resistive regimes (see *Section 5.3.2*) are such as to generate considerable heat dissipation.

However, a quantification of the AC losses in NI coils is not extensively reported in the literature. Studies have been performed regarding the performance of NI coils charged with current ramp profiles at different ramp-rates [191 – 193], while a limited number of works deals with the effect of AC magnetic fields [56, 194] or an AC transport current [195]. Further investigations are essential to examine possible operating conditions for which the use of NI coils can be considered valid. Furthermore, a cooling system can be properly designed only through the precise determination of all loss contributions in a superconducting device. Given that any NI coil is subjected to a time-varying regime during its operating, even if for short periods of time and with slow transients, it will always face AC losses that can be evaluated with the same tools developed for sinusoidal-varying regimes.

This chapter illustrates a numerical and experimental analysis regarding the measurement of AC losses in layer-wound coils, with and without insulation between turns. The same coils analyzed in *Chapter 5* are used for this work, wound with the same tape and having almost identical geometrical parameters. For the electromagnetic measurements, the signal acquisition system and post-processing technique described in *Chapter 3* are adopted, with proper modifications to account for the characteristics of each coil configuration. Moreover, even the numerical tools require distinct approaches for the two windings, to take into account the different current distribution between turns. To compute the Joule effect losses, the equivalent circuit described in *Section 5.2* is used, while the intra-tape AC losses are calculated with a FEM model based on the *H*-formulation, adapting the method described in *Section 2.3.2*.

6.1.   *AC losses measurements in a BSCCO tape sample*

Firstly, the AC losses in a straight sample of BSCCO tape are investigated. The same tape used to realize the two windings described in *Section 5.1*, a *High Strength Plus* BSCCO tape from *AMSC Corp* whose properties are reported in Tab. 5.1.1, is measured. The same experimental procedure described in *Chapter 3* is adopted. The tape sample has a length of 32 cm, and the two voltage taps used for the electromagnetic measurement are placed at its center,

at a distance of 8 cm from each other. The voltage measurement circuit configuration selected is the one reported in *Section 2.4.2*, with voltage taps twisted at a distance of $\frac{3}{2}w$ from the tape middle axis.

The implementation of the geometry of the BSCCO tape cross-section in the numerical models for computing AC losses in tapes, described in *Section 2.3* and *Section 2.4*, is not trivial since the models are developed for coated conductors and not for a multifilamentary superconducting material immersed in a silver matrix, as in the case of this tape. These modifications go beyond the scope of this work and would be analyzed in the future. For this investigation, it is sufficient to compare the measurements with the values obtained from the analytical formulae. Since only the AC transport losses are measured, neglecting the presence of external magnetic fields, Eq. (2.3.5.3) can be used. However, in the literature it is reported that the AC losses of BSCCO tapes are closer to the values predicted for tapes having an elliptical cross-section rather than those predicted by Eq. (2.3.5.3), written for thin strips. Indeed, the twisted multifilamentary arrangement present in BSCCO tapes behaves like a monofilamentary conductor having an elliptical cross-section [85]. Therefore, to verify this assumption the experiments are compared with both Norris' formulation for a thin strip and with Norris' formula for a wire in elliptical section [58], here reported:

$$\langle p(t) \rangle_{Elliptical} = f \, \frac{I_c \, \mu_0}{\pi} \left[(1 - I_m) \ln(1 - I_m) + (2 - I_m) \frac{I_m}{2} \right] \qquad \left[\frac{W}{m} \right] \qquad (6.1.1)$$
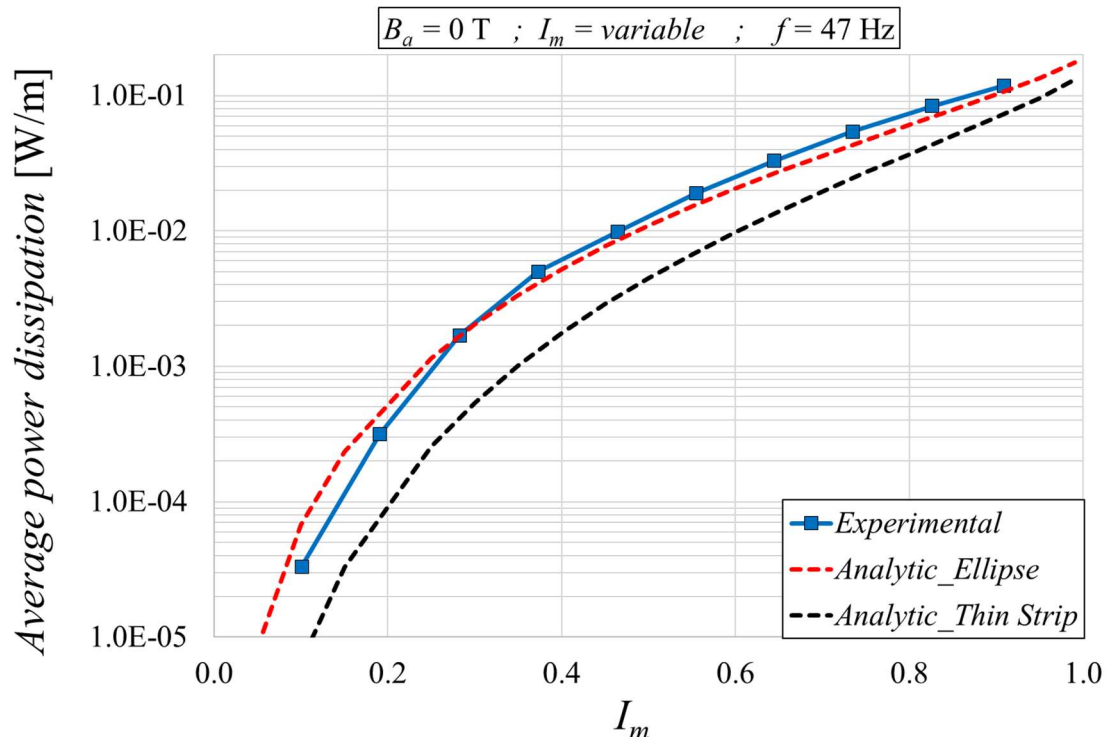
Figure 6.1.1. *Average power dissipation in the High Strengh Plus AMSC tape, for different I_m values and for a frequency set to 47 Hz. The figure is in semi-logarithmic scale.*

Fig. 6.1.1 shows the average power dissipation in the *High Strength Plus* tape, varying the amplitude of the transport current and for a frequency set to 47 Hz. Unlike a coated conductor (see Fig. 3.4.2 for the *SuNAM SCN04* tape, for example), the experimental results fit well the analytical trend for an elliptical wire rather than that for a thin strip. At low currents, the experimental results are lower than those predicted analytically, even if under these conditions the measured voltage signals reach levels close to the accuracy of the acquisition system and might lead to imprecision in the losses assessment. At high current amplitudes, the curves tend to converge, with the measurements being slightly higher than the analytical values. In fact, the analytical formulae do not take into account the presence of the silver matrix and the surrounding stainless steel layers, which introduce an additional contribution to the overall losses of the tape. Furthermore, the BSCCO tape tested has a relatively low *n-value*, as reported in Tab. 5.1.1, which conflicts with the critical state model assumption adopted by the analytical formula, especially in the high currents range.

Fig. 6.1.2 presents the AC losses varying the frequency of the transport current and for I_m equal to 0.75. As expected, the measurements are slightly higher than the analytical values, converging with the curve for an elliptical wire at a frequency of 197 Hz.
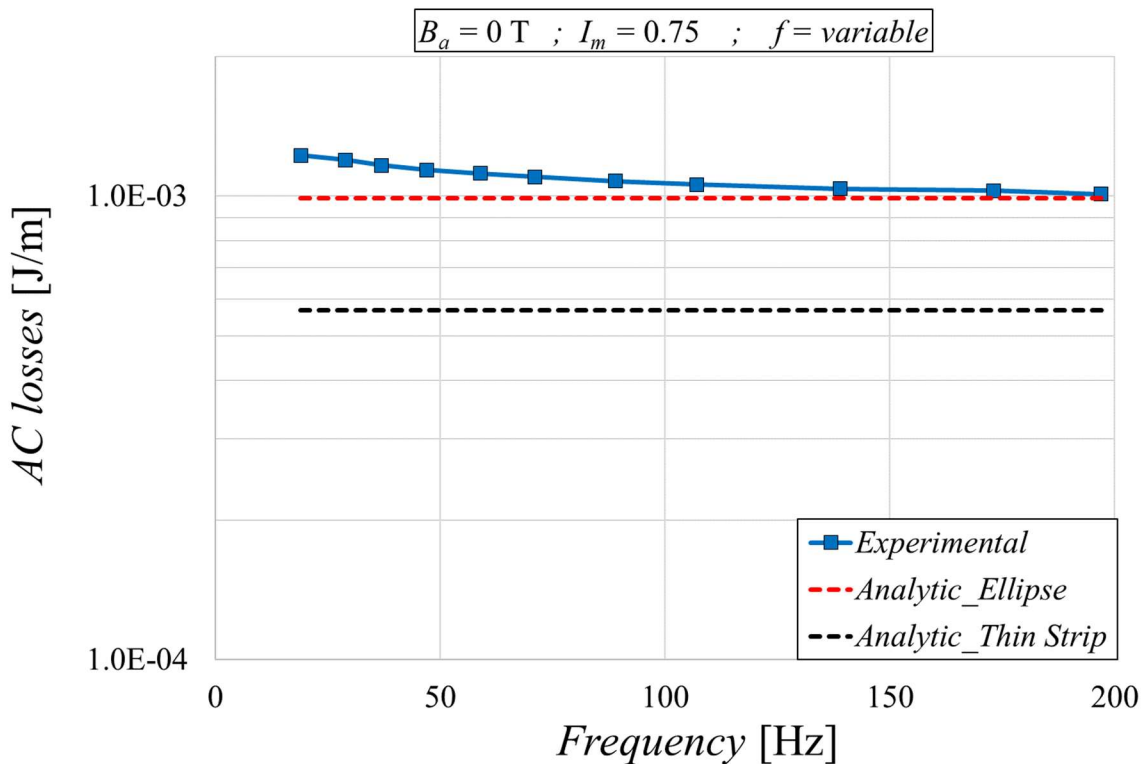
Figure 6.1.2. *Transport current AC losses in the High Strengh Plus AMSC tape, for different frequencies and for I_m equal to 0.75. The figure is in semi-logarithmic scale.*

6.2. Experimental set-up for the electromagnetic measurements of AC losses in inductive HTS coils

The measurement of AC losses in HTS inductive coils (regardless of their configuration) by means of the electromagnetic method involves different issues compared to

the measurements performed in straight tapes or anti-inductive coils. In fact, if on the one hand the measured voltage signals have a greater amplitude than those of a straight tape, as they are acquired from samples of greater length, on the other hand they present a considerable inductive signal that can mask the component in phase with the current, necessary to determine the losses. This complication also exists in tapes, but to a lesser extent as their self-field is limited. To reduce this problem, experimental set-ups for AC losses in coils involve inductive signal compensation systems. These systems are generally based on the use of one or more *cancel coils* [196 – 203], although there are some alternatives in the literature [204].
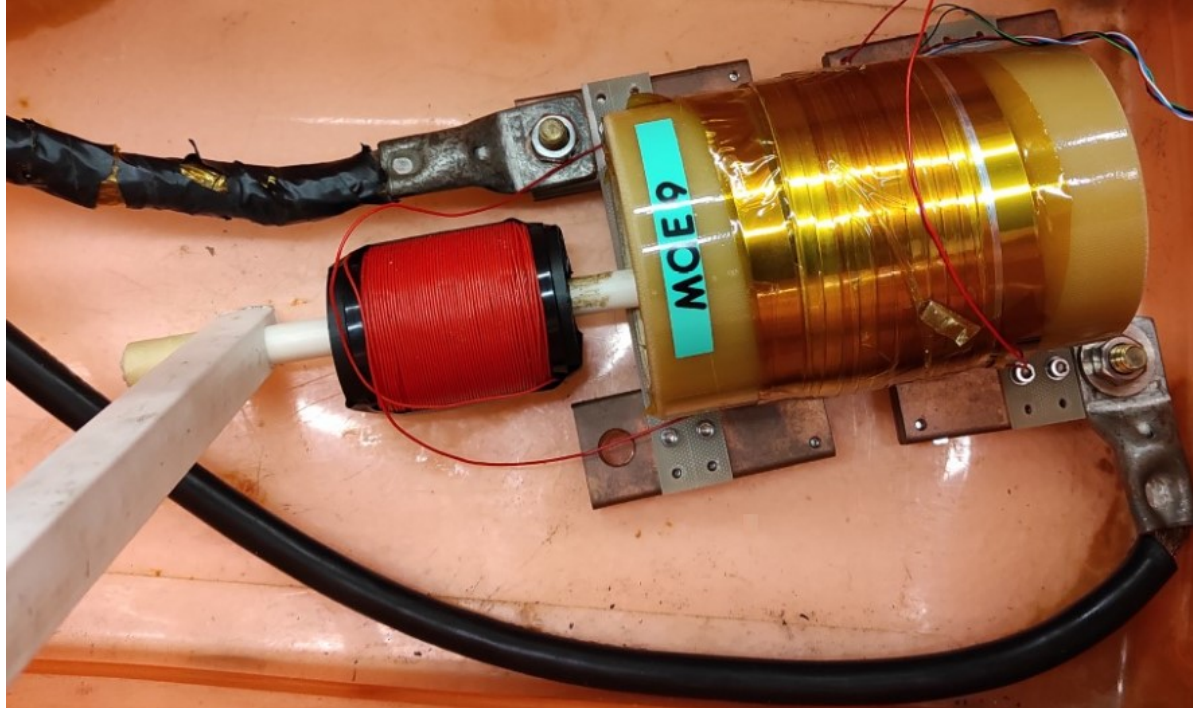
Figure 6.2.1. *Insulated HTS coil to be measured, with its cancel coil (in red) at its side. The cancel coil is moved axially inside the bore using to the white plastic support on the left.*

In this work, a cancel coil is inserted inside the bore of the HTS coil to be measured, so that the two coils are coaxial. The cancel coil is realized by winding a large number of turns of copper conductor having a small cross-section around a plastic mandrel. A small section guarantees a high electrical resistance and prevents even a small portion of the system supply current from flowing into the cancel coil, placed in parallel to the HTS coil. Then, the cancel coil links a flux which depends on the magnetic field generated by the HTS coil (plus any external fluxes, considered negligible in this work). The voltage difference generated at its ends is proportional to the inductive signal of the HTS coil. The voltage signal is in quadrature with the current signal and, since the cancel coil is counter-wound with respect to the winding direction of the HTS layer-wound coil, it is also in phase opposition with respect to the inductive component of the voltage signal measured from the HTS coil. By moving the cancel coil axially, it is possible to vary the quantity of flux that is linked and consequently the amplitude of the inductive signal produced at its ends. Fig. 6.2.1 shows the cancel coil used in this work, axially displaced inside the HTS coil bore by means of a plastic support equipped with an arm long enough to be safely moved manually when the whole system is immersed in liquid nitrogen bath.

Fig. 6.2.2 shows a diagram of the connections for the acquisition of the electromagnetic signals in the experimental set-up. Differently from Fig. 3.1.1 (which described the set-up used for tapes), the signal wire coming from one of the ends of the HTS coil is connected in series to the cancel coil. In this way, the acquired voltage signal is equal to the sum of the signals of the HTS and the cancel coils. As the cancel coil signal is in phase opposition with respect to the inductive component of the voltage signal of the HTS coil, it should reduce its intensity, thus making the desired phase component stand out. This also leads to an amplitude reduction of the measured voltage signal, approaching the accuracy limit of the acquisition system.
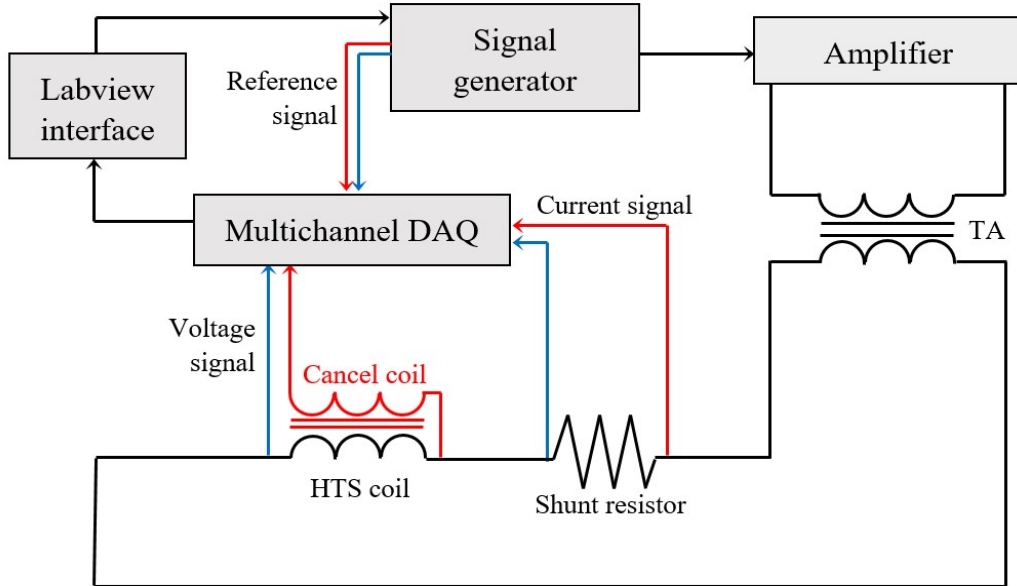
Figure 6.2.2. Connection scheme of the experimental set-up for AC current generation and data acquisition in insulated coils developed at the University of Bologna.

The most delicate part of the procedure lies in the correct positioning of the cancel coil. Ideally, it should generate a signal of identical amplitude to the inductive component of the HTS coil and thus cancel it completely. However, this is achieved for a certain value of the linked flux, which can vary considerably by moving the coil axially even by a few millimetres. In this work, the DAQ system controlled via *LabVIEW* interface is able to calculate almost instantaneously the phase shift between the current signal and the voltage signal coming from the series of the HTS and the cancel coils. The phase shift is computed considering for both signals, the first harmonic at the frequency of the reference signal. Therefore, a preliminary phase to the acquisition consists in the proper positioning of the cancel coil, making sure that the phase shift is reduced from its initial value close to 90°, to a sufficiently small value. Given the difficulty in the correct positioning, in this study it is considered acceptable to decrease the phase shift below 10°. It has been verified that the optimal cancellation depends on both the frequency and the amplitude of the transport current. In fact, by modifying these two parameters, the current distribution inside the conductor changes and so does its generated flux. Given the large number of operating conditions to be tested, it is decided to reposition the coil (if needed) at each operating frequency change, maximizing its compensation only for the maximum current amplitude expected during the test and to leave this arrangement also for tests carried out with the same frequency but at lower amplitudes.

Since the acquisition card allows to acquire two voltage signals at the same time, one of the two voltage channels is used to directly connect the signal wires coming from the ends of the HTS coil, without passing through the cancel coil. In this way, by comparing the results obtained with the two different voltage signals acquired, it is possible to analyse the effect of the compensation coil on the measured loss values.

It needs to be pointed out that the use of a cancel coil here described is valid only for the measurements carried out in the insulated coil. In fact, predicting the shape of the flux lines generated by the NI coil is more complex as transverse currents intervene, generating a magnetic field whose direction is different from that of the field produced by the longitudinal currents. It follows that placing a single cancel coil coaxially in the bore of the NI coil can lead to misleading results. Therefore, the connection scheme for the measurements carried out in the NI coil corresponds to the one presented in Fig. 3.1.1, without the use of any cancel coil. However, the challenges of measuring AC losses in a NI coil are fewer than with an insulated winding. In fact, given the onset of transverse currents of considerable amplitude flowing through turn-to-turn equivalent resistances, it is expected that the resistive component of the voltage signal measured at the ends of the NI coil would be greater than that of an insulated winding. In this sense, it is verified that the phase shift between the current signal and the voltage signal at the ends of the NI coil (without the use of the cancel coil) is less than 10°, and thus easily estimable without the use of compensation systems.

Then, dissimilarly to what described in *Chapter 2* and *Chapter 3* for tapes, a methodology regarding the geometry of the voltage measurement circuit is not developed for measuring coils, *i.e.* the use of a second pair of wires for compensation or twisting at a certain distance from the axis of the conductor. Simply, the voltage wires are carefully twisted together before reaching the channel of the acquisition card.

Finally, it is worth noting that all the remaining components of the DAQ system not mentioned in this section are the same as described in *Section 3.1*, as well as the post-processing system, which corresponds to the one reported in *Section 3.2*.

6.3.   *Computation of Joule losses due to transverse currents with the equivalent lumped parameter circuit for a layer-wound coil*

An estimation of the measured AC losses can be obtained using the equivalent circuit presented in *Section 5.2*. It is sufficient to impose that I_{op} is equal to an AC current having amplitude and frequency corresponding to the experimental values. The same equivalent parameters obtained for the two coils during the charging tests are also maintained for this study.

As an example of the model results, Fig. 6.3.1 presents the ratio between the longitudinal currents and I_{op}, in three branches of each layer of the equivalent circuit of the NI coil, located at the same height ($I_{L,2}$, $I_{L,13}$ and $I_{L,24}$ at the bottom, $I_{L,6}$, $I_{L,17}$ and $I_{L,28}$ in the middle, $I_{L,10}$, $I_{L,21}$ and $I_{L,32}$ at the top) computed during the second period simulated, at I_m set to 0.85 and the frequency set to 47 Hz. For a better understanding of the branch locations, see *Chapter 5*. The ratio between the amplitudes of the currents in the various branches follows the trends shown

in Fig. 5.3.2.1(a). It also appears that the currents of each branch have a distinct phase from the others, while remaining isofrequential.
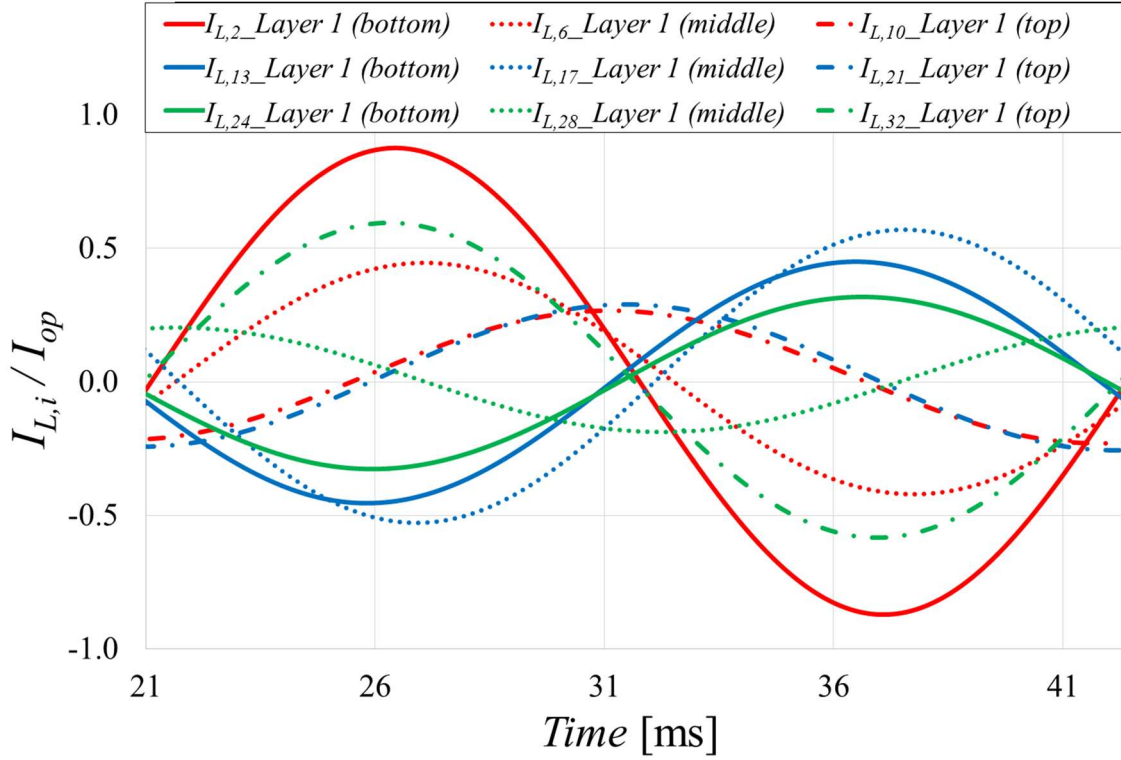
Figure 6.3.1. *Longitudinal currents flowing in selected branches of the equivalent circuit of the NI coil, computed during the second period simulated, at $I_m = 0.85$ and $f = 47$ Hz.*

Once the system of equation is solved, the power dissipation by Joule effect can be computed as described in *Section 5.3.3*.

The total power dissipated by each coil is calculated as the sum of the Joule losses due to the longitudinal and transverse currents in all branches of the circuit, integrated in the second period where the regime conditions are reached. Since the experimental tests are carried out at current amplitudes lower than the tape critical current, the longitudinal resistances assume very small values and their corresponding Joule losses are negligible for both the insulated and the NI coil. It follows that the model is not sufficiently detailed to calculate the Joule losses in an insulated coil when I_{op} is considerably lower than I_c, since its transverse currents are negligible, but it is a useful tool to computed part of the losses generated in a NI coil during AC operations. However, even in the latter case, the model does not take into account the current distribution into the conductor, which affects the value of the AC losses and thus must be determined differently.

6.4. H-formulation in cylindrical coordinates and with a 2-D axisymmetric approximation

To determine the current distribution inside the conductor in the coil, from which to estimate the AC losses due to the longitudinal currents, it is decided to proceed using of the *H*-formulation. In fact, this formulation is easily implemented in COMSOL *Multiphysics*, a

software that allows to simulate quite complex geometries with a certain ease. Future studies will concern the extension of the work described in this thesis regarding the application of the *A-V* formulation for a coated conductor, to describe the geometry of a layer-wound coil in MATLAB software.

In this case, to describe the geometry of a coil it is convenient to switch from Cartesian coordinates (*x, y, z*) to cylindrical coordinates (*r, θ, z*). Following the steps described in [69], Eq. (2.3.5.3) can be divided in its three components. Considering the curl in cylindrical coordinates and inserting the constitutive relationship between $\boldsymbol{B}$ and $\boldsymbol{H}$ (considering non-ferromagnetic materials), it yields:

$$\begin{cases} \dfrac{1}{r}\dfrac{\partial E_z}{\partial \theta} - \dfrac{\partial E_\theta}{\partial z} = -\mu_0 \dfrac{\partial H_r}{\partial t} \\[2mm] \dfrac{\partial E_r}{\partial z} - \dfrac{\partial E_z}{\partial r} = -\mu_0 \dfrac{\partial H_\theta}{\partial t} \\[2mm] \dfrac{1}{r}\left[\dfrac{\partial(rE_\theta)}{\partial r} - \dfrac{\partial E_r}{\partial \theta}\right] = -\mu_0 \dfrac{\partial H_z}{\partial t} \end{cases} \tag{6.4.1}$$

Applying a 2-D axisymmetric approximation, *i.e.* considering the cross-section of the coil to be symmetric around its central azimuthal axis, the angular magnetic field component (H_θ) is neglected. Consequently, since the current can flow along the angular coordinate only (J_θ), the radial and azimuthal components of the electric field (E_r and E_z) cancel out. It results:

$$\begin{cases} -\dfrac{\partial E_\theta}{\partial z} = -\mu_0 \dfrac{\partial H_r}{\partial t} \\[2mm] \dfrac{E_\theta}{r} + \dfrac{\partial E_\theta}{\partial \theta} = -\mu_0 \dfrac{\partial H_z}{\partial t} \end{cases} \tag{6.4.2}$$

which corresponds to the *H*-formulation in cylindrical coordinates and with a 2-D axisymmetric approximation.

Then, Ampere's law (Eq. (2.3.2.5)) can be expressed in cylindrical coordinates, neglecting the displacement field due to the quasi-static approximation:

$$J_\theta = -\frac{\partial H_z}{\partial r} + \frac{\partial H_r}{\partial z} \tag{6.4.3}$$

The formulation is implemented in COMSOL *Multiphysics*, with different techniques between the two coils, which are reported in separate sections.

6.4.1. Implementation of the H-formulation in COMSOL Multiphysics to compute the AC losses in insulated coils

The cross-section of a layer-wound insulated coil is introduced in COMSOL by creating a number of rectangular conductors corresponding to the number of coil turns into the system domain (30, in this case). The conductors are placed at a proper distance from the central axis of symmetry, accordingly to the turns position within the coil. As displayed in Fig. 6.4.1.1(a),

a certain distance is maintained between the turns (both radially and azimuthally), corresponding to the Kapton insulation. For simplicity, the properties of the electrical insulation are set identical to those of the surrounding air.

The whole cross-section of the conductors is assumed to be composed of superconducting material, whose properties are reported in Tab 5.1.1, thus neglecting the properties of the silver matrix and the stainless steel layers. The dependence of the critical current of the tape on the magnetic field components is ignored, introducing an additional approximation into the model. Selecting the 2-D axisymmetric space dimensions in COMSOL, the software applies automatically the symmetry condition around the central axis, thus allowing to represent just one half of the coil cross-section.
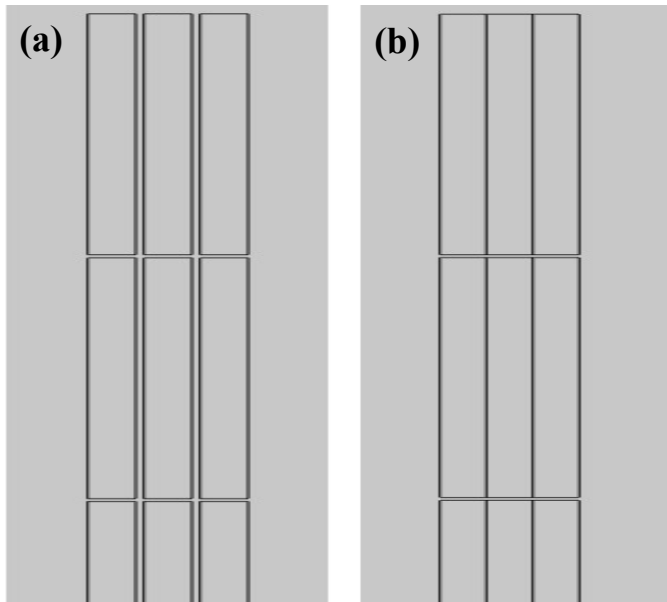
Figure 6.4.1.1. *Upper portion of the cross-section of (a) the insulated coil and (b) the NI coil, as implemented in COMSOL Multiphysics.*

It is evident that the geometry represented in COMSOL is a simplification with respect to the real coil configuration. In particular, it cannot represent accurately the layer-wound configuration, since revolving Fig. 6.4.1.1(a) around the central axis of the coil, each turn would correspond to a cylindrical close conductor, not connected to the upper and lower turns. Furthermore, this geometric representation does not allow to distinguish the layer-wound configuration from the pancake-wound one. However, this simplification can still give useful insights to the analyse the experimental data.

Eq. (6.3.2) is introduced in COMSOL as the general form as follows:

$$\begin{bmatrix} \mu_0 & 0 \\ 0 & \mu_0 \end{bmatrix} \begin{bmatrix} \dfrac{\partial H_r}{\partial t} \\ \dfrac{\partial H_z}{\partial t} \end{bmatrix} + \begin{bmatrix} \dfrac{\partial}{\partial r} & \dfrac{\partial}{\partial z} \end{bmatrix} \begin{bmatrix} 0 & E_\theta \\ -E_\theta & 0 \end{bmatrix} = \begin{bmatrix} 0 \\ -\dfrac{E_\theta}{r} \end{bmatrix} \tag{6.4.1.1}$$

In each turn of the insulated coil an identical sinusoidal current is imposed. Since all currents have the same phase, the initial conditions (which in the *H*-formulation cannot be imposed

directly on the current) impose the magnetic field and its derivative to be null at every point of the domain.

The domain boundary is defined as a square, one side of which is constituted by the symmetry axis of the system. The length of the sides of this square is chosen to be large enough (10 times the coil height) so that a zero magnetic field boundary condition can be imposed on them, being at a considerable distance from the conductor. It is not necessary to impose any boundary conditions on the central axis of the system, as a symmetry condition is automatically imposed by the solver.
Air is considered into the 2-D space between this contour and the conductors surface.

As illustrated in *Section 2.3.3*, a rectangular mesh is used to discretize the conductors (20 discretizing points across the tape width, which in this configuration is directed along the *z*-axis, and 3 points across its thickness, which in is directed along the *r*-axis), while a free triangular mesh is selected to discretize the surrounding air.

Once the solver has calculated the field components in each element, Eq. (6.4.3) is used to derive the current density in the conductors, through which compute the trend of the losses with Eq. (2.1.2), in which the integration along the angular coordinate is performed by multiplying the function for the length of each turn, considered to be perfectly circular. The AC losses of the coil are found as the sum of the contribution of each turn of the domain, integrating the function during the second period, in which the regime conditions are reached.

6.4.2. Implementation of the H-formulation in COMSOL Multiphysics to compute the AC losses in no-insulation coils

The implementation in COMSOL of a NI coil is achieved with some modifications compared to the passages described in the previous section. The solution of the equivalent circuit with an AC transport current, as described in *Section 6.3*, determines the current profiles in each longitudinal branch. However, the longitudinal branches of the circuit do not exactly correspond to the turns of the coil, since they are equal to $N_L \cdot (N_T+1)$ (33, in this case). Therefore, it is not possible to assign a specific current trend to the 30 turns of the coil, as performed in the previous section. To overcome this problem, the NI coil cross-section is implemented in COMSOL by adding a turn to each layer compared to the real number (N_T). In this way, the coil is higher than the real one and its magnetic field is slightly overestimated by the model; the length of the first and last turn of each layer should be halved but this is not achievable due to the axisymmetric conditions. However, this approximation is considered acceptable in this investigation. With this technique, it is possible to assign a certain current profile for each implemented conductor ($I_i(t)$), corresponding to the longitudinal currents resulting from the equivalent circuit analysis.

Differently from the insulated coil, the currents to be implemented in each conductor representing the NI coil have an amplitude and a phase independent of that of the adjacent conductors, as shown in Fig. 6.3.1.

By imposing pure sinusoidal currents, convergence problems arise in the solver at the first instant due to the initial condition of null field imposed (corresponding to null currents at the initial instant). The problem can be solved by separately computing the magnetic field corresponding to the initial currents distribution and imposing it as an initial condition in the different elements of the domain. However, this calculation requires computational time and it can result inaccurate; therefore, an alternative solution is preferred. From the first instant up to an instant t_1, the current in each conductor varies linearly, starting from zero and reaching the value assumed by the sinusoidal current of that specific conductor at the instant t_1; subsequently, the current profile is maintained sinusoidal. In terms of equations, it corresponds to:

$$\begin{cases} I_i(t) = t \left(\dfrac{Amp_i \sin(2\pi f t_1 + \phi_i)}{t_1} \right) & for\ t < t_1 \\ I_i(t) = Amp_i \sin(2\pi f t + \phi_i) & for\ t \geq t_1 \end{cases} \qquad (6.4.2.1)$$

where Amp_i and ϕ_i are the amplitude and the phase assigned to each conductor.
With this technique, the zero magnetic field initial condition can be maintained. In this work, t_1 is equal to a fifth of the period. It is proved that after the transient regime occurring due to the variation of the current profile at the instant t_1, the regime conditions are reached during the second period, which is then selected for the calculation of the losses.

In the representation of the cross-section of the NI coil, no spacing is considered between the conductors of adjacent layers, while a certain pitch is maintained between the conductors belonging to the same layer (see Fig. 6.4.1.1 (b)), as performed experimentally.
The meshing technique is the same adopted for the insulated coil.

When calculating the total losses, to account for the fact that the top and bottom conductors in each layer of the NI coil representation are actually half of a full turn, the losses generated in these conductors are halved before adding them to those of the other conductors.

6.5. Comparison between experimental and numerical results of AC losses in HTS coils in a layer-wound configuration

Fig. 6.5.1 presents the average power dissipation measured experimentally and computed numerically using the procedure described in *Section 6.4.1* for the insulated coil, varying I_m and with a frequency of 47 Hz. The value of I_m equal to 0.47 is chosen as the upper limit for the tests of the insulated coil, as it corresponds to the maximum current amplitude that does not produce any distortions in the current signals during the experiments. In fact, this phenomenon is interpreted as a manifestation of the superconductor entering the non-linear regime, an unsafe situation for the material that can potentially damage the device.
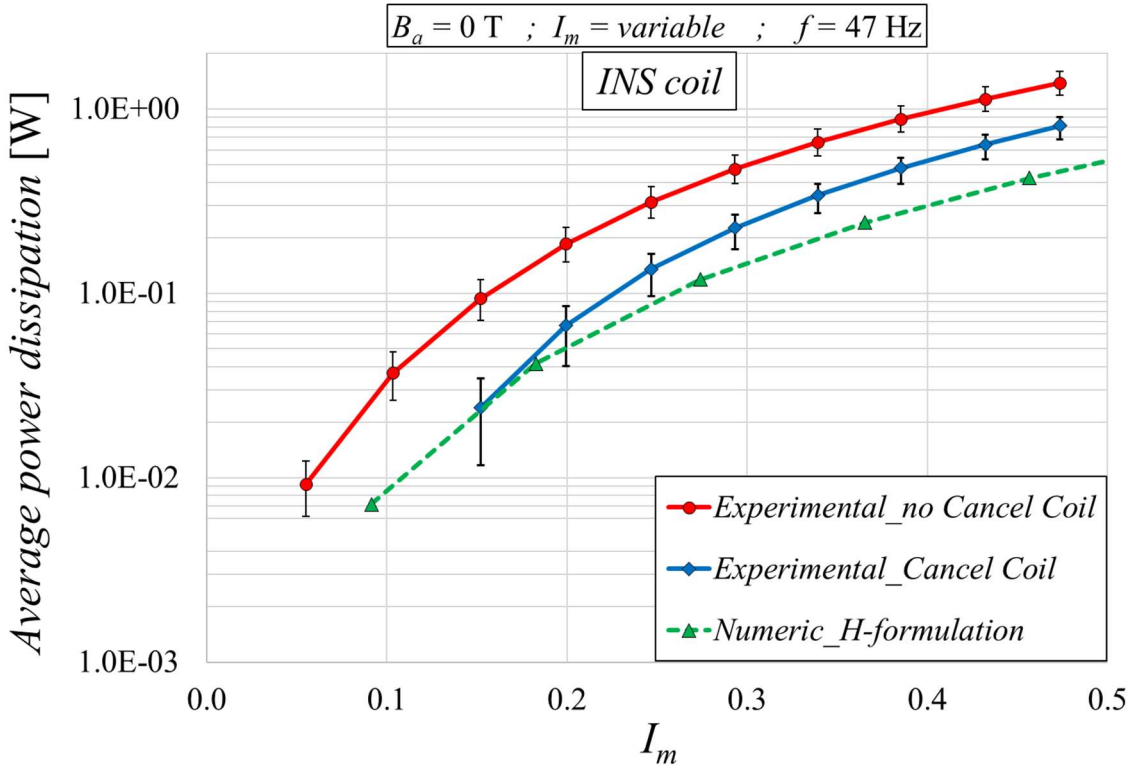
Figure 6.5.1. *Average power dissipation in the insulated coil for different I$_m$ values and the frequency set to 47 Hz. The figure is in semi-logarithmic scale.*

The experimental results obtained with and without the use of the cancel coil are shown. As it can be seen, the measurements realized with the cancel coil lead to lower loss values. On the one hand, this highlights the difficulty of the DAQ system and the post-processing technique to calculate the in phase component of the electromagnetic signals when the phase shift is close to 90°, but it demonstrates how the cancel coil intervenes in bringing out this resistive component, making it easier to identify. For this investigation with the insulated coil, the most accurate results are assumed to be those obtained through the use of a cancel coil.

Future studies will investigate if there is a threshold phase shift between the voltage and the current signals, above which a given acquisition system leads to misleading results (however, this parameter would also depend on the amplitude of the inductive and the resistive signals). Moreover, a range bar is correlated with each experimental point, get by graphing the maximum and the minimum values obtained for each operating condition during the repeatability tests performed in the coil at different moments (disassembling and reassembling the set-up at each test, and repeating the preliminary procedure for the cancel coil positioning). Thus, the red and blue curves represent the average (among all tests) of the measurements obtained for each operating condition. For both experimental curves, the percentage variations compared to the mean values are included between ± 33% at the lower current amplitudes and ± 15% at the higher current amplitudes, reducing proportionally as the current increases. The repeatability of the measurements is therefore sufficient but not optimal, indicating how the presence of an important phase shift (albeit compensated by the cancel coil) can affect the measurements. A worsening of the reproducibility with the reduction of the current amplitude can be explained by the fact that, accordingly, the amplitude of the voltage signal lowers, approaching the accuracy of the DAQ system.

As regards the numerical results, the calculation of the losses due to Joule effect is not presented in the plot for the insulated coils, since they have negligible values; therefore, only the results obtained through the *H*-formulation are displayed. The numerical curve is close to the experimental curve obtained with the cancel coil for low current amplitudes (especially if the range bars are considered). Increasing the currents, the two curves tend to diverge as they have a different slope, with the numerical results representing only the 47% of the experimental values when $I_m = 0.47$.
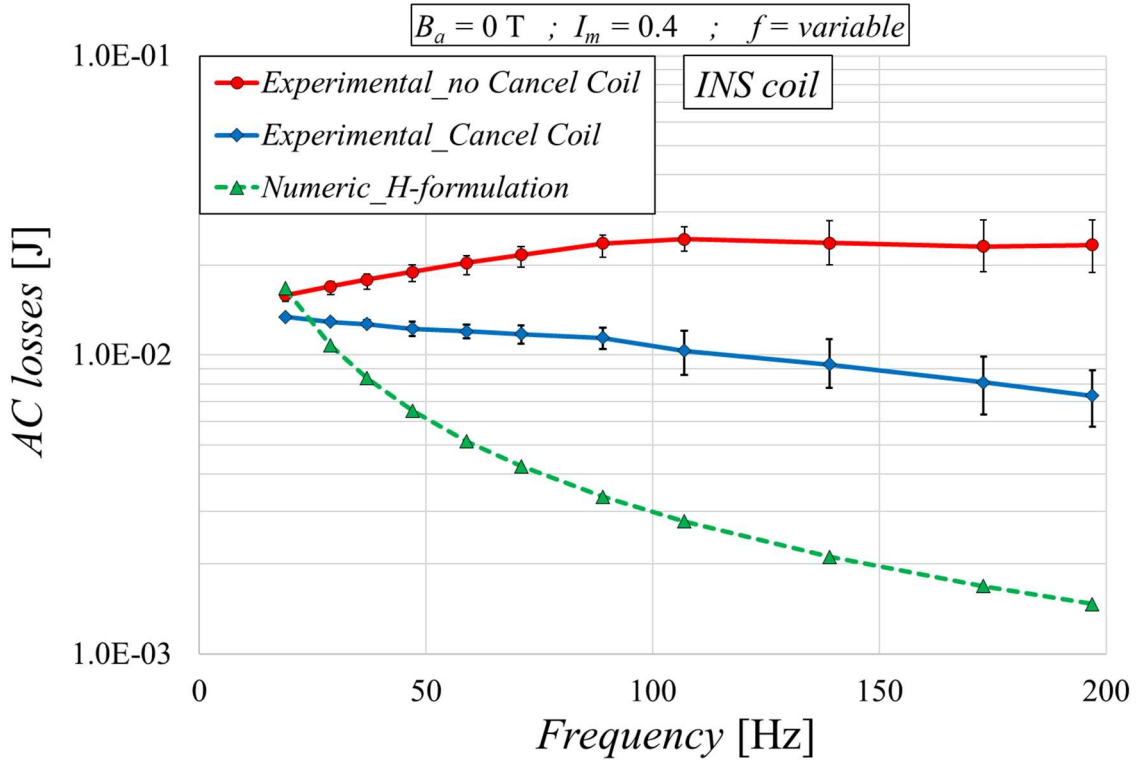
Figure 6.5.2. *Average power dissipation in the insulated coil for different frequencies and for I_m equal to 0.4. The figure is in semi-logarithmic scale.*

Fig. 6.5.2 shows the transport AC losses for the insulated coil, varying the frequency and with I_m set to 0.4. Even in this case, the presence of the cancel coil in the experimental set-up leads to lower measured losses. The curve obtained from the voltage signal acquired without the cancel coil appears to slightly increase with the frequency (despite after 100 Hz the losses seem to be frequency independent). Instead, the AC losses obtained with the cancel coil decrease with the frequency, as expected for straight tapes (both for the BSCCO tape, as in Fig. 6.1.2, and for (RE)BCO tapes, as in Fig. 3.4.3). Moreover, the range bars of the experimental curves do not have negligible amplitude. The variation with respect to the average measured value increases with the frequency: it is equal to $\pm 3\%$ at 19 Hz and to $\pm 21\%$ at 197Hz. This indicates that the measurements are more critical at high frequencies.

At low frequencies, the curve obtained through the implementation of the *H*-formulation in COMSOL is close to the experimental results obtained with the cancel coil: the discrepancies are around 20%. However, the numerical curve decreases with the frequency more rapidly than the experimental curve (the measurements are up to 5 times greater at a frequency of 197 Hz, compared to the numerical curve).

Fig. 6.5.3 presents the average power dissipation measured experimentally and computed numerically using the procedures described in *Section 6.3* and *Section 6.4.2* for the NI coil, varying I_m and with a frequency of 47 Hz. The upper limit for I_m is equal to 0.85, corresponding to the maximum value that can be generated by the power supply system at the given frequency, since in this case no distortions are produced in the current signal.
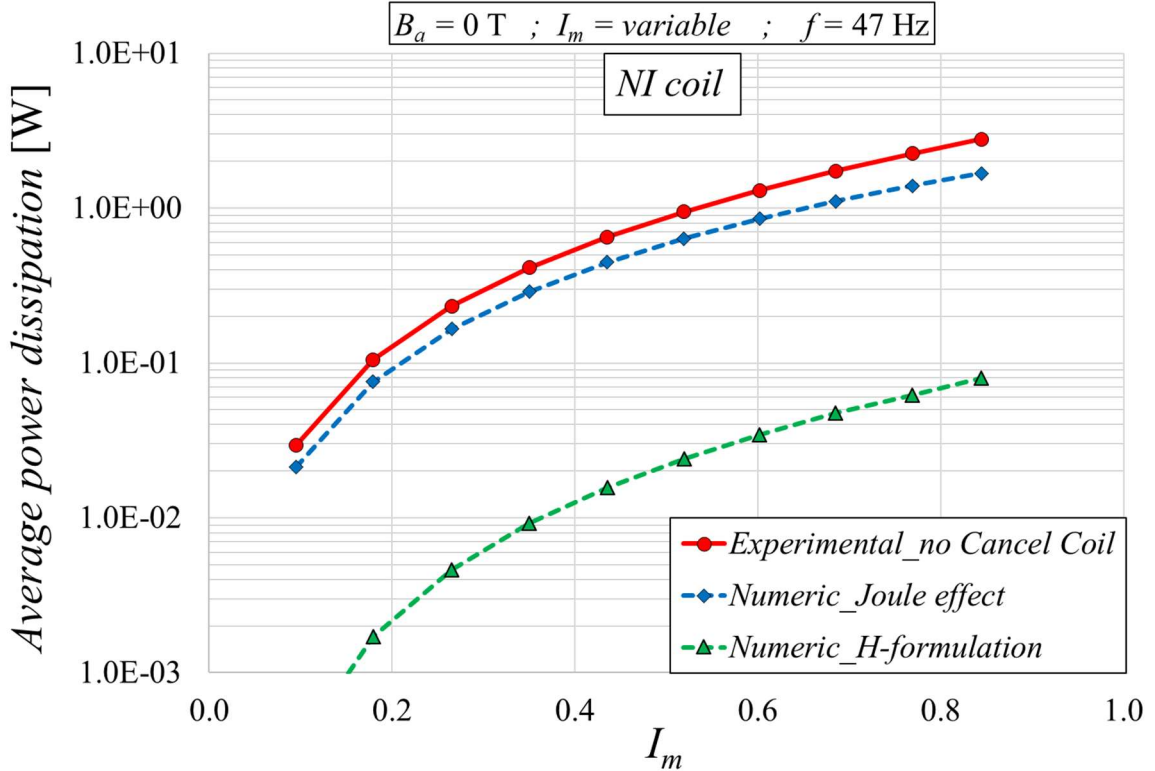
Figure 6.5.3. *Average power dissipation in the NI coil for different I_m values and the frequency set to 47 Hz. The figure is in semi-logarithmic scale.*

As explained, the cancel coil is not used during the NI coil tests, moreover, the experimental curve does not show range bars as the measurements are more repeatable than those performed with the insulated coil. This is attributable to a more evident resistive component of the voltage signal of the NI coil compared to the insulated winding, which makes its measurement less affected by the measurement conditions.

The curve describing the losses due to transverse currents (or due to Joule effect) has a similar trend to the experimental curve, with lower values. The discrepancy between the two curves is equal to 27% at low current amplitudes and up to 39% at high currents.

The curve referred to the losses computed with the *H*-formulation is much lower than the other curves, with values between 1% and 3% of the experimental results, despite having a similar trend. Theoretically, for a proper comparison between the numerical and experimental results, the two numerical curves could be added as they refer to mechanisms that are independent of each other but which affect the voltage (and therefore the losses) acquired at the coil ends: the red curve refers to the transverse currents while the green curve to the longitudinal currents. However, the AC losses due to the current distribution inside the conductors are almost negligible and do not considerably improve the convergence between the results.

Fig. 6.5.4 shows the transport AC losses for the NI coil, varying the frequency and with I_m set to 0.75. The losses due to the current distribution inside the conductors calculated with the *H*-formulation are practically negligible. The numerical curve referred to the losses for transverse currents tends to converge with the experimental curve as the frequency increases, as shown in the inset of the figure in linear scale, passing from discrepancies of 45% for a frequency of 19 Hz down to discrepancies of 32% for a frequency of 197 Hz. This seems to be due to the fact that, the faster the transient is to which an NI coil is subjected (*i.e.* higher the frequency) the greater is the amount of current flowing radially between the turns as compared to the total operating current, thus increasing the contribution of the losses due to the Joule effect.
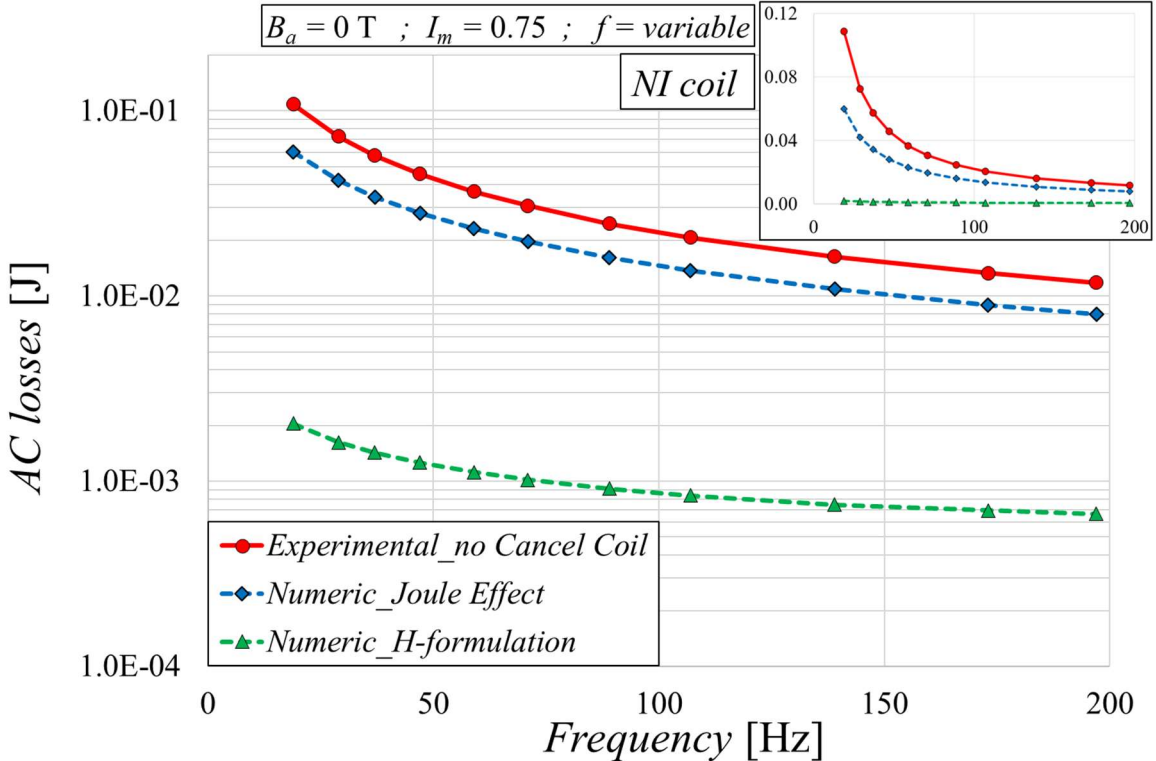
Figure 6.5.4. *Average power dissipation in the NI coil for different frequencies and for I_m equal to 0.4. The main figure is in semi-logarithmic scale. The same curves are displayed in the inset, using a linear scale.*

Finally, it is useful to display together the experimental curves referred to the two layer-wound coils, in order compare them under the same conditions. The expression of the losses per unit of length is avoided, as the difference between the tape length used to wind the two coils is lower than 0.3%.

(a)

$B_a = 0 \text{ T}$; $I_m = variable$; $f = 47 \text{ Hz}$

Average power dissipation [W]

NI_no Cancel Coil

INS_Cancel Coil

I_m

(b)

$B_a = 0 \text{ T}$; $I_m = 0.4$; $f = variable$

NI_no Cancel Coil

INS_Cancel Coil

AC losses [J]
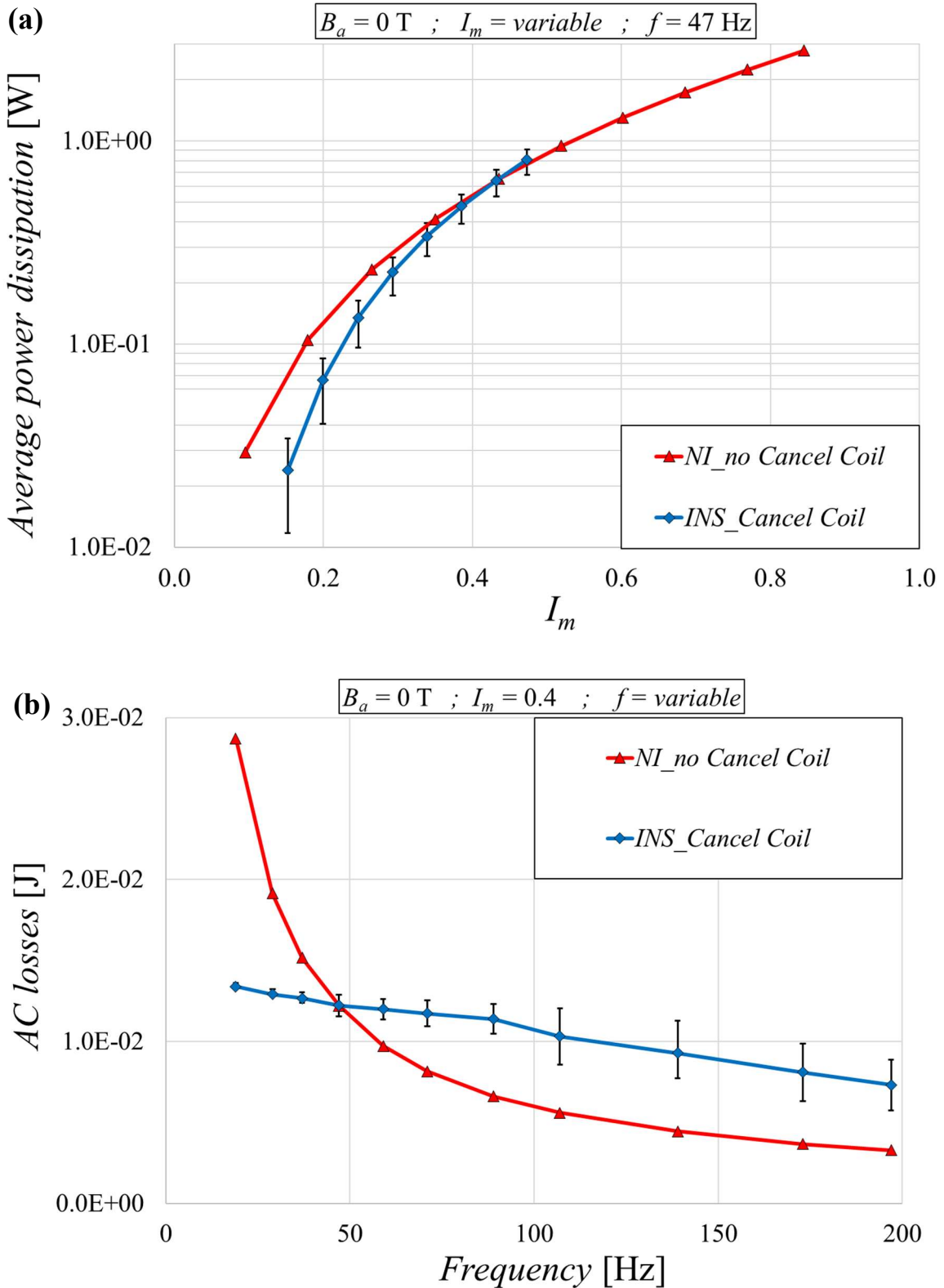
Frequency [Hz]

Figure 6.5.5. *(a)Comparison of the average power dissipation in the two test coils, for different I_m values and the frequency set to 47 Hz. (b) Comparison of the AC losses in the two test coils, for different frequencies and for I_m set to 0.4.*

Fig. 6.5.5(a) presents the average power dissipation measured for both coils varying I_m and for a frequency set to 47 Hz. The AC losses in the NI col are greater at low currents. The two

curves meet for $I_m \approx 0.5$, after which the losses in the insulated winding seem to increase more rapidly with the current than in the NI coil, even if this trend cannot be experimentally confirmed due to the safety limits imposed during the tests with the insulated coil. From the premises of this section, obtaining greater losses in the insulated coil than the NI winding appears counterintuitive. However, while in an insulated coil the supplied current flows in all turns with the same amplitude I_m, the same current distributes differently in a NI coil, flowing with a significantly lower amplitude in most of its turns. Consequently, the coil self-field is lower and the losses inside the superconductor are minor.

Fig. 6.5.5(b) shows the AC losses for both coils varying the frequency and for I_m equal to 0.4; note that in this case, the scale is linear. Both curves decrease with the frequency, with linear and exponential trends for the insulated and the NI coil, respectively. At low frequencies, the losses measured in the NI coil are greater than those in the insulated winding; the curves meet at 47 Hz after which the losses measured in the insulated coil are higher. It follows that, although theoretically faster transients should disadvantage an NI coil, the different current distribution generates greater losses in an insulated coil. It should be noted that, by varying the amplitude of the current at which this comparison is realized, the frequency at which the two experimental curves meet would change.

This investigation indicates that a layer-wound NI coil can be safely used under time-varying conditions, as its AC losses are comparable with those of its insulated counterpart. Indeed, the study identifies some operating conditions for which the NI test coil is subject to lower AC losses compared to the insulated coil, with the same geometry. This would reduce the heat load for its cooling system. However, this advantage is to the detriment of the performance of the NI coil, which is not correctly loaded if adopted only for AC applications and thus would produce a lower magnetic field than its insulated counterpart.

6.6. Conclusions

In this chapter, the two HTS coils analyzed in *Chapter 5* have been subjected to an AC current with variable amplitude and frequency, in liquid nitrogen environment, to determine their AC losses.

The experimental set-up described in *Chapter 3* has been modified for the measurement of the losses in the insulated coil, as it requires the use of a cancel coil to reduce the inductive component of the acquired voltage signal.

For the insulated coil, the experimental results have been compared with those obtained through a 2-D numerical model based on the *H*-formulation. The models demonstrate that the primary loss mechanism in an insulated coil supplied with a current below I_c is due to the current distribution inside the tape. The method here presented, can be used to describe this phenomenon but its results are underestimates compared to the measurements, especially for high currents and frequencies. This may be due both to the approximations of the model (2-D axisymmetric) and to alternative sources of loss not taken into account.

On the other hand, in an NI coil, the losses due to transverse currents superimpose to the previously mentioned loss mechanism. These loss terms have been obtained through an

equivalent lumped parameter circuit (already presented in *Section 5.2*). For the NI layer-wound coil analyzed in this study, the losses due to the transverse currents results dominant when the operating current is lower than I_c. This conclusion can legitimately be extended to any NI coil in a layer-wound configuration, although the tests should also be performed at higher frequencies (albeit of less practical interest). The equivalent parameters circuit here presented is able to describe the mechanism, although the numerical results are slightly underestimated compared to the measurements. The convergence with the experimental curve might be improved by discretizing each turn of the coil with a greater number of equivalent longitudinal branches. Alternatively, also the effect of the current distribution in the conductors, which for a NI coil seems to have a negligible effect, could be furtherly investigated.

Finally, the measurements show that the AC losses in the layer-wound NI coil are comparable with those of its insulated counterpart, an evidence that is not obvious from the general knowledge. However, this is related to an uneven charging of the NI coil, which in turn results less performing.

Conclusions

A numerical and experimental analysis of electrodynamic transients in HTS tapes and coils is presented in this work. The initial part of this study aims to deepen arguments not sufficiently investigated in the literature regarding the AC losses in tapes, reporting equations and methodologies in detail so as to provide a useful basis for future works. After that, aspects concerning the non-insulated winding configuration for HTS coils are explored, carrying out ramp charges tests in coils wound in various configurations of interest. The experimental results are interpret making use of equivalent circuits. Then, the models and the experimental set-up realized for HTS tapes are extended to determine the AC losses in layer-wound coils subjected to AC conditions.

First, two numerical models are developed for the analysis of AC losses in coated conductors having different geometrical and electrical properties. Both methods are based on the determination of the current distribution inside the conductor, subjected to an AC transport current or an AC magnetic field or a combination of the two. The models adopt different formulations for the resolution of Maxwell's equations and serve different purposes. Their results are compared, showing a very good agreement.
The first model implements a FEM analysis based on the *H*-formulation in COMSOL *Multiphysics* environment, with a 2-D approximation. A proper meshing technique is selected for the cross-section of each layer of the tape, to reduce the computational burden of the solver. The method has the advantage to be easily extendable to represent conductors provided with a ferromagnetic substrate.
Then, an integral model based on the *A-V* formulation is developed in MATLAB environment, applying a 2-D approximation. The model can speed-up the calculation time with respect to the FEM model, although it cannot describe ferromagnetic phenomena at the present. The method is used for two separate scopes. It can derive the conditions for which the simulation of the superconducting layer only, a simplification often adopted in the literature, is not acceptable for a correct evaluation of the AC losses. In particular, for the *SuNAM SCN04* tape, the contribution to the tape losses of the non-superconducting layers enhances when the frequency of the external magnetic field exceeds 1 kHz and the impact of these layers results relevant already at tens of hertz if the magnetic field is parallel to the tape main face. Furthermore, the integral model is adopted to quantify the undesired influence of the configuration of the voltage measurement circuit on the AC losses measured in tapes by means of an electromagnetic technique. The model confirms that twisting the two signal wires at a distance equal to $\frac{3}{2}$ the tape width from the tape middle axis is the best compromise to eliminate the effect of the measurement circuit and avoid linking excessive electromagnetic flux, which leads to a strong noise of the signal, an estimate reported in the literature but not extensively demonstrated before this study.
The work also describes an alternative configuration of the voltage measurement circuit compared to the one traditionally adopted. This technique involves the acquisition of an additional voltage signal for the suppressing the electromagnetic noise. However, this

alternative is effective for particularly wide tapes or in the cases in which the position at which the two signal wires are soldered onto the tape surface can be determined with absolute precision.

Secondly, this work presents an electromagnetic method for measuring AC losses in HTS tapes do not requiring the use of a lock-in amplifier. The calculation of the in phase components of the current and voltage signals are performed with respect to a third reference signal, via the *LabVIEW* interface. The post-processing technique adopted allows having a better control on the reconstructed signals and can increase the number of signal harmonics treated for the noise reduction compared to the use a lock-in amplifier.

The measurements performed on different tapes are compared with the results of the two numerical methods, as well as with the experimental results obtained with the same tapes in other laboratories using the lock-in amplifier. In all cases, a good agreement is found. Moreover, it the conclusions regarding the best configuration of the voltage measurement circuit obtained numerically are experimentally verified.

Then, a NI coil in the pancake-wound configuration is realized with the *SuNAM SCN04* tape, with the aim of checking its *defect-irrelevant* behaviour during DC operations, charging and rapid discharging tests. Some defects are intentionally inserted into the coil at specific locations in the form of lap joints, introducing high resistance elements in the winding. The NI coil is tested at temperatures included between 4.7 K and 80 K and charged up to various operating currents with increasing ramp-rates. The coil can be charged properly given the absence of the electrical insulation between turns, which allows a radial redistribution of the current, thus generating a magnetic field in its bore just below the design value. The coil is able to sustain the maximum ramp-rate during the tests, equal to 5 A/s. Furthermore, its behaviour is analysed by means of a simple equivalent lumped parameter circuit, which allows to analytically derive some effective parameters of the winding. It appears that around 4.3% to 5.5% of the operating current flows radially in the coil to avoid damaged areas, guaranteeing the stability of the winding.

Moreover, a study is presented regarding the electrical characteristics of two coils in a layer-wound technique, with and without electrical insulation between turns. The two coils are wound with the same BSCCO tape and with almost identical geometric characteristics. The tests are carried out by charging them at a ramp-rate of 1 A/s in liquid nitrogen bath. The electric field profiles measured at the ends of each layer, are interpreted for both coils through an equivalent lumped parameter circuit. The transverse equivalent resistances representing the contact between turns of adjacent layers, are obtained with best-fitting procedures of the experimental data. The model allows to compute the current distribution between the coils turns during the transport current ramp. It is concluded that the radial flow of currents occurring in the NI coil, is driven by inductive effects up to a certain level of transport current and by resistive effects for higher transport current amplitudes. These thresholds depend on the ramp-rate of the charge process. The distribution of the transverse currents explains the clear difference in the time evolution of the voltage of the outer layers with respect to the inner one in the NI coil as compared to its insulated counterpart.

Furthermore, the model reveals that the most stressed turns of a NI layer-wound coil, in terms of power dissipation, are those located in the proximity of the current leads.

Finally, the work focuses on the calculation of losses due to an AC transport current in HTS coils in a layer-wound technique. The same pair of BSCCO coils previously investigated during charging are supplied with currents of variable frequency and amplitude in a liquid nitrogen bath. The same experimental set-up and post-processing technique developed for the HTS tape are adopted for the windings, adding a cancel coil for the measurements performed on the insulated coil in order to reduce the high inductive component of the voltage signal.

The AC experiments are interpreted by means of the same equivalent lumped parameter circuit realized for current ramp profiles. With this circuit, the power dissipations produced by the transverse currents due to Joule effect are computed, as well as the current distribution between turns. The FEM model based on the *H*-formulation developed for tapes, is extended to consider the geometry of the coils, adopting a 2-D axisymmetric approximation. The model computes the loss due to the current distribution inside the conductors. Although both models lead to underestimate the experimental curves for both coils, they allow to qualitatively determining the loss mechanisms in each winding. In the NI coil, the losses are mainly due to transverse currents, while they are poorly affected by the intra-tape current distribution. In the insulated coil, the currents and transverse losses are null, and the power dissipations are entirely produced by the current distribution inside the tapes.

The measurements demonstrate that the layer-wound NI coil can be safely operated under time-varying conditions, as its AC losses are comparable (and even lower, for certain operating conditions) with those of its insulated counterpart. However, this is due to a non-optimal charging of the NI coil, which in turn would generate a lower magnetic field compared to its insulated counterpart.

Appendix

The expression of the mean value in a period of the power dissipated due to the non-conservative component of the electric field (see Eq. (2.4.2.4)) is:

$$\langle p_A(t) \rangle = \frac{1}{T} \int_0^T \left\{ -L_0 \int_{-\delta}^{\frac{\delta}{2}} \int_{-\frac{w}{2}}^{\frac{w}{2}} \frac{\partial A}{\partial t}(x, y, t) J(x, y, t) \, dx \, dy \right\} dt \tag{A1.1}$$

Inserting Eq. (2.4.4.5) into Eq. (A1.1), the vector potential:

$$\langle p_A(t) \rangle = -\frac{\mu_0 L_0}{4\pi T} \int_0^T \left\{ \int_{-\frac{\delta}{2}}^{\frac{\delta}{2}} \int_{-\frac{w}{2}}^{\frac{w}{2}} \int_{-\frac{L}{2}}^{\frac{L}{2}} \int_{-\frac{\delta}{2}}^{\frac{\delta}{2}} \int_{-w}^{\frac{w}{2}} \frac{\frac{\partial J}{\partial t}(x', y', t) J(x, y, t)}{d(x, y, 0, x', y', z')} \, dx'dy'dz' \, dx \, dy \right\} dt \tag{A1.2}$$

Moreover, considering that the derivative of the product of two functions can be expressed as follows:

$$\frac{\partial J}{\partial t}(x', y', t) J(x, y, t) = \frac{\partial}{\partial t}[J(x', y', t) J(x, y, t)] - J(x', y', t) \frac{\partial J}{\partial t}(x, y, t) \tag{A1.3}$$

Inserting Eq. (A1.3) into Eq. (A1.2), it results:

$$\langle p_A(t) \rangle = -\frac{\mu_0 L_0}{4\pi T} \int_0^T \left\{ \int_{-\frac{\delta}{2}}^{\frac{\delta}{2}} \int_{-\frac{w}{2}}^{\frac{w}{2}} \int_{-\frac{L}{2}}^{\frac{L}{2}} \int_{-\frac{\delta}{2}}^{\frac{\delta}{2}} \int_{-w}^{\frac{w}{2}} \frac{\frac{\partial}{\partial t}[J(x', y', t) J(x, y, t)]}{d(x, y, 0, x', y', z')} \, dx'dy'dz' \, dx \, dy \right\} dt$$

$$+\frac{\mu_0 L_0}{4\pi T} \int_0^T \left\{ \int_{-\frac{\delta}{2}}^{\frac{\delta}{2}} \int_{-\frac{w}{2}}^{\frac{w}{2}} \int_{-\frac{L}{2}}^{\frac{L}{2}} \int_{-\frac{\delta}{2}}^{\frac{\delta}{2}} \int_{-w}^{\frac{w}{2}} \frac{J(x', y', t) \frac{\partial J}{\partial t}(x, y, t)}{d(x, y, 0, x', y', z')} \, dx'dy'dz' \, dx \, dy \right\} dt \tag{A1.4}$$

Assuming valid to take out the integrand of the first term of the second member in Eq. (A1.4) from the space integrations, and being the regime periodic, the remaining integral over time of this term is null. That is:

$$\int_0^T \left\{ \int_{-\frac{\delta}{2}}^{\frac{\delta}{2}} \int_{-\frac{w}{2}}^{\frac{w}{2}} \int_{-\frac{L}{2}}^{\frac{L}{2}} \int_{-\frac{\delta}{2}}^{\frac{\delta}{2}} \int_{-w}^{\frac{w}{2}} \frac{\frac{\partial}{\partial t}[J(x', y', t) J(x, y, t)]}{d(x, y, 0, x', y', z')} \, dx'dy'dz' \, dxdy \right\} dt$$

$$= \int_0^T \frac{d}{dt} \left\{ \int_{-\frac{\delta}{2}}^{\frac{\delta}{2}} \int_{-\frac{w}{2}}^{\frac{w}{2}} \int_{-\frac{L}{2}}^{\frac{L}{2}} \int_{-\frac{\delta}{2}}^{\frac{\delta}{2}} \int_{-w}^{\frac{w}{2}} \frac{J(x', y', t) J(y, z, t)}{d(x, y, 0, x', y', z')} \, dz'dy'dx' \, dx \, dy \right\} dt = 0 \tag{A1.5}$$

Therefore, Eq. (A1.4) can be simplified as:

$$\langle p_A(t) \rangle = \frac{\mu_0 L_0}{4\pi T} \int_0^T \left\{ \int_{-\frac{\delta}{2}}^{\frac{\delta}{2}} \int_{-\frac{w}{2}}^{\frac{w}{2}} \int_{-\frac{L}{2}}^{\frac{L}{2}} \int_{-\frac{\delta}{2}}^{\frac{\delta}{2}} \int_{-w}^{\frac{w}{2}} \frac{J(x', y', t) \frac{\partial J}{\partial t}(x, y, t)}{d(x, y, 0, x', y', z')} \, dx'dy'dz' \, dx \, dy \right\} dt \tag{A1.6}$$

Both Eq.s (A1.2) and (A1.6) have the same term at first member. Consequently, also the second member of both equations are equal:

$$-\frac{\mu_0 L_0}{4\pi T}\int_0^T\left\{\int_{-\frac{\delta}{2}}^{\frac{\delta}{2}}\int_{-\frac{w}{2}}^{\frac{w}{2}}\int_{-\frac{L}{2}}^{\frac{L}{2}}\int_{-\frac{\delta}{2}}^{-\frac{\delta}{2}}\int_{-\frac{w}{2}}^{\frac{w}{2}}\frac{\frac{\partial J}{\partial t}(x',y',t)\,J(x,y,t)}{d(x,y,0,x',y',z')}dx'dy'dz'\,dx\,dy\right\}dt$$

$$=\frac{\mu_0 L_0}{4\pi T}\int_0^T\left\{\int_{-\frac{\delta}{2}}^{\frac{\delta}{2}}\int_{-\frac{w}{2}}^{\frac{w}{2}}\int_{-\frac{L}{2}}^{\frac{L}{2}}\int_{-\frac{\delta}{2}}^{\frac{\delta}{2}}\int_{-\frac{w}{2}}^{\frac{w}{2}}\frac{J(x',y',t)\frac{\partial J}{\partial t}(x,y,t)}{d(x,y,0,x',y',z')}dx'dy'dz'\,dx\,dy\right\}dt$$

(A1.7)

Supposing to change the integration order of Eq. (A1.7), it results:

$$-\int_0^T\left\{\int_{-\frac{L}{2}}^{\frac{L}{2}}\left[\int_{-\frac{\delta}{2}}^{\frac{\delta}{2}}\int_{-\frac{w}{2}}^{\frac{w}{2}}\int_{-\frac{\delta}{2}}^{\frac{\delta}{2}}\int_{-\frac{w}{2}}^{\frac{w}{2}}\frac{\frac{\partial J}{\partial t}(x',y',t)\,J(x,y,t)}{d(x,y,0,x',y',z')}dx'dy'\,dx\,dy\right]dz'\right\}dt$$

$$=+\int_0^T\left\{\int_{-\frac{L}{2}}^{\frac{L}{2}}\left[\int_{-\frac{\delta}{2}}^{\frac{\delta}{2}}\int_{-\frac{w}{2}}^{\frac{w}{2}}\int_{-\frac{\delta}{2}}^{\frac{\delta}{2}}\int_{-\frac{w}{2}}^{\frac{w}{2}}\frac{J(x',y',t)\frac{\partial J}{\partial t}(x,y,t)}{d(x,y,0,x',y',z')}dx'dy'\,dx\,dy\right]dz'\right\}dt$$

(A1.8)

Given that, the following equation can be written for the denominator terms in Eq. (A1.8):

$$d(x,y,0,x',y',z')=\sqrt{(x-x')^2+(y-y')^2+(0-z')^2}$$

$$=\sqrt{(x'-x)^2+(y'-y)^2+(z')^2}=d(x',y',0,x,y,z')$$

(A1.9)

which is equivalent to state that, when calculating the distance between the field point and the source point, the order of the points does not affect the results.

Then, the following operations are carried out on the first member of Eq. (A1.8) only. From the conclusions drawn from Eq. (A1.9) and considering that the integration extremes for the set of variables (x,y,z) and (x',y',z') are equal, it is possible to substitute y' with y, and x' with x. Thus, the first member of Eq. (A1.8) becomes:

$$-\int_0^T\left\{\int_{-\frac{L}{2}}^{\frac{L}{2}}\left[\int_{-\frac{\delta}{2}}^{\frac{\delta}{2}}\int_{-\frac{w}{2}}^{\frac{w}{2}}\int_{-\frac{\delta}{2}}^{\frac{\delta}{2}}\int_{-\frac{w}{2}}^{\frac{w}{2}}\frac{\frac{\partial J}{\partial t}(x',y',t)\,J(x,y,t)}{d(x,y,0,x',y',z')}dx'dy'\,dx\,dy\right]dz'\right\}dt$$

$$=-\int_0^T\left\{\int_{-\frac{L}{2}}^{\frac{L}{2}}\left[\int_{-\frac{\delta}{2}}^{\frac{\delta}{2}}\int_{-\frac{w}{2}}^{\frac{w}{2}}\int_{-\frac{\delta}{2}}^{\frac{\delta}{2}}\int_{-\frac{w}{2}}^{\frac{w}{2}}\frac{J(x',y',t)\frac{\partial J}{\partial t}(x,y,t)}{d(x,y,0,x',y',z')}dx'dy'\,dx\,dy\right]dz'\right\}dt$$

(A1.10)

Substituting Eq. (A1.10) at first member of Eq. (A1.8), it results that both members are equal except for their sign. For the equation to be correct, the only possible solution corresponds to:

$$\int_0^T \left\{ \int_{-\frac{L}{2}}^{\frac{L}{2}} \left[\int_{-\frac{\delta}{2}}^{\frac{\delta}{2}} \int_{-w}^{\frac{w}{2}} \int_{-\frac{\delta}{2}}^{\frac{\delta}{2}} \int_{-w}^{\frac{w}{2}} \frac{\frac{\partial J}{\partial t}(x', y', t) J(x, y, t)}{d(x, y, 0, x', y', z')} dx' dy' \, dx \, dy \right] dz' \right\} dt$$

$$= + \int_0^T \left\{ \int_{-\frac{L}{2}}^{\frac{L}{2}} \left[\int_{-\frac{\delta}{2}}^{\frac{\delta}{2}} \int_{-w}^{\frac{w}{2}} \int_{-\frac{\delta}{2}}^{\frac{\delta}{2}} \int_{-w}^{\frac{w}{2}} \frac{J(x', y', t)\frac{\partial J}{\partial t}(x, y, t)}{d(x, y, 0, x', y', z')} dx' dy' \, dx \, dy \right] dz' \right\} dt = 0 \tag{A1.11}$$

Finally, inserting Eq. (A1.11) into Eq. (A1.2), it proves that:

$$\langle p_A(t) \rangle = 0 \tag{A1.12}$$

References

[1] V. Z. Kresin *et al.*, *"Fundamentals of Superconductivity,"* Edited by *Springer US,* Jun. 1990.

[2] D. Van Delft *et al.*, *"The discovery of superconductivity," Physics Today*, vol. 63 no. 9, pp. 38–43, Sept. 2010.

[3] M. E. G. Hadlow *et al.*, *"Superconductivity and its applications to power engineering," Proceedings of the Institution of Electrical Engineers*, vol. 119, no. 8, pp.1001–1032, Aug. 1972.

[4] *"McGraw-Hill Concise Encyclopedia of Physics,"* Edited by *The McGraw-Hill Companies, Inc.*, 2002.

[5] P. Tixador, *"Les supraconducteurs, traité des nouvelles technologies série matériaux,"* Edited by *Hermès*, 1995.

[6] D. C. van der Laan *et al.*, *"Strain Effects in High Temperature Superconductors Investigated With Magneto-Optical Imaging," IEEE Trans. Appl. Supercond.*, vol. 13, no. 2, pp. 3534–3539, Jun. 2003.

[7] R. Zhang *et al.*, *"Strain dependence of critical superconducting properties of Nb_3Sn with different intrinsic strains based on a semi-phenomenological approach," Cryogenics*, vol. 17, pp. 30–37, Jul. 2017.

[8] G. Jing *et al.*, *"Advanced high-pressure transport measurement system integrated with low temperature and magnetic field," Chinese Phys. B,* vol. 27, no. 7, p. 077402, 2018.

[9] J. N. Rjabinin *et al.*, *"Magnetic properties and critical currents of superconducting alloys," Physikalische Zeitschrift der Sowjetunion*, vol .7, no.1, pp. 122–125, 1935.

[10] V. L. Ginzburg and L. D. Landau, *"On the Theory of Superconductivity," Zh. Eksp. Teor. Fiz.,* vol. 20, pp. 1064–1082, 1950.

[11] A. A. Abrikosov, *"The magnetic properties of superconducting alloys," Journal of Physics and Chemistry of Solids,* vol. 2, no. 3, pp. 199–208, 1957.

[12] P. Jensen Ray, *"Structural investigation of $La_{2-x}Sr_xCuO_{4+y}$: Following staging as a function of temperature," Master's Thesis dissertation, Niels Bohr Institute Copenhagen, Denmark*, Nov. 2015.

[13] L. D. Cooley *et al.*, *"Costs of high-field superconducting strands for particle accelerator magnets," Supercond. Sci. Technol.,* vol. 18, no. 4, pp. 51–65, Feb. 2005.

[14] J. G. Bednorz and K. A. Müller, *"Possible high Tc superconductivity in the Ba−La−Cu−O system," Zh. Eksp. Teor. Fiz.,* vol. 64, pp. 189–193, 1986.

[15] N. Ayai *et al.*, *"Progress in performance of DI-BSCCO family," Phys. C: Supercond.*, vol. 468, no. 15–20, pp. 1747–1752, Sept. 2008.

[16] *http://www.superpower-inc.com/content/2g-hts-wire*

[17] A. R. Strnad *et al.*, "*Dissipative Mechanism in Type-II Superconductors,*" *Phys. Rev. Lett.*, vol. 13, no. 26, pp. 794–797, Dec. 1964.

[18] M. Daibo *et al.*, "*Evaluation of the normal-zone propagation characteristics of (RE)BCO coated conductors with laminated Cu tape,*" *IEEE Trans. Appl. Supercond.*, vol. 21, no. 3, pp. 2428–2431, Feb. 2011.

[19] Z. P. Zhao *et al.*, "*Normal-zone propagation in adiabatic superconducting magnets: Normal-zone propagation velocity in superconducting composites,*" *Cryogenics*, vol. 31, pp. 817–825, Sept. 1991.

[20] A. Ballarino, "*Prospects for the use of HTS in High-field Magnets for Future Accelerator Facilities,*" *Proc. 5th Int. Part. Accel. Conf. IPAC2014*, 6 pages, 2014.

[21] H. Maeda *et al.,* "*Recent Developments in High-Temperature Superconducting Magnet Technology (Review),*" *IEEE Trans. Appl. Supercond.*, vol. 24, no. 3, pp. 1–12, Jun. 2014.

[22] D. Uglietti, "*A review of commercial high temperature superconducting materials for large magnets: from wires and tapes to cables and conductors,*" *Supercond. Sci. Technol.,* vol. 32, no. 5, p. 053001, Apr. 2019.

[23] J. X. Jin *et al.*, "*Enabling High-Temperature Superconducting Technologies Toward Practical Applications,*" *IEEE Trans. Appl. Supercond.*, vol. 24, no. 5, pp. 1–12, Oct. 2014.

[24] X.-Y. Xiao *et al.*, "*HTS Applied to Power System: Benefits and Potential Analysis for Energy Conservation and Emission Reduction,*" *IEEE Trans. Appl. Supercond.,* vol. 26, no. 7, pp. 1–9, Oct. 2016.

[25] J. X. Jin *et al.*, "*HTS Power Devices and Systems: Principles, Characteristics, Performance, and Efficiency,*" *IEEE Trans. Appl. Supercond.,* vol. 26, no. 7, pp. 1–26, Oct. 2016.

[26] S. Hahn *et al.,* "*45.5-tesla direct-current magnetic field generated with a high-temperature superconducting magnet,*" *Nature*, vol. 570, pp. 496–499, Jun. 2019.

[27] J. Bascunan *et al.*, "*A new High-Temperature Superconducting (HTS) 700-MHz insert magnet for a 1.3-GHz LTS/HTS NMR magnet,*" *IEEE Trans. Appl. Supercond.*, vol. 23, no. 3, p. 4400304, Jun. 2013.

[28] B. J. Parkinson *et al.*, "*Development of a cryogen free 1.5 T YBCO HTS magnet for MRI,*" *IEEE Trans. Appl. Supercond.,* vol. 23, no. 3, p. 4400405, Jun. 2013.

[29] O. Maruyama *et al., "Development of RBCO HTS power cables,*" *Physics Procedia*, vol. 36, pp. 1153–1158, Jun. 2012.

[30] A. Bergen *et al., "Design and in-field testing of the world's first (RE)BCO rotor for a 3.6 MW wind generator,*" *Supercond. Sci. Technol.*, vol. 32, no. 12, p. 125006, Oct. 2019.

[31] C. A. Baldan *et al., "Performance of modular SFCL using (RE)BCO coated conductor tapes under repetitive overcurrent tests," IEEE Trans. Appl. Supercond.*, vol. 26, no. 3, p. 5401905, Apr. 2016.

[32] J. Ciceron *et al., "Test in Strong Background Field of a Modular Element of a (RE)BCO 1 MJ High Energy Density SMES," IEEE Trans. Appl. Supercond.*, vol. 28, no. 8, p. 5701005, Jun. 2018.

[33] H. W. Weijers *et al., "High Field Magnets With HTS Conductors," IEEE Trans. Appl. Supercond.*, vol. 20, no. 3, pp. 576–582, Jun. 2010.

[34] Y Suetomi *et al., "Mechanism of notable difference in the field delay times of no-insulation layer-wound and pancake-wound (RE)BCO coils," Supercond. Sci. Technol.,* vol. 29, no. 10, p. 105002, Aug. 2016.

[35] T. Benkel, *"Contribution to the design and realization of a HTS insert to obtain high magnetic field," Ph.D. dissertation, Université Grenoble Alpes,* 2018.

[36] H. C. Jo *et al., "A Study on the Characteristic Evaluation of An HTS Coil with respect to the Winding Methods," IEEE Trans. Appl. Supercond.*, vol. 22, no. 3, p. 4902907, Jun. 2012.

[37] S. Hahn *et al., "No-insulation multi-width winding technique for high temperature superconducting magnet," Appl. Phys. Letters*, vol. 103, no. 17, p. 173511, Oct. 2013.

[38] S. Hahn *et al., "HTS pancake coils without turn-to-turn insulation," IEEE Trans. Appl. Supercond.*, vol. 21, no. 3, pp. 1592–1595, Jun. 2011.

[39] S. B. Kim *et al., "The normal-zone propagation properties of the non-insulated HTS coil in cryocooled operation," Phys. C*, vol. 471, pp. 1428–1431, May 2011.

[40] S. Hahn *et al., "'Defect-irrelevant' behavior of a no-insulation pancake coil wound with (RE)BCO tapes containing multiple defects," Supercond. Sci. Technol.*, vol. 29, p. 105017, Sept. 2016.

[41] K. R. Bhattarai *et al., "Quench Analysis of a Multiwidth No-Insulation 7-T 78-mm (RE)BCO Magnet," IEEE Trans. Appl. Supercond.*, vol. 27, no. 4, p. 4603505, Jun. 2017.

[42] M. Cho *et al., "Combined Circuit Model to Simulate Post-Quench Behaviors of No-Insulation HTS Coil," IEEE Trans. Appl. Supercond.*, vol. 29, no. 5, p. 4901605, Aug. 2019.

[43] Y. Wang *et al., "Self-protection mechanisms in no-insulation (RE)Ba$_2$Cu$_3$O$_x$ high temperature superconductor pancake coils," Supercond. Sci. Technol.*, vol. 29, no. 4, p. 045007, Mar. 2016.

[44] O. J. Kwon *et al., "Effects of turn-to-turn compactness in the straight sections of HTS racetrack coils on thermal and electrical characteristics," Supercond. Sci. Technol.*, vol. 26, no. 8. p. 085025, Jul. 2013.

[45] S. Choi *et al., "A Study on the No Insulation Winding Method of the HTS Coil," IEEE Trans. Appl. Supercond.*, vol. 22, no. 3, p. 4904004, Jun. 2012.

[46] K. Yanagisawa *et al., "A Long Charging Delay for a No-Insulation (RE)BCO Layer-Wound Coil and Its Influence on Operation With Outer LTS Coils," IEEE Trans. Appl. Supercond.*, vol. 26, no. 6, p. 4602304, Feb. 2019.

[47] D. Liu *et al., "Numerical analysis of thermal stability and mechanical response in a no-insulation high-temperature superconducting layer-wound coil," Supercond. Sci. Technol.*, vol. 32, p. 044001, Aug. 2016.

[48] Y Suetomi *et al., "A novel winding method for a no-insulation layer-wound (RE)BCO coil to provide a short magnetic field delay and self-protect characteristics," Supercond. Sci. Technol.*, vol. 32, p. 045003, Feb. 2019.

[49] T. Wang *et al., "Analyses of Transient Behaviors of No-Insulation (RE)BCO Pancake Coils During Sudden Discharging and Overcurrent," IEEE Trans. Appl. Supercond.,* vol. 25, no. 3, p. 4603409, Jun. 2015.

[50] H. Song and Y. Wang, *"Simulations of Nonuniform Behaviors of Multiple No-Insulation (RE)Ba$_2$Cu$_3$O$_{7-x}$ HTS Pancake Coils During Charging and Discharging," IEEE Trans. Appl. Supercond.,* vol. 26, no. 4, p. 4700105, Jun. 2015.

[51] X. Wang *et al., "Charging Behavior in No-Insulation (RE)BCO Pancake Coils," IEEE Trans. Appl. Supercond.*, vol. 25, no. 3, p. 4601805, Jun. 2015.

[52] T. Oki *et al., "Evaluation on Quench Protection for No-Insulation (RE)BCO Pancake Coil," IEEE Trans. Appl. Supercond.,* vol. 26, no. 4, p. 4702905, Jun. 2016.

[53] X. Wang *et al., "Turn-to-turn contact characteristics for an equivalent circuit model of no-insulation (RE)BCO pancake coil,"* Supercond. Sci. Technol., vol. 26, p. 035012, Jan. 2013.

[54] S. Noguchi *et al., "Turn-to-Turn Contact Resistance Measurement of No-Insulation (RE)BCO Pancake Coils," IEEE Trans. Appl. Supercond.*, vol. 29, no. 5, p. 4601605, Aug. 2019.

[55] Y. Kakimoto *et al., "Evaluation of Electromagnetic Behavior of No-Insulation (RE)BCO Pancake Coil With Multiple Defects,"* IEEE Trans. Appl. Supercond., vol. 29, no. 5, p. 4603005, Aug. 2019.

[56] S. Hahn *et al., "No-Insulation Coil Under Time-Varying Condition: Magnetic Coupling With External Coil," IEEE Trans. Appl. Supercond.,* vol. 23, no. 3, p. 4601705, Jun. 2013.

[57] A. Bossavit., *"Remarks about hysteresis in superconductivity modelling," Phys. B.*, vol. 275, pp. 142–149, 2000.

[58] W. T. Norris, *"Calculation of hysteresis losses in hard superconductors carrying AC isolated conductors and edges of thin sheets," J. Phys. Appl. Phys.*, vol. 3, no. 4, pp. 489–507, Apr. 1970.

[59] E. H. Brandt *et al*, *"Type-II-superconductor strip with current in a perpendicular magnetic field," Phys.l Review B*, vol. 48, no. 17, pp. 893–906, Nov. 1993.

[60] G. P. Mikitik *et al.*, "*Analytical Methods and Formulas for Modeling High Temperature Superconductors,*" *IEEE Trans. On Appl. Supercond.*, vol. 23, no. 2, p. 8001920, Apr. 2013.

[61] F. Grilli *et al.*, "*Computation of Losses in HTS Under the Action of Varying Magnetic Fields and Currents,*" *IEEE Trans. On Appl. Supercond.*, vol. 24, no. 1, p. 8200433, Feb. 2014.

[62] F. Grilli, "*Numerical Modeling of HTS Applications*", *IEEE Trans. On Appl. Supercond.*, vol. 26, no. 3, p. 0500408, Apr. 2016.

[63] Z. Hong *et al.*, "*Numerical solution of critical state in superconductivity by finite element software,*" *Supercond. Sci Technol.*, vol. 19, pp. 1246–1252, Oct. 2006.

[64] F. Grilli *et al.*, "*Modeling High-Temperature Superconducting Tapes by Means of Edge Finite Elements,*" *IEEE Trans. On Appl. Supercond.*, vol. 17, no. 2, p. 3155, Jun. 2007.

[65] K. Kajikawa *et al.*, "*Numerical Evaluation of AC Losses in HTS Wires With 2D FEM Formulated by Self Magnetic Field,*" *IEEE Trans. On Appl. Supercond.*, vol. 13, no. 2, p. 3630, Jun. 2013.

[66] V. Lahtinen *et al.*, "*A Finite Element Simulation Tool for Predicting Hysteresis Losses in Superconductors Using an H-Oriented Formulation with Cohomology Basis Functions,*" *J. Supercond. Nov. Magn.*, vol. 28, p. 2345–2354, Apr. 2015.

[67] F. Liang *et al.* "*AC loss modelling and experiment of two types of low-inductance solenoidal coils,*" *Supercond. Sci Technol.*, vol. 29, p. 115006, Oct. 2016.

[68] B. Shen *et al.*, "*Overview of H-Formulation: A Versatile Tool for Modeling Electromagnetics in High-Temperature Superconductor Applications,*" *IEEE Access*, vol. 8, pp. 100403–100414, May 2020.

[69] B. Shen *et al.*, "*Review of the AC loss computation for HTS using H formulation,*" *Supercond. Sci. Technol.,* vol. 33, no. 3, p. 033002, Feb. 2020.

[70] N. Amemiya., "*Numerical modelings of superconducting wires for AC loss calculations,*" *Phys. C: Supercond.*, vol. 310, issue 1–4, pp. 16–29, Dec. 1998.

[71] N. Enomoto., "*Electromagnetic field analysis of rectangular high Tc superconductor with large aspect ratio,*" *Phys. C: Supercond.*, vol.s 412–414, no. 2, pp. 1050–1055, Oct. 2004.

[72] F. Grilli *et al.*, "*Finite-Element Method Modeling of Superconductors: From 2-D to 3-D,*" *IEEE Trans. On Appl. Supercond.*, vol. 15, no. 1, pp. 17–24, Mar. 2005.

[73] A. Stenvall *et al*, "*Programming finite element method based hysteresis loss computation software using non-linear superconductor resistivity and T- φ formulation,*" *Supercond. Sci Technol.*, vol. 23, p. 075010, Jun. 2010.

[74] E. Berrospe-Juarez *et al.*, "*Screening Currents and Hysteresis Losses in the (RE)BCO Insert of the 32 T All-Superconducting Magnet Using T-A Homogenous Model,*" *IEEE Trans. On Appl. Supercond.*, vol. 30, no. 4, p. 4600705, Jun. 2020.

[75] H. Tonsho *et al.*, "*Theoretical and experimental study on AC loss in HTS tape in AC magnetic field carrying AC transport current,*" *IEEE Trans. On Appl. Supercond.,* vol. 13, no. 2, p. 2368, Jun. 2003.

[76] N. Nibbio *et al.*, "*Finite element method simulation of AC loss in HTS tapes with B-dependent E-J power law,*" *IEEE Trans. On Appl. Supercond.*, vol. 11, no. 1, p. 2631, Mar. 2001.

[77] S. Stavrev *et al.* "*Comparison of Numerical Methods for Modeling of Superconductors,*" *IEEE Trans. On Magnetics*, vol. 38, no. 2, pp. 849–852, Mar. 2002.

[78] S. Stavrev *et al.*, "*Numerical modelling of Bi-2223 multifilamentary tapes with position-dependent Jc,*" *Phys. C: Supercond.*, vol. 372-376, no. 3, pp. 1800–1805, Aug. 2002.

[79] E. H. Brandt, "*Superconductors of finite thickness in a perpendicular magnetic field: Strips and slabs,*" *Phys. Rev. B*, vol. 54, no. 6, pp. 4246–4264, Aug. 1996.

[80] S. Otten *et al.*, "*Simple and Fast Method for Computing Induced Currents in Superconductors Using Freely Available Solvers for Ordinary Differential Equations*," *IEEE Trans. On Appl. Supercond*, vol. 29, no.8, p. 8202008, Dec. 2019.

[81] E. Vinot *et al.* "*Different Formulations to Model Superconductors,*" *IEEE Trans. On Appl. Supercond.*, vol. 36, no. 4, pp. 1226–1229, Jul. 2000.

[82] J. K. Sykulsk *et al.* "*Modelling HTc superconductors for AC power loss estimation,*" *IEEE Trans. On Magnetics*, vol. 33, no. 2, pp. 1568–1571, Mar. 1997.

[83] J. K. Sykulsk *et al.* "*Highly non-linear field diffusion in HTC superconducting tapes,*" *COMPEL - The international journal for computation and mathematics in electrical and electronic engineering*, vol. 18, no. 2, pp. 215–224, Jun. 1999.

[84] J. K. Sykulsk *et al.* "*2D modeling of field diffusion and AC losses in high temperature superconducting tapes,*" *IEEE Trans. On Magnetics*, vol. 36, no. 4, pp. 1178–1182, Jul. 2000.

[85] S. Stavrev *et al.*, "*Comparison of the AC losses of BSCCO and YBCO conductors by means of numerical analysis,*" *Supercond. Sci Technol.*, vol. 18, pp. 1300–1312, Aug. 2005.

[86] E. Pardo *et al.*, "*Numerical simulations of the angular dependence of magnetization AC losses: coated conductors, Roebel cables and double pancake coils,*" *Supercond. Sci Technol.*, vol. 18, p. 014008, Oct. 2011.

[87] S. Stavrev *et al.*, "*Eddy current self-field loss in Bi-2223 tapes with a.c. transport current,*" *Phys. C: Supercond.*, vol. 307, pp. 105–116, Oct. 1998.

[88] S. Stavrev *et al.*, "*Frequency dependence of AC loss in Bi-2223/Ag-sheathed tapes,*" *Phys. C: Supercond.*, vol. 310, pp. 86–89, Dec. 1998.

[89] C.M. Friend *et al.*, "*A European Project on the AC Losses of Bi-2223 Tapes for Power Applications,*" *IEEE Trans. On Appl. Supercond.*, vol. 9, no. 2, pp. 1165–1168, Jun. 1999.

[90] H. Lee *et al.*, "*Estimation of the AC loss of a YBCO coated conductor with metal substrate by Using Numerical calculation,*" *IEEE Trans. On Appl. Supercond.*, vol. 15, no. 2, pp. 1558–1561, Jun. 2005.

[91] D. Miyagi *et al.*, "*Measurement of magnetic properties of Ni-alloy substrate of HTS coated conductor in LN₂,*" *Phys. C: Supercond.*, vol. 468, pp. 1743–1746, Sept. 2008.

[92] F. Gomory *et al.,* "*AC losses in coated conductors,*" *Supercond. Sci. Technol.*, vol. 23, no. 3, p. 034012, Feb. 2010.

[93] S. Li *et al.,* "*Transport AC losses of a second-generation HTS tape with a ferromagnetic substrate and conducting stabilizer,*" *Supercond. Sci. Technol.*, vol. 28, no. 12, p. 125011, Nov. 2015.

[94] G. Liu *et al.*, "*Experimental and numerical study of frequency-dependent transport loss in YBa₂Cu₃O₇₋δ coated conductors with ferromagnetic substrate and copper stabilizer,*" *J. Appl. Phys.*, vol. 121, no. 24, p. 243902, Jun. 2017.

[95] B. Shen *et al.*, "*Investigation and comparison of AC losses on stabilizer-free and copper stabilizer HTS tapes,*" *Phys. C: Supercond.*, vol. 541, pp. 40–44, Aug. 2017.

[96] P. Zhou *et al.,* "*Transition frequency of transport ac losses in high temperature superconducting coated conductors,*" *J. Appl. Phys.*, vol. 126, n. 063901, Aug. 2019.

[97] COMSOL Multiphysics® v. 5.5, *www.comsol.com*. *COMSOL AB*, Stockholm, Sweden, 2020

[98] MATLAB. Version 2020a, *The Math Works Inc.*, Natick, Massachusetts, United States, 2020.

[99] R. Brambilla *et al.*, "*Development of an edge-element model for AC loss computation of high-temperature superconductors,*" *Supercond. Sci Technol.*, vol. 20, pp. 16–24, Nov. 2006.

[100] D. N. Nguyen *et al.*, "*A new finite-element method simulation model for computing AC loss in roll assisted biaxially textured substrate YBCO tapes,*" *Supercond. Sci Technol.*, vol. 23, no. 2, p. 025001, Dec. 2009.

[101] D. N. Nguyen *et al.*, "*AC loss study of antiparallel connected YBCO coated conductors,*" *Supercond. Sci Technol.*, vol. 22, p. 055014, Apr. 2009.

[102] P. Krüger, "*Optimisation of hysteretic losses in high-temperature superconducting wires,*" Ph.D. dissertation, Karlsruher Institut für Technologie (KIT), 2013.

[103] B.Y. Soek *et al.* "*A study on mitigation method of perpendicular magnetic field in HTS superconducting coils for power transformer,*" *IEEE Trans. On Magnetics*, vol. 15, no. 2, pp. 1871–1874, Jun. 2005.

[104] Z. Jiang *et al.*, "*Dynamic resistance of a high-T c coated conductor wire in a perpendicular magnetic field at 77 K,*" *Supercond. Sci Technol.*, vol. 30, no. 23, p. 03LT01, Jan. 2017.

[105] M. Ciszek *et al.*, "*Energy loss in YBCO-123 coated conductor due to AC/DC transport current and AC external perpendicular magnetic field,*" *Phys. C: Supercond.*, vol. 387, no. 1–2, pp. 230–233, May 2003.

[106] Q. Li *et al.* "*Numerical Modeling of Dynamic Loss in HTS-Coated Conductors Under Perpendicular Magnetic Fields,*" *IEEE Trans. On Magnetics*, vol. 28, no. 2, p. 6600106, Mar. 2018.

[107] K. P. Thakur *et al.* "*Numerical Computation of AC Losses and Flux Profiles in High-Aspect-Ratio Superconducting Strips in Perpendicular AC Magnetic Field,*" *IEEE Trans. On Magnetics*, vol. 19, no. 6, pp. 3770–3778, Dec. 2009.

[108] R. Brambilla *et al.*, "*Integral equations for the current density in thin conductors and their solution by the finite-element method*," *Supercond. Sci. Technol.*, vol. 21, p. 105008, Jul. 2008.

[109] P. M. Knupp, "*Remarks on mesh quality,*" *45th AIAA Aerospace Sc. Meeting Exhibit*, Reno, NV, Jan. 7–10, 2007.

[110] V. M. Rodriguez-Zermeno *et al.* "*Towards Faster FEM Simulation of Thin Film Superconductors: A Multiscale Approach,*" *IEEE Trans. On Magnetics*, vol. 21, no. 3, pp. 3273–3276, Jun. 2011.

[111] O. Tsukamoto *et al.*, "*Dependence of AC Losses in HTS Coated Conductors With Magnetic Substrates on Tensile Stresses,*" *IEEE Trans. On Appl. Supercond*, vol. 17, no.2, pp. 3144–3147, Jun. 2007.

[112] O. Tsukamoto *et al.*, "*Transport current losses in HoBaCuO-123 coated conductors with a Ni-alloy substrate,*" *Phys. C: Supercond.*, vol. 426–431, no. 2, pp. 1290–1294, Oct. 2005.

[113] G. T. Ma, "*Hysteretic ac loss in a coated superconductor subjected to oscillating magnetic fields: Ferromagnetic effect and frequency dependence,*" *Supercond. Sci. Technol.*, vol. 27, no. 6, p. 065011, 2014.

[114] P. Zhou *et al.*, "*Frequency-Dependent Transport AC Losses of Coated Superconductors Up To Tens of Kilohertz,*" *IEEE Trans. On Appl. Supercond.*, vol. 29, no. 5, p. 8201705, Aug. 2019.

[115] C. Barth *et al.*, "*Electro-mechanical properties of (RE)BCO coated conductors from various industrial manufacturers at 77 K, self-field and 4.2 K, 19 T,*" *Supercond. Sci Technol.*, vol. 28, p. 045011, Feb. 2015.

[116] E. H. Brandt, "*Thin superconductors in a perpendicular magnetic AC field: General formulation and strip geometry,*" *Phys. Rev. B*, vol. 49, no. 13, pp. 9024–9040, 1994.

[117] M. Vojenciak *et al.*, "*Losses in Bi-2223/Ag tape at simultaneous action of AC transport and AC magnetic field shifted in phase,*" *Journal of Physics: Conference Series,* vol. 43, pp. 63–66, Sept. 2005.

[118] M. C. Bouzo *et al.,* "*Modelling of coupling between superconductors of finite length using an integral formulation,*" *Supercond. Sci. Technol.*, vol. 17, no. 10, pp. 1103–1112, Jul. 2004.

[119] D. X. Chen *et al.,* "*AC susceptibility and critical-current densities in sintered $YBa_2Cu_3O7_{-\delta}$ superconductors,*" *Appl. Phys. Lett.*, vol. 89, no. 7, p. 072501, Aug. 2006.

[120] M. Elbaa *et al.,* "*Analytical modeling of an inductor in a magnetic circuit for pulsed field magnetization of HTS bulks,*" *IEEE Trans. Appl. Supercond*, vol. 28, no. 4, p. 8201306, Jun. 2018.

[121] A. M. Campbel, "*AC losses in High Tc Superconductors,*" *IEEE Trans. On Appl. Supercond.*, vol. 5, no. 2, pp. 682–687, 1995.

[122] S. Fleshler *et al.,* "*Measurement of the ac power loss of $(Bi,Pb)_2Sr_2Ca_2Cu_3O_x$ composite tapes using the transport technique,*" *Appli. Phys. Lett.,* vol. 67, no. 21, pp. 3189–3191, Sept. 1995.

[123] Y. Yang *et al.*, "*The influence on geometry on self-field AC losses of Ag-sheated Pd-Bi2223 tapes,*" *Phys. C: Supercond.*, vol. 256, pp 378–386, 1996.

[124] H. Eckelmann *et al.,* "*AC transport current losses of multifilamentary Bi(2223) tapes with varying filament geometries,*" *Phys. C: Supercond.*, vol. 295, pp. 198–208, Oct. 1998.

[125] B. Klincok *et al.*, "*The voltage signal on a superconducting wire in AC transport,*" *Supercond. Sci. Technol.*, vol. 18, pp. 694–700, 2005.

[126] K. Ryu *et al.*, "*Influence of tape's critical currents and current distributions on AC loss measurement in a multi-tape conductor,*" *IEEE Trans. On Appl. Supercond.*, vol. 15, no. 2, pp. 1611–1614, Jun. 2005.

[127] A. A. Sonin, "*The physics basis of dimensional analysis,*" MIT Cambridge, Massachusetts, United States, 1997

[128] D. G Schaeffer *et al.,* "*Nondimensionalization and Scaling. In: Ordinary Differential Equations: Basics and Beyond,*" *Texts in Applied Mathematics*, *Springer*, vol. 65, New York, United States, 2016.

[129] J. F. Sánchez Pérez *et al.,* "*Searching fundamental information in ordinary differential equations. Nondimensionalization technique,*" *PLoS ONE 12,* vol. 10, p. 0185477, Oct. 2017.

[130] K. P. Thakur *et al.,* "*Frequency-dependent critical current and transport ac loss of superconductor strip and Roebel cable,*" *Supercond. Sci. Technol.*, vol. 24, no. 6, Apr. 2011.

[131] C. P. Bean "*Magnetization of High-Field Superconductors,*" *Reviews of Modern Physics. American Physical Society*, vol. 36, no. 1, pp. 31–39, Jan. 1964.

[132] F. Sirois *et al.*, "*Comparison of Constitutive Laws for Modeling High-Temperature Superconductors,*" *IEEE Trans. On Appl. Supercond.*, vol. 29, no. 1, Jan. 2019.

[133] M. Sander and F. Grilli, "*FEM-calculations on the frequency dependence of hysteretic losses in coated conductors,*" *J Phys.: Conf. Ser.*, vol. 234, p. 022030, 2010.

[134] E. Demencik *et al., "Determination of I-V curves of HTS tapes from the frequency dependent AC transport loss," IEEE Trans. Appl. Supercond.*, vol. 26, no. 3, p. 9001004, Apr. 2016.

[135] M. Yazdani-Asrami *et al.*, "*Investigation on Effect of Magnetic Field Dependency Coefficient of Critical Current Density on the AC Magnetizing Loss in HTS Tapes Exposed to External Field," Journal of Superconductivity and Novel Magnetism*, vol. 31, no. 12, pp. 3899–3910, May 2018.

[136] E. Pardo *et al.*, "*Current distribution and ac loss for a superconducting rectangular strip with in-phase alternating current and applied field," Supercond. Sci. Technol.*, vol. 20, no.4, pp. 351–364, Mar. 2007.

[137] H. Shin *et al., "Critical Current Degradation Behavior in YBCO Coated Conductors Under Torsional Strain," IEEE Trans. On Appl. Supercond.*, vol. 17, no. 2, pp. 3274–3277, Jun. 2007.

[138] Y. Duan *et al., "Delamination and current-carrying degradation behavior of epoxy-impregnated superconducting coil winding with 2G HTS tape caused by thermal stress," AIP Advances*, vol. 10, no. 2, n. 025320, Feb. 2020.

[139] J. Ogawa *et al.*, "*n value and Jc distribution dependence of AC transport current losses in HTS conductors," Phys. C: Supercond.*, vol. 401, pp. 171–175, 2004.

[140] "*High Temperature Superconductors (HTS) for Energy Applications - 1st Edition,*" Edited by *Ziad Melhem*, Dec. 2011.

[141] S. Gourlay *et al.*, "*Unit 21 - HTS accelerator magnets,*" from the material available from the *US Particle Accelerator School*, Jun. 2018.

[142] A. Arsenault *et al.*, "*Implementation of the H-ϕ formulation in COMSOL Multiphysics for simulating the magnetization of bulk superconductors and comparison with the H-formulatio*n," arXiv:2006.13784.

[143] J. W. Eaton *et al.*, "*GNU Octave Manual – Free Your Numbers – 5th edition," Network Theory Limited*, Jan. 2020.

[144] J. A. Eikelboom, "*Apparatus for calorimetric measurement of a.c. losses in superconductors," Cryogenics,* vol. 31, no. 5, pp. 363–365, May 1991.

[145] Y. Liu *et al. "Investigations on the Calorimetric Method for Measurement of the AC Losses in Superconducting Tapes," J. Supercond. Nov. Magn.,* vol. 29, pp. 1173–1179, Jan. 2016.

[146] P. K. Ghoshal *et al., "Calorimetric method of ac loss measurement in a rotating magnetic field," AIP: Review of Scientific Instruments*, vol. 81, p. 074702 Jul. 2010.

[147] M. Breschi *et al.*, "*An electromagnetic method for measuring AC losses in HTS tapes without lock-in amplifier," Journal of Physics: Conference Series,* vol. 1559, no. 1, p. 012066, Jun. 2020.

[148] D. N. Nguyen *et al.*, "*Electrical measurements of AC losses in high temperature superconducting coils at variable temperatures,*" *Supercond. Sci. Technol.,* vol. 26, no. 9, p. 095001, Jul. 2013.

[149] S. Safran *et al., "AC loss characterization of single pancake BSCCO coils by measured different methods,*" *Phys. C: Supercond. and its Appl.*, vol. 541, pp. 45-49, Oct. 2017

[150] J. P. Murphy *et al., "Experiment Setup for Calorimetric Measurements of Losses in HTS Coils Due to AC Current and External Magnetic Fields,*" *IEEE Trans. On Appl. Supercond.*, vol. 23, no. 3, p. 4701505, Jun. 2013.

[151] S. P. Ashworth *et al., "Local calorimetry to measure AC losses in HTS conductors,*" *Cryogenic,* vol. 41, no. 2, pp. 77–89, Feb. 2001.

[152] M. P. Oomen, "*AC loss in superconducting tapes and cables,*" *Ph.D dissertation, University of Twente, Enschede, The Netherlands*, Apr. 2000.

[153] R. Pei et al., *"High-precision digital lock-in measurements of critical current and AC loss in HTS 2G-tapes,*" *in 2008 SICE Annual Conference*, pp. 3147–3150, 2008.

[154] S. K. Olsen *et al., "Alternating current losses of a 10 meter long low loss superconducting cable conductor determined from phase sensitive measurements,*" *Supercond. Sci. Technol.*, vol. 12, no. 6, pp. 360–365, Jun. 1999.

[155] B. Shen *et al., "Power dissipation in HTS coated conductor coils under the simultaneous action of AC and DC currents and fields,*" *Supercond. Sci. Technol.*, vol. 31, no. 7, p. 075005, Jul. 2018.

[156] *https://www.keysight.com/it/en/assets/7018-05928/data-sheets/5992-2572.pdf*

[157] LabVIEW Professional Development System. Version 18.0.1f4. *National Instruments Corp*.

[158] *https://www.picotech.com/oscilloscope/4444/picoscope-4444-overview*

[159] *https://www.qsc.com/it/live-sound/prodotti/amplificatori-di-potenza/serie-gx/gx5/*

[160] A. W. Oppenheim *et al., "Discrete-time signal processing,*" *Third edition, Prentice Hall*, 2010.

[161] *Private communication, courtesy of Prof. F. Grilli.*

[162] M. Solovyov *et al., "Non-uniformity of coated conductor tapes,*" *Supercond. Sci Technol.*, vol. 26, no.11, p. 115013, Oct. 2013.

[163] *"Encyclopedia of Physical Science and Technology (3rd Edition)" Academic Press*, Oct. 2001.

[164] S. Wimbush and N. Strickland, "*Critical current characterisation of SuNAM SAN04200 2G HTS superconducting wire,*" Figshare Dataset, *https://doi.org/10.6084/m9.figshare. 5182354.v1*, 2017.

[165] C. Senatore *et. al., "Progresses and challenges in the development of high-field solenoidal magnets based on RE123 coated conductor," Supercond. Sci. Technol.*, vol. 27, p. 103001, Sept. 2014.

[166] S. Ito *et. al., "Bridge-type mechanical lap joint of HTS STARS conductors using anintegrated joint piece," Fusion Eng. and Design*, vol. 146, part. A, pp. 590–593, Sept. 2019.

[167] S. Ito *et. al., "Bridge-Type Mechanical Lap Joint of a 100 kA-Class HTS Conductor having Stacks of GdBCO Tapes," Plasma and Fusion Research*, vol. 9, p. 3405086, Apr. 2014.

[168] K. Kawai *et al., "Optimization of a Mechanical Bridge Joint Structure in a Stacked HTS Conductor," IEEE Trans. On Appl. Supercond.*, vol. 23, no. 3, p. 4801704, Jun. 2013.

[169] H. Shin *et al., "Joint characteristics of ultrasonic welded CC bridge joints for HTS coil applications," Supercond. Sci. Technol.*, vol. 33, p. 115007, Sept. 2020.

[170] K. L. Kim *et al., "Effect of Winding Tension on Electrical Behaviors of a No-Insulation (RE)BCO Pancake Coil," IEEE Trans. On Appl. Supercond.*, vol. 24, no. 3, p. 4600605, Jun. 2014.

[171] *www.ni.com/pdf/manuals/377024a.pdf*

[172] *www.arepoc.sk/uploaded/download/HallProbes.PDF*

[173] *https://nanoscience.oxinst.com/assets/uploads/products/nanoscience/documents/Mercury%20Instrumentation%20Brochure_Aug2018.pdf*

[174] Y. G. Kim *et al. "Investigation of HTS racetrack coil without turn-to-turn insulation for superconducting rotating machines," IEEE Trans. Appl. Supercond.,* vol. 22, no. 3, p. 5200604, Jun. 2012.

[175] Y. G. Kim *et al. "Rotating Permanent Magnets Based Flux Pump for HTS No-Insulation Coil," IEEE Trans. Appl. Supercond.,* vol. 29, no. 5, p. 5202106, Aug. 2019.

[176] X. Wang *et al. "Charging Behavior in No-Insulation (RE)BCO Pancake Coils," IEEE Trans. Appl. Supercond.,* vol. 25, no. 3, p. 4601805, Jun. 2015.

[177] J. Geng *et al., "A parallel co-wound no-insulation (RE)BCO pancake coil for improving charging delays," Supercond. Sci. Technol.*, vol. 32, no. 3, p. 084002, Jun. 2019.

[178] S. Kim *et al., "Method for generating linear current-field characteristics and eliminating charging delay in no-insulation superconducting magnets," Supercond. Sci. Technol.*, vol. 30, no. 3, p. 035020, Feb. 2017.

[179] Y. Wang *et al., "An equivalent circuit grid model for no-insulation HTS pancake coils," Supercond. Sci. Technol.*, vol. 28, no. 4, p. 045017, Mar. 2015.

[180] J. W. Ekin*., 'Experimental techniques for low-temperature measurements – Cryostat Design, Material Properties, and Superconductor Critical-Current Testing', Oxford University Press,* 2006.

[181] *https://copperalliance.org.uk/knowledge-base/resource-library/busbars-guidance- design-installation*

[182] *https://www.amsc.com*

[183] M. Breschi, *et al. "Dependence of Critical Current and Quench Energy of BSCCO-2223 Tapes on Bending Diameter," IEEE Trans. on Appl. Supercond.*, vol. 26, n. 3, p. 8000605, Feb. 2016.

[184] *https://literature.cdn.keysight.com/litweb/pdf/5964-8267.pdf?id=1000002297-1:epsg:man*

[185] *https://www.danisense.com/images/pdf/0-600A/DS600UB-1V.pdf*

[186] W. H. Hayt and J. E. Kemmerly, "*Engineering Circuit Analysis (5th Ed.)," New York: McGraw Hill*, 1993.

[187] J. R. Cash and A. H. Karp, *"A variable order Runge-Kutta method for initial value problems with rapidly varying right-hand sides," Trans. On Math. Softw.*, vol. 16, no.3, pp. 201–222, Sept. 1990.

[188] S. C. Wimbush and N. M. Strickland, "*A Public Database of High-Temperature Superconductor Critical Current Data," IEEE Trans. Appl. Supercond.*, vol. 27, no. 4, p. 8000105, Jun. 2017.

[189] Z. Ni *et al., "Globally Optimal Algorithm for Design of 0.7 T Ac-tively Shielded Whole-Body Open MRI Superconducting Magnet System," IEEE Trans. Appl. Supercond.*, vol. 23, no. 3, p. 4401104, Jun. 2013.

[190] Q. Wang *et al., "Design and Test of Conduction-Cooled High Ho-mogenous Magnetic Field Superconducting Magnet for Gyrotron," IEEE Trans. Appl. Supercond.*, vol. 17, no. 2, p. 2319, Jun. 2007.

[191] Z. Zhang *et al., "An Experimental Investigation of the Transient Response of HTS Non insulation Coil," J. Supercond. Nov. Magn.*, vol. 30, pp. 387–393, Oct. 2016.

[192] Y. Wang *et al., "Ramping turn-to-turn loss and magnetization loss of a No-Insulation $(RE)Ba_2Cu_3O_x$ high temperature superconductor pancake coi," J. Appl. Phys.*, vol. 121, p. 113903, Mar. 2017.

[193] Y. Wang *et al., "Non-uniform ramping losses and thermal optimization with turn-to-turn resistivity grading in a $(RE)Ba_2Cu_3O_x$ magnet consisting of multiple no-insulation pancake coils," J. Appl. Phys.*, vol. 122, p. 053902, Aug. 2017.

[194] Y. Pan *et al., "The Field Decay Characteristic for a Closed HTS No-Insulation Coil With Partial Tape Exposed to an AC Magnetic Field," IEEE Trans. Appl. Supercond.*, vol. 29, no. 5, p. 8201805, Aug. 2019.

[195] Y. J. Hwang *et al., "Evaluations on AC Electrical Characteristics of No-Insulation Coil for Power Devices," IEEE Trans. Appl. Supercond.*, vol. 23, no. 3, p. 4700604, Jun. 2013.

[196] J. Zhu *et al., "A Novel AC Loss Measurement Technology for High Temperature Superconducting Cable With Large Current Capacity Using a Compensation Coil," IEEE Trans. Appl. Supercond.*, vol. 25, no. 3, p. 4701204, Jun. 2015.

[197] D. N. Nguyen *et al., "Electrical measurements of AC losses in high temperature superconducting coils at variable temperatures," Supercond. Sci. Technol.*, vol. 26, p. 095001, Jul. 2013.

[198] S. Imparato *et al., "Experimental Evaluation of AC Losses of a DC Restive SFCL Prototype," IEEE Trans. Appl. Supercond.*, vol. 20, no. 3, pp. 1199–1202, Jun. 2010.

[199] W. Yuan *et al., "Measurements and calculations of transport AC loss in second generation high temperature superconducting pancake coils," J. Appl. Phys.*, vol. 110, p. 113906, Dec. 2011.

[200] M. D. Ainslie *et al., "Modeling and Electrical Measurement of Transport AC Loss in HTS-Based Superconducting Coils for Electric Machines," IEEE Trans. Appl. Supercond.*, vol. 21, no. 3, pp. 3265–3268, Jun. 2011.

[201] Y Wang *et al., "Review of AC Loss Measuring Methods for HTS Tape and Unit," IEEE Trans. Appl. Supercond.*, vol. 24, no. 5, p. 9002306, Oct. 2014.

[202] J. Souc *et al., "Theoretical and experimental study of AC loss in high temperature superconductor single pancake coils," Supercond. Sci. Technol.*, vol. 22, no. 1, p. 015006, Nov. 2008.

[203] J. Kim *et al., "Transport AC Loss Measurements in Superconducting Coils," IEEE Trans. Appl. Supercond.*, vol. 21, no. 3, pp. 3269–3272, Jun. 2011.

[204] Y. Liao *et al., "An Automatic Compensation Method for Measuring the AC loss of a Superconducting Coil," IEEE Trans. Appl. Supercond.*, vol. 26, no. 7, p. 9001805, Oct. 2016.